

#### **Archive ouverte UNIGE**

https://archive-ouverte.unige.ch

Thèse 2015

**Open Access** 

This version of the publication is provided by the author(s) and made available in accordance with the copyright holder(s).

From ion selective optodes to photoelectric conversion

\_\_\_\_\_\_

Xie, Xiaojiang

#### How to cite

XIE, Xiaojiang. From ion selective optodes to photoelectric conversion. Doctoral Thesis, 2015. doi: 10.13097/archive-ouverte/unige:75039

This publication URL: <a href="https://archive-ouverte.unige.ch/unige:75039">https://archive-ouverte.unige.ch/unige:75039</a>

Publication DOI: <u>10.13097/archive-ouverte/unige:75039</u>

© This document is protected by copyright. Please refer to copyright holder(s) for terms of use.

Section de chimie et biochimie

Prof. Eric Bakker

Département de chimie minérale et analytique

## From Ion Selective Optodes to Photoelectric Conversion

### THÈSE

Présentée à la Faculté des Sciences de l'Université de Genève

Pour obtenir le grade de Docteur ès Sciences, mention Chimie

par

Xiaojiang XIE

de Chine

Thèse N° 4810

**GENÈVE** 

Migros Print-Shop Plainpalais

2015

### Table of Contents:

Abstract / R ésum é	3
List of publications.	5
Chapter 1. Introduction to Miniaturized Ion Selective Optodes, Photodynamic Optical Ion Sensor and Photoelectr Based on Photo-Isomerization	
Chapter 2. Ultrasmall Fluorescent Ion-Exchanging Nanospheres Containing Selective Ionophores	38
Chapter 3. Potassium-Selective Optical Microsensors Based on Surface Modified Polystyrene Microspheres	51
Chapter 4. pH Independent Particle-Based Ion Optode Sensors based on Exhaustive Ion-Selective Nanospheres	59
Chapter 5. Ionophore based Ion-Selective Optical NanoSensors Operating in Exhaustive Sensing Mode	66
Chapter 6. Potentiometric Response from Ion-Selective Nanospheres with Voltage-Sensitive Dyes	77
Chapter 7. Oxazinoindolines as Fluorescent H <sup>+</sup> Turn-On Chromoionophores for Optical and Electrochemical Ion S	ensors85
Chapter 8. Direct Optical Carbon Dioxide Sensing based on a Polymeric Film Doped with a Selective Molecular Ionophore	
Chapter 9. A Non-Severinghaus Potentiometric Dissolved CO <sub>2</sub> Sensor with Improved Characteristics	121
Chapter 10. Reversible Photodynamic Chloride-Selective Sensor Based on Photochromic Spiropyran	131
Chapter 11. Light Controlled Reversible Release and Uptake of Potassium Ions from Ion-Exchanging Nanospheres.	138
Chapter 12. Visible Light Induced Photoacid Generation within Plasticized PVC Membranes for Copper (II) Ion Ex	traction148
Chapter 13. Photocurrent Generation Based on a Light-Driven Proton Pump in an Artificial Liquid Membrane	154
Chapter 14. Photoelectric Conversion based on Proton-Coupled Electron Transfer Reactions	170
Acknowledgements	178

#### **Abstract**

Our planet is covered with water in which a large number of ions play various roles. Ion selective sensors are important tools for the detection of ionic species in both qualitative and quantitative ways. Ionophore based ion selective optical sensors (optodes) are very specific and versatile owing to the use of highly selective ionophores. This type of ion selective sensors is often composed of an ionophore, an ion exchanger and a chromoionophore. In this thesis work, ion selective optodes based on polymeric films, microspheres and nanospheres are presented. Electrochemical and optical carbon dioxide sensors were successfully obtained using a tweezers-like carbonate ionophore. A new family of chromoionophore based on oxazinoindolene was synthesized and characterized in plasticized poly(vinyl chloride) (PVC) films and ion selective electrodes. Ion selective optical nanosensors with average diameter of ca. 50 nm, where bis(2-ethylhexyl) sebacate (DOS) and a copolymer Pluronic F-127 constituted the matrix, were obtained with solvent displacement. Microsensors were fabricated by adsorption of lipophilic sensing components on the hydrophobic surface of polystyrene.

In addition to operating the sensors in conventional equilibrium based and passive sensing mode, exhaustive detection mode and photoactivated mode have been explored. The exhaustive detection mode was achieved with ion selective optical nanospheres because of the increased surface to volume ratio and thus ultrafast sensor response. This exhaustive sensing mode was used to overcome the pH cross response at a certain pH. However, owing to the use of chromoionophore, the pH cross-response cannot be completely eliminated. Voltage sensitive dyes were then introduced into ion selective nanospheres, converting electrochemical signal into fluorescence out. The voltage sensitive dyes were not pH sensitive in a wide range of pH and the pH dependence was no longer a problematic issue. The calibration curves for potassium ion selective optical nanosensors were the same in acidic or basic solution. The photoactivated mode was enabled by a photoswitchable compound, spiropyran, which exhibited a much higher pKa in the ring opened Mc form. The Mc form can be switched back to the ring closed Sp form by visible light irradiation. A photoswitchable chloride ion selective optical sensor was developed as the first example. The switching of the photoactivable sensor also induced an ion flux at the sensor-sample interface. This light triggered ion flux was successly used to bring about phototriggered ion concentration perturbations in aqueous solutions. The free potassium ion concentration was modulated by using ion selective nanospheres incorporating spiropyran, ion exchanger and valinomycin. Phototriggered ion perturbation was also achieved by doping plasticized PVC membrane with a photoacid generator to create additional anionic sites for ion exchange.

Owing to the basicity change of the different forms of spiropyran, an artificial proton pump in polymeric liquid membrane was created and used in a photoelectrochemical cell to convert light to electricity. Both direct current and alternating current were obtained. Coupling the photoswitchable spiropyran with proton coupled electron transfer (PCET) reactions gave birth to a new family of solar cells. Although the energy conversion efficiency is not yet high, there is still much more to explore, suggesting many future opportunities for this newly-born field.

#### R ésum é

Notre plan àte est recouverte d'eau dans laquelle un grand nombre d'ions jouent des rôtes differents. Les capteurs s'éctifs pour de ions sont des outils importants pour la detection qualitative et quantitative d'esp àces ioniques. Les capteurs optiques s'éctifs (optodes) pour des ions sont très spécifiques et polyvalent grâce à l'utilisation d'ionophores hautement s'éctifs. Ce type de capteurs s'éctifs est souvent composé d'un ionophore, d'un échangeur d'ions et d'un chromoionophore. Dans ce travail de thèse, optodes s'éctifs pour des ions basés sur des films polymériques, des microsphères et des nanosphères sont présentés. Des capteurs pour dioxyde de carbone dectrochimiques et optiques ont d'é obtenus avec succès en utilisant un ionophore carbonate de principe moléculaire de pincette. Une nouvelle famille de chromoionophores basé sur des oxazinoindolènes a d'é synthétisé et caractérisé en poly plastifié (chlorure de vinyle) (PVC) et des films pour des dectrodes s'éctives d'ions. Des nanocapteurs optiques s'éctifs pour des ions avec un diamètre moyen de ca. 50 nm, où le bis (2-éthylhexyl) s'ébacate (DOS) et le copolymère Pluronic F-127 constitue la matrice ont été obtenu par d'éplacement de solvant. Les microcapteurs ont aussi étéfabriqués par adsorption des composants lipophiles de d'éction sur la surface hydrophobe de polystyrène.

Appart que d'exploiter les capteurs en équilibre classique àbase et le mode de d'éection passive, le mode de d'éection exhaustive et le mode photoactiv é ont été explorés. Le mode de déection exhaustive a été réalis ée avec les nanosphères optiques s'ectifs pour des ions en raison de l'augmentation de surface par rapport au volume, qui rend la réponse du capteur ainsi ultrarapide. Ce mode de déection exhaustive a été utilisé pour surmonter l'influence de pH de réaction crois ét dans une certaine gamme de pH. Toutefois, en raison de l'utilisation de chromoionophore, la réponse transversale de pH ne peut pas être complètement diminée. Des colorants sensibles aux changements de tensions d'ectriques ont été ensuite introduits dans des nanosphères s'électifs pour des ions par conversion d'un signal dectrochimique en fluorescence. Les colorants sensibles à la tension ne sont pas sensibles au pH dans une large gamme et la dépendance de pH n'éait plus problématique. Les courbes d'étalonnage des nanocapteurs optiques s'éctifs pour l'ion potassium sont les mêmes en mileu acide ou basique. Le mode photoactivé a été établi par un composé de spiropyranne photoactivable, qui montre un pKa beaucoup plus devé dans la forme cyclique ouverte de Mc. La forme Mc peut être remise dans la forme d'anneau fermé Sp par irradiation avec lumi ère visible. Un capteur optique photochangeable et s'électif pour chlorure a étémis en évidence comme étant le premier exemple. La commutation du capteur photoactivable induisait également un flux d'ions à l'interface capteur-solution. Cette lumi ère d'éclenchait un flux d'ions qui était utilisé pour faire osciller la concentration de ions dans la solution aqueuse. La concentration du potassium libre a été modul ée par des nanosphères s'éectifs pour ions, incorpor és avec spiropyranne, échangeur d'ions et valinomycine. La perturbation d'ions par photoactivation a également ét ér éalis é par dopage d'une membrane de PVC plastifi é par gén érateur de photoacide pour cr éer des sites anioniques supplémentaires pour déclencher l'échange d'ions.

En raison de la basicité différente du spiropyranne sous différentes formes, une pompe à protons dans la membrane artificielle liquide polymère a étécrééet utilisé dans une cellule photo dectrochimique pour convertir la lumière en dectricité Des courants continus et des courants alternatifs ont été obtenu. Le couplage du spiropyranne photoactivable avec un transfert d'électrons couplé à une réaction de protons (PCET) ont donné naissance à une nouvelle famille de cellules solaires. Bien que l'efficacité de conversion d'énergie n'est pas encore élevé il y reste encore beaucoup à explorer et probablement beaucoup plus de fruits s'attendent dans ce nouveau domaine.

#### **List of Publications**

#### Review and Opinion Articles:

- 1) Xiaojiang Xie\* and Eric Bakker\*, "Ion Selective Optodes: From Bulk to Nanoscale", *Anal. Bioanal. Chem.*, in press, DOI: 10.1007/s00216-014-8413-4
- 2) <u>Xiaojiang Xie</u>\* and Eric Bakker\*, "Creating electrochemical gradients by light: from bio-inspired concepts to photoelectric conversion", *Phys. Chem. Chem. Phys.*, 2014, 16, 19781-19789
- 3) <u>Xiaojiang Xie</u>\* and Eric Bakker\*, "Bringing Ion-Selective Sensors to the Nanoscale: Blurring the Lines Between Sensing and Bulk Solution Chemistry", *The Analytical Scientist*, 2014, 20, 17-18
- 4) Xiaojiang Xie\* and Eric Bakker\*, "Detecting and Manipulating Ions: From Potentiometry to the Nanoscale", *Q&More*, 2014, 02, 5-7

#### Research Articles:

- 1) Jingying Zhai, Xiaojiang Xie and Eric Bakker\*, "Anion-Exchange Nanospheres as Titration Reagents for Anionic Analytes", *Anal. Chem.*, submitted
- Jingying Zhai, <u>Xiaojiang Xie</u> and Eric Bakker\*, "Ion-selective Optode Nanoparticles as Heterogeneous Indicator Reagents in Complexometric Titrations", *Anal. Chem.*, 2015, 87 2827-2831
- 3) <u>Xiaojiang Xie</u>, Jingying Zhai, Gaston A. Crespo and Eric Bakker\*, "Ionophore-Based Ion-Selective Optical NanoSensors Operating in Exhaustive Sensing Mode", *Anal. Chem.*, 2014, 86 (17), 8770–8775
- 4) <u>Xiaojiang Xie</u>, Jingying Zhai and Eric Bakker\*, "Potentiometric Response from Ion-Selective Nanospheres with Voltage-Sensitive Dyes", *J. Am. Chem. Soc.*, 2014, 136 (47), 16465–16468
- 5) <u>Xiaojiang Xie</u>, Günter Mistlberger, and Eric Bakker\*, "Visible Light Induced Photoacid Generation within Plasticized PVC Membranes for Copper (II) Ion Extraction", *Sensors and Actuators*, *B*, 2014, 204, 807-810
- 6) Jingying Zhai, Xiaojiang Xie and Eric Bakker\*, "Receptor-doped ion-exchange nanospheres as novel reagents for complexometric titrations", *Chem. Commun.*, 2014, 50, 12659-12661
- 7) Eric Bakker\*, Mary-Lou Tercier-Waeber, Thomas Cherubini, Miquel Coll Crespi, Gast on A. Crespo, Maria Cuartero, Majid Ghahraman Afshar, Zdenka Jarolimova, St ohahraman Afshar, Zdenka Jarolimova, St ohahraman Mongin, Bastien N ol, Nadezda Pankratova, Romain Touilloux, Xiaojiang Xie, Jingying Zhai, "Environmental Sensing of Aquatic Systems at the University of Geneva", *Chimia*, 2014, 68(12). DOI: 10.2533/chimia.2014.899
- 8) Zdeňka Jarolímová, Gastón A. Crespo, <u>Xiaojiang Xie</u>, Majid Ghahraman Afshar, Marcin Pawlak and Eric Bakker\*, "Chronopotentiometric Carbonate Detection with All-Solid-State Ionophore-Based Electrodes", *Anal. Chem.*, 2014, 86 (13), 6307–6314

- 9) Majid Ghahraman Afshar, Gast ón A. Crespo, <u>Xiaojiang Xie</u>, and Eric Bakker\*, "Direct Alkalinity Detection with Ion-Selective Chronopotentiometry", *Anal. Chem.*, 2014, 86 (13), 6461–6470
- 10) Xiaojiang Xie, Gaston A. Crespo, Günter Mistlberger and Eric Bakker\*, "Photocurrent generation based on a light-driven proton pump in an artificial liquid membrane", Nat. Chem., 2014, 6(3), 202-207 Highlight by Chimia, 2014, 68(4), 271 and Chemistry World, 02. Feb, 2014
- 11) <u>Xiaojiang Xie</u>\* and Eric Bakker\*, "Photoelectric Conversion Based on Proton-Coupled Electron Transfer Reactions", *J. Am. Chem. Soc.*, 2014, 136 (22), 7857–7860 Selected in *ACS Virtual Issue: Inorganic Chemistry Driving the Energy Sciences*
- 12) <u>Xiaojiang Xie\*</u>, Jingying Zhai, Gastón A. Crespo, Istvan Szilagyi, and Eric Bakker\*, "Potassium-Selective Optical Microsensors based on Surface Modified Polystyrene Microspheres", *Chem. Commun.*, 2014, 50(35), 4592-4595
- 13) Xiaojiang Xie, Jingying Zhai and Eric Bakker\*, "pH Independent Nano-Optode Sensors Based on Exhaustive Ion-Selective Nanospheres", *Anal. Chem.*, 2014, 86(6), 2853-2856
- 14) <u>Xiaojiang Xie</u>\*, and Eric Bakker<sup>\*</sup>, "Light-Controlled Reversible Release and Uptake of Potassium Ions from Ion-Exchanging Nanospheres", *ACS Appl. Mater. Interfaces*, 2014, 6 (4), 2666–2670
- 15) <u>Xiaojiang Xie</u>, Günter Mistlberger, and Eric Bakker\*, "Ultrasmall Fluorescent Ion-Exchanging Nanospheres Containing Selective Ionophores", *Anal. Chem.*, 2013, 85 (20), 9932–9938
- 16) Xiaojiang Xie, Gastón A. Crespo, and Eric Bakker\*, "Oxazinoindolines as Fluorescent H<sup>+</sup> Turn-On Chromoionophores For Optical and Electrochemical Ion Sensors", *Anal. Chem.*, 2013, 85 (15), 7434–7440
- 17) Günter Mistlberger\*, Xiaojiang Xie, Marcin Pawlak, Gast ón A. Crespo, and Eric Bakker\*, "Photoresponsive Ion Extraction/Release Systems: Dynamic Ion Optodes for Calcium and Sodium Based on Photochromic Spiropyran", *Anal. Chem.*, 2013, 85 (5), 2983–2990
- 18) Xiaojiang Xie and Eric Bakker\*, "Non-Severinghaus Potentiometric Dissolved CO2 Sensor with Improved Characteristics", *Anal. Chem.*, 2013, 85 (3), 1332–1336
- 19) <u>Xiaojiang Xie</u>, Günter Mistlberger, and Eric Bakker\*, "Reversible Photodynamic Chloride-Selective Sensor Based on Photochromic Spiropyran", *J. Am. Chem. Soc.*, 2012, *134* (41), 16929–16932
- 20) Günter Mistlberger, Gast ón A. Crespo, <u>Xiaojiang Xie</u>, and Eric Bakker\*, "Photodynamic ion sensor systems with spiropyran: photoactivated acidity changes in plasticized poly(vinyl chloride)", *Chem. Commun.*, 2012, 48(45), 5662-5664
- 21) Xiaojiang Xie, Marcin Pawlak, Mary-Lou Tercier-Waeber, and Eric Bakker\*, "Direct Optical Carbon Dioxide Sensing Based on a Polymeric Film Doped with a Selective Molecular Tweezer-Type Ionophore", *Anal. Chem.*, 2012, 84 (7), 3163–3169
- 22) Eric Bakker\*, Gaston A. Crespo, Ewa Grygolowicz-Pawlak, Günter Mistlberger, Marcin Pawlak, <u>Xiaojiang Xie</u>, "Advancing membrane electrodes and optical ion sensors", *Chimia*, 2011, 65(3), 141-149

# Chapter 1. Introduction to Miniaturized Ion Selective Optodes, Photodynamic Optical Ion Sensor and Photoelectric Conversion Based on Photo-Isomerization

This chapter serves as a general introduction to this thesis work and provides an overview of the current state of research within the fields. Apart from this introductory chapter and the final acknowledgement, the thesis work has been divided into three sections. Section 1 is composed of chapter 2 to chapter 9, focusing on the miniaturization of ion selective optodes and how to overcome the pH cross-response. Section 2 is composed of chapter 10 to chapter 12, where photodynamic optical ion sensors and ion perturbation will be discussed. Section 3 is composed of chapter 13 and 14, focusing on photoelectric conversion based on photo-isomerization reactions.

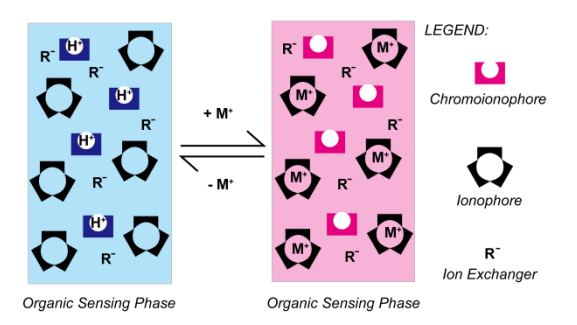
#### PART 1. INTRODUCTION TO MINIATURIZED ION SELECTIVE OPTODES

This has been published in: Xiaojiang Xie\* and Eric Bakker\*, "Ion Selective Optodes: From Bulk to Nanoscale", *Anal. Bioanal. Chem.*, in press, DOI: 10.1007/s00216-014-8413-4

The quantification and monitoring of ionic species is a ubiquitous challenge encountered in but not limited to environmental science, biochemical research, food chemistry and clinical diagnostics. Among other techniques such as electrochemical methods, atomic (flame) emission spectrometry (AES), mass spectroscopy, atomic absorption spectrometry (AAS), fluorimetry and capillary electrophoresis (CE), ion selective optical sensors provide a number of advantages with low cost and high versatility and compatibility with other assays. A variety of optical ion sensors have been discovered, including fluorescent molecular probes, surface modified nanomaterials and biologically expressed proteins.

It is unlikely that one type of sensor will dominate the entire field because each has its advantages and limitations with regard to specific application. For instance, when applied to intracellular imaging, many synthetic molecular probes may leach, sequestre, have a limited loading concentration and cause cytotoxicity and photo-toxicity. They cannot differentiate cell types or cellular compartments. But on the other hand, they are bright and easy to handle. The delivery can be noninvasive as well. Autofluorescent protein-based genetically encoded indicators can be expressed in vivo at specific locations but the whole process can be time-consuming. However, the varieties of the fluorophores for autofluorescent proteins are quite limited and their brightness needs improvement. Functionalized nanomaterials can overcome some of the disadvantages mentioned above, but delivery of large nanoparticles can be quite invasive and their selectivity and biocompatibility can also be problematic.

Ionophore-based ion selective optical sensors, also called ion selective optodes, take advantage of the excellent selectivity of readily



Scheme 1.1.1. Schematic illustration of how an ion selective optode containing a lipophilic pH indicator (chromoionophore), an ion receptor (ionophore) and an ion exchanger ( $R^-$ ) works with constant pH condition. The three sensing components are embedded in an organic hydrophobic environment that remains electrically neutral. Increasing the  $M^+$  level will result in a decrease in the protonation degree of the chromoionophore (and vice versa), which can be optically detected.

available ionophores (ion receptors). The working principle is shown in Scheme 1.1.1. Compared to other types of optical ion sensors, such as organic fluorescent molecular probes, the recognition of the analyte does not directly result in an optical signal change from a reporter covalently attached to the binding moiety. Instead, the recognition part and the optical reporter are two separate entities. An ionophore is used for the ion recognition while a lipophilic pH indicator (also called chromoionophore) acts as the optical reporter. As the analyte level in the sample increases, the hydrogen ion concentration in the sensor decreases on the basis of ion-exchange. Therefore, the analyte activity can be detected indirectly by monitoring the hydrogen ion level in the sensor.

Ion selective optodes are versatile optical sensing tools that emerged from the field of polymeric membrane ion selective electrodes (ISEs) and are attractive for their sensor specificity because of the selective ionophores directly adopted from their ISEs counterparts. Moreover, the use of a separate chromoionophore simplifies the signal transducing mechanism between the recognition of the target ion and the optical signal output. Several reviews have appeared in the past that emphasized different attributes, such as sensor response mechanism, materials and potential applications. Pecently, there has been a growing interest in micrometer and nanometer sized ion selective optodes that allow one to apply them to reduced sample volumes. The following highlights recent advances in ionophore based ion selective optodes associated with their miniaturization and summarize the criteria and possible issues likely to be met to realize and utilize such miniaturized sensors.

#### 1.1.1 Ion Selective Optodes Mechanism

In 1982, Charlton et al. introduced a K<sup>+</sup> assay where valinomycin doped test strips were used to detect K<sup>+</sup> based on the coextraction of K<sup>+</sup> and an anionic dye that was incubated beforehand in diluted samples.<sup>26</sup> This anionic dye, erythrosine B, provided a colorimetric reading for the sensor strip. This formed the first sensor concept that closely resembled modern ion optodes. However, the field of ion optodes did not grow rapidly until 1989, when Morf et al. proposed to add a lipophilic pH indicator to the sensing phase instead of mixing dye molecules with the sample.<sup>27</sup> This lipophilic pH indicator was named chromoionophore. The same group subsequently reported neutral carrier based optodes for ammonium and calcium ions, representing the first successful examples.<sup>28,29</sup>

Today, classical film-based ion optodes contain the following materials: an ionophore, an ion exchanger, a chromoionophore and a nonreactive hydrophobic polymer or solvent matrix. The actual combination of the materials is dependent on the target ions and can differ from case to case. Exhaustive combinations for cationic sensor and anionic sensor have been listed in the literature and will not be repeated

$$(a) \\ \bigcirc Q \\ \bigcirc Q \\ \bigcirc CH_3 \\ \bigcirc Q \\ \bigcirc CH_2 \\ \bigcirc CH_3 \\ \bigcirc Q \\ \bigcirc Q$$

**Figure 1.1.1.** Chemical structures and abbreviations for the sensing components of a  $Ca^{2+}$  selective optode (reference 28) and a  $CO_3^{2-}$  selective optode (reference 30).

here.<sup>25</sup> For a cationic optode sensor, such as for Na<sup>+</sup>, K<sup>+</sup> and Ca<sup>2+</sup>, the sensing components typically include an electrically neutral chromoionophore, a cation exchanger and an ionophore, which is mostly neutral as well. To detect anionic species such as NO<sub>2</sub><sup>-</sup>, NO<sub>3</sub><sup>-</sup>, CO<sub>3</sub><sup>2-</sup> and Cl<sup>-</sup>, a charged chromoionophore, an anion exchanger and a neutral ionophore are combined. Fig. 1.1.1 shows the chemical structures of the required sensing components for a Ca<sup>2+</sup> selective optode<sup>28</sup> and a CO<sub>3</sub><sup>2-</sup> selective optode (see Chapter 8)<sup>30</sup> as examples. CO<sub>2</sub> sensors based on ion selective optodes and its counter-part ISEs will be demonstrated in Chapter 8 and 9.

It is known that cation-selective optodes respond to the ratio of the analyte activity and the proton activity, while anion responsive optodes to the product of the analyte activity and the proton activity.<sup>21</sup> The reason for this is that the chromoionophores used in these sensors made protons inevitably the reference ions in all these sensing schemes. Wolfbeis and co-workers investigated ion optodes modified with polarity sensitive dyes in the absence of chromoionophore.<sup>31-33</sup> This approach resembles Charlton's work in 1982, but the polarity sensitive dyes used are more lipophilic than erythrosine B. Voltage sensitive dyes were recently incorporated in ionophore-based ion selective nanospheres to act as reference ions (Chapter 6).<sup>34</sup> In this case, the reference ions are no longer protons but the electrically charged voltage sensitive dyes. The voltage sensitive dye partitions between the organic sensing phase and the aqueous sample phase, the process of which being governed by thermodynamic equilibria. This part will be further discussed in Chapter 6.

Fluorescence intensity and absorbance are by far the two major readout modes for ion optodes. However, other techniques such as luminescence decay time, refractive index or surface plasmon resonance (SPR) have been successfully applied. For instance, Freiner et al. proposed a waveguide setup where the refractive index of an ion optode film changes upon analyte binding.<sup>35</sup> Suzuki and co-workers reported on a SPR sodium ion sensor using an ion optode film.<sup>36</sup> Werner and co-workers presented a potassium ion sensor based on the ion-exchange principle and using fluorescence decay time as readout.<sup>37</sup>

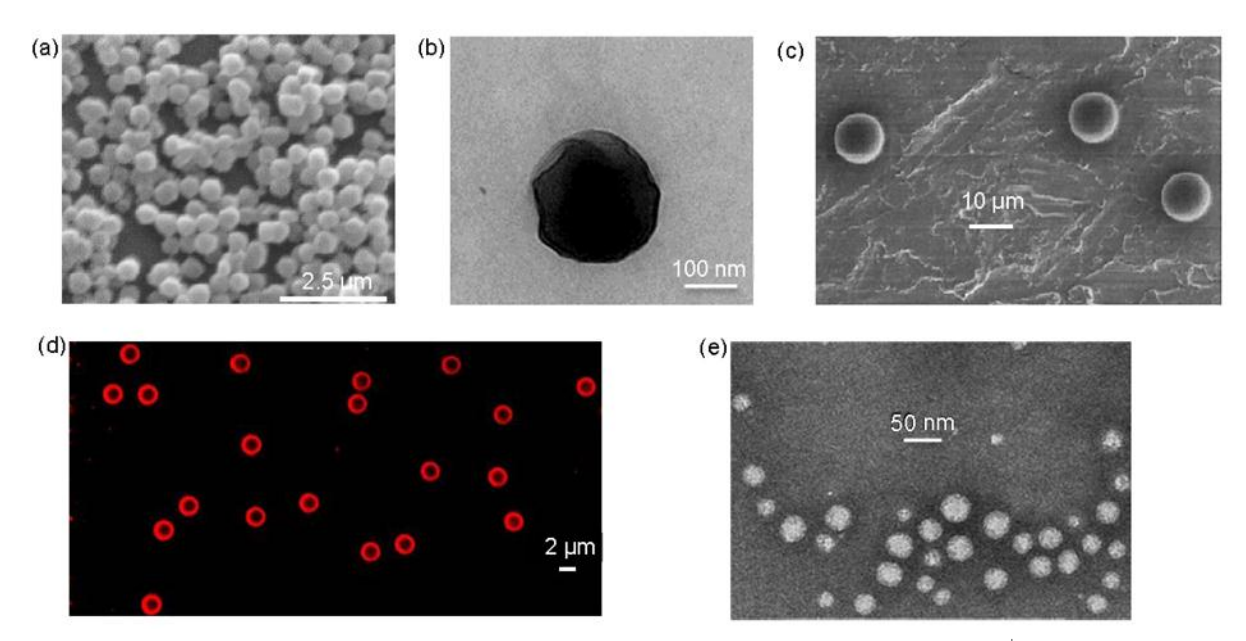


**Figure 1.1.2.** Microscopic images of different miniaturized ion selective optodes. (a) SEM image of K<sup>+</sup> selective PEBBLE sensor adapted from reference 43; (b) TEM image of Na<sup>+</sup> selective nanosensor adapted from reference 47; (c) SEM image of plasticized PVC microspheres adapted from reference [59]; (d) confocal fluorescence image of surface modified polystyrene microparticles adapted from reference 71 (e) TEM image of Na<sup>+</sup> selective nanospheres adapted from reference 72. Copyright: American Chemical Society

#### 1.1.2 Ion selective Microspheres and Nanospheres

While film-based ion optodes can be applied to fiber optics, <sup>23</sup> flow cells<sup>28</sup> and waveguide devices, <sup>38</sup> they are too bulky to operate in small amount of volume such as living cells. The emergence of miniaturized ion optodes in the form of microspheres and nanospheres can help tackle this challenge. At the same time, the miniaturized particles can be interrogated in a parallel fashion and become potential chemical bioimaging tools.

Kopelman and co-workers reported on nanosensors that were coined PEBBLEs (probes encapsulated by biologically localized embedding). <sup>39-44</sup> Using inert, cross-linked acrylamide as a matrix, PEBBLE sensors can incorporate water soluble ion indicators such as rhod-2 and Calcium Green to detect ions without much interference from pH and has proven valuable in the study of a number of intracellular analytes. However, the leaching of the hydrophilic indicator dye remains an issue and must be corrected for in practice. Hydrophobic PEBBLEs have been demonstrated for K<sup>+</sup> (Fig. 1.1.2a), NO<sub>2</sub><sup>-</sup> and Cl<sup>-</sup> and applied in live C6 glioma cells and rat conceptuses. <sup>42,45</sup> The particles exhibited an average diameter from 300 to 700 nm. However, the usable lifetime of the sensors was limited

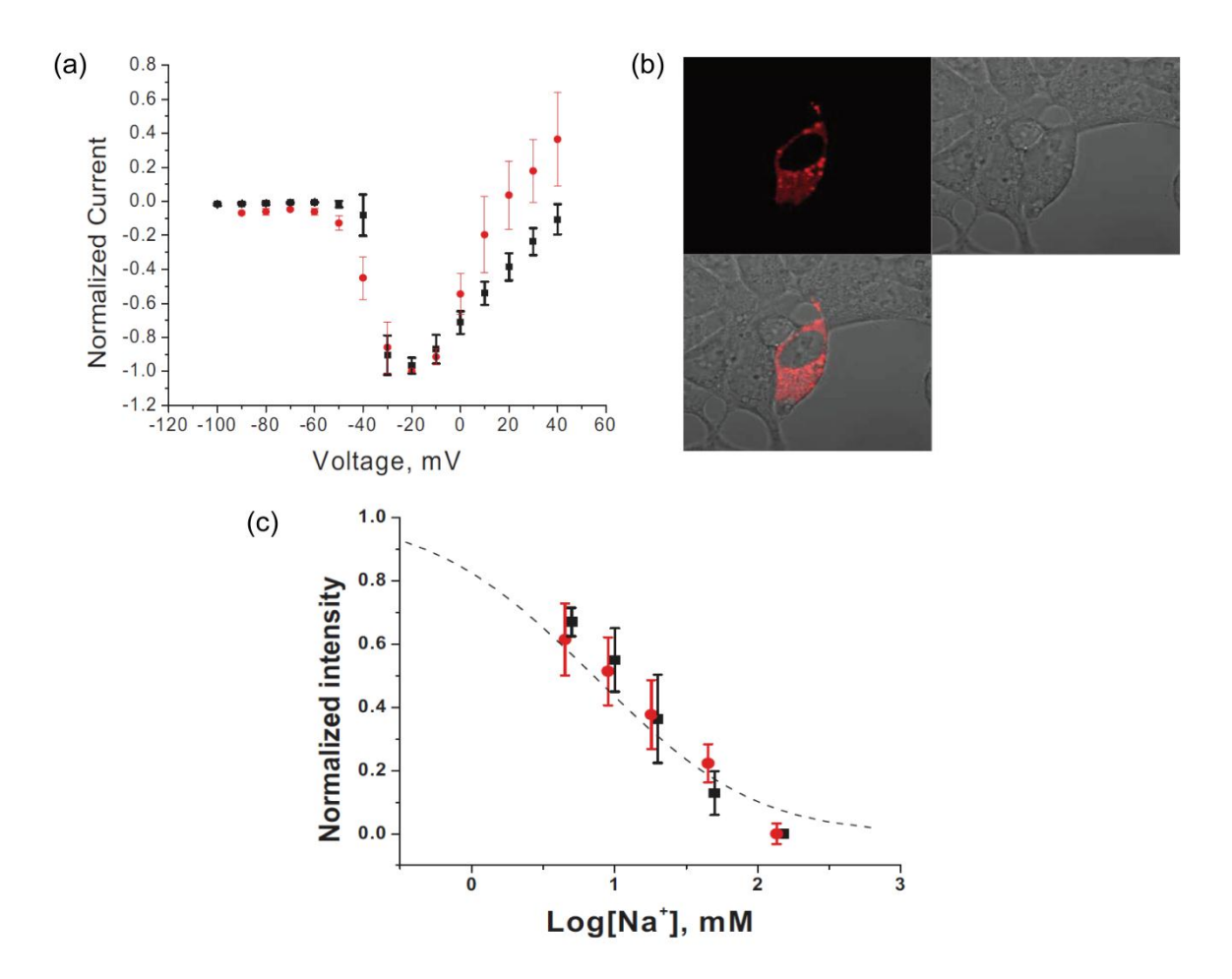


**Figure 1.1.3.** Intracellular sodium measurements using Na<sup>+</sup> selective nanosensors from reference 48. (a) IV response curve of wholecell patched HEK PN1 cells. Normalized sodium current using control internal filling solution (black squares) and internal filling solution containing sodium nanosensors (red circles). Data represent five experiments plus standard deviation. (b) HEK PN1 cell loaded with sodium nanosensors using microinjection. Confocal image showing fluorescence (633/680 nm), bright field and overlay. (c) Concentration calibration of nanosensors in vitro (black squares) and in cell-free solution (red circles). Copyright: National Academy of Sciences

to several hours due to leaching of the sensing materials (i.e., chromoionophore, ion exchanger and ionophore). Moreover, the preparation was time consuming and the sensing components had to be adsorbed by the nanospheres after they had been crosslinked. This makes it difficult to produce multicomponent sensor particles with known and optimized compositions.

The situation was improved later on by Clark and co-workers who demonstrated sodium-selective polymeric nanosensors with an average diameter of ca. 120 nm (Fig. 1.1.2b) and a lifetime in solution of roughly one week.<sup>46</sup> The nanospheres were prepared under sonication. The core was made up of classical ion optode materials while the surface was covered with PEG-lipid molecules to offer stabilization. The nanosensors were successfully applied in isolated cardiomyocytes to visualize sodium and potassium flux across cell membrane, as shown in Fig. 1.1.3.<sup>47,48</sup>

The same group also reported on biodegradable optode-based Na<sup>+</sup> selective nanosensors using polycaprolactone as matrix.<sup>49</sup> The nanosensors were prepared by a solvent displacement method followed by centrifugation and washing. These nanosensors exhibited an average diameter of ca. 260 nm and lifetime of at least 2 weeks at physiological temperature. When in the presence of lipase, the nanosensors degraded within 4 h at the lipase concentrations found in the liver but still were present after 3 days at the lipase levels found in serum. Polymer-free nanospheres with an average diameter of ca. 250 nm were later reported through a similar methodology.<sup>50</sup>

In addition, Tohda and Gratzl fabricated ion selective microscopic beads for Na<sup>+</sup> and K<sup>+</sup> by a spray drying method.<sup>51-53</sup> Together with microbeads modified with glucose oxidase and those containing just reference dye, the ion selective beads were assembled into a plastic bar coined "sliver sensor" 100 to 300 µm wide and 1 to 1.5 mm long, and inserted under the skin. It was shown that this optical sensing array could successfully monitor pH, Na<sup>+</sup>, K<sup>+</sup> and glucose in the interstitial fluid *in vitro*. Michalska and co-workers recently reported that ion optode components can be loaded into cross linked poly(maleic anhydride-alt-1-octadecene) self-assembled micelles.<sup>54</sup> Carboxylate groups were formed after hydrolysis of the anhydride groups on the copolymer, which could function both as surfactant and ion exchanger. Loading the nanospheres with chromoionophore I alone resulted in a pH sensitive system.

Earlier, Seitz and co-workers derivatized lightly cross-linked polymer microspheres that swell and shrink as a function of analyte concentration. Inophores were incorporated into poly(4-hydroxy-3-nitro)styrene microspheres to demonstrate that ion binding accompanied by loss of protons causes the polymer to swell. The particles exhibited diameters from 0.3 to 3 µm. Although they are not ion optode based microspheres, the ion exchange process is quite similar to ionophore based ion selective optodes.

Bakker and co-workers reported on ion selective microspheres that function as film-based optodes and that were prepared using a sonicating particle caster. The microspheres exhibited monodispersity and average diameter on the order of several micrometers (Fig. 1.1.2c). Based on this platform, microsensors with selectivity toward Na<sup>+</sup>,<sup>56-58</sup> Ag<sup>+</sup>,<sup>59</sup> K<sup>+</sup>,<sup>56,60-63</sup> Ca<sup>2+</sup>,<sup>56</sup> Pb<sup>2+</sup>,<sup>64</sup> NO<sub>2</sub><sup>-</sup>,<sup>45</sup> Cl<sup>-</sup>,<sup>45,56</sup> and PO<sub>4</sub><sup>3-65</sup> were successfully fabricated. The multiplexed flow cytometric sensing of blood electrolytes in physiological samples using these fluorescent ion optode microspheres was demonstrated.<sup>66</sup> Although PEG was used to stabilize the microspheres, they were still quite prone to coagulation owing to their relatively large size. The excessive amount of aqueous waste generated during the fabrication had to be removed to concentrate the microspheres.

Approaches based on commercial templates were also reported. Quantum dots were incorporated into ion selective optode materials to make both microspheres and nanospheres.<sup>67,68</sup> Quantum dots can serve as an additional label for these sensors because they are rather inert. The excitation and emission are tunable by changing their size. They exhibit a wide excitation range, narrow emission bandwidth and good photostability. Such core-shell structures were made of a quantum dot core, surrounded by a second polymeric coating of the sensing components and a third layer of amphiphilic molecules. At the same time, the fluorescence output may become complicated owing to

spectral overlap and possible inner filter and FRET-based energy transfer processes. Silica particles were also reported as template.<sup>69</sup> Since the surface of the commercial silica particles was hydrophilic, silanization was required before doping the core with ion optode sensing components. The particles obeyed optode theory, albeit with rather long response times of ca. 10 min. On the other hand, the surface of non-modified polystyrene particles is highly hydrophobic and may be utilized to make optode based microsensor. We recently reported that the simple adsorption of ion exchanger, chromoionophore and valinomycin on the surface of commercial polystyrene particles resulted in a functional optode sensor.<sup>70</sup> As shown in Fig. 1.1.2d, the modification is only limited to the surface because diffusion within polystyrene is extremely slow. The polystyrene based micro-optodes will be further discussed in Chapter 3.

The fabrication of most nanosphere or nanoparticle form ion optodes requires sonication, polymerization, centrifugation, dialysis or similar procedures. These steps can be time consuming and limit the mass production the sensors. Solvent displacement, also called precipitation, is a newly introduced method for the preparation of functionalized nanomaterials. Recently, Xie et al. introduced a new precipitation based approach to yield ion selective nanospheres, which may alternatively be called nano-emulsions (see Chapter 2).<sup>71</sup> The fabrication of the nanospheres required one only to dissolve all the sensing components in tetrahedrofuran and subsequent mixing with aqueous solution. The nanospheres could be used immediately after the removal of tetrahedrofuan by purging with compressed air. No further laborious purification steps were required. These nanospheres exhibited typical average diameter of 40 to 100 nm with good monodispersity (Fig. 1.1.2e). It was demonstrated that the nanospheres still behave as film-based optodes. The nanosensors not only functioned as conventional ion optodes, but also enabled an exhaustive sensing mode that will be discussed below in more detail. The nanospheres were also used to introduce the concept of light controlled ion concentration perturbations (see Chapter 11).<sup>72</sup> When the chromoionophore is removed, they were also shown to serve as titration reagents that may potentially replace traditional water soluble chelators owing to their much reduced pH cross-response.<sup>73</sup>

#### 1.1.3 Detection Mode: Equilibrium and Exhaustive

Conventionally, ion selective optodes are interrogated under equilibrium conditions. In other words, the sensing film or particles are in contact with the sample solution to allow for a passive partition of the analyte ions between the aqueous phase and the organic sensing phase until thermodynamic equilibrium is reached. The optical readout, typically absorbance or fluorescence, is recorded to calculate the degree of protonation for the chromoionophore, which is then plotted against the logarithm of the analyte concentration (activity, more strictly). A sigmoidal calibration curve is obtained at fixed pH. In addition to passive sensing equilibration, the sensing process also can be triggered by light, as demonstrated by the development of photodynamic ion selective sensors for Cl<sup>-</sup> (see Chapter 10), Ca<sup>2+</sup> and Na<sup>+</sup>. These sensors are normally doped with photo-responsive compounds such as a spiropyran or a photoacid generator. We refer to the publications cited above for a rigorous discussion of this sensing principle.

To obtain the theoretical ion optode response function, one must consider the phase transfer equilibrium of the extraction process, the charge balance within the sensing phase, the mass conservation and formation constants for the chromoionophore and the ionophore. Detailed derivations have been discussed in the literature. Here, the response function for a cationic analyte  $M^{z+}$  is shown in Eqn. 1.1, where,  $a_{M^{z+}}^{aq}$  and  $a_{H^+}^{aq}$  are the activity of  $M^{z+}$  and  $H^+$  in the aqueous sample,  $K_{ex}$  is the overall phase extraction equilibrium constant, n is the complex formation stoichiometry for the ionohpore,  $R_T$ ,  $Ind_T$  and  $L_T$  are the total concentration of ion exchanger, chromoionophore and ionophore in the sensing phase,  $1-\alpha$  is the degree of protonation of the chromoionophore. This response function should apply to both film-based and miniaturized particle based ion optodes:

$$a_{M^{z+}}^{aq} = \frac{1}{zK_{ex}} \left( \frac{a_{H^{z}}^{aq} \alpha}{1 - \alpha} \right)^{z} \frac{R_{T} - (1 - \alpha) Ind_{T}}{\left\{ L_{T} - z^{-1} n \left[ R_{T} - (1 - \alpha) Ind_{T} \right] \right\}^{n}}$$
(1.1)

The sensing process is associated with the redistribution of the analyte ions together with hydrogen ions between the sensing phase and the sample phase. For a cationic analyte, ion exchange between protons and the analyte occurs, while for an anionic analyte, coexraction of the analyte and protons takes place. Therefore, ion selective optodes, whether film or particle based, respond to changes in sample pH as well. The calibration curve at different pH values can be very different. For instance, for a calcium selective optode, changing the sample pH by one unit will shift the sensor response by two orders of magnitude (Fig. 1.1.4a). One advantage of this pH cross response is the ability to tune the sensor response range. For example, a sensor that responds to  $Ca^{2+}$  from  $10^{-6}$  M to  $10^{-2}$  M at pH 8 will do so in the range of  $10^{-4}$  M to 1 M at pH 7. On the other hand, the pH cross response is typically regarded as a major drawback of ion selective optodes. In practice, the sample pH must be controlled or measured at the same time. For sensing carbon dioxide, this problem is avoided by the direct sensing of carbon dioxide activity through the use of a coupled extraction of carbonate and hydrogen ions. (see Chapter 8) This functions in contrast to the Severinghaus  $CO_2$  probe, which determines the  $CO_2$  level through indirect measurement of pH change in aqueous solution upon  $CO_2$  extraction (see Chapter 9).<sup>30</sup>

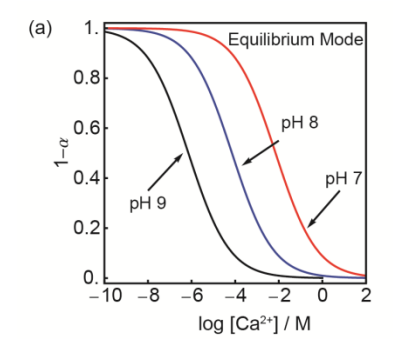
Recently, we have shown that the pH dependence can be overcome by operating the ion selective sensors in what is called an exhaustive sensing mode (Chapter 4 and 5).<sup>76,77</sup> In this case, the sample analyte will ideally be completely consumed by the probes. The response will only depend on the total amount of the analyte and make the exhaustive sensors potentially calibration free. In a classical equilibrium based sensing mode described by Eqn. 1.1, on the other hand, the sample concentration is usually considered unchanged before and after exposure to the sensor.

The exhaustive detection mode can only work when there are more binding sites in the sensing phase than the amount of analyte in the sample. If a thin optode film is used, a thin layer of sample is preferred since large sample volumes will result in extremely long response times. Using suspensions of nanospheres or microspheres, on the other hand, may avoid this limitation because of a massively increased surface to volume ratio and much smaller diffusion distances.

While the analyte is consumed during the exhaustive sensing process, the remaining analyte concentration should still be at equilibrium with the sensor. For the exhaustive mode to be valid, the remaining analyte concentration must be negligible compared to the initial concentration. Based on mass balance and partition equilibria of the analyte, a theoretical model has been put forward for exhaustive sensors based on absorbance measurements, shown in Eqn. 1.2:

$$a_{M^{z+}}^{aq} = a_{M^{z+}}^{\overline{aq}} + \frac{1}{z} \frac{A_0 - A}{\varepsilon b}$$

$$\tag{1.2}$$



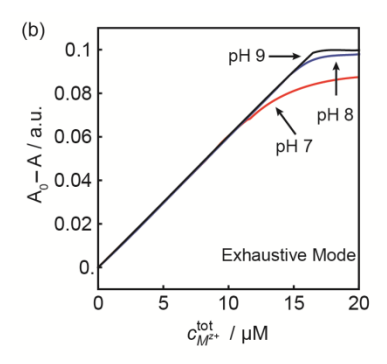


**Figure 1.1.4.** (a) Theoretical equilibrium based Ca<sup>2+</sup> ion selective optode response at different pH simulated using Eqn. 1.1; (b) Theoretical exhaustive mode ion optode response at different pH.

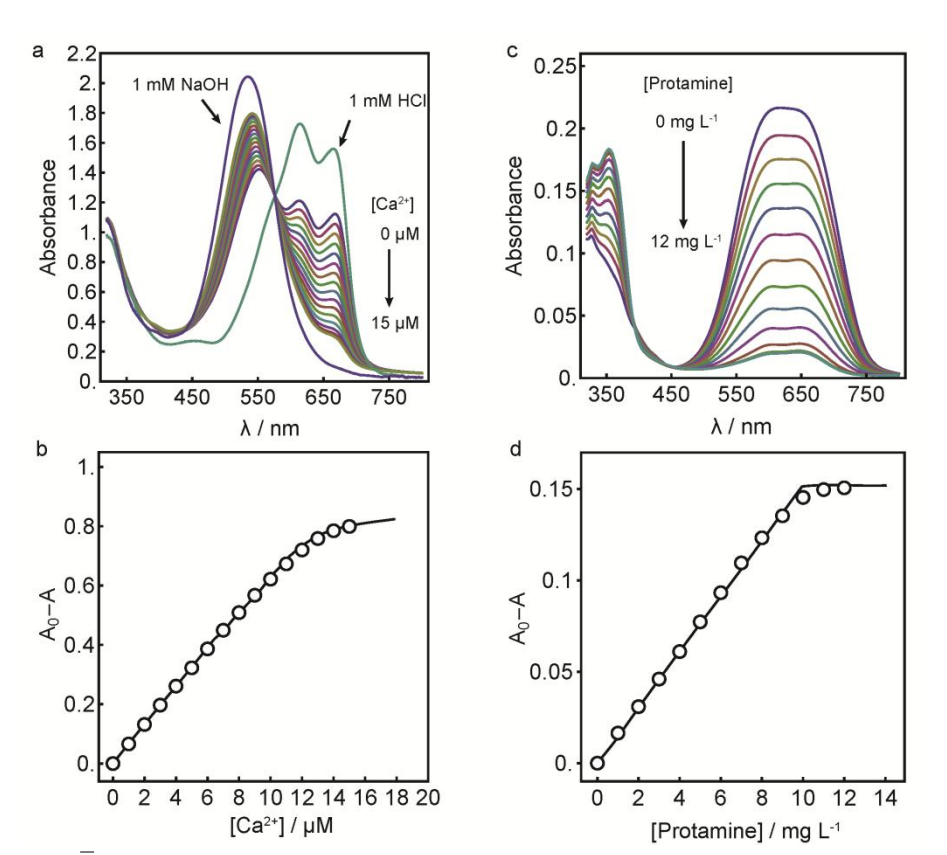


**Figure 1.1.5.** (a) Absorption  $Ca^{2+}$ exhaustive of nanosensors in response to various Ca<sup>2+</sup> concentrations in 10 mM Tris-HCl buffer at pH 7.4; (b) Calibration curve for the Ca<sup>2+</sup> nanosensors using the absorbance difference at 663 nm fit with theoretical curve; (c) Absorption spectra of protamine exhaustive nanosensors in response to various protamine levels in 10 mM tris-HCl buffer and 0.1 M NaCl at pH 7.4; (d) Calibration curve for the protamine nanosensors using the absorbance difference at 641 nm. Adapted from reference Copyright: American Chemical Society

where  $a_{M^{z_1}}^{aq}$  represents the remaining  $M^{z_1}$  activity in the aqueous phase which follows Eqn. 1.1,  $A_0$ —A is the change in absorbance,  $\varepsilon$  is the molar extinction coefficient for the chromoionophore, and b the optical path length for the nanosphere suspension. An important feature of the ion selective optodes working in this mode is that the response is linear with analyte concentration, as shown in Fig. 1.1.5 for protamine selective nanooptodes and calcium selective nanooptodes. The linear range is related to the amount of nanospheres used. A wider linear range occurs upon high loading of the nanospheres. Compared to sigmoidal calibrations, a linear calibration curve is statistically much easier to handle.

The exhaustive sensing mode has of course its own limitations. In particular, it is not applicable to samples that cannot afford large concentration perturbations. For instance, exhaustive sensors are not suitable for interrogation of ion concentration in live cells because the massive consumption of the ions could potentially kill the cells. Even when the cells can survive such dramatic ion concentration perturbation, the outcome is likely biased due to possible compensation by the cells themselves. An equilibrium sensing mode is preferred in this case since the sample concentration will not be altered.

#### 1.1.4 Response Time

The response time of ion optodes is generally given by the diffusion of all mobile species in the sensing organic phase and the aqueous sample phase. For plasticized PVC films with thicknesses of several micrometers, and with reasonably high sample concentrations, the limiting step is the diffusion of the sensing components within the film. In this case, assuming a mean diffusion coefficient for all mobile species and a film thickness of d, the time required to achieve 95% of the steady-state response  $t_{95}$  can be simply estimated through Eqn. 1.3:<sup>78</sup>

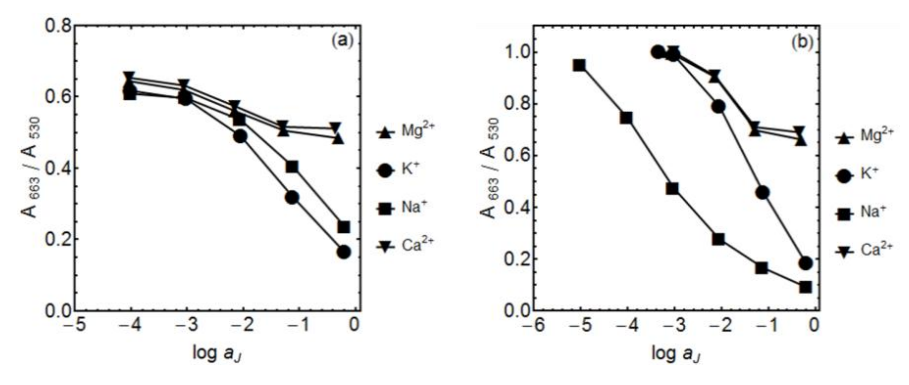


**Figure 1.1.6.** Selectivity for nanospheres comprised of CH1 and KTFPB in 10 mM pH 7.4 Tris-HCl buffer, without (a) and with (b) NaX inside the nanosphere reported in reference 72. Copyright: American Chemical Society

$$t_{95} = 1.13 \frac{d^2}{D_m} \tag{1.3}$$

where  $D_{\rm m}$  is the diffusion coefficient in the sensing phase. On the other hand, if the analyte level in the aqueous phase is very low, the response time may become limited by mass transport in the aqueous phase. For instance, Lerchi et al. observed earlier that the response time of extremely sensitive optodes for transition metals is mainly dependent on mass transport in solution.<sup>79,80</sup> The slow response at low analyte level can be overcome by using ion selective microspheres and nanospheres. As a result of the enhanced surface to volume ratio and spherical diffusion characteristics, mass transport is dramatically accelerated. For instance, Wygladacz et al. reported that for  $Ag^+$  selective plasticized PVC microspheres with an average diameter of 10  $\mu$ m, a response time of less than 15 min was found for  $10^{-9}$  M AgNO<sub>3</sub> compared with a response time of 8 h in the case of film-based optodes.<sup>59</sup> For polyions such as protamine, the diffusion in the organic sensing phase can be quite slow. Previous film-based optical sensors for protamine based on ion exchange principles exhibited response times too long to obtain an equilibrium signal. Xie et al. showed that for protamine selective nanooptodes, the time to reach thermodynamic equilibrium was nearly instantaneous (see Chapter 5). Moving from a sensing film fixed to a support to freely moving suspended particles dramatically increases the mass transport efficiency.<sup>77</sup>

#### 1.1.5 Selectivity

When ion optodes are miniaturized from the bulk to the nanoscale out of the same material, no dramatic change in the selectivity pattern is expected. The reason for this assumption is that the selectivity for ion optodes mainly depends on the ionophores. Without incorporating ionophores, the selectivity is determined by the thermodynamic equilibrium and in general follows the Hoffmeister series. It has been shown that for PVC based ion selective microspheres, the selectivity pattern remains similar with film-based optodes based on the same material. On Na<sup>+</sup> selective nanooptodes incorporating quantum dots have shown similar selectivity for Na<sup>+</sup> over K<sup>+</sup> compared with PVC based microspheres. The selectivity for the decyl methacrylate based K<sup>+</sup> selective PEBBLE over Na<sup>+</sup> is even slightly better than in plasticized PVC films.

However, other factors may influence the selectivity pattern as well. Since the response function is directly derived from fundamental phase transfer and complexation equilibria, different microenvironments will affect the partition equilibrium of the uncomplexed ions. For instance, as shown in Fig. 1.1.6, ionophore-free nanospheres reported by Bakker and co-workers showned a similar response to all ions. <sup>71</sup> Similarly, for nanospheres doped with additional ionophores, the response for all interfering ions was found to be nearly the same. These

observations indicate that the nanosphere core forms a relative polar environment compared with film-based optodes. We speculate that the higher polarity of the core is caused by the insertion of the surfactants, which is more polar than conventional plasticized PVC.

#### 1.1.6 Choice of Materials

#### 1.1.6.1 Surfactant

In order to realize micrometer size or nanometer size ion optodes, surfactants may be required to prevent the particles from coagulating. However, the presence of surfactant may also interfere with the sensing process. In particular, ionic surfactants such as sodium dodecyl sulfate (SDS) should be avoided since they may spontaneously extract together with cations into the sensor phase and repel anionic species. Cationic surfactants such as hexadecyltrimethylammonium bromide (CTAB) can repel cations and promote coextraction with anions. Nonionic surfactants including polyethylene glycol, Pluronic F-127, Triton X-100, Tween 20 and Brij 30 have been used to successfully fabricate ion selective microspheres and nanospheres. These surfactants bear similar hydrophilic groups but differ in the hydrophobic parts. Since the hydrophobic part may insert into a nanoscale organic sensing core, the surfactant is likely to influence the polarity of the particle core and shift the apparent pKa of the chromoionophore in some cases. <sup>71</sup> Moreover, the hydrophilic chains of these nonionic surfactants are composed of poly(ethylene oxide), which is known to be biocompatible and beneficial for *in vivo* applications.

#### 1.1.6.2 Optical Reporter

As for film-based optodes, the choice of chromoionophore for micro/nanooptodes depends on several variables. First, the chromoionophore has to be compatible with the instrumental detection mode. Most chromoionophores are suitable for interrogation under absorption mode, established for the family of Nile blue derivatives. They exhibit very high molar extinction coefficients but typically a less attractive quantum yield. Reducing the amount of dye when used in fluorescence mode or imaged under fluorescence microscope may pose a problem.

Recently other compounds have been reported as new chromoionophores (see Chapter 7 for a new variety of chromoionophore based on oxazinoindolene). 81,82 However, the palette of chromoionophores still needs expansion, especially for those with a high quantum yield. To design a chromoionophore, there are more factors to consider besides quantum yield, such as the pKa value, spectral range, molar extinction coefficient, photostability, lipophilicity and so on. Together with the ionophore used, the pKa value will influence the response range of the sensor. Long wavelength absorption in the visible range and the near infrared region is preferred. Ratiometric dyes are also preferred because they provide a more accurate determination. In addition, the scope of chromoionophore should not be limited to organic dyes. Semiconductor fluorophores, metal ion complexes and biologically expressed fluorophores are potential candidates as well. These materials easily provide higher quantum yields, better photostability and narrow absorption and emission bands.

#### 1.1.6.3 Ion Exchanger

The most commonly used ion exchangers are organic analogs based on tetraphenylborate (e.g. tetrakis[3,5-bis(trifluoromethyl)phenyl]borate, TFPB) and tetraalkylammonium salts (e.g. tridodecylmethylammonium, TDMA). Others such as carboxylated poly(vinyl chloride) (PVC) and organic sulphonate can also serve as ion exchanger but may result in incomplete dissociation due to the relatively high pKa of these functional groups. Some of the hydrophilic groups of these compounds also can act as amphiphiles when they are used to make nanosensors. Ion exchangers are made very lipophilic to prevent leaching. The leaching from microspheres and nanospheres may be dramatically accelerated due to the larger surface to volume ratio.

#### 1.1.6.4 Ionophore

Ionophores help stabilize the target ions and ensure the sensor selectivity. Nowadays, plenty of ionophores are available for cations that include nearly all main group and transition metal ions. For one target ion, one can even find several ionophores with different complex formation constants. Ionophores with higher complex formation constants can shift the sensor response to a lower concentration range and make them more sensitive.

Despite the huge success in developing cation selective ionophores, the advancement of anion selective ionophores is in comparison much less developed. Anions such as SO<sub>4</sub><sup>2-</sup> and PO<sub>4</sub><sup>3-</sup> are extremely hydrophilic and thus the complex formation constant for an ionophore must be sufficiently large to compensate the solvation energy difference between aqueous and organic phases. In addition, achieving high specificity is very difficult. Some so-called "anti-crown ether" compounds have been reported to be highly selective to chloride. However, for ions such as nitrate, sulfate and phosphate, the interference from highly lipophilic anions such as perchlorate and thiocyanate remains a problem. Highly selective ionophores for fluoride have been reported. <sup>83</sup> Recently, salophen-based metal ion complexes have been proposed as ionophores for nitrite, salicylate, copper (II) and monohydrogen phosphate. <sup>84-89</sup> However, these compounds may be susceptible to hydrolysis. Although their lifetime in film-based sensor films can be prolonged by an increase in viscosity and film thickness, when loaded into nanospheres or microspheres, hydrolysis will be accelerated due to the increased surface to volume ratio. In addition, in contrast to most cation selective ionophores that remain optically silent in the visible range, most metal complex based ionophores do absorb in this range and the spectrum can change upon binding with the anion of interest. This should also be taken into account when designing optical sensors.

#### 1.1.6.5 Matrix Material

Most film-based ion optodes have adopted plasticized PVC as matrix materials since it is the major material used for ion selective electrodes (ISEs). For miniaturized microsphere and nanosphere based ion optodes, more versatile matrix materials are being explored, including polyacrylamide, polystyrene, polycaprolactone, decyl methacrylate and polymer free solvent as described above. The choice of matrix material will help to control the micro/nanosensor size, response time, selectivity and biocompatibility.

#### 1.1.7 Future perspective

Despite a history of around 25 years for ion selective optodes, the field of miniaturized ion optodes is still young and rapidly growing. New and exciting concepts and extensions to conventional techniques are regularly introduced into the field, such as different detection modes and various sensor materials. Ion selective optode nanosensors and microsensors have opened new avenues in applied and academic research fields including imaging in biological environmental samples. In the meantime, some aspects still remain unsatisfactory and require a radical improvement, such as the pH cross response, relative signal change, brightness and photostability of the chromoionophore for interrogation in fluorescence mode, selectivity of anion specific ionophores. It is also important to discover more convenient and less laborious methods to fabricate miniaturized optode-based sensors. As these characteristics being improved, ion selective optode sensors will likely become widely accepted and find their way to an increasing number of real-world applications.

#### 1.1.8 Referecences for Part 1 of Chapter 1

- (1) Spichiger, U. E.; Freiner, D.; Bakker, E.; Rosatzin, T.; Simon, W. Sens. Actuator B 1993, 11, 263.
- (2) Gholivand, M. B.; Babakhanian, A.; Kaki, S.; Mohammadi, M.; Moradi, P. Sensor Lett. 2013, 11, 1651.
- (3) Meyerhoff, M. E.; Yang, V. C.; Wahr, J. A.; Lee, L. M.; Yun, J. H.; Fu, B.; Bakker, E. Clin. Chem. 1995, 41, 1355.
- (4) Diamond, D.; Coyle, S.; Scarmagnani, S.; Hayes, J. Chem. Rev. 2008, 108, 652.

- (5) Hamaguchi, Y.; Hamaguchi, M. S.; Mohri, T. Cell 1990, 22, 258.
- (6) Mistlberger, G.; Xie, X.; Pawlak, M.; Crespo, G. A.; Bakker, E. Anal. Chem. 2013, 85, 2983.
- (7) Bakker, E.; Qin, Y. Anal. Chem. 2006, 78, 3965.
- (8) Akcin, N.; Koyuncu, I.; Akcin, G. Rev. Anal. Chem. 2011, 30, 65.
- (9) Li, X.; Zhou, D.; Xu, J.; Chen, H. Talanta 2007, 71, 1130.
- (10) Alvarez, M. A.; Carrillo, G. *Talanta* **2012**, 97, 505.
- (11) Aragay, G.; Pons, J.; Merko q, A. Chem. Rev. 2011, 111, 3433.
- (12) Thakur, A.; Mandal, D.; Ghosh, S. Anal. Chem. 2013, 85, 1665.
- (13) Town, R. M.; Leeuwen, H. P. V. Electroanalysis 2004, 16, 458.
- (14) He, Q.; Miller, E. W.; Wong, A. P.; Chang, C. J. J. Am. Chem. Soc. 2006, 128, 9316.
- (15) Buccella, D.; Horowitz, J. A.; Lippard, S. J. J. Am. Chem. Soc. 2011, 133, 4101.
- (16) Mank, M.; Griesbeck, O. Chem. Rev. 2008, 108, 1550.
- (17) Carter, K. P.; Young, A. M.; Palmer, A. E. Chem. Rev. 2014, 114, 4564.
- (18) Han, J.; Burgess, K. Chem. Rev. 2010, 110, 2709.
- (19) Chen, T.-W.; Wardill, T. J.; Sun, Y.; Pulver, S. R.; Renninger, S. L.; Baohan, A.; Schreiter, E. R.; Kerr, R. A.; Orger, M. B.; Jayaraman, V.; Looger, L. L.; Svoboda, K.; Kim, D. S. *Nature* **2013**, *499*, 295.
- (20) Seiler, K.; Simon, W. Sens. Actuat. B 1992, 6, 295.
- (21) Bakker, E.; Bühlmann, P.; Pretsch, E. Chem. Rev. 1997, 97, 3083.
- (22) Spichiger-Keller, U. E. Sens. Actuat. B 1997, 38-39, 68.
- (23) Kurihara, K.; Ohtsu, M.; Yoshida, T.; Abe, T.; Hisamoto, H.; Suzuki, K. Anal. Chem. 1999, 71, 3558.
- (24) Spichiger, U.; Simon, W.; Bakker, E.; Lerchi, M.; Biihlmann, P.; Haug, J.-P.; Kuratli, M.; Ozawa, S.; West, S. Sens. Actuator B 1993, 11, 1.
- (25) Mistlberger, G.; Crespo, G. A.; Bakker, E. Annu. Rev. Anal. Chem. 2014, 7, 483.
- (26) Chariton, S. C.; Fleming, R. L.; Zipp, A. Clin. Chem. 1982, 28, 1857.
- (27) Morf, W. E.; Seiler, K.; Lehmann, B.; Behringer, C.; Hartman, K.; Simon, W. Pure & Appl. Chem. 1989, 61, 1613.
- (28) Morf, W. E.; Seiler, K.; Rusterholz, B.; Simon, W. Anal. Chem. 1990, 62, 738.
- (29) Seiler, K.; Morf, W. E.; Rusterholz, B.; Simon, W. Anal. Sci. 1989, 5, 557.
- (30) Xie, X.; Pawlak, M.; Tercier-Waeber, M.-L.; Bakker, E. Anal. Chem. 2012, 84, 3163.
- (31) Wolfbeis, O. S. Sens. Actuator, B 1995, 29, 140.
- (32) Murkovic, I.; Lobnik, A.; Mohr, G. J.; Wolfbeis, O. S. Anal. Chim. Acta 1996, 334, 125.
- (33) Huber, C.; Werner, T.; Krause, C.; Wolfbeis, O. S. Analyst 1999, 124, 1617.
- (34) Xie, X.; Zhai, J.; Bakker, E. J. Am. Chem. Soc. 2014, 136, 16465.
- (35) Freiner, D.; Kunz, R. E.; Citterio, D.; Spichiger, U. E.; Gale, M. T. Sens. actuator B 1995, 29, 277.
- (36) Kurihara, K.; Nakamura, K.; Hirayama, E.; Suzuki, K. Anal. Chem. 2002, 74, 6323.
- (37) Krause, C.; Werner, T.; Huber, C.; Klimant, I.; Wolfbeis, O. S. Anal. Chem. 1998, 70, 3983.
- (38) Hisamoto, H.; Kim, K.-H.; Manabe, Y.; Sasaki, K.; Minamitani, H.; Suzuki, K. Anal. Chim. Acta 1997, 342, 31.
- (39) Clark, H. A.; Hoyer, M.; Philbert, M. A.; Kopelman, R. Anal. Chem. 1999, 71, 4831.
- (40) Clark, H. A.; Kopelman, R.; Tjalkens, R.; Philbert, M. A. Anal. Chem. 1999, 71, 4837.
- (41) Park, E. J.; Brasuel, M.; Behrend, C.; Philbert, M. A.; Kopelman, R. Anal. Chem. 2003, 75, 3784.
- (42) Brasuel, M.; Kopelman, R.; Miller, T. J.; Tjalkens, R.; Philbert, M. A. Anal. Chem. 2001, 73, 2221.
- (43) Si, D.; Epstein, T.; Lee, Y.-E. K.; Kopelman, R. Anal. Chem. 2012, 84, 978.

- (44) Buck, S. M.; Xu, H.; Brasuel, M.; Philbert, M. A.; Kopelman, R. *Talanta* **2004**, *63*, 41.
- (45) Barker, S. L. R.; Thorsrud, B. A.; Kopelman, R. Anal. Chem. 1998, 70, 100.
- (46) Dubach, J. M.; Harjes, D. I.; Clark, H. A. Nano Lett. 2007, 7, 1827.
- (47) Dubach, J. M.; Das, S.; Rosenzweig, A.; Clark, H. A. Proc. Natl. Acad. Sci. 2009, 106, 16145.
- (48) Harjes, D. I.; Dubach, J. M.; Rosenzweig, A.; Das, S.; Clark, H. A. Macromol. Rapid Commun. 2010, 31, 217.
- (49) Balaconis, M. K.; Clark, H. A. Anal. Chem. 2012, 84, 5787.
- (50) Ruckh, T. T.; Mehta, A. A.; Dubach, J. M.; Clark, H. A. Scient. Rep. 2013, 3, 3366.
- (51) Tohda, K.; Gratzl, M. ChemPhysChem 2003, 4, 155.
- (52) Tohda, K.; Gratzl, M. Anal. Sci. 2006, 22, 383.
- (53) Tohda, K.; Gratzl, M. Anal. Sci. 2006, 22, 937.
- (54) Kisiel, A.; Kłucinska, K.; Głebicka, Z.; Gniadek, M.; Maksymiuk, K.; Michalska, A. Analyst 2014, 139, 2515.
- (55) Seitz, W. R.; Rooney, M. T. V.; Miele, E. W.; Wang, H.; Kaval, N.; Zhang, L.; Doherty, S.; Milde, S.; Lenda, J. *Anal. Chim. Acta* **1999**, *400*, 55.
- (56) Wygladacz, K.; Bakker, E. Anal. Chim. Acta 2005, 532, 61.
- (57) Ngeontae, W.; Xu, C.; Ye, N.; Wygladacz, K.; Aeungmaitrepirom, W.; Tuntulani, T.; Bakker, E. Anal. Chim. Acta 2007, 599, 124.
- (58) Tsagkatakis, I.; Peper, S.; Retter, R.; Bell, M.; Bakker, E. Anal. Chem. 2001, 73, 6083.
- (59) Wygladacz, K.; Radu, A.; Xu, C.; Qin, Y.; Bakker, E. Anal. Chem. 2005, 77, 4706.
- (60) Tsagkatakis, I.; Peper, S.; Bakker, E. Anal. Chem. 2001, 73, 315.
- (61) Ye, N.; Wygladacz, K.; Bakker, E. Anal. Chim. Acta 2007, 596, 195.
- (62) Peper, S.; Ceresa, A.; Qin, Y.; Bakker, E. Anal. Chim. Acta 2003, 500, 127.
- (63) Retter, R.; Peper, S.; Bell, M.; Tsagkatakis, I.; Bakker, E. Anal. Chem. 2002, 74, 5420.
- (64) Telting-Diaz, M.; Bakker, E. Anal. Chem. 2002, 74, 5251.
- (65) Wygladacz, K.; Qin, Y.; Wroblewskic, W.; Bakker, E. Anal. Chim. Acta 2008, 614, 77.
- (66) Xu, C.; Wygladacz, K.; Retter, R.; Bell, M.; Bakker, E. Anal. Chem. 2007, 79, 9505.
- (67) Xu, C.; Bakker, E. Anal. Chem. 2007, 79, 3716.
- (68) Dubach, J. M.; Harjes, D. I.; Clark, H. A. J. Am. Chem. Soc. 2007, 129, 8418.
- (69) Xu, C.; Wygladacz, K.; Qin, Y.; Retter, R.; Bell, M.; Bakker, E. Anal. Chim. Acta 2005, 537, 135.
- (70) Xie, X.; Crespo, G. A.; Zhai, J.; Szil ágyi, I.; Bakker, E. Chem. Commun. 2014, 50, 4592.
- (71) Xie, X.; Mistlberger, G.; Bakker, E. Anal. Chem. 2013, 85, 9932.
- (72) Xie, X.; Bakker, E. ACS Appl. Mater. Interfaces 2014, 6, 2666.
- (73) Zhai, J.; Xie, X.; Bakker, E. Chem. Commun. 2014, 50, 12659.
- (74) Xie, X.; Mistlberger, G.; Bakker, E. J. Am. Chem. Soc. 2012, 134, 16929.
- (75) Johns, V. K.; Patel, P. K.; Hassett, S.; Calvo-Marzal, P.; Qin, Y.; Chumbimuni-Torres, K. Y. Anal. Chem. 2014, 86, 6184.
- (76) Xie, X.; Zhai, J.; Bakker, E. Anal. Chem. 2014, 86, 2853.
- (77) Xie, X.; Zhai, J.; Crespo, G. A.; Bakker, E. Anal. Chem. 2014, 86, 8770.
- (78) Crank, J. The Mathematics of Diffusion; Oxford University Press: New York, 1993.
- (79) Lerchi, M.; Bakker, E.; Rusterholz, B.; Simon, W. Anal. Chem. 1992, 64, 1534.
- (80) Lerchi, M.; Reitter, E.; Simon, W.; Pretsch, E.; Chowdhury, D. A.; Kamata, S. Anal. Chem. 1994, 66, 1713.
- (81) Xie, X.; Crespo, G. A.; Bakker, E. Anal. Chem. 2013, 85, 7434.
- (82) Xie, X.; Li, X.; Ge, Y.; Qin, Y.; Chen, H.-Y. Sens. Actuator B 2010, 151, 71.

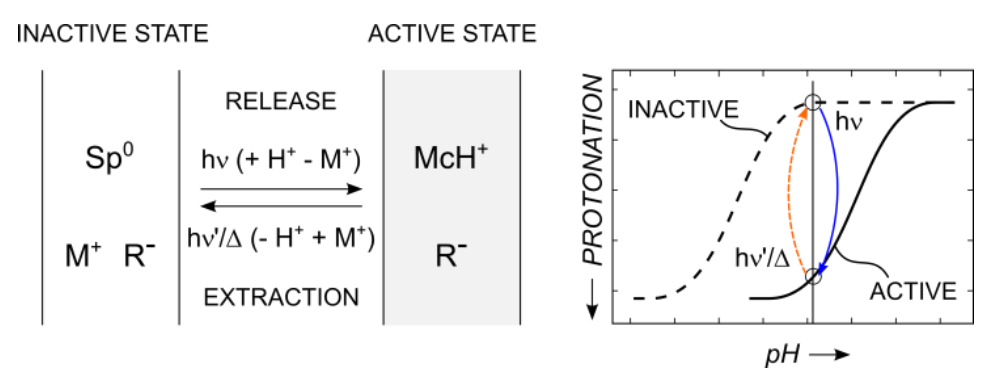
- (83) Badr, I. H. A.; Meyerhoff, M. E. J. Am. Chem. Soc. 2005, 127, 5318.
- (84) Zare, H. R.; Memarzadeh, F.; Gorji, A.; Ardakani, M. M. J. Braz. Chem. Soc. 2005, 16, 571.
- (85) Shahrokhian, S.; Amini, M. K.; Kia, R.; Tangestaninejad, S. Anal. Chem. 2000, 72, 956.
- (86) Gholivand, M. B.; Niroomandi, P.; Yarib, A.; Joshagani, M. Anal. Chim. Acta 2005, 538, 225.
- (87) Nél, B.; Asfhar, M. G.; Crespo, G. A.; Pawlak, M.; Dorokhin, D.; Bakker, E. Electroanalysis 2014, 26, 473.
- (88) Kim, J.; Kang, D. M.; Shin, S. C.; Choi, M. Y.; Kim, J.; Lee, S. S.; Kim, J. S. Anal. Chim. Acta 2008, 614, 85.
- (89) Ganjali, M. R.; Mizani, F.; Salavati-Niasari, M. Anal. Chim. Acta 2003, 481, 85.

## PART 2. INTRODUCTION TO PHOTODYNAMIC ION SELECTIVE OPTICAL SENSORS AND LIGHT TRIGGERED PERTURBATION

Ion optodes based on the competitive ion exchange between a hydrophobic sensor phase and an aqueous sample solution were widely applied since their introduction in the late 1980s.<sup>1-4</sup> In cases where the ionophore or analyte ion carrier is silent concerning the optical response to a binding event, one can take advantage of a secondary reporter dye. The protonation degree of the reporter dye indirectly monitors the concentration of the analyte in the membrane phase, as the sensing phase must obey the electroneutrality principle. This is an elegant approach because it enables the measurement of various ions using their respective ionophores with the same reporter dye and optical setup. On the other hand, one can tune the response region from trace level sensing to completely nonresponsive systems by choosing the indicator of the respective pKa.<sup>5</sup> After the preparation of the sensor, however, the response function is fixed given that the nature and total concentration of all components remains constant.

Recently, there is a lot of interest in making dynamic sensors that work in an active mode, exhibiting ON and OFF states. By switching the sensor ON and OFF, background noises can be eliminated. Moreover, the kinetic information during the switching steps provides us more chemical information of the sample. Replacing one of the sensor components with a dynamically changeable version of the component will transform ion selective optodes from passive to dynamic devices. The triggered change of the affinity of the ionophore, the charge of the ion exchanger, or the pKa of the indicator will suddenly allow for a controlled change in sensor characteristics in space and time.

Earlier, photoresponsive optical sensor was reported for protons based on photoacid generators<sup>7</sup> or the photoisomerization of organic compounds<sup>8,9</sup>. Here, the aim is to extend the target from pure hydrogen ions to any ion of interest. This proposed photodynamic sensing concept is illustrated in Scheme 1.2.1. In an initial, inactive state, the sensing phase contains an indicator of low basicity together with the ion-exchanger. Consequently, any available hydrogen ions in the organic phase will quantitatively exchange with another ion  $M^+$  from that sample. This ion may optionally be chemically stabilized with an ionophore (not shown). As the sensor is illuminated with radiation hv, the indicator is transformed to a more basic form, thereby expelling the ions  $M^+$  and taking up hydrogen ions instead. Illumination with  $hv^*$  may bring the system back to the initial state, thereby reversing the above processes. Depending on the change in  $pK_a$  and the sample composition this leads to two distinct cases: 1) the sensor is switched between a non-responsive and a responsive state (small  $pK_a$  change) and 2) the sensor is switched between two non-responsive states on the opposite side of the equilibrium curve (large  $pK_a$  change). Before photo activation (dashed line), the indicator is neutral (Sp<sup>0</sup>), and the counter ion of the ion exchanger is a secondary ion  $M^+$ . After activation the indicator dye attracts a proton and changes its charge to +1 (McH<sup>+</sup>). To respect the charge balance condition, the secondary ion  $M^+$  is released from the membrane. This may be performed in both directions, as long as there is a stimulus available that selectively



**Scheme 1.2.1.** Correlation between protonation degree of an indicator and pH value in the sample in a competitive, non-selective optical ion sensor. Irradiation with hv changes the weakly basic indicator Sp to a more basic compound Mc. This change in pKa also shifts the equilibrium curve. e.g. from a state were the indicator is uncharged to a state where it attracts protons and therefore expels ions  $M^+$ .

triggers the specific reactions. Potential triggers are of both physical and chemical nature. While light is most often used for triggering such reactions, other stimuli, such as heat, <sup>10</sup> mechanical stress, <sup>11</sup> and electrical activation <sup>12</sup> have been reported. The advantage of using light is the relative ease of combining spatial and temporal control of the trigger by using readily available imaging equipment such as microscopes or spectrometers.

$$\begin{array}{c|c} & & & & & & & \\ & & & & & \\ & & & & \\ & & & & \\ & & & & \\ & & & \\ & & & \\ & & & \\ & & & \\ & & \\ & & \\ & & \\ & & \\ & & \\ & & \\ & & \\ & & \\$$

Scheme 1.2.2. Photo-isomerization reaction of a lipophilic spiropyran derivative.

In the search of the chromoionophores that could change pKa values upon light stimulation, spiropyran (Sp) compounds attracted much of our attention. Spiropyrans are well known photochromic compounds that could change the color upon UV and visible light illuminations. There has been extensive research on spiropyrans due to their potential applications in various areas. <sup>13-16</sup> The photoreaction of spiropyran is shown in Scheme 1.2.2. Upon UV light irridiation, the C-O bond of Sp is cleaved and an intramolecular conformational change results in the deeply colored ring opened merocyanin (Mc) form. The Mc form is thermodynamically unstable and will transform back to the Sp form even in the dark. Visible light is able to accelerate the ring closure step. The lifetime of the metastable Mc form can vary from seconds in nonpolar solvent to several days in polysiloxane copolymers. <sup>16</sup>

The Mc form can exist as highly charged zwitterion or in nonionic ortho-quinoidal form. The zwitterionic Mc form is expected to have

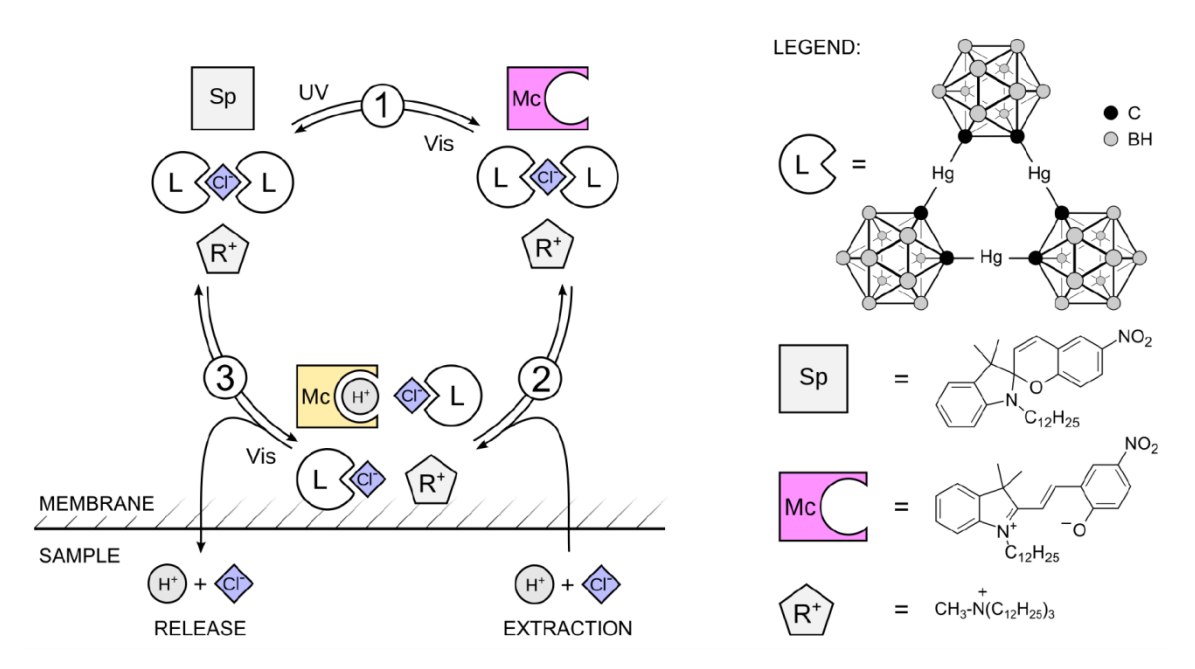
**Scheme 1.2.3.** Molecular chemosensors based on the structural modification of spiropyran for: (a) Li<sup>+</sup>, (b) Ca<sup>2+</sup> and (c) histidine.

much higher pKa value than that for the Sp form, because of the phenolate group in the Mc structure. The light induced basicity change in plasticized PVC membrane was confirmed by potentiometric studies in our group.<sup>17</sup>

In solutions of nonpolar solvents, most spiropyrans and spirooxazines exist as ring-closed Sp isomers, but upon dissolving in polar solvents they can undergo thermal ring opening to the corresponding Mc forms. The equilibrium constant for the thermal ring-opening reaction can vary with temperature, nature of the substituents in the spiropyran structure, solvent polarities and so on.

Many chemosensors for metal ions and amino acids based on modification on the structure of spiropyran or copolymerization methods have been reported. Such chemosensors often utilize the ionic interaction or hydrogen bonding between the ring-opened zwitterion and the analyte. Some examples described in the literature are shown here in Scheme 1.2.3 as representatives of such sensing concept. Most of the compounds are dissolved in solvent and illuminated with UV light before detecting the analyte, with some, exceptionally, immobilized in solid or polymeric matrix. However, robust photo-switchable ion sensors based on bulk optode principles have, to the best of our knowledge, not been reported prior to our work (Chapter 10).

A reversible photodynamic sensor using Cl<sup>-</sup> as the model ion was reported for the first time by Xie et al. (see Chapter 10).<sup>24</sup> The photodynamic sensor uses DOS PVC as matrix and functions on the basis of the pKa change of a spiropyran derivative upon UV and visible light irradiations. The plasticized PVC film contains a lipophilic spiropyran derivative, a chloride selective ionophore (L) and anionic exchanger (R<sup>+</sup>Cl<sup>-</sup>), as shown in Scheme 1.2.4. Under visible light, spiropyran exists in a stable ring-closed form (Sp) with very low basicity (pKa=2.3±0.1)<sup>25</sup>. When illuminated by UV light, it transforms into a strongly colored ring-opened merocyanine (Mc) form. This transformation is designed here to promote the co-extraction of H<sup>+</sup> and Cl<sup>-</sup> from the contacting aqueous solution into the sensing film where Cl<sup>-</sup> will be stabilized by the ionophore and H<sup>+</sup> will protonate Mc to form McH<sup>+</sup>. The spectral difference between Mc and McH<sup>+</sup> helps to visualize the co-extraction process using optical techniques. Visible light will reverse the process by promoting the ring closing reaction. H<sup>+</sup> and Cl<sup>-</sup>, being highly hydrophilic species, will leave the sensing film to the contacting aqueous phase. Later on, ionophore based photoactivated optical sensors for Ca<sup>2+</sup> and Na<sup>+</sup> were demonstrated by Mistlberger et al.<sup>25</sup> Using a visible light sensitive photoacid and



**Scheme 1.2.4.** Illustration for the chloride selective photodynamic sensing mechanism and chemical structures for the compounds used.

similar principle, the group of Chumbimuni-Torres also reported on a photoactivable Ca<sup>2+</sup> selective optical sensor. <sup>26</sup>

In addition to function as photodynamic ion selective optical sensor, the photoswitching induces ion flux at the sensor-sample interface that can also be used for local ion concentration perturbation. Artificial control of parameters such as the concentration of certain ions or molecules can help understand the function and mechanism of diverse *in vivo* biochemical processes.<sup>27-29</sup> Conventionally, this challenge was tackled by "caged molecules". Local increase of free Ca<sup>2+</sup> concentration using "caged calcium" such as NP-EGTA has been successful.<sup>27,30-33</sup> The photolysis, albeit irreversible, is able to raise the free Ca<sup>2+</sup> level in a short time. Caged compounds for other chemical messengers such as ATP and glutamate have been also reported.<sup>28,34</sup> Photoacid generators (PAG) have been used to induce a pH imbalance in cancer cells.<sup>35</sup> Despite the continuing emergence of caging compounds for various targets in recent years, the number of ions that can be released is rather limited. The ionophore based photodynamic optical ion sensing principle provides an attractive alternative for light induced ion concentration perturbation. Using K<sup>+</sup> as the model ion, we have demonstrated for the first time that the free K<sup>+</sup> level in an aqueous sample can be modulated by light. This work is discussed in Chapter 11 in detail.

#### 1.2.1 References for Part 2 of Chapter 1

- (1) He, H.; Uray, G.; Wolfbeis, O. S. Anal. Chim. Act. 1991, 246, 251.
- (2) Morf, W. E.; Seiler, K.; Lehmann, B.; Behringer, C.; Hartman, K.; Simon, W. Pure & Appl. Chem. 1989, 61, 1613.
- (3) Morf, W. E.; Seiler, K.; Rusterholz, B.; Simon, W. Anal. Chem. 1990, 62, 738.
- (4) Bakker, E.; Bühlmann, P.; Pretsch, E. Chem. Rev. 1997, 97, 3083.
- (5) Lerchi, M.; Bakker, E.; Rusterholz, B.; Simon, W. Anal. Chem. 1992, 64, 1534.
- (6) Bakker, E.; Crespo, G.; Grygolowicz-Pawlak, E.; Mistlberger, G.; Pawlak, M.; Xie, X. Chimia 2011, 65, 141.
- (7) Shvarev, A. J. Am. Chem. Soc. 2006, 128, 7138.
- (8) Emond, M.; Saux, T. L.; Maurin, S.; Baudin, J.-B.; Plasson, R.; Jullien, L. Chem. Eur. J. 2010, 16, 8822.
- (9) Emond, M.; Sun, J.; Grégoire, J.; Maurin, S.; Tribet, C.; Jullien, L. Phys. Chem. Chem. Phys. 2011, 13, 6493.
- (10) Shiraishi, Y.; Itoh, M.; Hirai, T. Phys. Chem. Chem. Phys. 2010, 12, 13737.
- (11) Davis, D. A.; Hamilton, A.; Yang, J.; Cremar, L. D.; Gough, D. V.; Potisek, S. L.; Ong, M. T.; Braun, P. V.; Mart nez, T. J.; White, S. R.; Moore, J. S.; Sottos, N. R. *Nature* 2009, 459, 68.
- (12) Monk, P. M. S.; Mortimer, R. J.; Rosseinsky, D. R. *Electrochromism: Fundamentals and Applications*; VCH: Weinheim, Germany/Basel, Switzerland, 2008.
- (13) Ziółkowski, B.; Florea, L.; Theobald, J.; Benito-Lopez, F.; Diamond, D. Soft Matter 2013, 9, 8754.
- (14) Levitus, M.; Talhavini, M.; Negri, R. M.; Atvars, T. D. Z.; Aramend á, P. F. *J. Phys. Chem. B* 1997, *101*, 7680.
- (15) Buback, J.; Kullmann, M.; Langhojer, F.; Nuernberger, P.; Schmidt, R.; Würthner, F.; Brixner, T. J. Am. Chem. Soc. 2010, 132, 16510.
- (16) Berkovic, G.; Krongauz, V.; Weiss, V. Chem. Rev. 2000, 100, 1741.
- (17) Mistlberger, G.; Crespo, G. A.; Xie, X.; Bakker, E. Chem. Commun. 2012, 48, 5662.
- (18) Byrne, R.; Ventura, C.; Lopez, F. B.; Walther, A.; Heise, A.; Diamond, D. Biosensors and Bioelectronics 2010, 26, 1392.
- (19) Fries, K. H.; Driskell, J. D.; Samanta, S.; Locklin, J. Analytical Chemistry 2010, 82, 3306.
- (20) Liu, Y.; Fan, M.; Zhang, S.; Sheng, X.; Yao, J. New J. Chem. 2007, 31, 1878.
- (21) Yagi, S.; Nakamura, S.; Watanabe, D.; Nakazumi, H. Dyes and Pigments 2009, 80, 98.
- (22) Liu, Y.; Fan, M.; Zhang, S.; Sheng, X.; Yao, J. Nwe J. Chem. 2007, 31, 1878.

- (23) Kimura, K.; Yamashita, T.; Yokoyama, M. J. Phys. Chem. 1992, 96, 5614.
- (24) Xie, X.; Mistlberger, G.; Bakker, E. J. Am. Chem. Soc. 2012, 134, 16929.
- (25) Mistlberger, G.; Crespo, G. A.; Xie, X.; Bakker, E. Chem. Commun. 2012, 48, 5662.
- (26) Johns, V. K.; Patel, P. K.; Hassett, S.; Calvo-Marzal, P.; Qin, Y.; Chumbimuni-Torres, K. Y. Anal. Chem. 2014, 86, 6184.
- (27) Ellis-Davies, G. C. R. Chem. Rev. 2008, 108, 1603.
- (28) Yu, H.; Li, J.; Wu, D.; Qiu, Z.; Zhang, Y. Chem. Soc. Rev. 2010, 39, 464.
- (29) Figueroa, L.; Shkryl, V. M.; Zhou, J.; Manno, C.; Momotake, A.; Brum, G.; Blatter, L. A.; Ellis-Davies, G. C. R.; R ós, E. *J. Physiol.* 2012, *590*, 1389.
- (30) Adam, S. R.; Kao, J. P. Y.; Grynkiewicz, G.; Minta, A.; Tsien, R. Y. J. Am. Chem. Soc. 1988, 110, 3212.
- (31) Ellis-Davies, G. C. R.; Kaplan, J. H. J. Org. Chem. 1988, 53, 1966.
- (32) Adams, S. R.; Kao, J. P. Y.; Tsien, R. Y. J. Am. Chem. Soc. 1989, 111, 7957.
- (33) Ellis-Davies, G. C. R.; Kaplan, J. H. Proc. Natl. Acad. Sci. 1994, 91, 187.
- (34) Olson, J. P.; Kwon, H.-B.; Takasaki, K. T.; Chiu, C. Q.; Higley, M. J.; Sabatini, B. L.; Ellis-Davies, G. C. R. *J. Am. Chem. Soc.* 2013, *135*, 5954.
- (35) Yue, X.; Yanez, C. O.; Yao, S.; Belfield, K. D. J. Am. Chem. Soc. 2013, 135, 2112.

## PART 3. INTRODUCTION TO CREATING ELECTROCHEMICAL GRADIENTS BY LIGHT FOR PHOTOELECTRIC CONVERSION

This has been published in: Xiaojiang Xie\* and Eric Bakker\*, "Creating electrochemical gradients by light: from bio-inspired concepts to photoelectric conversion", *Phys. Chem. Phys.*, 2014, 16, 19781-19789

There is ongoing research interest in learning from natural biochemical machinery to advance current technology. Solar energy arrives on Earth at an annual rate of ca. 120'000 terawatts which is significantly higher than the current annual worldwide energy consumption rate of ca. 15 terawatts. Adking efficient use of solar energy is a promising solution for the increasing global energy demand. Developing highly efficient solar cells has therefore become an extremely popular area in fundamental and applied science. Polar

Solar energy is harvested in nature by living organisms to produce (electro)chemical energy for almost all life on Earth. Photosynthesis is one of the most fundamentally important biological processes. In chlorophyll based photosynthetic centers, absorption of sunlight creates an electronic excitation in the peripheral antenna of photosynthetic systems (PSI and PSII) and the subsequent transfer of the excitation energy to reaction centers (RC). During the photoreaction, a proton gradient across the cell membrane is formed to generate proton-motive force, which eventually results in the production of adenosine triphosphate (ATP) by ATP synthase. These RCs are one of the most advanced photovoltaic devices developed by nature, with a quantum yield of ca. 100%, while this does not yet guarantee a high conversion efficiency.

Some archaea, such as *Halobacterium halobium*, do not possess the oxygenic photosynthetic system of green plants.<sup>16,17</sup> These microorganisms have instead developed photoproteins such as bacteriorhodopsin (bR), proteorhodopsin and halorhodopsin in the cell membrane to delocalize H<sup>+</sup> and Cl<sup>-</sup> and ATP upon light absorption.<sup>18-21</sup>

Nature seems to find its own way to harness solar energy by converting it to electrochemical and chemical energy. Either way, electrochemical gradients are formed after light absorption that are utilized to power various biological processes. An electrochemical gradient is a convenient energy form for biosystems. From a technological angle, following the generation of electrochemical gradient is the potential for its conversion to electrical energy in the form of an electric current. The concepts of light triggered electrochemical gradients and photoelectric conversion are therefore linked.

There has been extensive research work on mimicking the natural photosynthetic center in recent years. 4-6,23 In this perspective article, recent results on light-induced electrochemical gradients in bio-inspired artificial light harvesting systems and their implication for photoelectric conversion are discussed. We are focusing on fundamental mechanisms, potentials and limitations, with an emphasis on chemical principles. Conventional semiconductor based solar cells as well as dye sensitized solar cells (DSSC) are not the focus of this review.

#### 1.3.1 Mimicking Nature: Producing Electrochemical Gradients by Light-induced Charge Separation

Light-induced charge separation is ubiquitous in natural photosynthetic processes. Efficient electron transport and hole movement enable long distance charge separation and the generation of electrochemical gradients. In photoproteins of green plants, numerous chromophores are used to achieve the separation of charge and to avoid back reactions.<sup>24</sup>

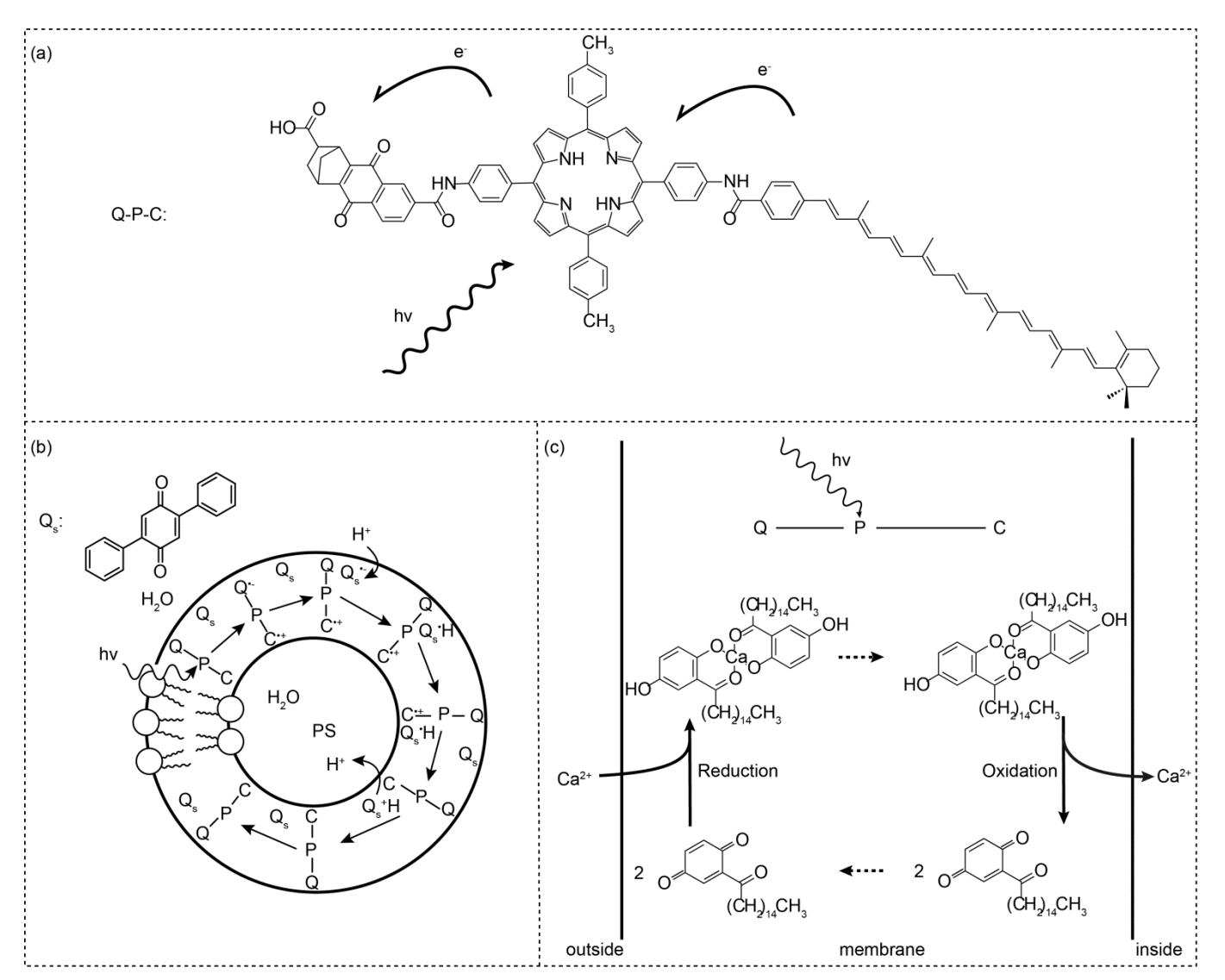


**Figure 1.3.1.** (a) Light induced charge separation in carotenoid polyene (C)-tetraarylporphyrin (P)-carboxylated norbornene (Q) triad. (b) Light-induced proton pumping across the bilayer lipid membrane containing oriented Q-P-C and  $Q_s$ . (c) Schematic representation of a liposome-based, light-powered transmembrane  $Ca^{2+}$  pump. The Q-P-C artificial reaction centre crosses the membrane, with its hydrophilic quinone moiety near the external interface. The shuttle molecule for  $Ca^{2+}$  is oxidized at the inner side and reduced at the outer side by the charge separated Q-P-C. Adapted from reference 25 and 27.

Although a direct duplication of the natural system is not possible owing to its high complexity, artificial light driven ion pumps have been attempted. A molecular triad Q-P-C containing carotenoid (C), porphyrin (P) and naphthoquinone (Q) moieties as shown in Figure 1.3.1 has been devised to make artificial photosynthetic centers and transport ions across biological lipid bilayer. <sup>25-27</sup> The triad undergoes photoinduced electron transfer from the excited singlet state of the porphyrin moiety to first yield the intermediate species Q\*-P\*-C, and subsequently the long range charge separated species Q\*-P-C\*+. The generation of the intermediate Q\*-P\*+-C has a quantum yield of nearly 1 while the conversion from Q\*-P\*+-C to Q\*-P-C\*+ has to compete with the charge recombination step (Q\*-P\*+-C to Q-P-C) and results in an overall quantum yield of 0.15. <sup>28</sup>

As illustrated in Figure 1.3.1 (b), a light controlled artificial proton pump has been proposed by doping liposomes with Q-P-C and 2,5-diphenylbenzoquinone ( $Q_s$ ), which acts as a shuttle for protons.<sup>25</sup> In this design, Q-P-C must align uniformly to result in the unidirectional

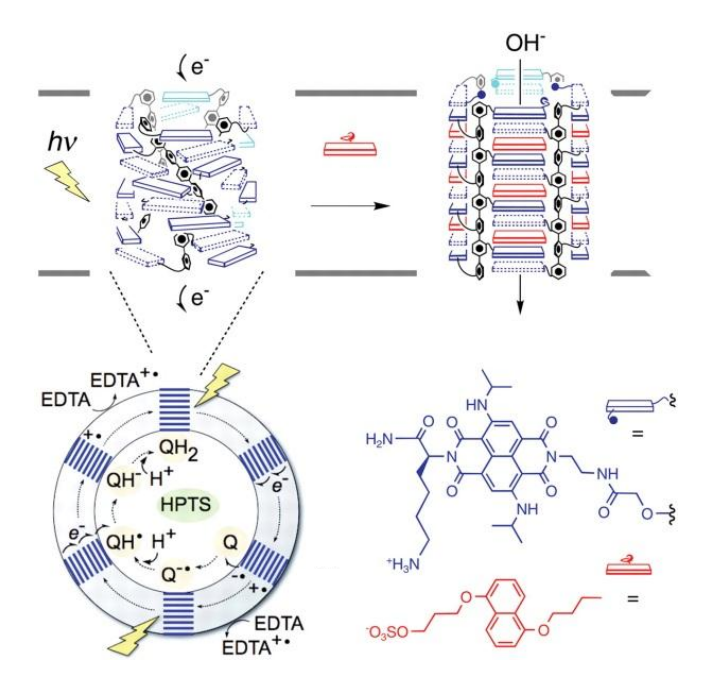


**Figure 1.3.2.** Photoproduction of H<sup>+</sup> gradient across lipid bilayers using  $\pi$ -stacked rigid-rod fluorescent supramolecules. Reproduced from reference 30 with permission. Copyright: The American Association for the Advancement of Science.

transport of  $H^+$ . Active transport of  $Ca^{2+}$  has been achieved by replacing Q with a chelator molecule for  $Ca^{2+}$ , as shown in Figure 1.3.1 (c).<sup>27</sup> The transport of  $Ca^{2+}$  also results in an increase of the transmembrane potential.

Reported by Imahori and co-workers, light irradiation on a similar ferrocene (Fc) –phorphyrin (P) - $C_{60}$  molecular triad yielded Fc<sup>+</sup>-P- $C_{60}$  with a lifetime of ca. 0.01 ms and a quantum yield of 0.25-0.99. The compound was used to control the transport of K<sup>+</sup> across a cell membrane.<sup>29</sup>

As shown in Figure 1.3.2, Matile et al. reported on a blue, red-fluorescent rigid-rod photosystem in which the  $\pi$ -stack supports sufficient charge separation for conversion into electrochemical gradients.<sup>30</sup> The photoproduction of proton gradients was achieved with lipid bilayer vesicles loaded with quinone acceptor and surrounded with the electron donor EDTA. The establishment of the proton gradient differs from the molecular triad approach since there is no shuttle for protons within the membrane. The pH change inside the vesicles is a result of electron infusion and the resulting reduction of entrapped quinone molecules. The concept has been adapted to devise multifunctional photosystems (see below).

Transition metal ion complexes that exhibit metal to ligand charge transfer (MLCT) have been employed to create transmembrane gradients as well. Hurst and co-workers reported on the transport of pyrylium ions in vesicle based photocatalytic systems containing tris(2, 2'-bipyridine)-Co(III) ion and zinc porphyrin. Hvasanov *et al.* demonstrated a light driven proton pump across a polymer bilayer. Ruthenium(II)-terpyridine was linked to cytochrome c and coupled to cytochrome c oxidase to drive the electron transport chain.

To summarize, the generation of intra/intermolecular long range charge separation in artificial light harvesting systems has been achieved in the past few decades. Charge recombination must be suppressed as much as possible. Although only a few examples are reported, this direction should be continued due to the insight it can provide to further solar energy utilization.

$$N_{+}$$
  $N_{+}$   $N_{+$ 

Figure 1.3.3. Proton pump cycle of bR in Halobacterium halobium, with dark arrows showing the dark transitions.

#### 1.3.2 Photo-isomerization for Ion Transportation

Bacteriorhodopsin (bR), a retinal containing photochromic protein with a molecular weight of 26784 daltons produced by halobacteria, is the second biggest photosynthetic system. Conceptually similar to the biological machinery of vision, the bR photosynthetic system works differently from the more developed chlorophyll system of green plants. As shown in Figure 1.3.3, light is absorbed by bR with an absorption maximum at 568 nm ( $B_{568}$ ) and causes the photoisomerization of the protein-bound all-trans retinal about its 14–15 single bond to the 13-cis isomer ( $K_{590}$ ).  $K_{590}$  has a reduced pKa and rearranges the proton conductive pathways, resulting in the proton displacement from the inner side of the cell membrane to the outer surroundings. After photoisomerization, the retinal molecule is released from the protein and a new molecule takes its place. Freely dissolved retinal does not absorb in the visible range, thereby efficiently localizing the light absorption step in the membrane protein.

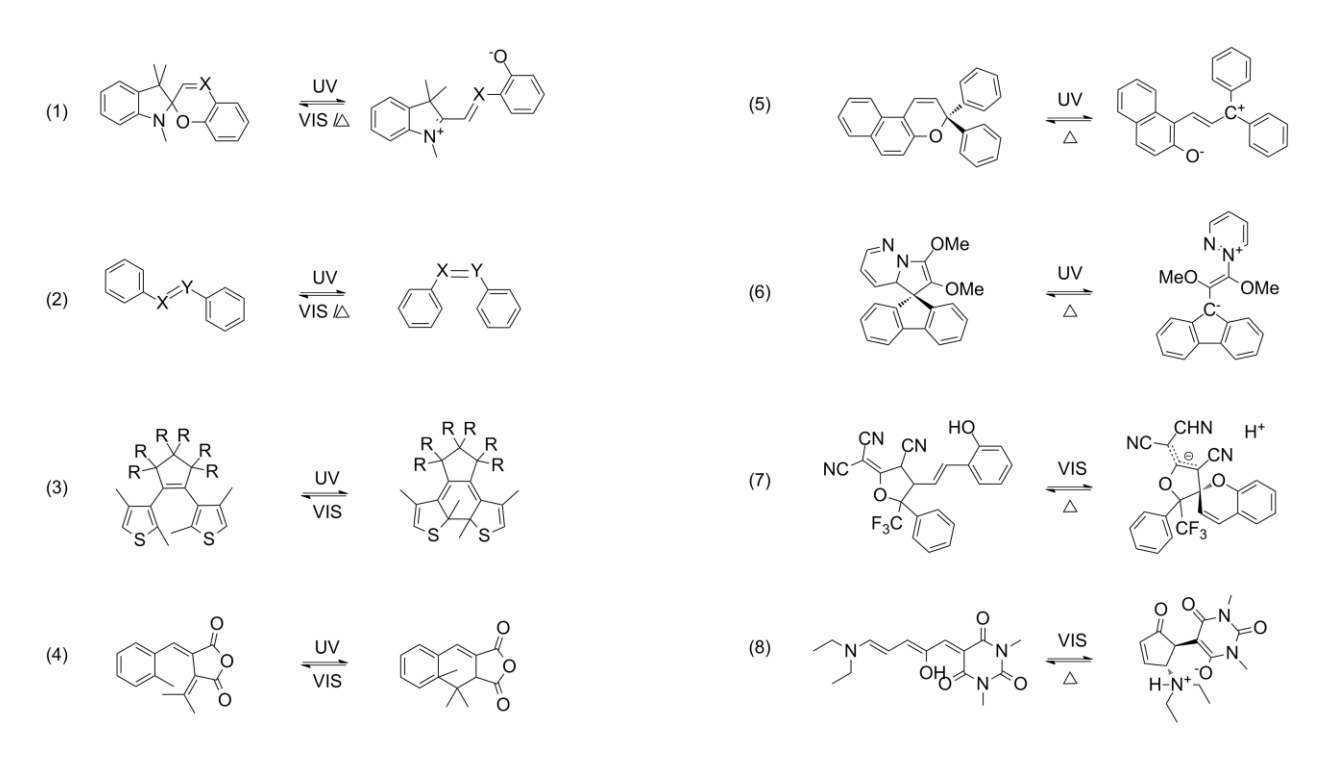


**Figure 1.3.4.** Photo-isomerization of some well-known photoswitchable compounds. (1) spiropyran (X=C) and spirooxazine (X=N), (2) azobenzene (X=Y=N), stylbene (X=Y=C) and Shiff base (X=C, Y=N), (3) diarylethene (R=F or H), (4) fulgide, (5) chromene (6) dihydroindolizine (7) visible light responsive photoacid from reference 38, (8) visible light switchable compound form reference 39.

Other photochromic proteins such as proteorhodopsin and halorhodopsin share similar mechanisms.  $^{21,35,36}$  Unlike in the chlorophyll system, it is the photo-isomerization after light absorption that results in the affinity change for H $^+$  and the electrochemical gradient.

Since photo-isomerization usually causes changes in molecular light absorption, some of the compounds are also called photochromic compounds, or molecular photoswitches. The rhodopsin based photosynthetic centers in nature are much younger than the chlorophyll based ones found in green plants.<sup>37</sup> Why did nature take such a long time to evolve this second photosystem? As far as the number of different models is concerned, natural photochromic proteins are rather rare. Indeed, not many molecular varieties exist that can undergo photo-isomerization, even taking synthetic ones into account. Figure 1.3.4 shows the core structures of some well-known photochromic compounds.

Photochromic compounds are sensitive to photons and many of them transform upon UV light radiation, since the energy required to relocate atoms is rather high. Only a few chemicals can be switched by visible light from their thermally stable state. 38-40 Nature has developed retinal, which is sensitive to visible light in its protein bound form. The likely reason lies in the emission maximum of sunlight,

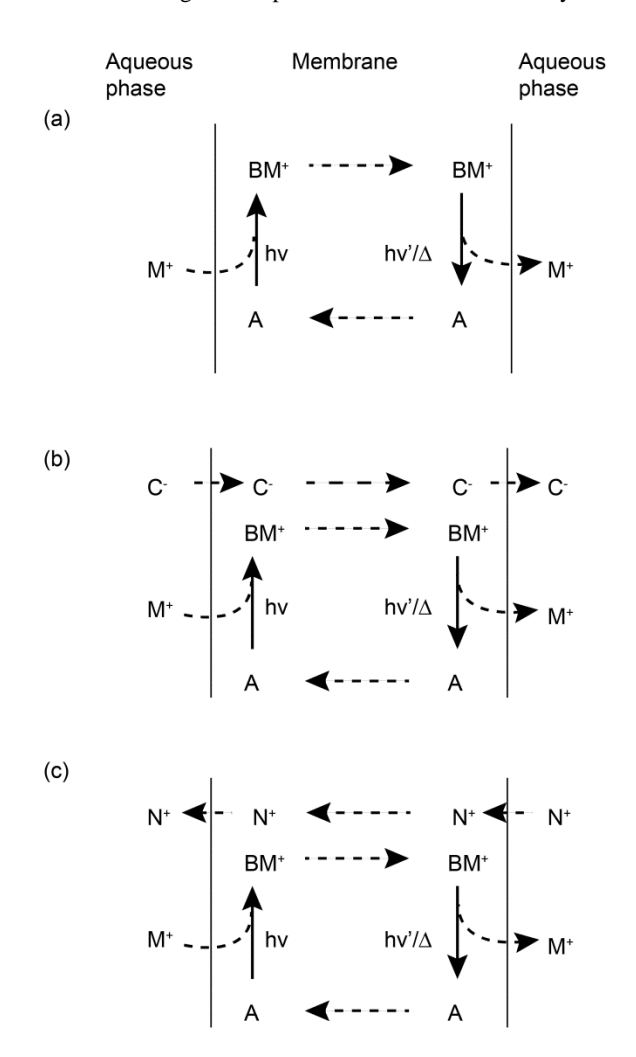


**Figure 1.3.5.** Light induced ion transport across a liquid membrane containing a photoswitchable compound that undergoes a photoreaction from A to B. B has a higher affinity for  $M^+$  and carries  $M^+$  across the membrane where it is converted back to A, either thermally ( $\Delta$ ) or catalyzed by light of a different wavelength (hv'). (a) Transporting  $M^+$  with no interfering ions, (b) Co-transport of  $M^+$  and a lipophilic anion  $C^-$ , (c) Counter-transport of  $M^+$  and  $N^+$ .

which is similar to this absorption maximum in its protein bound form.

A limited number of artificial systems to transport ions and create electrochemical gradient that resemble bR have been reported. In order to create an ion flux based on the photochromic compounds, the compound's affinity for a certain ion must change upon light irradiation. For example, azobenzenes, diarylethenes and spiropyrans (Sp) are widely studied compounds that can be used to make so-called photocontrollable molecular switches.<sup>41</sup>

In principle, as shown in Figure 1.3.5, light triggered transportation of ions can be induced by incorporating molecular switches into membranes, thereby separating two chambers containing the interactive ions. In the simplest approach (Figure 1.3.5 (a)), ions are transported directly by the photo-responsive carriers, resulting in a net charge separation. Electrochemical gradients will form within the membrane and an electric potential difference will arise at the two sides of the membrane. In less energetically challenging designs (Figure 1.3.5 (b) and (c)), the electrochemical gradient is coupled to a counter acting or co-transporting ion flux, without net charge accumulation at the two membrane sides. The conteracting flux will cause a diminished electric potential difference.

Kumano *et al.* used azobenzene bridged crown ether to transport K<sup>+</sup> across a thick plasticized poly(vinyl chloride) (PVC) membrane, accompanied by co-transport of chloride or p-toluenesulfonate ions. <sup>42</sup> The *cis* isomer exhibits a higher affinity for K<sup>+</sup> and thus facilitates the K<sup>+</sup> uptake at the UV side. Sakamoto *et al.* reported on several azacrown modified spiropyrans as photo-responsive carriers for alkali metal ions. <sup>43</sup> These molecules were shown to transport alkali metal ions across dichloromethane membrane in the presence of the picrate ion, which was co-transported to provide visual perception of the transportation. Azobenzenes were also embedded in vesicles as modulators for potassium ion permeation. <sup>44</sup>

Bakker and colleagues reported that the photo-isomerization of spiropyrans results in two structures of very different basicity.<sup>45</sup> The light induced basicity change highly resembles the photo-properties of the retinal compounds in natural bR. Chloride ions can be co-extracted into a polymeric membrane together with H<sup>+</sup> by UV light illumination, generating a electrochemical gradient of Cl<sup>-</sup> at the aqueous-

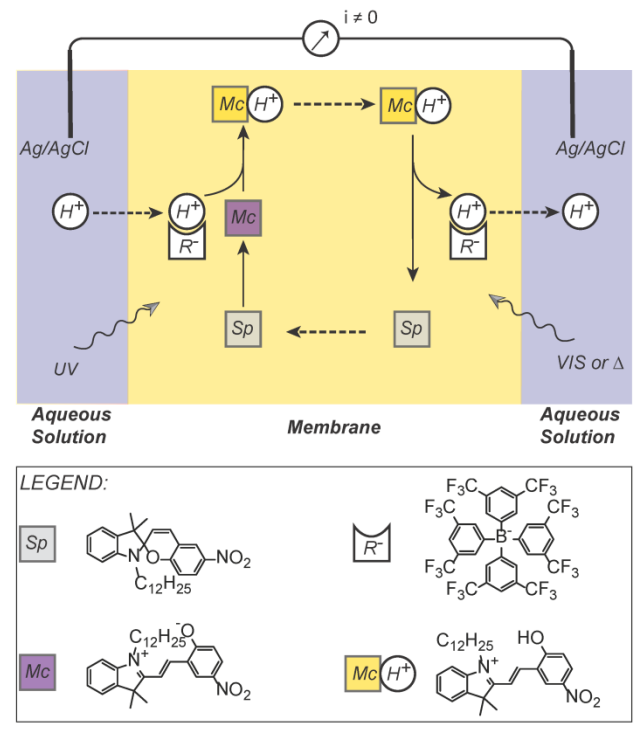


Figure 1.3.6. Scheme showing the photocurrent generation principle. The left side of the membrane is illuminated with UV light while the right side is irradiated with visible light or kept in the dark. The membrane contains 5 mg Sp, 6.5 mg ETH 500 and 3 mg K<sup>+</sup>R<sup>-</sup> in 50 mg nitrophenyloctylether as solvent. The aqueous solutions both contain 0.1M HCl. For simplicity, ETH 500 and Cl<sup>-</sup> are not shown. The Dashed arrows represent mass transport of the species.

polymeric phase boundary (Chapter 10).<sup>46</sup> Later, nanospheres containing Sp and other receptors (ionophores) were shown capable of modulating the surrounding K<sup>+</sup> concentration (Chapter 11).<sup>47</sup> Recently, it was demonstrated that H<sup>+</sup> can be relocated by polymeric liquid membrane embedded with Sp, forming an artificial proton pump (Figure 1.3.6, see Chapter 13).<sup>48</sup> This is the first time that photoswitchable compounds were used to create a proton pump in rather thick (ca. 25 µm) polymeric membrane, converting light to electrochemical energy and later to current. In order to increase the proton transport rate, asymmetric light illumination was required, while only one sided illumination is needed in photovoltaic cells and natural photosynthetic systems. Proton pumping was still observed with just one sided UV or visible light irradiation but the gradient was much smaller. This part will be discussed in Chapter 13 in more detail.

#### 1.3.3 From Artificial Photosynthesis to Photoelectric Conversion

#### 1.3.3.1 Utilizing Light-induced Charge Separation: A Chemical Approach

If charged species are transported across a membrane without any counteracting flux, an electrochemical potential difference will establish between the two sides of the membrane. Electrochemically, this gradient can be used to generate electric energy, given that the two chambers separated by the membrane are connected through an external load (Figure 1.3.6).

Despite the conceptual elegance of electrochemical gradients created by charge separation in liposomes and polymersomes, direct conversion from light energy to electrical energy requires alternative designs. After light induced charge separation, electrons or holes must move toward an electrode, as in DSSC.<sup>49</sup>

Self-assembled monolayers (SAMs) are expected to provide a promising avenue for this purpose. There have been so far many examples of light-induced energy/electron transfer on gold electrodes and semiconductors. Early on, photocurrent generation in metal bisphosphonate multilayer thin films with a power conversion efficiency of 0.05% were reported.<sup>50</sup> Later, molecular triads with a long lived long range charge separated state were self-assembled on gold electrodes to generate photocurrents.<sup>51</sup> Similarly, gold electrodes modified with mixed self-assembled monolayers of porphyrin-ferrocene-thiol triad, boron-dipyrrin and ferrocene-porphyrin-fullerene triad were used to convert light to current with efficiencies near 1%.<sup>52</sup> Fullerenes or ruthenium tris(bipyridyl) complexes modified self-assembled monolayers on gold electrodes able to modulate the photocurrent generation were also reported.<sup>53</sup> However, efficient energy conversion (overall efficiency 1%-10%) from light to current was hampered due to the difficulty in assembling the donor-acceptor linked molecules unidirectionally.

Matile and co-workers reported on a zipper assembly of photoactive rigid-rod naphthalenediimide  $\pi$ -stack architectures on gold nanoparticles and gold electrodes, representing a different approach to achieving highly ordered long range charge separation. <sup>54</sup> Upon light illumination, electrons and holes can move across the  $\pi$ -stack in opposite directions, similar to the process reported in the photoproduction of H<sup>+</sup> gradients in lipid bilayers. Later, the same group proposed a self-organizing surface-initiated polymerization (SOSIP) to create ordered functional photosystems on transparent conductive glass surfaces. <sup>55</sup> Despite the fact that the efficiency so far is not yet sufficient for practical use, the conceptual design to achieve self-organized photosystem is quite elegant.

#### 1.3.3.2 Photoprotein Modified Electrode

On the other hand, it has long been recognized that the natural RC pigment proteins can be utilized *in vitro*. Instead of mimicking the natural photoinduced charge separation, researchers have taken one step back and introduced photoprotein-modified electrodes.

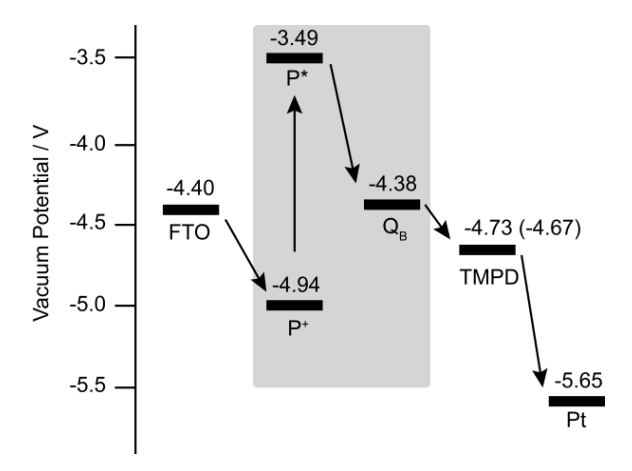


**Figure 1.3.7.** Vacuum potentials of key components of a photoelectric cell composed of a photoprotein modified FTO electrode, a Pt counter electrode and TMPD as redox shuttle, adapted from reference 56.

As reported by Welland and co-workers, such photoelectrochemical cells are typically constructed with a conductive glass anode modified with photoprotein, an electrolyte solution containing the electron transducer, and a platinum cathode. Figure 1.3.7 shows the vacuum potentials for the key components. Upon light irradiation, a charge separation is formed to produce P<sup>+</sup>-Q<sub>B</sub>. While P<sup>+</sup> is reduced at the fluorine-doped tin oxide (FTO) electrode, Q<sub>B</sub> is oxidized by the redox mediator *N,N,N',N'*-tetramethyl-p-phenylenediamine (TMPD), which later delivers the electrons to the Pt counter electrode. These photoelectrochemical cells can produce direct current upon continuous illumination and also alternating current in response to discontinuous illumination. Despite the extremely high yield of primary charge separation and the relative large open-circuit voltage (ca. 0.21 V), the external power conversion efficiency is relatively low. One possible reason is the buried location of the electron transfer molecules inside the RC, which could increase the intermolecular distance and cause elevated electron-tunneling barrier.

As in the artificial photosynthetic centers, the orientation and alignment of the RC is very important. An additional mediator could also help reduce the electron-tunneling barrier. For instance, incorporating cytochrome c into the immobilized RC can significantly improve the electron transfer process between RC and the gold electrode.<sup>58</sup>

In conceptually similar work, Yaghoubi *et al.* showed that the photosynthetic reaction center can be immobilized through a carboxylic acid terminated cytochrome c linker for applications in photoprotein-based bio-photovoltaic devices. <sup>59</sup> Choi *et al.* have reported on bio-photodiodes with self-assembled heterolayers containing green fluorescent proteins, cytochrome c or organic molecules such as viologen through Langmuir-Blodgett techniques. <sup>60,61</sup>

Construction of solar cells with bR has attracted attention in recent years because of bR's high long term stability and bio-functionality against thermal, chemical, and photochemical degradation.<sup>22</sup> Following the early reconstruction of bR in proteoliposomes to generate electric potentials<sup>62</sup>, Thavasi *et al.* studied the feasibility of bR as bio-photosensitizer in excitonic solar cells.<sup>63</sup> Recently, bR was molecularly linked to quantum dots to introduce photovoltaic devices towards improvement in solar cell efficiency.<sup>64</sup> The theoretical efficiency limit for such photovoltaic device should obey the Shockley–Queisser limit.<sup>65</sup>

In conclusion, bR is now becoming a promising candidate in photoelectric conversion. However, the variety of photoproteins that can be fixed on an electrode remains limited. Construction of the electrodes requires attention since the unidirectional orientation of the protein array is the key to obtaining a high efficiency.

#### 1.3.3.3 Photo-Isomerization for Photoelectric Conversion: How Far Can It Go?

At the heart of every photoelectric conversion device, there lies the photon to electrical transduction mechanism. How to generate a photovoltage and make the most efficient use of it? In natural systems, relocation of ionic species can influence the electrostatic fields and build up the electric potential difference. However, in electrochemical cells, electrode potentials are closely related to the concentration (more strictly, the activity) of the redox active species by the Nernst equation. A photovoltage is formed when a photoreaction changes the concentration of the redox active species, which defines the electrode potential. Current will flow once the two electrodes are connected. The steady state photocurrent density can be limited by a number of factors including electrode material, light intensity, photoreaction rate, electrode reaction kinetics, mass transport, and the ohmic drop from the solvent.<sup>66</sup>

Previous photoelectric conversion methodologies involve mostly utilization of charge separation processes after light absorption. Photoisomerization, the process that occurs in photochromic proteins, seems to be much less explored. There are very few reports on
photoelectric conversion based on photo-isomerization mechanism. Previously it has been proposed that spiropyran can be used in
photoelectric conversion. As As shown in Figure 1.3.6, a polymeric membrane doped with Sp and ion exchanger has been shown to transport
H<sup>+</sup> under asymmetric light illumination. The pumping of H<sup>+</sup> creates an electrochemical gradient across the membrane. Therefore, when the
two sides of the membrane are connected to appropriate electrode elements, current will flow. In addition to direct current, alternating
current can be produced by applying alternating UV and visible light to one side of the membrane. Nevertheless, the design requires two
aqueous solutions bracketing the membrane and acting as source and sink for proton transport, and additional Ag/AgCl elements as ion to
electron transducers. These elements cannot renew themselves and will place a limit on the efficiency of the photoconversion system. Soon
afterward, Xie and Bakker proposed a new approach in which photoswitchable compounds can be used together with proton-coupled
electron transfer (PCET) reactions for photoelectric conversion (Chapter 14). As shown in Figure 1.3.8, the electrode potential is defined
by the PCET redox pair, quinone/hydroquinone. Since for a PCET redox couple, the redox potential also depends on H<sup>+</sup> concentration,
changing the local pH will result in an change on this potential. Be redox potential is therefore related to the specific form of Sp at the
electrode. At the UV side, the photomerocyanine (Mc) prevails, with a much higher basicity than the ring-closed form. On the opposite side,
Mc is converted back to Sp upon visible light illumination.

Unfortunately, the efficiency for this initial device is ca. 0.02%, limited mainly by the large PCET redox barrier at the electrode surface.<sup>67</sup>

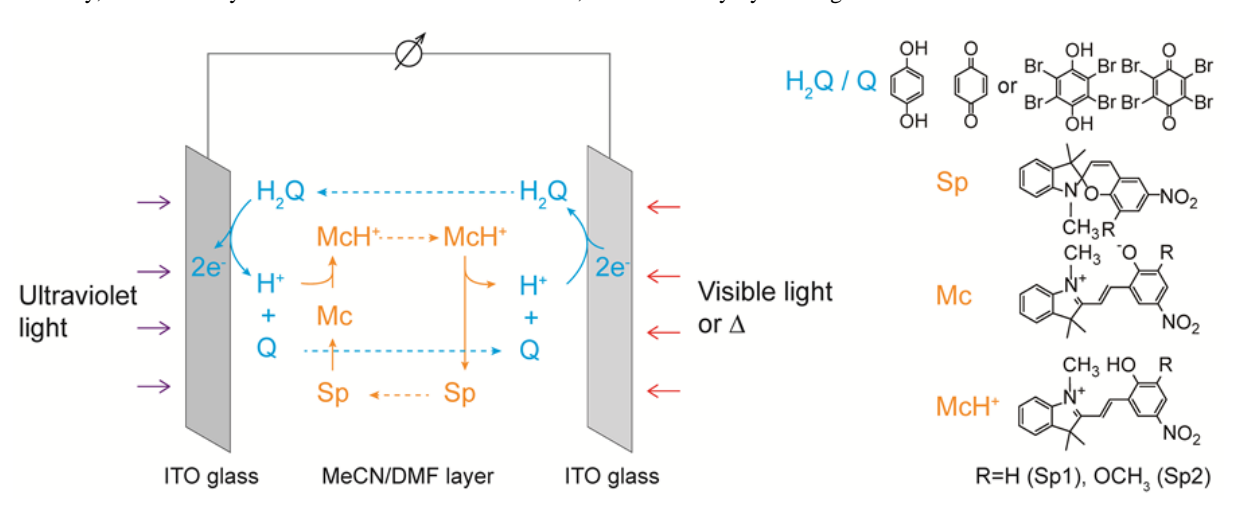


**Figure 1.3.8.** Photoelectric cell based on PCET and a photo-isomerization reaction. Ultraviolet light (UV) is introduced from one side where Sp is transformed to Mc. The opposite side where the ring-opened form is transformed back to Sp is illuminated by visible light or left in dark ( $\Delta$ ). A photovoltage is formed with the electrode potential at the UV side lower than the other. Tetrabutylammonium hexafluorophosphate is used as supporting electrolyte.

In that work, ITO glasses act merely as conductive and optically transparent substrates. A thin coating of catalyst on the ITO substrate, resulting in minimal attenuation of the incident light, would be most promising to effectively catalyse the PCET reaction. On the other hand, other photo-isomerizable compounds inducing a basicity change could also be explored. Azobenzene based photoswitches that exhibit large acidity changes upon light irradiation were reported by Jullien and co-workers. Visible light sensitive reversible photoacids were also recently introduced. Excited state photoacids such as 8-Hydroxypyrene-1,3,6-trisulfonic acid (HPTS) could potentially be promising as well for this purpose.

Similar to the light driven proton pump bR, the molecular isomerization of photochemical compounds is not only driven by photon energy but also thermal energy. The influence of temperature on such photoelectric devices should be studied carefully. Photoelectric conversion based on photo-isomerization reactions is a young topic and there is much to be explored. As more photoswitchable compounds are being discovered, the field is expected to become more active.

#### 1.3.4 Concluding Remarks

There are two general types of photosynthetic systems in nature: the older chlorophyll system in green plants and the more recent bR system in *Halobacterium halobium*. Artificial photosystems converting light energy to electrochemical gradients and electrical energy have been widely explored with a significant focus on mimicking the chlorophyll based one. In these approaches, light absorption results in a charge separation state followed by electron and hole transport. However, artificial photosystems that implement lessons from the other photosynthetic system bR have been less explored. It has taken nature more than a billion years to develop the bR photosystem<sup>37</sup>, so perhaps making efficient use of solar energy through photo-isomerizing molecules can be time consuming as well. Nevertheless, its potential and importance should not be overlooked.

Admittedly, the varieties of photoswitchable molecules are not yet sufficiently versatile, and there has been comparably slow progress to diversify the available molecular toolbox. With some key developments summarized in this perspective article, we expect that efficient energy conversion devices based on photo-isomerization reactions will eventually be realized.

#### 1.3.5 References for Part 3 of Chapter 1

- (1) Hoffert, M. I.; Caldeira, K.; Benford, G.; Criswell, D. R.; Green, C.; Herzog, H.; Jain, A. K.; Kheshgi, H. S.; Lackner, K. S.; Lewis, J. S.; Lightfoot, H. D.; Manheimer, W.; Mankins, J. C.; Mauel, M. E.; Perkins, L. J.; Schlesinger, M. E.; Volk, T.; Wigley, T. M. L. Science 2002, 298, 981.
- (2) Barber, J. Chem. Soc. Rev. 2009, 38, 185.
- (3) Nocera, N. S. L. a. D. G. Proc. Nat. Acad. Sc. 2006, 103, 15729.
- (4) Gust, D.; Moore, T. A.; Moore, A. L. Acc. Chem. Res. 2001, 34, 40.
- (5) Gust, D.; Moore, T. A.; Moore, A. L. Acc. Chem. Res. 2009, 42, 1890.
- (6) Vulley, V. I. J. Phys. Chem. Lett. 2011, 2, 503.
- (7) LaVan, D. A.; Cha, J. N. Proc. Nat. Acad. Sc. 2006, 103, 5251.
- (8) Robert E. Blankenship; David M. Tiede; James Barber; Gary W. Brudvig; Graham Fleming; Ghirardi, M.; Gunner, M. R.; Junge, W.; Kramer, D. M.; Melis, A.; Moore, T. A.; Moser, C. C.; Nocera, D. G.; Nozik, A. J.; Ort, D. R.; Parson, W. W.; Prince, R. C.; Sayre, R. T. Science 2011, 332, 805.
- (9) Burschka, J.; Pellet, N.; Moon, S.-J.; Humphry-Baker, R.; Gao, P.; Nazeeruddin, M. K.; Gräzel, M. Nature 2013, 499, 316.
- (10) Gholivand, M. B.; Babakhanian, A.; Kaki, S.; Mohammadi, M.; Moradi, P. Sensor Lett. 2013, 11, 1651.
- (11) Grätzel, M. Nature 2001, 414, 338.

- (12) Günes, S.; Neugebauer, H.; Sariciftci, N. S. Chem. Rev. 2007, 107, 1324.
- (13) Nelson, N.; Ben-Shem, A. Nat. Rev. Mol. Cell Biol. 2004, 5, 1.
- (14) Cheng, Y.-C.; Fleming, G. R. Annu. Rev. Phys. Chem. 2009, 60, 241.
- (15) Zhu, X.-G.; Long, S. P.; Ort, D. R. Annu. Rev. Plant Biol. 2010, 61, 235.
- (16) El-Sayed, M. A. Acc. Chem. Res. 1992, 25, 279.
- (17) Bamann, C.; Nagel, G.; Bamberg, E. Curr. Opin. Neurobiol. 2010, 20, 610.
- (18) Heberle, J.; Fitter, J.; Sass, H. J.; Buldt, G. Biophys. Chem. 2000, 85, 229.
- (19) Lanyi, J. K. Biophys. Chem. 1995, 56, 143.
- (20) Pal, R.; Sekharan, S.; Batista, V. S. J. Am. Chem. Soc. 2013, 135, 9624.
- (21) Tamogami, J.; Kikukawa, T.; Nara, T.; Shimono, K.; Demura, M.; Kamo, N. Biochemistry 2012, 51, 9290.
- (22) Hampp, N. Chem. Rev. 2000, 100, 1755.
- (23) Wen, L.; Hou, X.; Tian, Y.; Zhai, J.; Jiang, L. Adv. Funct. Mater. 2010, 20, 2636.
- (24) Wasielewski, M. R. Chem. Rev. 1992, 92, 435.
- (25) Steinberg-Yfrach, G.; Liddell, P. A.; Hung, S.-C.; Moore, A. L.; Gust, D.; Moore, T. A. Nature 1997, 385, 239.
- (26) Steinberg-Yfrach, G.; Rigaud, J.-L.; Durantini, E. N.; Moore, A. L.; Gust, D.; Moore, T. A. Nature 1998, 392, 479.
- (27) Bennett, I. M.; Farfano, H. M. V.; Bogani, F.; Primak, A.; Liddell, P. A.; Otero, L.; Sereno, L.; Silber, J. J.; Moore, A. L.; Moore, T. A.; Gust, D. *Nature* 2002, *420*, 398.
- (28) Hung, S.-C., Arizona State Univ., 1995.
- (29) Numata, T.; Murakami, T.; Kawashima, F.; Morone, N.; Heuser, J. E.; Takano, Y.; Ohkubo, K.; Fukuzumi, S.; Mori, Y.; Imahori, H. *J. Am. Chem. Soc.* 2012, *134*, 6092.
- (30) Bhosale, S.; Sisson, A. L.; Talukdar, P.; Furstenberg, A.; Banerji, N.; Vauthey, E.; Bollot, G.; Mareda, J.; Roger, C.; Wurthner, F.; Sakai, N.; Matile, S. *Science* 2006, *313*, 84.
- (31) Liang, S.; Zhu, L.; Hurst, J. K. Langmuir 2012, 28, 12171.
- (32) Khairutdinov, R. F.; Hurst, J. K. Nature 1999, 402, 509.
- (33) Hvasanov, D.; Peterson, J. R.; Thordarson, P. Chem. Sci. 2013, 4, 3833.
- (34) Schulten, K.; Tavan, P. Nature 1978, 272, 85.
- (35) Mukohata, Y.; Ihara, K.; Tamura, T.; Sugiyama, Y. J. Biochem. 1999, 125, 649.
- (36) Essen, L.-O. Curr. Opin. Struct. Biol. 2002, 12, 516.
- (37) Baltscheffsky, H. Origin and Evolution of Biological Energy Conversion; Wiley, 1996.
- (38) Johns, V. K.; Peng, P.; DeJesus, J.; Wang, Z.; Liao, Y. Chem. Eur. J. 2014, 20, 689.
- (39) Helmy, S.; Leibfarth, F. A.; Oh, S.; Poelma, J. E.; Hawker, C. J.; Alaniz, J. R. d. J. Am. Chem. Soc. 2014, 136, 8169.
- (40) Shi, Z.; Peng, P.; Strohecker, D.; Liao, Y. J. Am. Chem. Soc. 2011, 133, 14699.
- (41) Natali, M.; Giordani, S. Chem. Soc. Rev. 2012, 41, 4010.
- (42) Kumano, A.; Niwa, O.; Kajiyama, T.; Takayanagi, M.; Kano, K.; Shinkai, S. Chem. Lett. 1983, 1327.
- (43) Sakamoto, H.; Takagaki, H.; Nakamura, M.; Kimura, K. Anal. Chem. 2005, 77, 1999.
- (44) Lei, Y.; Hurst, J. K. Langmuir 1999, 15, 3424.
- (45) Mistlberger, G.; Crespo, G. A.; Xie, X.; Bakker, E. Chem. Commun. 2012, 48, 5662.
- (46) Xie, X.; Mistlberger, G.; Bakker, E. J. Am. Chem. Soc. 2012, 134, 16929.
- (47) Xie, X.; Bakker, E. ACS Appl. Mater. Interfaces 2014, 6, 2666.
- (48) Xie, X.; Crespo, G. A.; Mistlberger, G.; Bakker, E. Nat. Chem. 2014, 6, 202.
- (49) O'Regan, B.; Gräzel, M. *Nature* 1991, *353*, 737.

- (50) Byrd, H.; Suponeva, E. P.; Bocarsly, A. B.; Thompson, M. E. *Nature* 1996, 380, 610.
- (51) Imahori, H.; Yamada, H.; Ozawa, S.; Ushida, K.; Sakata, Y. Chem. Commun. 1999, 1165.
- (52) Imahori, H.; Norieda, H.; Yamada, H.; Nishimura, Y.; Yamazaki, I.; Sakata, Y.; Fukuzumi, S. J. Am. Chem. Soc. 2001, 123, 100.
- (53) Xie, H.; Jiang, K.; Zhan, W. Phys. Chem. Chem. Phys. 2011, 13, 17712.
- (54) Sakai, N.; Sisson, A. L.; Burgi, T.; Matile, S. J. Am. Chem. Soc. 2007, 129, 15758.
- (55) Sakai, N.; Lista, M.; Kel, O.; Sakurai, S.-i.; Emery, D.; Mareda, J.; Vauthey, E.; Matile, S. J. Am. Chem. Soc. 2011, 133, 15224.
- (56) Tan, S. C.; Crouch, L. I.; Mahajan, S.; Jones, M. R.; Welland, M. E. ACS Nano 2012, 6, 9103.
- (57) Tan, S. C.; Crouch, L. I.; Jones, M. R.; Wellland, M. Angew. Chem. Int. Ed. 2012, 51, 6667.
- (58) Lebedev, N.; Trammell, S. A.; Spano, A.; Lukashev, E.; Griva, I.; Schnur, J. J. Am. Chem. Soc. 2006, 128, 12044.
- (59) Yaghoubi, H.; Jun, D.; Beatty, J. T.; Takshi, A. MRS Symp. Proc. 2013, 1572, mrss13.
- (60) Choi, J.-W.; Fujihira, M. Appl. Phys. Lett. 2004, 84, 2187.
- (61) Choi, J.-W.; Nam, Y.-S.; Lee, W.-H.; Kim, D.; Fujihira, M. Appl. Phys. Lett. 2001, 79, 1570.
- (62) Drachev, L. A.; Kondrashin, A. A.; Samuilov, V. D.; Skulachev, V. P. PEBS Lett. 1975, 50, 219.
- (63) Thavasi, V.; Lazarova, T.; Filipek, S.; Kolinski, M.; Querol, E.; Kumar, A.; Ramakrishna, S.; Padrós, E.; Renugopalakrishnan, V. J. Nanosci. Nanotechnol. 2009, 9, 1679.
- (64) Renugopalakrishnan, V.; Barbiellini, B.; King, C.; Molinari, M.; Mochalov, K.; Sukhanova, A.; Nabiev, I.; Fojan, P.; Tuller, H. L.; Chin, M.; Somasundaran, P.; Padrós, E.; Ramakrishna, S. *J. Phys. Chem. C* 2014, *in press*.
- (65) Shockley, W.; Queisser, H. J. J. Appl. Phys 1961, 32, 510.
- (66) Bard, A. J.; Faulkner, L. R. Electrochemical Methods: Fundamentals and Applications; 2 ed.; John Wiley & Sons, Inc., 2001.
- (67) Xie, X.; Bakker, E. J. Am. Chem. Soc. 2014, 136, 7857.
- Weinberg, D. R.; Gagliardi, C. J.; Hull, J. F.; Murphy, C. F.; Kent, C. A.; Westlake, B. C.; Paul, A.; Ess, D. H.; McCafferty, D. G.; Meyer, T. J. Chem. Rev. 2012, 112, 4016.
- (69) Hammes-Schiffer, S. Chem. Rev. 2010, 110, 6937.
- (70) Emond, M.; Saux, T. L.; Maurin, S.; Baudin, J.-B.; Plasson, R.; Jullien, L. Chem. Eur. J. 2010, 16, 8822.
- (71) Minkin, V. I. Chem. Rev. 2004, 104, 2751.

# Chapter 2. Ultrasmall Fluorescent Ion-Exchanging Nanospheres Containing Selective Ionophores

This work has been published in: Xiaojiang Xie, Günter Mistlberger, and Eric Bakker\*, Anal. Chem., 2013, 85, 9932–9938

#### 2.1 Introduction

There is an ongoing search to develop sensing strategies for small inorganic ions since they are nutritionally and biologically essential. The fact that they are not biodegradable and remain in ecological systems has made their natural level important aspects in environmental monitoring. The analysis of ions largely relies on electrochemical methods and optical sensors, followed by atomic (flame) emission spectrometry (AES), atomic absorption spectrometry (AAS), as well as fluorimetry and capillary electrophoresis (CE). Although electrochemical methods such as potentiometry, voltammetry, and coulometry are very sensitive, miniaturization is difficult and limits their application in small biological samples such as single cells. Ion-selective microelectrodes have been used to directly measure intracellular concentrations of common inorganic ions. However, they assess ion concentration only at a single location in the cell, tend to be noisier and more difficult to handle than larger, more traditionally sized ion-selective electrodes and require a reference electrode to be inserted at the point of measurement.

Optical sensors are advantageous in this regard since they are easier to miniaturize and in principle suitable for chemical imaging applications. Ion-selective indicators, whose light emission reflects the local concentration of the ion, have been used for this purpose. Examples include indo-1, rhod-2 and fluo-3 for Ca<sup>2+</sup>, lucigenin and SPQ (M-440) for Cl<sup>-</sup> and Sodium Green for Na<sup>+</sup>. <sup>12-16</sup> Although these indicators are widely used, they suffer from some drawbacks such as cytotoxicity, heavy metal interference (i.e., selectivity), dye leakage and sequestration. <sup>17</sup> Moreover, their synthesis is difficult, making these compounds expensive. Experiments with large amount of these indicators can be very costly.

The palette of detectable ions can be expanded with ion-selective optodes, which work on the principle of partitioning of ions between the sample and a sensing phase. <sup>1,18</sup> The above mentioned ion-selective indicators are not required. These sensors normally contain a lipophilic pH indicator (also called chromoionophore), an ion exchanger and an ionophore (chemical receptor) for the ionic analyte. These are embedded in a polymeric matrix such as plasticized poly(vinyl chloride) (PVC). The protonation degree of the chromoionophore in the sensing phase reflects the concentration of the analyte in the sample phase and the sample pH. <sup>18</sup> Compared with the above mentioned ion indicators, the sensor response range is tunable through variation of the optode composition and the selectivity is often superior owing to the use of very selective ionophores.

Recently, miniaturized forms of the bulk optode have emerged, and microtiter plate based optodes, microbeads and nanospheres also have been prepared by surface coating, polymerization and sonication. <sup>19-22</sup> Our group has been developing polymeric microsphere that behave on the same basis of bulk ion-selective optodes. Monodisperse optical ion-selective microspheres have been successfully developed through heterogeneous polymerization, solvent casting or using a sonic particle caster. <sup>20,23-25</sup> It is known that for ion-selective bulk optodes and their ion-selective electrode (ISE) counterparts, electroneutrality of the sensing phase must hold. <sup>18</sup> While for an extremely thin membrane, such as a lipid bilayer, electroneutrality can be partially violated. Previous theoretical work on ISEs indicates a membrane thickness reduction to around 30 nm results in electroneutrality no longer being applicable. <sup>26</sup> Will ultrasmall bulk optodes with sizes of less than 50 nm still be functional? If so, will they work on the same basis as expected from bulk optode theory? These questions are not yet answered since the reliable production of ultrasmall nanospheres has been difficult using existing techniques. The group of Kopelman has reported both acrylamide and PVC-type nanometer-sized sensing spheres that proved to be useful in interrogating intracellular environments. <sup>17,19,27,28</sup> The probes encapsulated by biologically localized embedding (PEBBLE) nanosensors have a bimodal size distribution and their preparation requires polymerization followed by further purification, which is laborious and time consuming. <sup>19</sup> Some

other nanosensors relying on other materials such as quantum dots and metal beads have also been reported. Nevertheless, the most widely adopted approaches are based on polymeric and sol-gel matrix.<sup>29-32</sup>

In this work, we present a very simple and convenient method to produce monodisperse ultrasmall ion-selective nanospheres ( $\sim$ 40 nm in diameter). The nanosensor can be produced easily by injection of a tetrahydrofuran (THF) solution containing the sensing components into deionized water. A nonionic, highly biocompatible surfactant triblock copolymer referred to as Pluronic<sup>®</sup> F-127 (F127) is dissolved in the cocktail. It is composed of a central hydrophobic chain of poly(propylene oxide) flanked by two hydrophilic chains of poly(ethylene glycol) (PEG). Pluronic F-127 plays an important role in the formation of the nanospheres as evidenced by a dual nanosensor for pH and  $O_2$  recently reported using F127, where micelles were formed with F127 and the sensing components, followed by silica growth on the surface.<sup>33</sup> We postulate here that the hydrophobic poly(propylene oxide) chains can interact with other hydrophobic sensing components to help construct the core of the ion-selective nanosphere, while the hydrophilic PEG chains may act as surfactant to prevent the nanosensors from coalescing. These ultrasmall nanospheres are found to be stable, versatile and easy to fabricate. This allows them to be a powerful nanoscale tool to detect small inorganic ions and will likely find application in chemical biology and environmental science. Using Na<sup>+</sup> as an example, we incorporate here a neutral Na<sup>+</sup>-selective ionophore into the nanospheres, making them sensitive and selective to Na<sup>+</sup>. As an early application, the Na<sup>+</sup> concentration in three different commercial mineral water samples was successfully measured using the Na<sup>+</sup>-selective nanospheres.

#### 2.2 Experimental Section

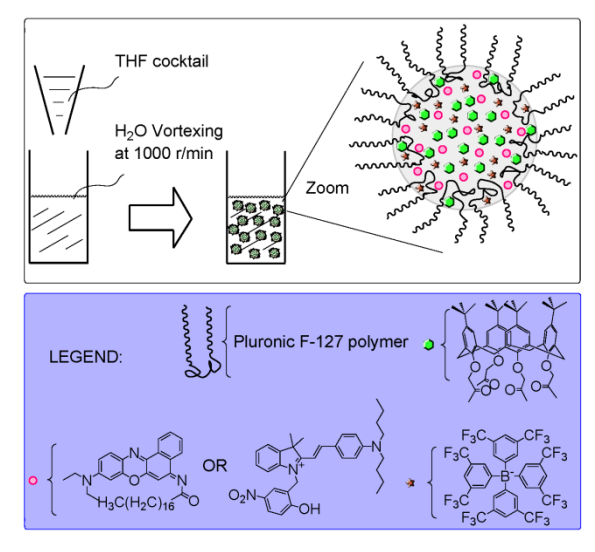
**2.2.1 Reagents.** Pluronic<sup>®</sup> F-127 (F127), bis(2-ethylhexyl) sebacate (DOS), sodium ionophore X (NaX), boric acid, tetrahydrofuran (THF), potassium tetrakis-[3,5-bis(trifluoromethyl)phenyl]borate (KTFPB), 2-amino-2-hydroxymethyl-propane-1,3-diol (Tris), poly(vinyl chloride) (PVC), chromoionophore I (CH1), 8-Hydroxypyrene-1,3,6-trisulfonic acid trisodium salt (HPTS), sodium chloride (NaCl), sodium phosphate monobasic (NaH<sub>2</sub>PO<sub>4</sub>) were obtained from Sigma-Aldrich. Polyethylene glycol (PEG) was purchased from AppliChem. Mineral waters were obtained from Coop<sup>®</sup>. (E)-N,N-dibutyl-4-(2-(6,6-dimethyl-2-nitro-6,12-dihydro-5aH-benzo[5,6][1,3]oxazino[3,2-a]indol-5a-yl)vinyl)aniline (Ox) was synthesized according to synthesis of similar compounds in previous report.<sup>34</sup>

#### 2.2.2 Preparation of Ion-Selective Nanospheres

1.81 mg of KTFPB, 0.53 mg of Ox (or 0.58 mg of CH1), 8 mg of DOS, 25 mg of F127, and 2.5 mg of sodium ionophore X (NaX) were dissolved in 3 mL of THF to form a homogeneous solution. 0.5 mL of the solution was pipetted and injected into 4.5 mL of deionized water on a vortex with a spinning speed of 1000 r/min. The resulting clear mixture was blown with condensed air on the surface for 20 min to remove THF and gave a clear particle suspension (Table 2.1(E)). Other particles shown in Table 2.1 were prepared in the same way with THF cocktail with different composition and water solution containing the corresponding surfactant. (A): 0.67 mg of PVC and 1.33 mg of DOS into 4.5 mL of 3% (w/w) PEG solution. (B): 0.67 mg of PEG and 1.33 mg of DOS into 4.5 mL of deionized water. (F): 1.33 mg of DOS into 4.5 mL of deionized water. (F): 1.33 mg of DOS into 4.5 mL of deionized water. (F): 1.33 mg of DOS into 4.5 mL 10% (w/w) F127 solution.

#### 2.2.3 Instrumentation and Measurements

The size of the nanospheres was measured with a particle size analyzer Zetasizer Nano ZS (Malvern Inc.). The absorbance was measured with a UV-Vis spectrometer (SPECORD 250 plus, Analytic Jena, AG, Germany) and fluorescence was measured with a fluorescence spectrometer (Fluorolog3, Horiba Jobin Yvon). Calibration curves were measured in 10 mM pH 7.4 Tris-HCl buffer solutions with gradual



**Scheme 2.1.** Representation of the preparation of Na<sup>+</sup>-selective nanospheres and the proposed microscopic structure. The grey spherical background represents DOS acting as a solvent for other components.

addition of NaCl. Atomic absorption spectroscopic measurements were carried out on a GTA 120 graphite tube atomizer (VARIAN Inc.) and an AA240 FS fast sequential atomic absorption spectrometer (VARIAN Inc.).

For size variation experiment (Fig.2.5 (d)), 0.5 mL of the THF cocktail (3 mL) containing 1 mg of KTFPB, 0.56 mg of Ox, 8 mg of DOS and 13.4 mg of F127 was precipitated into 3 mL of deionized water. THF cocktail for Fig. 2.5 (c) is 4 times diluted than Fig. 2.5 (d). The resulting particles suspension is diluted with deionized water and the size of the nanoparticles are measured with dynamic light scattering particle size analyzer.

For transmission electron microscopy (TEM) imaging of the nanospheres, the sodium-selective nanosphere suspension was dispersed on to a Formvar/Carbon film coated TEM grid, counter-stained with uranyl acetate, dried in the air and visualized using a FEI Tecnai<sup>TM</sup> G2 Sphera transmission electron microscope.

Sodium levels in mineral water were measured with the nanoparticles under absorbance mode. Ratio of the absorbance at 571 nm over 320 nm was taken for the calibration in a pH 7.4 Tris-HCl buffer solution. Samples were diluted with pH 7.4 Tris-HCl buffer solution to reach the same condition as for the calibration. Calibration was performed with sodium concentration in the range from 0.1 mM to 0.3 mM.

For experiments shown in Fig.S2.2, a 5 mM universal buffer (NaH<sub>2</sub>PO<sub>4</sub>+Boric acid+Citric acid) with 1 μM HPTS and Na<sup>+</sup>-selective nanosphere was used. Amount of nanospheres added was controlled to get comparable absorbance intensity with HPTS. The sample contained 0.1 M LiCl. Na<sup>+</sup> background was adjusted to be 30 mM and 100 mM in two cases.

#### 2.3 Results and Discussion

Ion-selective optical sensors (optodes) can be more easily miniaturized compared to electrochemical sensors. So far, the procedures to miniaturize these sensors mostly involve sonication, precipitation, or polymerization, followed by purification processes such as dialysis and centrifugation. <sup>19,20,35</sup> The entire procedures based on polymerization are complicated and time consuming. A sonic particle caster is able to prepare micrometer sized particles, however, reducing the size further below 100 nm is very difficult and the efficiency of this method is low since a large amount of aqueous solution is needed compared with the amount of particles formed. <sup>20,25</sup> Methods based on precipitation are more promising to obtain nanoparticles. To make ion-selective particles, typically, a THF cocktail containing PVC, plasticizer, a chromoionophore, an ion-exchanger and an ionophore is injected into a vortexing aqueous solution containing a surfactant.

The composition of the cocktail is the same as in a bulk optode. As shown in Table 2.1 (A), when a cocktail containing PVC-DOS is precipitated in a PEG solution, particles with an average size of 150 nm are obtained. The size of the formed nanoparticles depends on many factors during the precipitation, such as the polymer concentration, polymer structure and vortex speed. Nevertheless, with this method, the size of the particles obtained is always above 100 nm. Pluronic F-127 is an interesting polymer with two distal hydrophilic polyethylene glycol chains connected by a hydrophobic poly(propylene oxide) segment. Its molecular weight is around 12,500 Da. We envision that with such a polymer, it is possible to make more compact nanoparticle structures since it plays both the role of PVC and surfactant. To explain, the PEG chain can act as surfactant while the poly(propylene oxide) chain is able to insert into the plasticizer and stabilize the core of the nanostructure. Since the PEG chain acts as surfactant, no additional surfactant is needed.

Based on these assumptions, as shown in Scheme 2.1, a cocktail containing DOS and F127 was dissolved in THF and precipitated in deionized water to obtain a mixture containing the desired nanoparticles. THF was removed after precipitation by simply blowing condensed air onto the mixture surface. As shown in Table 2.1 (D), nanoparticles with average size of  $\sim$ 60 nm in diameter were obtained. The small polydispersity index (PDI) value indicates that the nanoparticles have a

Table 2.1. Average diameter and polydisperse index (PDI) for particles precipitated in different ways.

	Sequences	z-av / nm	PDI
(A)	PVC-DOS in	150±2	0.07 ±0.03
	PEG		
(B)	PEG-DOS in	372±8	0.7±0.05
	PEG		
(C)	PEG-DOS in	1100±300	$0.85 \pm 0.04$
	$\rm H_2O$		
(D)	F127-DOS in	61±1	0.08±0.01
	$H_2O$		
(E)	F127-DOS in	40±1	$0.04\pm0.02$
	$\mathrm{H_2O}^*$		
(F)	DOS in F127	96±1	0.1±0.03

<sup>\*</sup>With sensing components as indicated in experimental section.

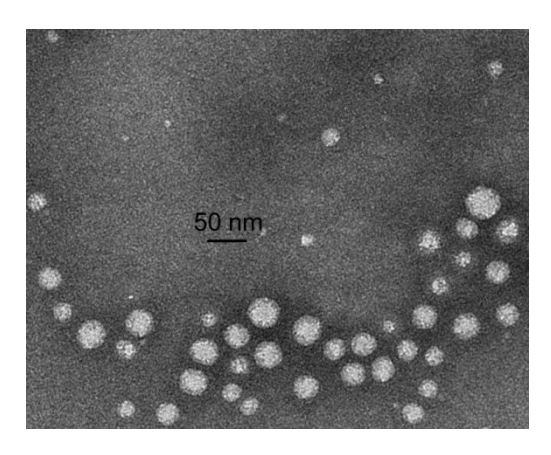
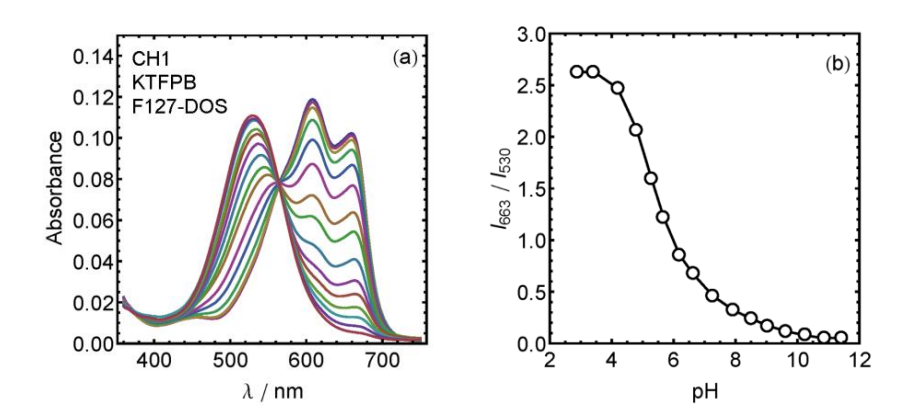


Figure 2.1. Transmission electron microscopy (TEM) image for the Na<sup>+</sup>-selective nanospheres (see Chapter 2).

narrow size distribution. Since the nanoparticles are very small, the particle suspension appears as a clear solution. Elevating the polymer concentration can result in larger size particles, as explained in previous reports.<sup>35</sup> For instance, when the 0.5 mL of the same THF cocktail was injected into 3 mL of water, instead of 4.5 mL, an average diameter around 130 nm was observed. In contrast with F127 based nanospheres, the suspension that resulted from the PVC-DOS system contains larger-size particles and appears to be heterogeneous as evidenced by its ability to scatter light. To confirm that an amphoteric polymer like F127 is essential, PEG was used as a replacement of F127 under the same conditions. The resulting particles showed much larger sizes and PDI values (Table 2.1 (C)). Even when additional surfactant was used, the size of the particles decreased to around 372 nm but the size distribution range was still wide (Table 2.1 (B)). When F127 was dissolved in the aqueous solution prior to casting the resulting nanoparticles still had a small diameter and narrow size distribution, as shown in Table 2.1 (F).

With added hydrophobic sensing components, nanoparticles showed an average hydrodynamic size of 40 nm, as shown in Table 2.1(E). The nanoparticles were also imaged using transmission electron microscopy (TEM). As shown in Fig. 2.1, the nanoparticles exhibited a round shape with a diameter smaller than 40 nm. The size obtained from light scattering measurements is slightly bigger than observed in



**Figure 2.2.** pH response of F127-DOS based nanospheres containing CH1 and KTFPB in 5 mM universal buffer (NaH<sub>2</sub>PO<sub>4</sub>+Boric acid+Citric acid+0.1 M KCl). (a): Absorption spectra at different pH, (b): Calibration curve using absorbance ratio between 663 nm and 530 nm.

TEM since the former technique is dependent on hydrodynamic size.

As a conventional optode, DOS is a very lipophilic molecule and can act as a good solvent for many lipophilic organic molecules. Doping the lipophilic core with a chromoionophore and ion-exchanger should allow the nanoparticles to be pH responsive. To test this, we chose chromoionophore I (CH1), a lipophilic pH indicator, and KTFPB as ion-exchanger. The pH response of the nanoparticles in absorbance mode is shown in Fig. 2.2. CH1 is a ratiometric dye and indeed shows a visible response to pH with an isosbestic point at 565 nm. The apparent basicity ( $pKa=\sim5.9$ ) of CH1 observed here is lower than in a bulk optode film, indicating that the nanoparticle core and the surface differ in solvent properties such as hydrophobicity, which in turn affects the basicity of the chromoionophore.

One could argue that the chromoionophores are distributed on the surface to equally explain the functioning of the nanosensors and even the reduced basicity. If the chromoionophore is truly inserted into the nanoparticles, protonation should be accompanied by the transfer of a hydrophilic cation (initially ion paired with the ion-exchanger) from the nanospheres to the surrounding solution. For a given pH, the protonation state of the indicator should depend on the nature and concentration of this cation. Therefore, one expects an ion selectivity of the optode response. Consequently, the response of the nanoparticle suspension was evaluated to different commonly seen cations. As shown in Fig. 2.3 (a), without any addition of ionophore, a Hofmeister selectivity series was observed as expected for such an ion-exchange

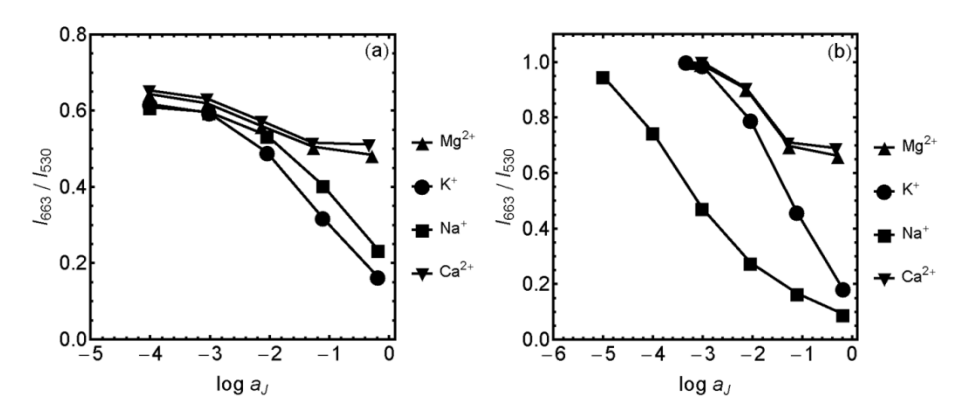
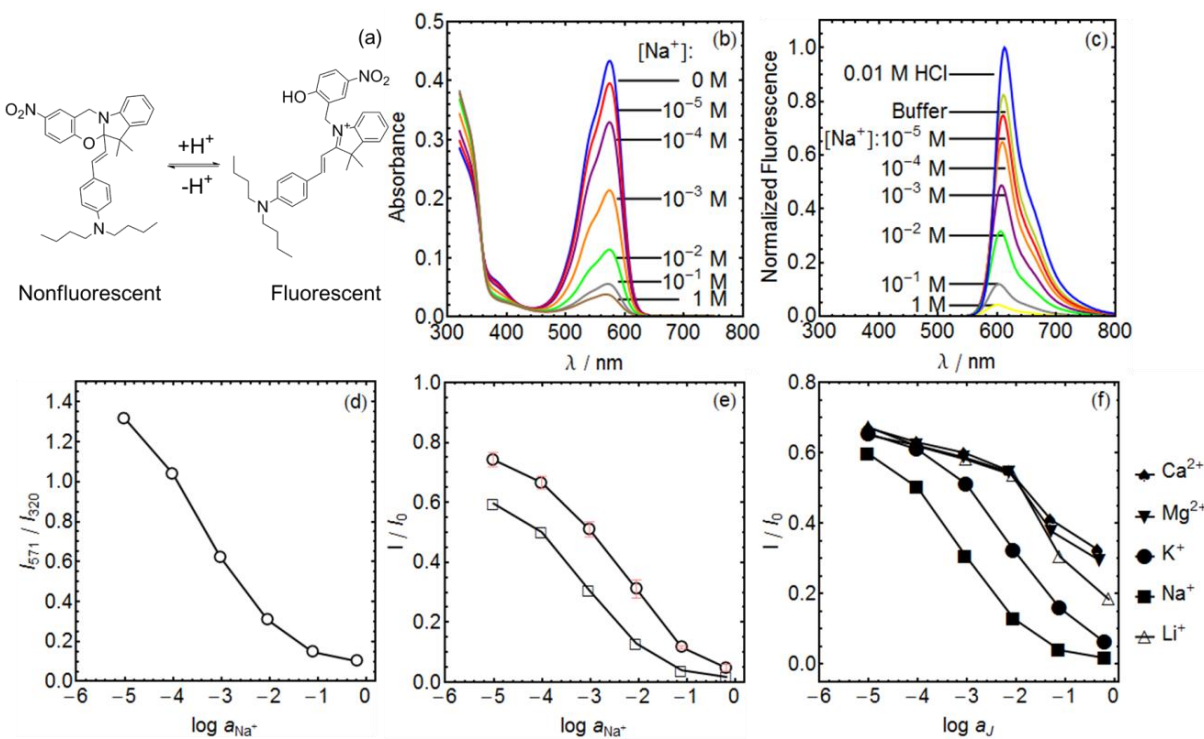


Figure 2.3. Selectivity for nanospheres comprised of CH1 and KTFPB in 10 mM pH 7.4 Tris-HCl buffer, without (a) and with (b) NaX inside the nanosphere.

principle, with  $K^+>Na^+>Mg^{2+}>Ca^{2+}$ . With addition of the sodium ionophore NaX as shown in Fig. 2.3 (b) the nanoparticles became highly selective for Na<sup>+</sup>. This suggests that these nanospheres do indeed behave as bulk extraction systems that do not appear to violate electroneutrality as expected for ultra-small dimensions approaching the Debye length. Compared with membrane based Na<sup>+</sup>-selective sensors, the selectivity for Na<sup>+</sup> over K<sup>+</sup> is somewhat reduced due to the different environment of the receptors. Since the surface of the nanoparticle is likely more hydrophilic than that of a bulk optode film and a certain leveling effect on the interaction between the ionophore and the metal ion is possible.

The indicator CH1 is not fully protonated under neutral pH conditions, wich may be due to its apparently diminished basicity when incorporated in the nanoparticles. To improve on this characteristic, a compound with higher basicity or with lower spectral background after deprotonation (i.e., a turn-on pH indicator) is preferred. Fluorescent probes offer considerable advantages that include a high sensitivity and specificity, and versatile measurement parameters (excitation and emission spectra, intensities, lifetimes or anisotropy). Further Na<sup>+</sup>-selective nanoparticles were therefore prepared with a fluorescent turn-on pH sensitive dye, labeled here as Ox, that belongs to a new oxazinoindoline chromoionophore family that we recently introduced. As shown in Fig. 2.4 (a), Ox can exist in a non-fluorescent ring-closed form and a fluorescent ring-open form. The ring-opening reaction can be mediated by H<sup>+</sup> and render the dyes pH sensitive. A new Ox dye with enhanced lipophilicity compared with previous work was here synthesized (See Supporting Information for details). Ox is reported to have a higher pKa than CH1 when interrogated in optical mode (Chapter 7). The Na<sup>+</sup> response for this Ox based nanoparticles is shown in Fig. 2.3. In absorbance mode (Fig. 2.4 (b) and (d)), the nanoparticles also exhibited a ratiometric response to Na<sup>+</sup>. The calibration data does not correspond quantitatively to that expected for a bulk optode, likely because the 40 nm nanosphere size does allow some redistribution of sensing components between surface and bulk during ion-exchange. (See Fig. S2.1 in Supporting Information)

The Na<sup>+</sup> response of the nanospheres was also evaluated in fluorescence mode and the results are shown in Fig. 2.4 (c) and (e). Error bars are given for three different batches of nanospheres precipitated under identical conditions and indicate that the particles prepared with this method respond in a reproducible fashion. The circles in Fig. 2.4 (e) were measured with particle suspensions that exhibit the same concentration as for the absorbance data in Fig. 2.4 (b), while the squares were measured with 30 times diluted nanoparticle suspensions. We noticed that the concentrated ones give a Na<sup>+</sup> response window that is shifted in direction of higher Na<sup>+</sup> concentrations, while the response from the diluted suspension is in good agreement with calibration in absorbance mode.



**Figure 2.4.** (a) Chemical structure and acid-base reaction of fluorescent turn-on Ox dye. (b) Absorption spectra at various Na<sup>+</sup> concentration for a Na<sup>+</sup>-selective nanoparticle suspension using Ox as chromoionophore in pH 7.4 Tris-HCl buffer, blue line being measured in buffer with no Na<sup>+</sup> as blank. (c) Fluorescence spectra at various Na<sup>+</sup> concentrations for a Na<sup>+</sup>-selective nanoparticle suspension using Ox as chromoionophore in pH 7.4 Tris-HCl buffer. (d) Calibration for the Na<sup>+</sup> response in absorbance mode (b) using the absorbance ratio between 571 nm and 320 nm as output. (e) Circles: Calibration for Na<sup>+</sup> response in fluorescence mode using normalized emission intensity at 610 nm, I<sub>0</sub> being the maximum intensity in 0.01 M HCl (blue line in (c)). Error bars are from 3 different batches of nanospheres. Squares: Na<sup>+</sup> response obtained with nanosphere suspension diluted 30 times compared with circles. (f) Selectivity of the Na<sup>+</sup>-selective nanosphere measured in 10 mM pH 7.4 Tris-HCl buffer solution in fluorescence mode.

In principle, this shift could either indicate insufficient stability of the nanoparticles or a modulated fluorescence owing to the high dye concentration. This was evaluated with spectroscopic studies on suspensions of varying dilution. Na<sup>+</sup>-selective nanoparticles were prepared and then diluted step by step with constant pH (7.4) and a Na<sup>+</sup> (1 mM) background under conditions that are very sensitive to the variation in Na<sup>+</sup> concentration. The relation between the absorbance and the concentrations of the nanosphere remained linear, as shown in Fig. S2.3, indicating that Beer's law still holds throughout the dilution experiment. Should there be a compositional change due to dilution, the Na<sup>+</sup> response, which was evaluated with the absorbance ratio between 571 nm and 320 nm (I<sub>571</sub>/I<sub>320</sub>), would change dramatically. However, as shown in Fig. 2.5 (a) and (b), the Na<sup>+</sup> response was stable up to a 40-fold dilution. Evaluation at stronger dilution was difficult because the ab sorbance became too low for reliable quantitation (Fig. 2.5 (a)). The size of the nanoparticles with dilution of the suspension was also evaluated using dynamic light scattering and found to be stable. These results suggest that the stability of the nanoparticles is indeed excellent. In fact, these particles can be stored in the dark for more than 4 weeks without noticeable decomposition and sedimentation. Moreover, the photostability of the nanospheres under these experimental conditions is sufficient. As shown in Fig. S2.4, no substantial photobleaching of Ox was seen during a continuous absorbance measurement of 1 h. The selectivity of the Na<sup>+</sup>-selective nanoparticles containing Ox was evaluated and the result shown in Fig. 2.4 (f). Similar to the selectivity of CH1 based nanoparticles, Na<sup>+</sup> is highly preferred while interference from other ions is still suppressed.

Since the nanoparticle suspension is transparent, it is now possible to measure different parameters in one sample using spectroscopic methods. Here, as a proof of concept, the Na<sup>+</sup>-selective nanoparticles and HPTS were simultaneously used to measure Na<sup>+</sup> concentration as

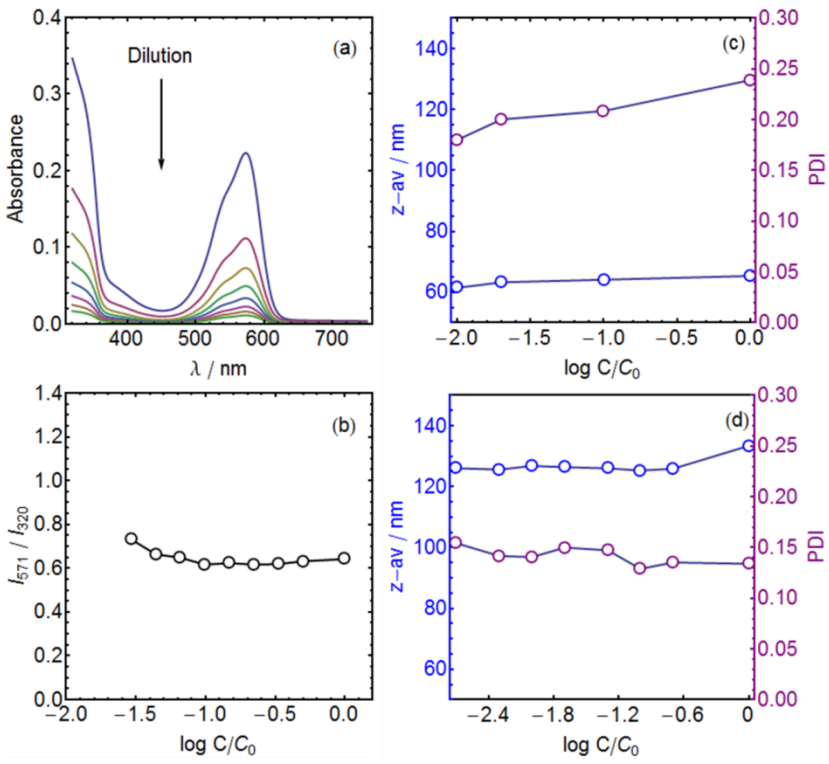


**Figure 2.5.** (a) Absorption spectra recorded as the Na $^+$ -selective nanoparticle suspension was diluted with constant Na $^+$  background (1 mM) and pH (10 mM pH 7.4 Tris-HCl buffer). The dilution factor is indicated on the x-axis of Fig. 5(b). (b) Variation of the Na $^+$  response with sample dilution. (c) Nanosphere size variation as the particle is diluted with H<sub>2</sub>O, the nanospheres were precipitated with THF cocktail containing 1% (w/w) F127-DOS (d). Nanosphere size variation as the particle is diluted with H<sub>2</sub>O, the nanospheres were precipitated with THF cocktail containing 4% (w/w) F127-DOS.

well as pH (Fig. S2.2 in Supporting Information). HPTS was chosen because of its high hydrophilicity and spectral separation with Ox. The pH of the suspension containing a fixed Na $^+$  concentration (3 mM and 100 mM) was gradually changed while the absorbance signal was recorded. As the pH changes, the degree of protonation (1– $\alpha$ ) for both HPTS and Ox in the Na $^+$ -selective nanosphere will vary. However, owing to the ion-exchange reaction between protons and sodium ions, the nanospheres are not only responsive to pH but also on the Na $^+$  concentration in the sample. Therefore, information concerning both pH and Na $^+$  concentration can now be revealed at the same time. The ionic strength of the sample was adjusted by addition of LiCl in order to minimize effects of varying activity coefficients on the pH indicator response. As shown in Fig. S2.2, the pH readout from HPTS for samples containing different Na $^+$  concentrations were the same, while a shift in the degree of protonation for Ox in the nanoparticles is observed, from which the sodium level can be inferred.

Table 2.2. Na<sup>+</sup> concentrations assessed in commercial water samples

Mineral	AAS	Nanoparticle	Label
Water Brand	$/ \text{ mg L}^{-1}$	/ mg L <sup>-1</sup>	$/ \text{ mg L}^{-1}$
Crystalp	19.3±0.1	19.5±0.9	19.9
Evian	5.9±0.1	5.6±0.5	6.5
Vichy	1010±2	1080±32	1172

As an early stage application, the Na<sup>+</sup>-selective nanoparticles were used to measure the sodium concentration in mineral waters. Three different commercial mineral water samples were measured with the nanoparticles in absorbance mode and the results were compared with atomic absorption spectroscopy (AAS). As shown in Table 2.2, the nanoparticles give very close results compared to AAS. The nanoparticle measurement errors are mainly introduced during the sample preparing stage, since a fresh nanoparticle suspension is needed for each measurement.

#### 2.4 Conclusion

In conclusion, a simple and convenient method based on precipitation of lipophilic components in  $H_2O$  for preparing ion-selective nanoparticles is presented. The preparation process can be finished in less than 30 min, and does not require further complicated purifications. Na<sup>+</sup>-selective and pH sensitive nanoparticles incorporating fluorescent turn-on and ratiometric dyes were prepared and studied as model systems. With the help of an amphoteric polymer F127, the nanoparticles exhibit very small size ( $\sim$ 40 nm) and a narrow size distribution. Perhaps surprisingly, the nanospheres appear to exhibit selective ion-exchange chemistry, although with response curve that do not quantitatively correspond to bulk optode theory. The resulting particle suspension is transparent and can allow for a spectroscopic interrogation of different parameters at the same time. Na<sup>+</sup> concentrations in commercial mineral waters were successfully determined. The nanoparticles are highly stable upon dilution and long storage. Further work to obtain deeper understanding on the microscopic structure of the nanospheres and to build nanospheres sensitive and selective to other ions is on-going in our laboratory.

#### 2.5 Supporting Information for Chapter 2

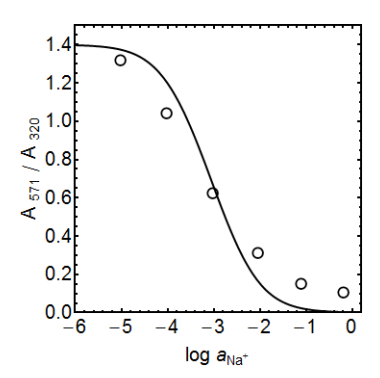


**Figure S2.1.** Na<sup>+</sup> calibration data (Circles) obtained from experiments with Na<sup>+</sup>-selective nanospheres in 10 mM pH 7.4 Tris-HCl buffer fit with theoretical bulk optode theory (Solid Curve).

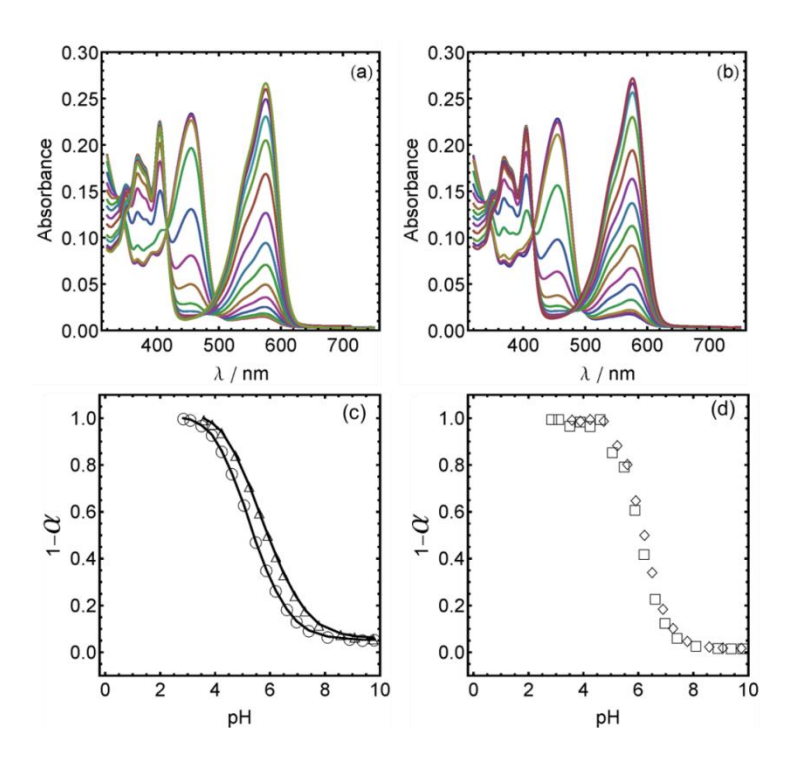


**Figure S2.2.** pH and Na<sup>+</sup> response of a Na<sup>+</sup>-selective nanosphere suspension containing 1 μM HPTS in 5 mM universal buffer with 30 mM Na<sup>+</sup> (a) and 100 mM Na<sup>+</sup> (b) as background. (c) The degree of protonation as a function of pH calculated from the nanosphere. Circle: 100 mM Na<sup>+</sup> background, Triangle: 30 mM Na<sup>+</sup> background. (d)The degree of protonation as a function of pH calculated from HPTS. Square: 100 mM Na<sup>+</sup> background, Diamond: 30 mM Na<sup>+</sup> background. The ionic strength of all solutions was adjusted with addition of 0.1 M LiCl.

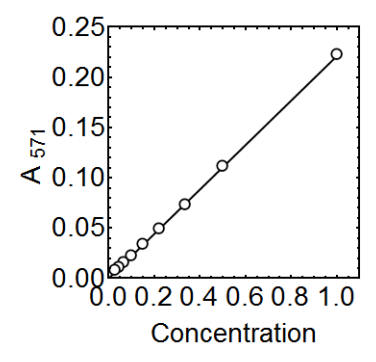


**Figure S2.3.** Relationship between the concentrations of the nanoparticles during dilution experiment (Fig. 2.5(a)) and the absorbance values at 571 nm of the nanosphere suspension. The original nanosphere suspension concentration was taken to be 1 as a reference and others were calculated according to the dilution factors.

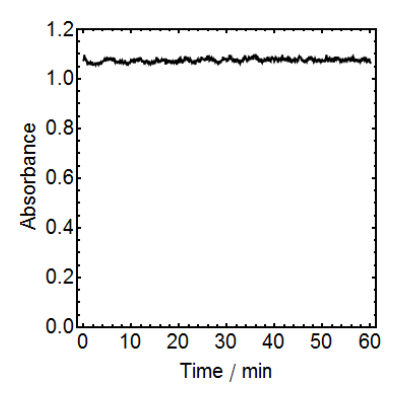
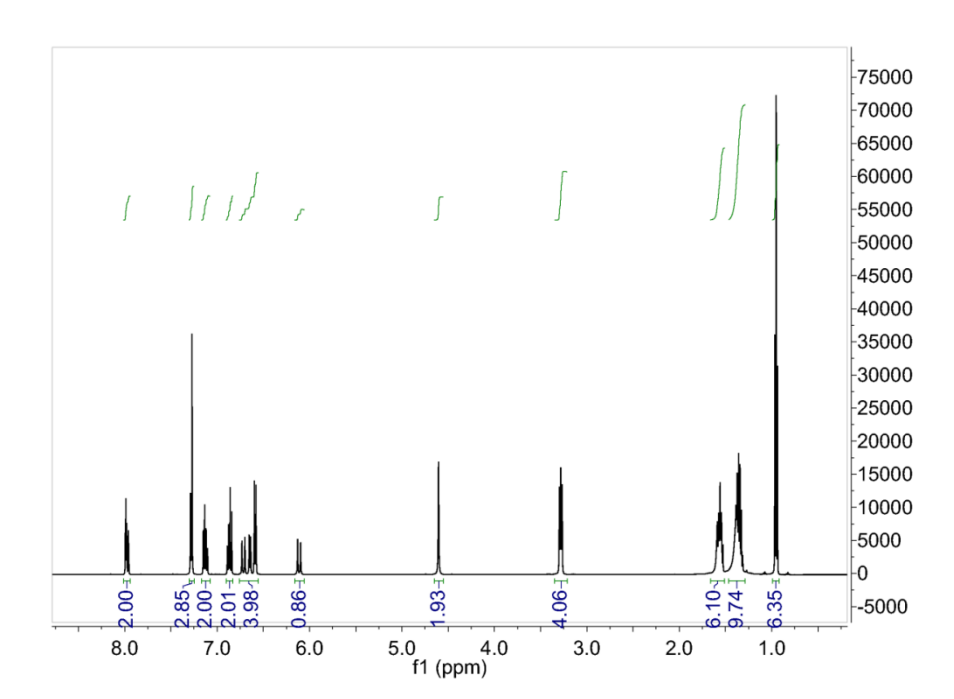


**Figure S2.4.** Evaluation of the photostability of the Na<sup>+</sup>-selective nanosphere under absorption mode with a 0.5 nm slit width. The Y axis shows the absorbance value at 571 nm, monitored as a function of time.

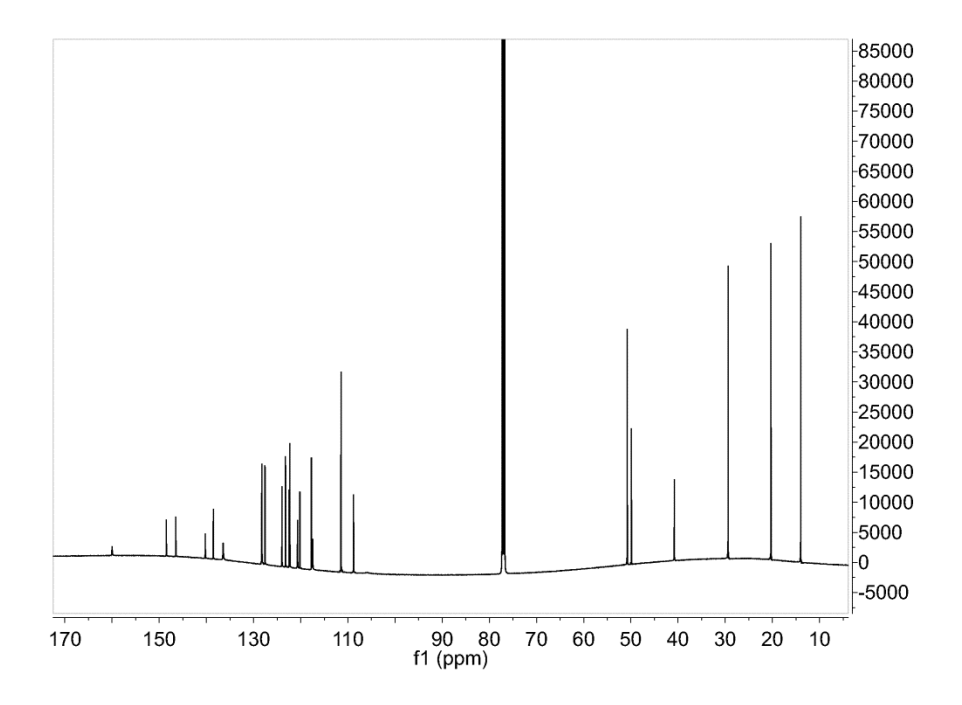
## Structural Information for Ox:

ESI-MS: m/z=526.3 [M+H]<sup>+</sup>

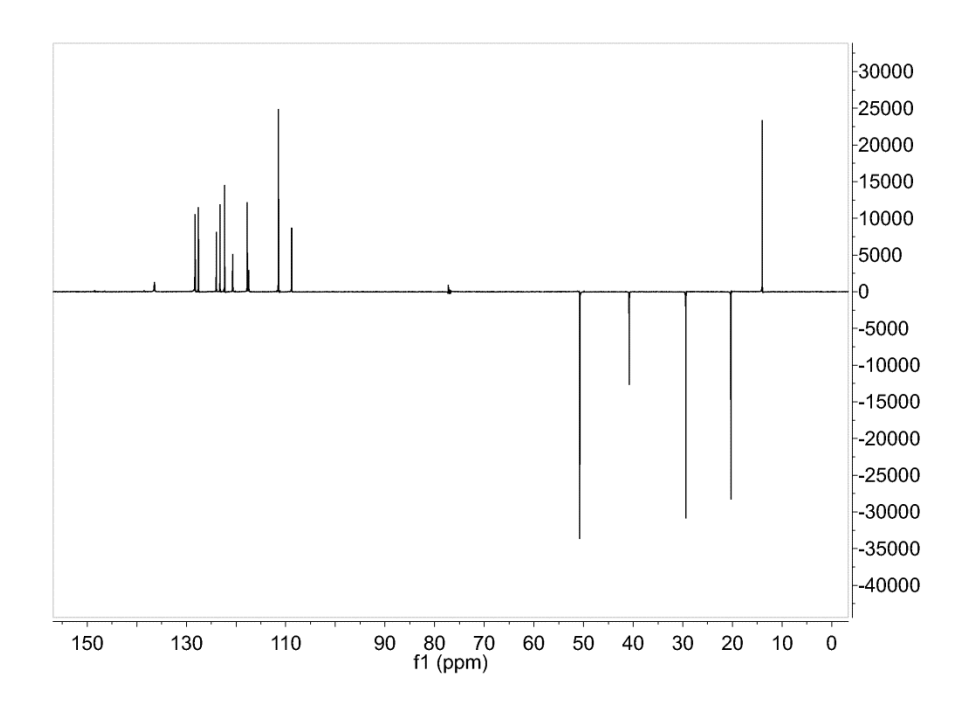
<sup>1</sup>H-NMR:



# <sup>13</sup>C-NMR:



# DEPT 135 °:



#### 2.6 References for Chapter 2

- (1) Mistlberger, G.; Xie, X.; Pawlak, M.; Crespo, G. A.; Bakker, E. Anal. Chem. 2013, 85, 2983.
- (2) Bakker, E.; Qin, Y. Anal. Chem. 2006, 78, 3965.
- (3) Akcin, N.; Koyuncu, I.; Akcin, G. Rev. Anal. Chem. 2011, 30, 65.
- (4) Li, X.; Zhou, D.; Xu, J.; Chen, H. Talanta 2007, 71, 1130.
- (5) Alvarez, M. A.; Carrillo, G. *Talanta* **2012**, 97, 505.
- (6) Aragay, G.; Pons, J.; Merko q, A. Chem. Rev. 2011, 111, 3433.
- (7) Thakur, A.; Mandal, D.; Ghosh, S. Anal. Chem. 2013, 85, 1665.
- (8) Town, R. M.; Leeuwen, H. P. V. Electroanalysis 2004, 16, 458.
- (9) Hu, Z.; Buehrer, T.; Mueller, M.; Rusterholz, B.; Rouilly, M.; Simon, W. Anal. Chem. 1989, 61, 574.
- (10) Chumbimuni-Torres, K. Y.; Dai, Z.; Rubinova, N.; Xiang, Y.; Pretsch, E.; Wang, J.; Bakker, E. J. Am. Chem. Soc. 2006, 128, 13676.
- (11) Wen, R.; II, B. O. J. Neurosci. Meth. 1990, 31, 207.
- (12) June, C. H.; Rabinovitch, P. S. Methods Cell Biol. 1990, 33, 37.
- (13) Hamaguchi, Y.; Hamaguchi, M. S.; Mohri, T. Cell 1990, 22, 258.
- (14) Ma, A.; Rosenzweig, Z. Anal. Chem. 2004, 76, 569.
- (15) Bahmanjah, S.; Zhang, N.; Davis, J. T. Chem. Commun. 2012, 48, 4432.
- (16) Kim, M. K.; Lim, C. S.; Hong, J. T.; Han, J. H.; Jang, H.-Y.; Kim, H. M.; Cho, B. R. Angew. Chem. Int. Ed. 2010, 49, 364.
- (17) Si, D.; Epstein, T.; Lee, Y.-E. K.; Kopelman, R. Anal. Chem. 2012, 84, 978.
- (18) Bakker, E.; Bühlmann, P.; Pretsch, E. Chem. Rev. 1997, 97, 3083.
- (19) Clark, H. A.; Hoyer, M.; Philbert, M. A.; Kopelman, R. Anal. Chem. 1999, 71, 4831.
- (20) Tsagkatakis, I.; Peper, S.; Bakker, E. Anal. Chem. 2001, 73, 315.
- (21) Dubach, J. M.; Harjes, D. I.; Clark, H. A. J. Am. Chem. Soc. 2007, 129, 8418.
- (22) Dubach, J. M.; Das, S.; Rosenzweig, A.; Clark, H. A. PNAS 2009, 106, 16145.
- (23) Telting-Diaz, M.; Bakker, E. Anal. Chem. 2002, 74, 5251.
- (24) Retter, R.; Peper, S.; Bell, M.; Tsagkatakis, I.; Bakker, E. Anal. Chem. 2002, 74, 5420.
- (25) Xu, C.; Wygladacz, K.; Retter, R.; Bell, M.; Bakker, E. Anal. Chem. 2007, 79, 9505.
- (26) Morf, W. E.; Pretsch, E.; Rooij, N. F. d. J. Electroanal. Chem. 2010, 641, 45.
- (27) Shortreed, M.; Bakker, E.; Kopelman, R. Anal. Chem. 1996, 68, 2656.
- (28) Park, E. J.; Brasuel, M.; Behrend, C.; Philbert, M. A.; Kopelman, R. Anal. Chem. 2003, 75, 3784.
- (29) Sandros, M. G.; Shete, V.; Benson, D. E. Analyst 2009, 131, 229.
- (30) Aslan, K.; Wu, M.; Lakowicz, J. R.; Geddes, C. D. J. Am. Chem. Soc. 2007, 129, 1524.
- (31) Burns, A.; Sengupta, P.; Zedayko, T.; Baird, B.; Wiesner, U. Small 2006, 2, 723.
- (32) Hammond, V. J.; Aylott, J. W.; Greenway, G. M.; Watts, P.; Webster, A.; Wiles, C. Analyst 2008, 133, 71.
- (33) Wang, X.-d.; Stolwijk, J. A.; Lang, T.; Sperber, M.; Meier, R. J.; Wegener, J.; Wolfbeis, O. S. J. Am. Chem. Soc. 2012, 134, 17011.
- (34) Xie, X.; Crespo, G. A.; Bakker, E. Anal. Chem. 2013, 85, 7434.
- (35) Borisov, S. M.; Mayr, T.; Mistlberger, G.; Waich, K.; Koren, K.; Chojnacki, P.; Klimant, I. Talanta 2009, 79, 1322.

# Chapter 3. Potassium-Selective Optical Microsensors Based On Surface Modified Polystyrene Microspheres

This work has been published in: Xiaojiang Xie\*, Jingying Zhai, Gastón A. Crespo, Istvan Szilagyi, and Eric Bakker\*, *Chem. Commun.*, 2014, 50, 4592-4595

Ion selective optodes are one of the most recognized optical ion sensors and have been intensively explored in the past few decades. <sup>1-6</sup> Classical optodes are composed of a polymeric solvent cast film containing a lipophilic pH indicator (also called chromoionophore), an ion exchanger and an optically silent ionophore selective to the analyte. Cation selective optodes function on the basis of extraction equilibria between the aqueous phase and the bulk of the sensing film. <sup>5</sup> The extraction competition between the analyte ion and H<sup>+</sup> defines the protonation degree of the chromoionophore in the optode film, where the signal readout comes from.

While film based optodes are rather robust and effective, they are bulky and therefore cannot be used in small spaces such as cells. The response time can be also quite long, making it difficult to monitor dynamic processes. Recently, miniaturized forms of optodes have emerged to overcome the disadvantages. Nanometer-sized sensing spheres based on acrylamide and poly(vinyl chloride) (PVC) have been shown to be successful in interrogating intracellular environments. Polymeric microspheres and nanospheres that behave on the same basis of bulk ion-selective optodes have been developed in our group. Microtiter plate based optodes, microbeads and nanospheres have also been prepared by surface coating, polymerization and sonication. 15

However, in general, the number of matrix materials for these micro/nanosensors are very limited and the procedures to prepare the sensors are sophisticated. In this work, we report on the preparation and characterization of  $K^+$ -selective microspheres through simple surface modification on polystyrene (PS) particles without any added plasticizer.

PS exhibits a slow self-diffusion coefficient of below 10<sup>-13</sup> cm<sup>2</sup> s<sup>-1</sup> at room temperature <sup>16</sup>, making optode based equilibria rather unrealistic.

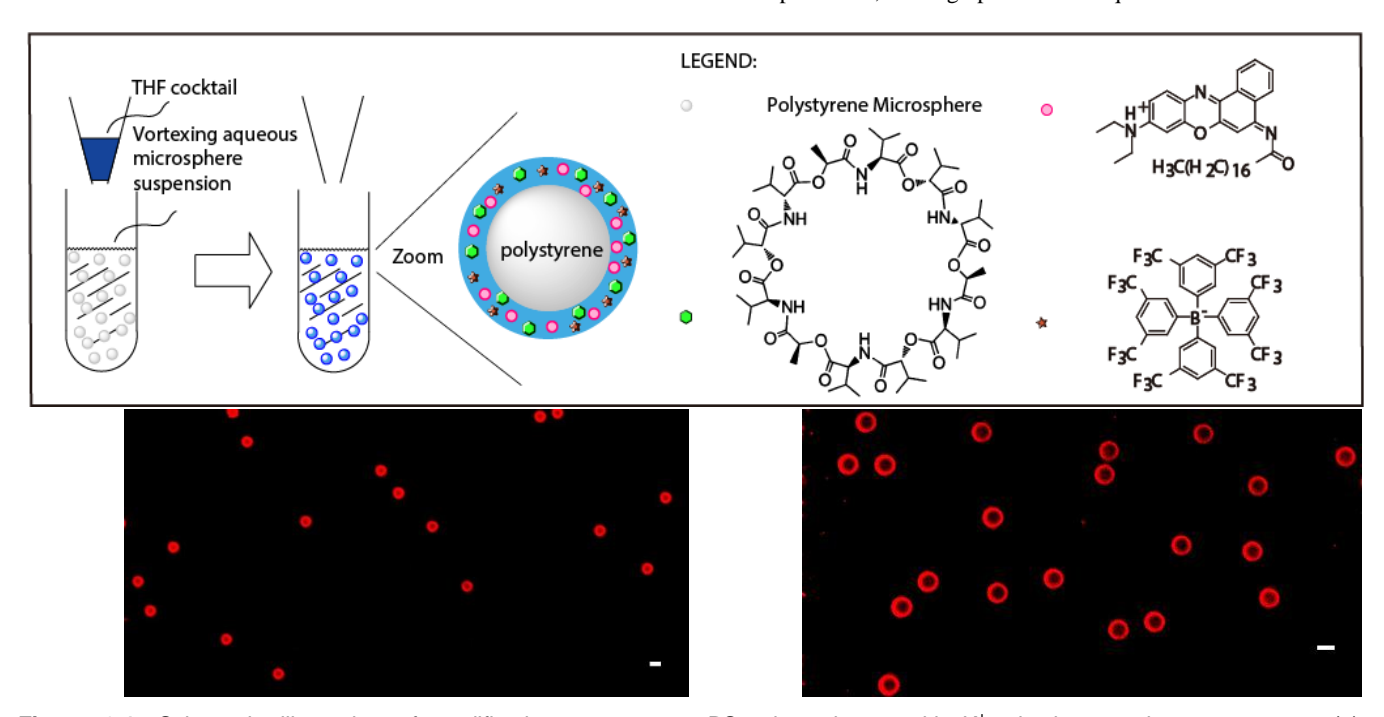


Figure 3.1. Schematic illustration of modification process on PS microspheres with  $K^+$ -selective sensing components (a). Fluorescence confocal microscopic images for  $K^+$ -selective PS microspheres with 0.8  $\mu$ m diameter (b) and 2.0  $\mu$ m diameter (c) in  $H_2O$ .

Indeed, ion-selective optical microsensors using polystyrene as matrix have not yet been reported, and cast optode films based on PS did not give functional optode response in this work (see below). Instead of of the typical bulk phase equilibria encountered with ion optodes, the mass extraction equilibrium is here established between the surface region and the aqueous surrounding, which unusual and quite surprising. To our knowledge, it is the first example of ion selective optodes functioning on the basis of surface modification.

The surface of PS microspheres (non-modified) is very hydrophobic in character and provides for strong physical adsorption of molecular species with hydrophobic regions, including drugs and proteins. <sup>17-19</sup> The ion-selective optodes components are always highly hydrophobic and therefore should be easily adsorbed on the surface of the PS microsphere surface. Here, PS microspheres with average diameter of 0.8 µm and 2.4 µm (characterized by dynamic light scattering (DSL)) in the form of aqueous suspensions are used as templates. To produce the K<sup>+</sup>-selective PS microspheres, a tetrahydrofuran (THF) solution containing chromoionophore I (Ind), sodium tetrakis[3,5-bis(trifluoromethyl)phenyl]borate (Na<sup>+</sup>R<sup>-</sup>) and potassium ionophore I (valinomycin, L) is prepared (see supporting information for the detailed composition). As shown in Fig. 3.1(a), the THF cocktail is then injected into the aqueous PS microsphere suspension on a vortex with a spinning speed of 1000 rpm. A clear blue suspension is immediately obtained, indicating that Ind is in its protonated state. THF is subsequently removed by purging compressed air on the surface of the suspension for 20 min. The preparation process, compared with others such as polymerization, is much more convenient and less time consuming. In addition, it is easier to produce in large quantity compared with previous methods using a particle caster. <sup>13</sup>

The average diameter of the resulting K<sup>+</sup>-selective PS microspheres was determined by dynamic light scattering as 0.8 µm with a polydispersity index of 0.11 (2.4 µm for the carboxylate modified latex (CML) with polydispersity index (PDI) of 0.12). This means that the size of the particles was not drastically altered during doping. Confocal fluorescence microscopy was used to identify the localization of the sensing components with the microspheres, i.e., to assess whether the sensing components are distributed evenly in the microsphere or limited to a certain region. Fig 3.1 (b) and (c) show the confocal images of the modified PS microspheres, with the red color representing the fluorescence emission from the chromoionophore. The modification appears to have only taken in the surface region of the PS particles. Confocal images of microspheres modified with a reference fluorescent dye (Lumogen Red) using the same procedure also showed emission limited to the surface of the microspheres (Fig. S3.1). The modified PS particles remained suspended over a number of weeks and the sensing components remained in the surface region as confirmed by confocal microscopy.

As shown in Fig 3.2, the K<sup>+</sup>-selective PS microspheres (0.8 µm) suspension in 10 mM Tris-HCl (pH 7.4) exhibited a strong absorption

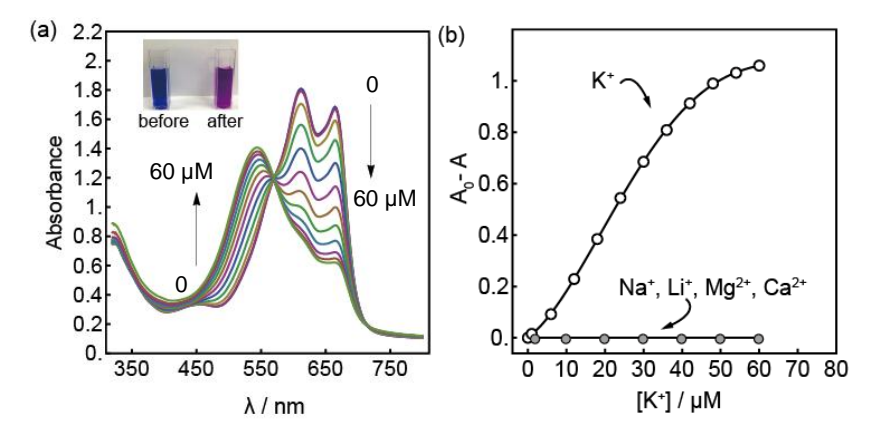


Figure 3.2. (a) Absorbance change for the  $K^+$ -selective PS microspheres (0.8  $\mu$ m) in 10 mM pH 7.4 Tris-HCl with different levels of KCl. Inset: pictures of the microsphere suspension before and after addition of  $K^+$  (60  $\mu$ M). (b) Calibration curves using absorbance difference at 663 nm ( $A_0$ -A) for  $K^+$  and other interfering ions as indicated, where  $A_0$  is the initial absorbance in buffer.

around 630 nm which originated from the protonated chromoionophore (HInd<sup>+</sup>), and the suspension exhibited a deep blue color. Compared to our previous work with nanospheres where the micro-environment is quite hydrophilic, <sup>14</sup> the basicity of the chromoionophore in the hydrophobic region of the PS particle surface is much higher. Valinomycin is able to bind with K<sup>+</sup> and form a stable complex (LK<sup>+</sup>). As K<sup>+</sup> is added, the peak around 630 nm gradually decreases while the absorbance around 540 nm and a reddish color gradually arise, indicating the formation of deprotonated chromoionophore (Ind).

For traditional film based ion-selective optodes, electroneutrality must hold for the bulk of the film.<sup>5</sup> When a given amount of  $K^+$  is extracted into the sensing phase, the same amount of  $H^+$  will be released into the aqueous phase, so that the bulk of the sensor is electrically neutral. If this is not the case, a charge excess will accumulate on the surface. Zeta-potentials were measured for the  $K^+$ -selective microspheres in 10 mM pH 7.4 Tris-HCl buffer. As the  $K^+$  concentration was increased (up to 70  $\mu$ M), the zeta-potential remained at  $\pm 0.2$  mV (which is within the instrumental error range), confirming that the surface is neutral, and suggesting that electroneutrality still holds for these microsensors. Therefore, the sensing process can be expressed using Eqn. 3.1, with (s) and (aq) designating the microsphere surface and the surrounding aqueous phase.

$$HInd^{+}(s) + R^{-}(s) + L(s) + K^{+}(aq) = Ind(s) + R^{-}(s) + LK^{+}(s) + H^{+}(aq)$$
 (3.1)

Under the conditions used here, the  $K^+$ -selective PS microspheres exhibited an exhaustive sensing mode, as recently established by our group using emulsion based (plasticizer and surfactant) nanospheres (Chapter 4).<sup>20</sup> In an exhaustive mode, the added analyte will be consumed by the sensor and result in a response range that also depends on the quantity of sensor material. In this case, the  $K^+$  response indeed depended on the amount of the microspheres. When smaller amounts of microspheres were used ( $A_0 = 0.36$ , microsphere ion-exchange capacity of ca. 13  $\mu$ M, Fig. S3.2), a relative narrow detection range from 0 to 10  $\mu$ M was observed. Higher microsphere concentration ( $A_0 = 1.68$ , microsphere ion-exchange capacity of ca. 60  $\mu$ M) resulted  $K^+$  response from 0 to 60  $\mu$ M with a linear range from 10 to 40  $\mu$ M, as shown in Fig 3.2. The detection limits are adjustable through tuning the microsphere concentration and able to cover most environmental and biological samples. At lower pH, the equilibrium based sensing of  $K^+$  without sample depletion should take place instead of the exhaustive mode. As shown in Fig. S3.3, a linear relationship between the sensor response and the logarithms of  $K^+$  concentration from  $10^{-6}$  to  $10^{-1}$  M was observed in 10 mM Mes-NaOH buffer (pH 5.6).

The K<sup>+</sup> response from the modified PS microspheres of 2 µm diameter was similar (Fig. S3.4). However, the initial absorbance at pH 7.4 without addition of K<sup>+</sup> showed both maxima from Ind and HInd<sup>+</sup>, meaning that chromoionophore I was only partially protonated. Such

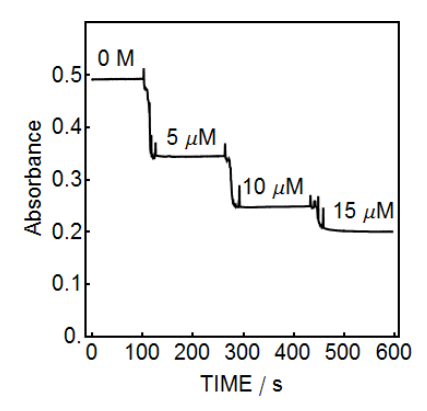


Figure 3.3. Response time of the K<sup>+</sup>-selective PS microspheres in 10 mM pH 7.4 Tris-HCl. Addition of different concentrations of KCl and mixing by pipetting the suspension up and down with a glass pipette are indicated by the spikes.

difference is perhaps due to the presence of carboxylates on the surface of the PS microspheres that render the micro-environment of PS microsphere surface more hydrophilic. A decreased basicity was also observed in previous work reported for ion-selective nanospheres where the surface was covered by other surfactants such as Pluronic F-127.<sup>14</sup>

The selectivity of the  $K^+$ -selective PS microspheres was found to be excellent. As shown in Fig. 3.2(b), other commonly seen ions such as Na $^+$ , Ca $^{2+}$ , Mg $^{2+}$  and Li $^+$  did not interfere in the active range for  $K^+$ . Interference became only visible when these ions reached high concentrations (> 10 mM) (Fig. S3.5). The microspheres appear to exhibit the required selectivity for intracellular experiments.

One important reason that accounts for the vacancy of PS-based ion-selective optodes is the very slow diffusion of the sensing components in polystyrene. In this early study, sensing films of ca. 5  $\mu$ m thickness and containing the same components as the PS microsheres were prepared by drop casting, but the films showed no response to K<sup>+</sup> even after days. This suggests that the micron-sized sensing beads exhibit much shorter response time owing to their reduced dimensions and the localization of the surface doping. Indeed, the  $t_{95\%}$  response time was found as ca. 5 s (Fig. 3.3), noting that the convective mixing was not optimized for speed.

In summary, a novel method of preparing ion-selective optical microsensors by modification on the surface of polystyrene microparticles was introduced here. Physical entrapment of the sensing components on the surface of the PS particle was achieved by precipitation of the sensing components in aqueous PS particle suspension. The resulting microspheres showed a narrow size distribution, long shelf life, high sensitivity and selectivity to  $K^+$  and a fast response time. The present study suggests that surface modification of PS particles may comprise a route to mass production of a new family of ion-selective optical sensors that work on the basis of ion-selective optodes. These microsensors may become valuable tools for the analysis of small ion quantities of environmental and biological samples.

#### 3.1 Supporting Information for Chapte 3

#### 3.1.1 Experimental Section

- 3.1.1.1Reagents. 3-octadecanoylimino-7-(diethylamino)-1,2-benzophenoxazine (Chromoionophore I), latex beads (polystyrene, 0.8 μm mean particle size by DSL, without azide), potassium ionophore I (L, valinomycin), tetrahydrofuran (THF), sodium tetrakis-[3,5-bis(trifluoromethyl)phenyl]borate (NaTFPB), 2-amino-2-hydroxymethyl-propane-1,3-diol (Tris), 2-(N-Morpholino)ethanesulfonic acid (Mes), potassium chloride, calcium chloride, lithium chloride, and magnesium chloride were obtained from Sigma-Aldrich. Lumogen Red was obtained from BASF. CML latex (4.2 % w/v, 2.4 μm by DSL, 2.0 μm by TEM) was purchased from Invitrogen<sup>TM</sup> (Eugene, Oregon, USA).
- 3.1.1.2 Preparation of Exhaustive  $K^+$ -selective Microspheres. 1.0 mg of NaTFPB, 0.5 mg of Chromoionophore I, 2.0 mg of potassium ionophore I were dissolved in 3.0 mL of THF to form a homogeneous solution. 10  $\mu$ L of commercial PS particle concentrates was diluted to 40 mL in  $H_2O$ . 0.5 mL of the THF solution was pipetted and injected into 4.5 mL of the diluted PS particle suspension on a vortex with a spinning speed of 1000 r/min. The resulting blue mixture was blown with compressed air on the surface for 20 min to remove THF. For the preparation of Lumogen Red modified PS microspheres, a THF solution containing Lumgen Red (0.23 mg in 3 mL THF) was used. Microsphere concentratin was calculated with the ion exchanger NaTFPB.
- **3.1.1.3 Instrumentation and Measurements.** The size and zeta-potentials of the modified microspheres were measured with Zetasizer Nano ZS (Malvern Inc.) particle size analyzer in the dynamic light scattering mode at 173 ° scattering angle in 1 cm plastic cuvette. The absorbance was measured with a UV-Vis spectrometer (SPECORD 250 plus, Analytic Jena, AG, Germany). Confocal microscopic images were obtained under Zeiss LSM 700 upright confocal microscope using 555 nm laserline as

excitation and 63x objective lens. Calibration curves were measured in buffer solutions at the indicated pH (10 mM Tris-HCl or 10 mM Mes-NaOH) values with gradual addition of KCl or other salt stock solutions. Response time was recorded under absorption mode in 10 mM pH 7.4 Tris-HCl buffer. Aliquots of KCl solution were pipetted and injected into a cuvette containing the modified PS microspheres (0.8 µm). Disposable poly(methyl methacrylate) cuvettes with path length of 1 cm were for absorbance interrogation.

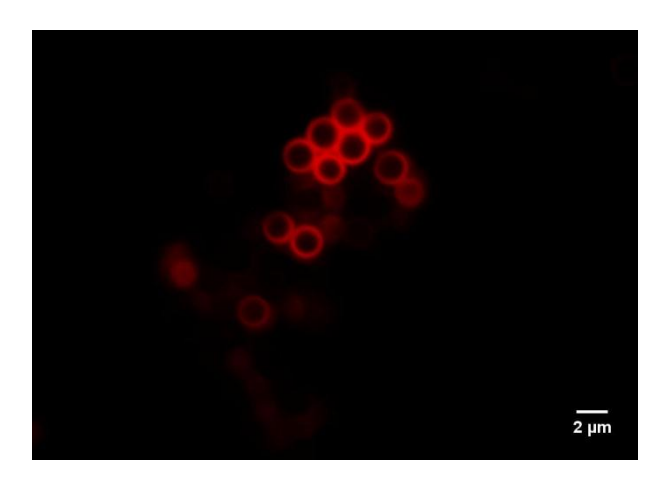
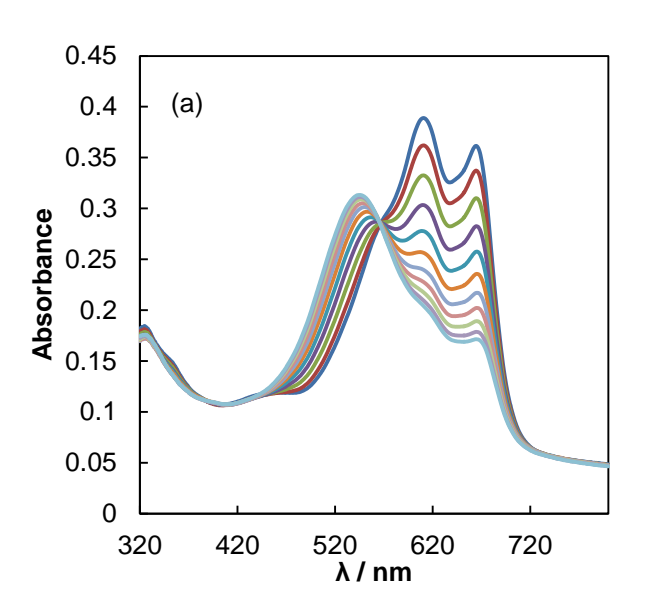


Figure S3.1. Fluorescence confocal microscope image for Lumogen Red adsorbed CML latex microspheres of 2.0 µm diameter in H<sub>2</sub>O.



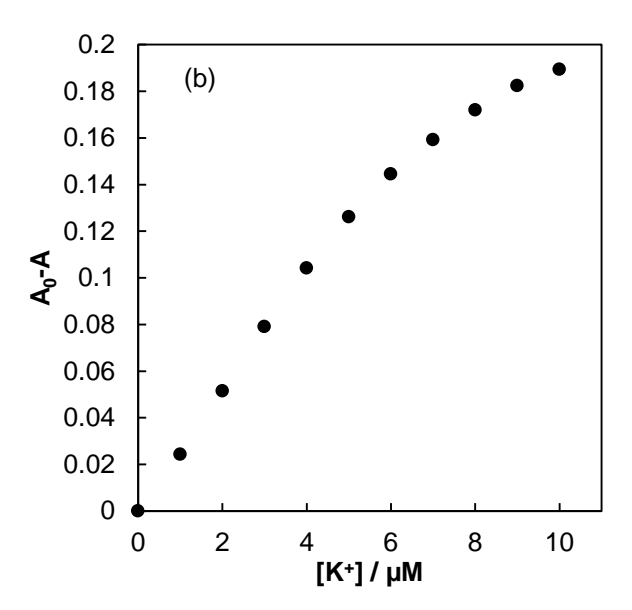


Figure S3.2. (a) Absorbance change for the  $K^+$ -selective PS microspheres (0.8  $\mu$ m) in 10 mM pH 7.4 Tris-HCl with different levels of KCl (for concentrations, see b). (b) Calibration curve using absorbance difference at 663 nm ( $A_0$ -A) against  $K^+$  concentration, where  $A_0$  is the initial absorbance in buffer.

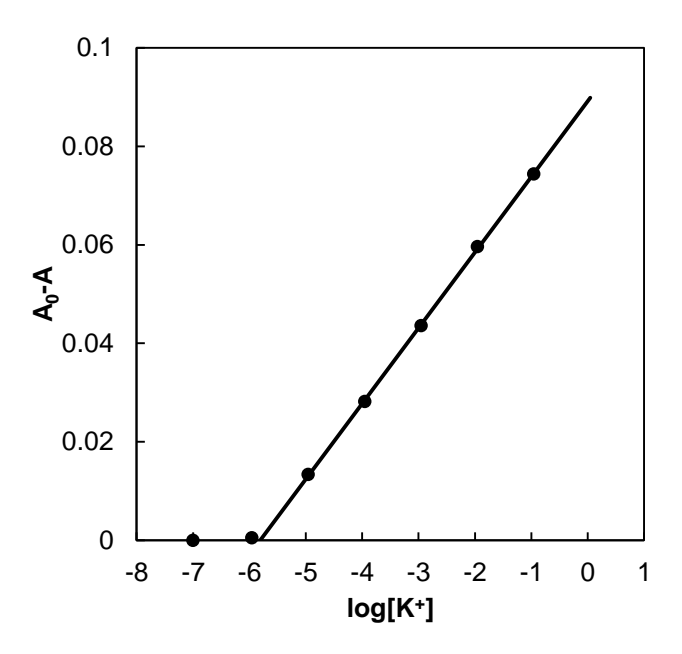


Figure S3.3. Calibration curve for the  $K^+$ -selective PS microspheres (0.8  $\mu$ m) in pH 5.6 10 mM MES-NaOH buffer using the absorbance difference at 663 nm ( $A_0$ -A) against the logarithm of  $K^+$  concentration, where  $A_0$  is the initial absorbance in buffer.

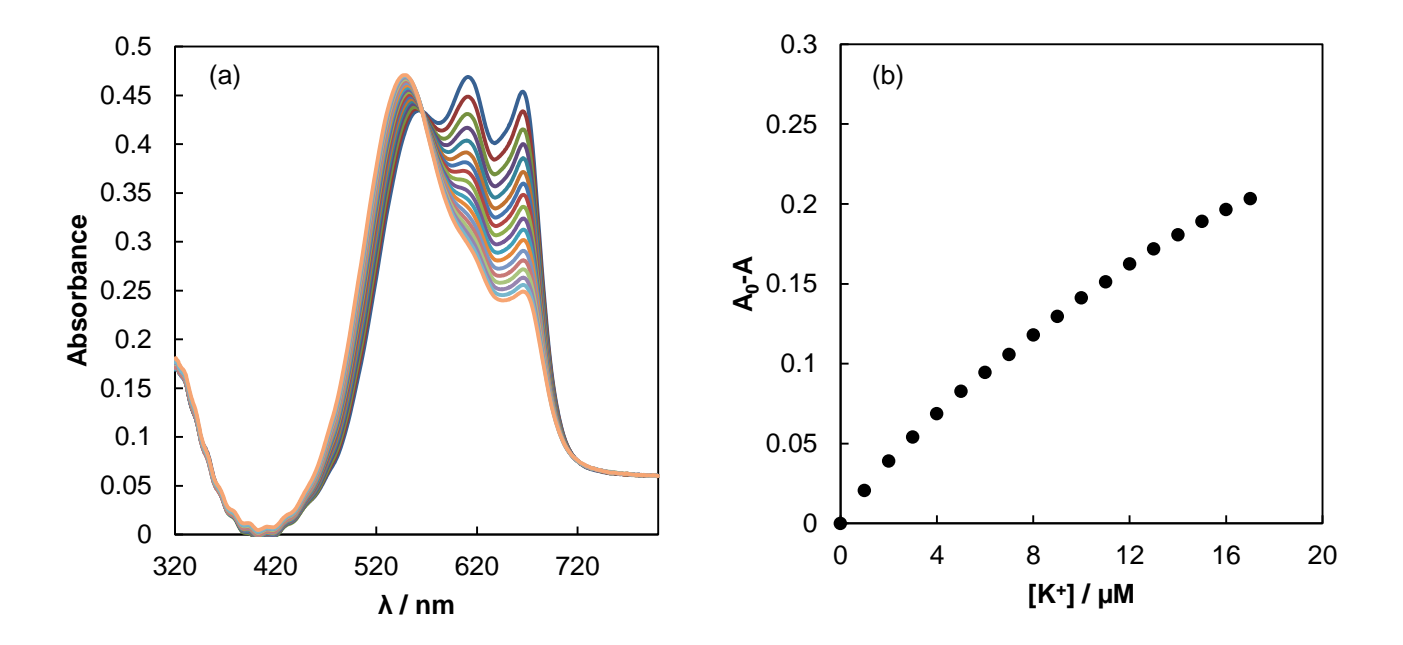


Figure S3.4. (a) Absorbance change for the  $K^+$ -selective PS microspheres (2.0  $\mu m$ , carboxylate modified) in 10 mM pH 5.6 Mes-NaOH with different level of KCl. (b) Calibration curve using absorbance difference at 663 nm (A<sub>0</sub>-A) against  $K^+$  concentration, where A<sub>0</sub> is the initial absorbance in buffer.

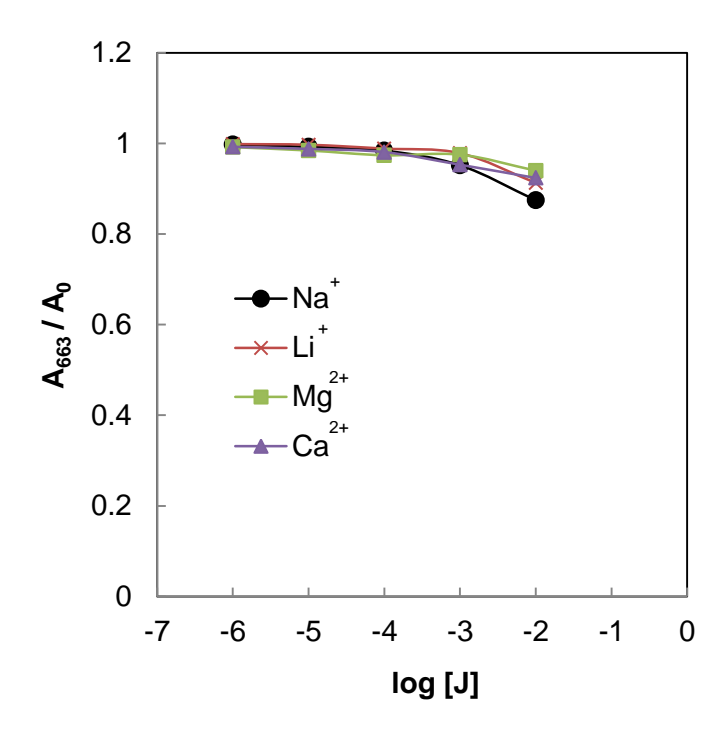


Figure S3.5. Interference from other commonly seen ions to the  $K^+$ -selective PS microspheres (0.8  $\mu$ m) evaluated in absorbance mode. The absorbance value at 663 nm divided by the initial absorbance ( $A_{663}/A_0$ ) was plotted against the logarithm of the interfering ion (J) concentration.

### 3.2 References for Chapter 3

- (1) M. Lerchi, E. Bakker, B. Rusterholz and W. Simon, *Anal. Chem.*, 1992, **64**, 1534-1540.
- (2) C. Krause, T. Werner, C. Huber and O. S. Wolfbeis, *Anal. Chem.*, 1999, **71**, 5304-5308.
- (3) X. Xie, G. Mistlberger and E. Bakker, J. Am. Chem. Soc., 2012, **134**, 16929-16932.
- (4) I. H. A. Badr and M. E. Meyerhoff, J. Am. Chem. Soc., 2005, 127, 5318-5319.
- (5) E. Bakker, P. Bühlmann and E. Pretsch, *Chem. Rev.*, 1997, **97**, 3083-3132.
- (6) X. Xie, X. Li, Y. Ge, Y. Qin and H.-Y. Chen, Sens. Actuators, B, 2010, 151, 71-76.
- (7) S. Dai, Q. Ye, E. Wang and M. E. Meyerhoff, Anal. Chem., 2000, 72, 3142-3149.
- (8) J. M. Dubach, D. I. Harjes and H. A. Clark, J. Am. Chem. Soc., 2007, 129, 8418-8419.
- (9) I. Tsagkatakis, S. Peper and E. Bakker, *Anal. Chem.*, 2001, **73**, 315-320.
- (10) E. J. Park, M. Brasuel, C. Behrend, M. A. Philbert and R. Kopelman, *Anal. Chem.*, 2003, **75**, 3784-3791.
- (11) A. Burns, P. Sengupta, T. Zedayko, B. Baird and U. Wiesner, Small, 2006, 2, 723-726.
- (12) J. M. Dubach, S. Das, A. Rosenzweig and H. A. Clark, *Proc. Natl. Acad. Sci.*, 2009, 106, 16145-16150.
- (13) M. Telting-Diaz and E. Bakker, Anal. Chem., 2002, 74, 5251-5256.
- (14) X. Xie, G. Mistlberger and E. Bakker, *Anal. Chem.*, 2013, **85**, 9932-9938.
- (15) I. H. A. Badr and M. E. Meyerhoff, Anal. Chim. Acta, 2005, 553, 169-176.
- (16) M. Antonietti, J. Coutandin and H. Sillescu, Macromol. Rapid Comm., 1984, 5, 525-528.
- (17) M. Lücka, W. Schröderb, B.-R. Paulkec, T. Blunkd and R. H. Müller, Biomaterials, 1999, 20, 2063-2068.

- (18) J. Lee, P. A. Martic and J. S. Tan, J. Colloid. Interf. Sci., 1989, 131, 252-266.
- (19) Z. Adamczyk, A. Bratek-Skicki, P. Dąbrowska and M. Nattich-Rak, *Langmuir*, 2012, **28**, 474-485.
- (20) X. Xie, J. Zhai and E. Bakker, Anal. Chem., 2014, 86, 2853.

# Chapter 4. pH Independent Nano-Optode Sensors Based on Exhaustive Ion-Selective Nanospheres

This work has been published in: Xiaojiang Xie, Jingying Zhai and Eric Bakker\*, Anal. Chem., 2014, 86, 2853–2856

#### 4.1 Introduction

Ion selective bulk optodes<sup>1-6</sup> are composed of lipophilic sensing components embedded in a lipophilic matrix material such as plasticized PVC or other polymers.<sup>1</sup> These sensors have recently been miniaturized in the form of microparticles and nanoparticles<sup>7-10</sup> and have found significant resonance in research and applied work. <sup>3,11-13</sup>

Cation selective bulk optodes function on the basis of bulk extraction equilibria with an extraction competition between the analyte ion and  $H^{+,1}$  The mole fraction of protonated chromoionophore in the sensing phase is related to the analyte concentration in the aqueous sample at fixed pH. The optode response function can be adequately predicted by theory in agreement with experimental results.<sup>1</sup>

According to theory, the equilibrium sensor response is dependent on the sample pH. For routine analysis, therefore, the pH of the sample must be measured or controlled. This pH dependence has been the major drawback of ion selective optodes and has, to a great extent, limited the application of this powerful technology. In this communication, using Ca<sup>2+</sup> as a model ion, we show for the first time that the pH dependence for ion selective optodes can be overcome with what we call exhaustive ion selective nanosensors. Conventionally, an optode sensor response is measured at equilibrium where the sample is not altered by the sensor. In an exhaustive mode, however, all the analyte in the sample will be consumed by the sensor for sensing purposes. This is achieved here with samples containing an optode nanoparticle suspension.

#### 4.2 Experimental Section

**4.2.1 Reagents.** Pluronic® F-127 (F127), bis(2-ethylhexyl) sebacate (DOS), tetrahydrofuran (THF), sodium tetrakis-[3,5-bis(trifluoromethyl)phenyl]borate (NaTFPB), 2-amino-2-hydroxymethyl-propane-1,3-diol (Tris), 3-octadecanoylimino-7-(diethylamino)-1,2-benzophenoxazine (chromoionophore I), calcium chloride (CaCl<sub>2</sub>) were obtained from Sigma-Aldrich. (E)-N,N-dibutyl-4-(2-(6,6-dimethyl-2-nitro-6,12-dihydro-5aH-benzo[5,6][1,3]oxazino[3,2-a]indol-5a-yl)vinyl)aniline (Ox) was synthesized according to a previous report.<sup>6</sup>

**4.2.2 Preparation of Exhaustive Ca<sup>2+</sup>-Selective Nanosensors.** 1.9 mg of NaTFPB, 1.4 mg of Chromoionophore I (or 1.1 mg of Ox), 8.0 mg of DOS, 5.0 mg of F127, and 6.5 mg of calcium ionophore IV were dissolved in 3.0 mL of THF to form a homogeneous solution. 0.5 mL of this solution was pipetted and injected into 4.5 mL of deionized water on a vortex with a spinning speed of 1000 r/min. The resulting clear mixture was blown with compressed air on the surface for 20 min to remove THF, giving a clear particle suspension (3.8 mL). The nanosphere charge capacity, which represents the total concentration of the exchangeable ions in the nanospheres suspension, was calculated with the NaTFPB concentration and used to estimate the particle concentration.

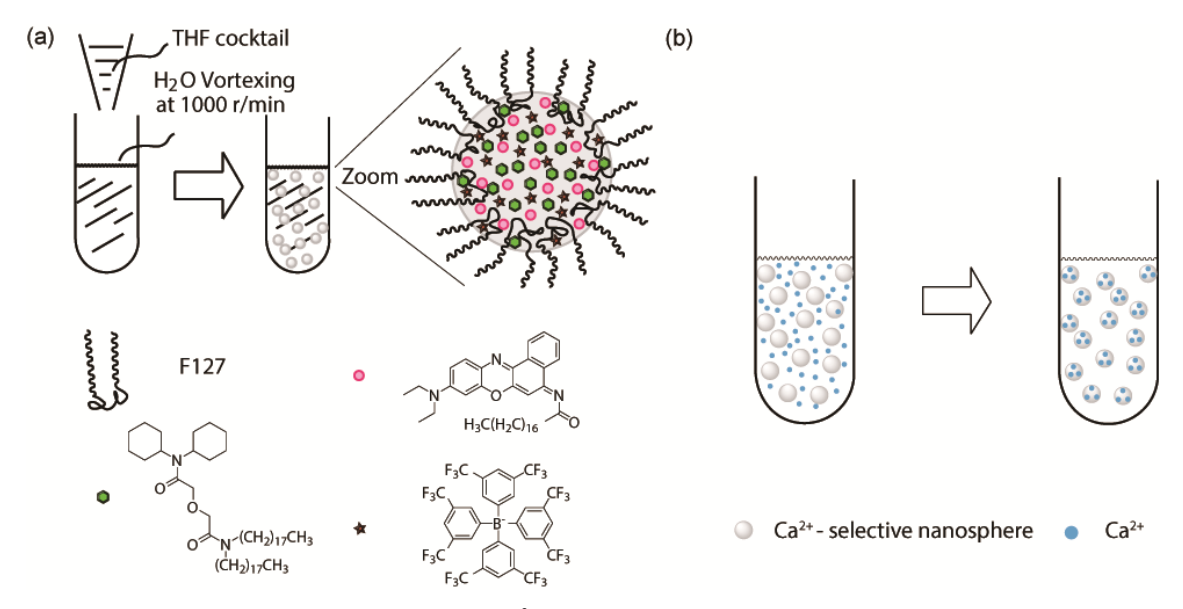


**Figure 4.1.** (a) Preparation and proposed microstructure of  $Ca^{2+}$ -selective nanooptodes. The grey spherical background represents DOS acting as a solvent for the sensing components. (b) Scheme showing the exhaustive sensing process where all  $Ca^{2+}$  in the sample is consumed by the nanospheres.

**4.2.3 Instrumentation and Measurements.** The size of the nanospheres was measured with the particle size analyzer Zetasizer Nano ZS (Malvern Inc.). The absorbance was measured with a UV-Vis spectrometer (SPECORD 250 plus, Analytic Jena, AG, Germany). Calibration curves were measured in buffer solutions at the indicated pH values with gradual addition of CaCl<sub>2</sub> or other salt stock solutions. 1.5 mL of the nanospheres suspension was mixed with 1.5 mL of concentrated buffer solutions in a disposable poly(methyl methacrylate) cuvette with path length of 1 cm for absorbance interrogation. No preconditioning step was required before using the nanospheres.

#### 4.3 Results and Discussion

The nanosensors were prepared by a precipitation method recently introduced by our group (Chapter 2).<sup>10</sup> A THF solution containing chromoionophore I, NaTFPB, Ca<sup>2+</sup> ionophore IV, DOS, and an amphoteric copolymer F127 was injected into vortexing H<sub>2</sub>O to form a nanosphere suspension (Fig. 4.1). After removal of THF, the nanosensors exhibited an average diameter of 64 nm (polydispersity index 0.17) as determined by dynamic light scattering.

 $Ca^{2+}$ -selective optodes have been previously studied and sigmoidal calibration curves were observed when evaluated under equilibrium conditions. <sup>14</sup> Such S-shaped calibration curves were also obtained for the  $Ca^{2+}$  selective nanosensors studied here when interrogated at mildly acidic pH. To most accurately measure the equilibrium sensor response, a relatively low nanosphere charge capacity (ca. 1.5  $\mu$ M) was used. As shown in Fig. 4.2a, the response  $1-\alpha_{eff}$  values <sup>15</sup> of the nanosensors were found to be pH dependent, with a roughly two orders of magnitude shift in the curve upon each pH unit change. While this dependence is well established and described by optode response theory, <sup>1,14</sup> it is one of the biggest obstacles for adopting such optodes in practice since the H<sup>+</sup> concentration must be known as well.

To overcome this pH dependence, ion-selective exhaustive nanosensors are introduced here. In this detection mode, the nanosensors no longer work under typical equilibrium conditions where the sample concentration is not altered. Instead, the ion extraction process is exhaustive, resulting in a significant sample concentration change. As shown in Fig. 4.2b, even using ca. 0.7 µM nanosphere charge capacity, calibration at low Ca<sup>2+</sup> concentration deviates from the theoretical sigmoidal curve. When the Ca<sup>2+</sup> concentration level is below the sensing nanosphere charge capacity, the analyte concentration in the sample will be altered. For ideally operating exhaustive nanosensors, all sample Ca<sup>2+</sup> should be consumed by the nanospheres. To achieve this, the nanospheres must be present in sufficient

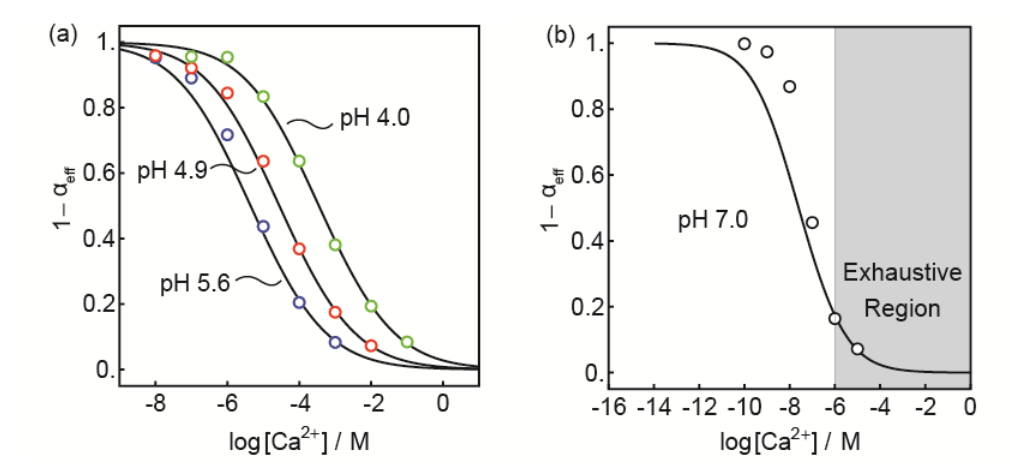


**Figure 4.2.** (a) Calibration curves of the Ca<sup>2+</sup>-selective nanosensor under equilibrium conditions at different pH (pH 4 HCl, 10 mM pH 4.9 Mg(oAc)<sub>2</sub>, 10 mM pH 5.6 Mes-NaOH), avoiding calcium depletion. (b) Sensor response measured for Ca<sup>2+</sup>-selective nanospheres at pH 7.0 (3 mM Tris-HCl) together with expected sigmoidal calibration curve.

quantity to extract all available calcium ions in the sample aliquot. From Fig. 4.2b it is also clear that the sensor becomes extremely sensitive to  $Ca^{2+}$ .

To achieve the detection range from  $10^{-7}$  M to  $10^{-5}$  M  $Ca^{2+}$ , which covers the normal intracellular free calcium level, <sup>16</sup> the binding between the ionophore and the analyte has to be strong. In practice, this means that the response curve must lie to the left of the desired concentration range, as shown in Fig. 4.2b. If the affinity of the ionophore for the analyte is weak, the response range under equilibrium conditions will shift to higher concentrations. An exhaustive sensing system can then only be achieved with an even higher loading of the nanosensors or with a much smaller sample volume.

Based on the law of mass conservation, the following relationship (Eqn. 4.1) should apply whether the sensor is exhaustive or not:

$$n_{Ca}(tot) = n_{Ca}^{aq} + n_{Ca}^{ns} (4.1)$$

where  $n_{Ca}(tot)$ ,  $n_{Ca}^{aq}$ , and  $n_{Ca}^{ns}$  are the number of moles of  $Ca^{2+}$  in the system, remaining in the aqueous phase, and in the nanospheres, respectively. The calcium concentration in the nanospheres is related to that of the concentration change of protonated indicator, and one obtains:

$$n_{Ca}(tot) = n_{Ca}^{aq} + \frac{1}{2}(n_{HInd}^{ns}(0) - n_{HInd}^{ns})$$
(4.2)

where  $n_{HInd}^{ns}(0)$  and  $n_{HInd}^{ns}$  are the number of moles of protonated indicator before and after calcium extraction. The amount of Ca<sup>2+</sup> being extracted into the nanosphere is equal to half of the amount of H<sup>+</sup> being exchanged (charge balance), which is related to the protonation degree of the chromoionophore. By applying Lambert-Beer's law, one obtains Eqn. 4.3 as:

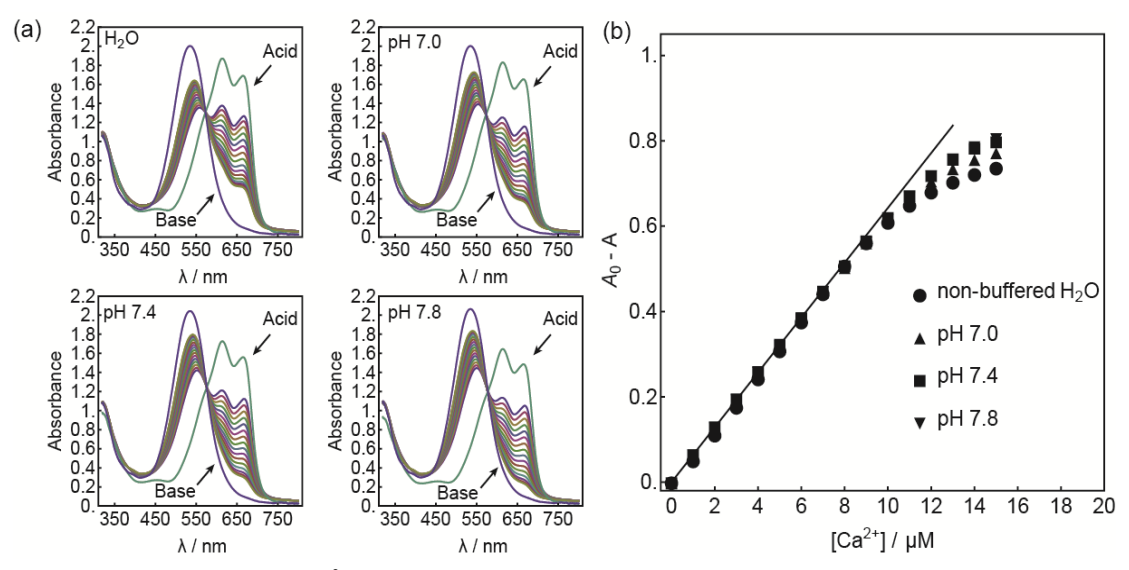


**Figure 4.3.** (a) Absorbance spectra of the  $Ca^{2+}$ -selective nanooptodes operated exhaustively at different pH (Tris-HCl, 10 mM) with various  $Ca^{2+}$  concentrations. Acid and Base indicate 1 mM HCl and 1 mM NaOH (b) Calibration for the experiments in (a) using the absorbance difference at 663 nm ( $A_0$ –A), with  $A_0$  being the absorbance in buffer.

$$[Ca^{2+}]_{tot} = [Ca^{2+}]_{aq} + \frac{1}{2} \frac{A_0 - A}{\varepsilon b}$$
 (4.3)

where  $[Ca^{2^+}]_{tot}$  and  $[Ca^{2^+}]_{tot}$  are the Ca<sup>2+</sup> concentrations in the system and in the aqueous phase, respectively,  $A_0$  and A are the absorbances of the protonated chromoionophore before and after extraction of Ca<sup>2+</sup>, and  $\mathcal{E}$  and b the molar absorptivities and the optical path length.

If the nanosensors are exhaustive, the remaining  $Ca^{2+}$  concentration in the aqueous phase approaches zero. In that case, a linear relationship is expected between the absorbance difference ( $A_0$ –A) and total  $Ca^{2+}$  concentration. Indeed, linear calibration curves tend to be preferred over the previously observed S-shape curves. We also note that in Eqn. 4.3 the sensor response ( $A_0$ -A) is now directly proportional to the  $Ca^{2+}$  concentration without influence from the sample pH.

To prove this hypothesis, we evaluated the  $Ca^{2+}$  response of a  $Ca^{2+}$  selective nanosensor suspension (ca. 44  $\mu$ M) in absorbance mode at different pH values. Fig. 4.3a shows the observed absorption spectra of the nanosphere suspension containing various levels of  $Ca^{2+}$  and at different pH. The spectra recorded in buffers without  $Ca^{2+}$  showed an absorbance peak around 663 nm but is much lower than that in 1 mM HCl. This indicates an excess chromoionophore over ion exchanger in the nanospheres, which is confirmed in Fig. S4.1 (see supporting information). Upon addition of  $Ca^{2+}$ , the absorbance at this wavelength starts to decrease. The absorbance at 663 nm was used for the calibration curves shown in Fig. 4.3b. The same calibration curve was observed at different sample pH, even in unbuffered H<sub>2</sub>O where the pH was not well controlled. A linear relationship in the range of 0 to  $10^{-5}$  M was observed. At higher  $Ca^{2+}$  concentrations, the sensor response started to deviate from linearity, indicating that the nanospheres were approaching saturation and  $[Ca^{2+}]_{aq}$  was no longer negligible.

Calcium ionophore IV has been reported for the selective detection of  $Ca^{2+}$  in ion-selective electrodes and optodes.<sup>6,14,17</sup> The nanosensors were here confirmed to be highly selective to  $Ca^{2+}$  over other metal ions. As shown in Fig. S4.2, the ions  $Mg^{2+}$ ,  $Na^+$ ,  $K^+$ , and  $Li^+$  exhibited

interference only at levels above their intracellular concentration. Since most chromoionophores are also fluorescent and the theory is also applicable for fluorescence mode, the principle could become potentially applicable for intracellular experiments.

#### 4.4 Conclusion

The pH dependent response of bulk ion optodes has historically been a major disadvantage for ion-selective optodes. We have presented here for the first time exhaustive ion-selective nanosensors to overcome this pH cross-response using  $Ca^{2+}$  as a model ion. The nanosensors showed identical calibration curves in the  $Ca^{2+}$  concentration range from  $10^{-7}$  M to  $10^{-5}$  M at different pH. This work may potentially allow one to expand the use of ion-selective optodes for a wider variety of applications.

### 4.5 Supporting Information for Chapter 4

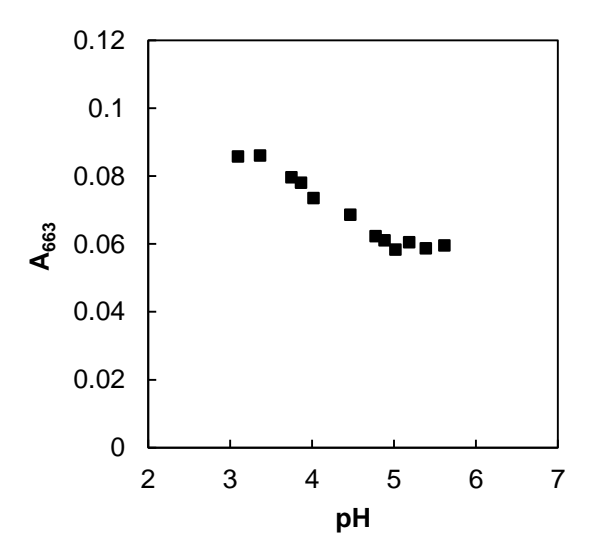


**Figure S4.1.** Absorbance intensity change of calcium selective nanosphere suspension at 663 nm at different pH in a background of pure water. The pH was adjusted by gradual addition of H<sub>2</sub>SO<sub>4</sub>. The absorbance plateau above pH indicates an excess of chromoionophore over ion-exchanger and an incomplete protonation in pure water that is not given by an interference.

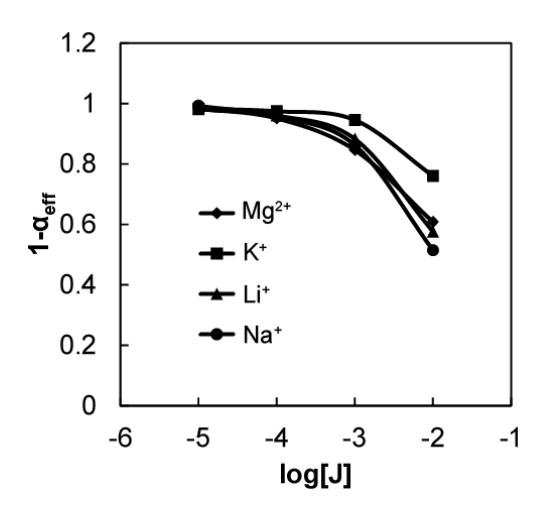


Figure S4.2. Selectivity of the Ca<sup>2+</sup>-selective nanooptodes in 10 mM pH 7.4 Tris-HCl buffer measured in absorbance mode.

The degree of protonation  $1-\alpha_{eff}$ , <sup>15</sup> is calculated using the following equation:

$$1 - \alpha_{eff} = \frac{A - A_{min}}{A_{max} - A_{min}}$$

where,  $A_{min}$  is the minimum absorbance of the nanospheres at 663 nm for Chromoionophore I (574 nm for Ox) measured at 1 mM NaOH, and  $A_{max}$  is the maximum absorbance in buffer solutions without addition of any  $Ca^{2+}$ .

#### 4.6 References for Chapter 4

- (1) Bakker, E.; Bühlmann, P.; Pretsch, E. Chem. Rev. 1997, 97, 3083.
- (2) Kim, S. B.; Cho, H. C.; Cha, G. S.; Nam, H. Anal. Chem. 1998, 70, 4860.
- (3) Retter, R.; Peper, S.; Bell, M.; Tsagkatakis, I.; Bakker, E. Anal. Chem. 2002, 74, 5420.
- (4) Burns, A.; Sengupta, P.; Zedayko, T.; Baird, B.; Wiesner, U. Small 2006, 2, 723.
- (5) Jokic, T.; Borisov, S. M.; Saf, R.; Nielsen, D. A.; Kühl, M.; Klimant, I. Anal. Chem. 2012, 84, 6723.
- (6) Mistlberger, G.; Xie, X.; Pawlak, M.; Crespo, G. A.; Bakker, E. Anal. Chem. 2013, 85, 2983.
- (7) Tsagkatakis, I.; Peper, S.; Bakker, E. Anal. Chem. 2001, 73, 315.
- (8) Telting-Diaz, M.; Bakker, E. Anal. Chem. 2002, 74, 5251.
- (9) Dubach, J. M.; Harjes, D. I.; Clark, H. A. J. Am. Chem. Soc. 2007, 129, 8418.
- (10) Xie, X.; Mistlberger, G.; Bakker, E. Anal. Chem. 2013, 85, 9932.
- (11) Dubach, J. M.; Das, S.; Rosenzweig, A.; Clark, H. A. Proc. Natl. Acad. Sci. 2009, 106, 16145.
- (12) Dubach, J. M.; Harjes, D. I.; Clark, H. A. Nano Lett. 2007, 7, 1827.
- (13) Cash, K. J.; Clark, H. A. Anal. Chem. 2013, 85, 6312.
- (14) Morf, W. E.; Seiler, K.; Rusterholz, B.; Simon, W. Anal. Chem. 1990, 62, 738.
- (15) Antico, E.; Lerchi, M.; Rusterholz, B.; Achermann, N.; Badertscher, M.; Valiente, M.; Pretsch, E. Anal. Chim. Acta 1999, 388, 327.

- (16) Alberts, B.; Johnson, A.; Lewis, J.; Raff, M.; Roberts, K.; Walter, P. In *Molecular Biology of the Cell*; 5 ed.; Garland Science, Taylor&Francis Groups, LLC: 2007.
- (17) Perera, H.; Shvarev, A. Anal. Chem. 2008, 80, 7870.

# Chapter 5. Ionophore based Ion-Selective Optical NanoSensors Operating in Exhaustive Sensing Mode

This work has been published in: Xiaojiang Xie, Jingying Zhai, Gaston A. Crespo and Eric Bakker\*, Anal. Chem., 2014, 86, 8770–8775

#### 5.1 Introduction

Optical ion sensors are important research tools in fundamental chemical science and applied field work such as biochemistry, clinical medicine and environmental monitoring. <sup>1-5</sup> Ionophore based ion selective optical sensors (ion selective optodes) have been developed in recent years for various target analytes. <sup>6-9</sup>

In contrast to ion indicators<sup>10-12</sup>, a direct chemical linkage between the chelator and the optical reporter (such as a chromophore) is not needed in ion selective optode sensors. Instead, ionophores (L) are employed to selectively recognize the analyte ion while a lipophilic pH indicator (chromoionophore, Ind) is used as optical reporter. Such a simplification has endowed the sensors with excellent selectivity, tunable optical window, and adjustable response range.

Ion selective optodes function on the basis of phase extraction equilibria.<sup>6,13</sup> For instance, a cation selective optode is usually composed of a lipophilic pH indicator (chromoionophore), a cation exchanger (R<sup>-</sup>) and an ionophore, all embedded in a water immiscible matrix material such as plasticized PVC film. Upon sample contact, an extraction competition is established between hydrogen ions and the analyte ions in the aqueous phase, while the bulk of the organic phase remains electrically neutral. Therefore, the degree of the protonation of the indicator will reflect the analyte concentration, transducing the binding event into a signal output. For anion selective systems, coextraction (H<sup>+</sup> and analyte anion) occurs instead of ion exchange.<sup>6,14-17</sup>

In practice, the sensors are usually equilibrated with the sample solution before reading the signal output. In most contributions that have appeared in the literature, the analyte concentration in the sample is considered unaltered when the sensor is read out. <sup>6,9,18,19</sup> With this class of sensors, the response is known to be pH dependent and the sample pH needs either be kept constant or monitored at the same time. The pH cross response is admittedly a disadvantage and has limited to a significant extent the application of this otherwise attractive technology.

We describe here optical ion sensors operated in what we coin an exhaustive sensing mode. Here, the target analyte will be completely consumed by the sensor upon equilibration of the sensors with the sample. We have recently demonstrated in preliminary work that such a sensing mode can potentially overcome the pH dependence of ion selective optodes using Ca<sup>2+</sup> as a model target ion (Chapter 4).<sup>20</sup> Of course, an exhaustive sensing mode cannot be applied when the sample concentration should not be altered.

In this work, the fundamental and applied aspects of the exhaustive sensing mode are discussed in depth, and the exhaustive sensing mode is extended to protamine, a polyion with high physiological and medical importance.<sup>21</sup> Previous optical sensors for protamine based on similar principles have been reported. <sup>22,23</sup> However, owing to the relative thickness of the sensing film, the response times were too long to obtain an equilibrated state.

Unlike the classical membrane based sensors, the exhaustive sensors are composed of emulsified nanospheres that exhibit small size (typical average diameter below 100 nm), high thermal stability and simple preparation. <sup>24,25</sup> The nanosensors exhibited much faster response compared to film based optodes. As an early application of the exhaustive sensing mode, the nanosensors are used here to determined total calcium and heparin levels in human plasma.

#### 5.2 Experimental section

**5.2.1 Reagents.** Pluronic<sup>®</sup> F-127 (F127), bis(2-ethylhexyl) sebacate (DOS), tetrahydrofuran (THF), protamine sulfate from herring, tetrakis-[3,5-bis(trifluoromethyl)phenyl]borate (NaTFPB), 2-amino-2-hydroxymethyl-propane-1,3-diol octadecanoylimino-7-(diethylamino)-1,2-benzophenoxazine (chromoionophore I), Eriochrome<sup>®</sup> Black T, calcium chloride (CaCl<sub>2</sub>) and ethylenediaminetetraacetic acid (EDTA) were obtained from Sigma-Aldrich. Dinonylnaphthalene sulfonate (DNNS acid form in 50 % heptane) purchased from Santa Cruz Biotechnology, inc.. (1E,3E)-4-(6,6-dimethyl-2-nitro-6,12-dihydro-5aHbenzo[5,6][1,3]oxazino[3,2-a]indol-5a-yl)-N,N-dimethylbuta-1,3-dien-1-amine (ox blue) was synthesized according to a previous report. 19 Human blood plasma was provided by Hopital Universitaire de Geneve (HUG). All solutions and buffers were freshly prepared before starting the experiments.

**5.2.2 Instrumentations**. The size of the nanospheres was measured with the particle size analyzer Zetasizer Nano ZS (Malvern Inc.). The absorbance was measured with a UV-Vis spectrometer (SPECORD 250 plus, Analytic Jena, AG, Germany). Calibration curves were measured in buffer solutions at the indicated pH values with gradual addition of CaCl<sub>2</sub>, protamine, or other salt stock solutions. Disposable poly(methyl methacrylate) cuvettes with path length of 1 cm were used for absorbance interrogation. No preconditioning of the nanospheres is required.

**5.2.3 Sensor Preparation**. To prepare the calcium selective nanosensors, 1.9 mg of NaTFPB, 1.4 mg of Chromoionophore I, 8.0 mg of DOS, 5.0 mg of F127, and 6.5 mg of calcium ionophore IV were dissolved in 3.0 mL of THF to form a homogeneous solution. 0.5 mL of this solution was pipetted and injected into 4.5 mL of deionized water on a vortex with a spinning speed of 1000 r/min. The resulting clear mixture was blown with compressed air on the surface for 20 min to remove THF, giving a clear particle suspension. To prepare the nanosensors for protamine, 2.2 mg of Ox Blue, 4.1 mg of DNNS, 5.0 mg of F127 and 8.0 mg of DOS were dissolved in 3 mL of THF and the same procedure used for the calcium selective nanospheres was followed.

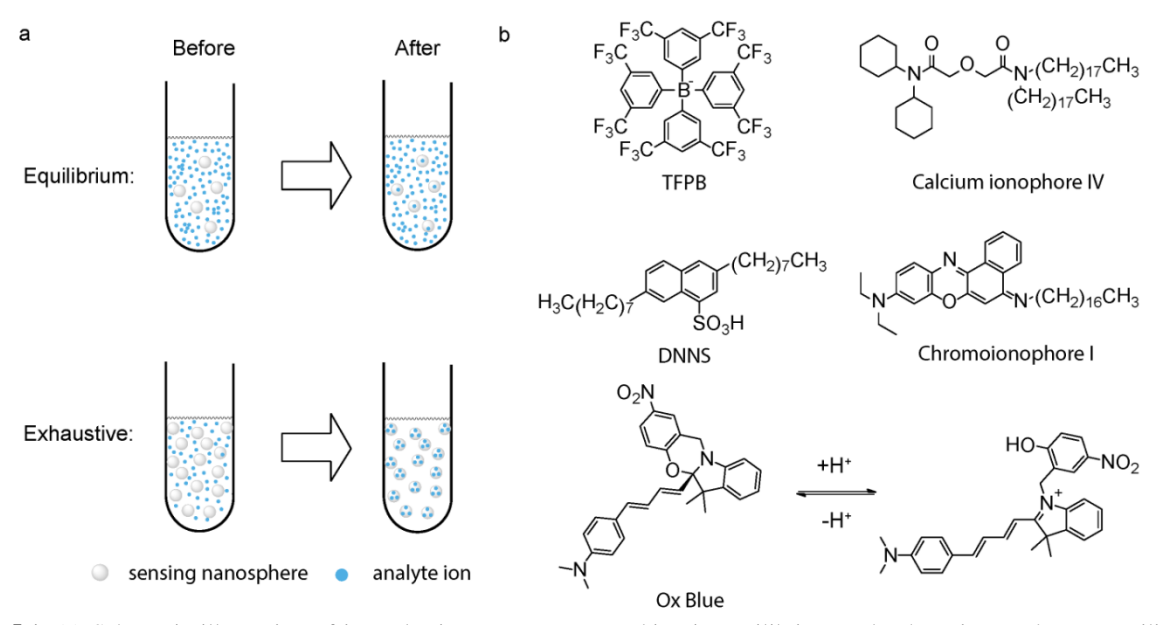


**Figure 5.1.** (a) Schematic illustration of ion selective nanosensors working in equilibrium and exhaustive modes. In equilibrium mode, the analyte concentration is not altered while in the exhaustive mode, the analyte ions are consumed completely by the sensors. (b) Chemical structures and abbreviation of the main sensor components used in this work and the proton induced ring openning reaction of ox blue, which is employed as chromoionophore for the protamine nanosensors.

The film based sensor for protamine (Figure 5.3 (a)) was prepared using previously described methods. <sup>15,26</sup> The THF cocktail for film casting contained 0.58 mg of CH I, 1.2 mg of DNNS, 20 mg of PVC and 40 mg of DOS.

5.2.4 Total Blood Plasma Calcium Measurement. The total calcium concentration in plasma was determined optically using the nanosensors and also by EDTA titration. For optical measurement using nanospheres, standard addition was used. Specifically, 3  $\mu$ L of plasma was taken into cuvettes containing the sensing nanospheres (3 mL) and different amount of added CaCl<sub>2</sub> (0, 1, 2 and 3  $\mu$ M) and the absorbance spectra was recorded. Absorbance values at 663 nm were taken into calculation. For EDTA titration, 3 mL plasma was mixed with 6 mL of HNO<sub>3</sub> (65%, w/w) and 3 mL of H<sub>2</sub>O<sub>2</sub> (30%, w/w) overnight to digest the plasma sample. Later, the mixture was neutralized by NaOH to pH 7 and diluted to 100 mL. Ca<sup>2+</sup> titration was then performed using 0.1 M EDTA stock solution in the presence of 2% (w/w) of Eriochrome<sup>®</sup> Black T to indicate the end point.

#### 5.3 Results and Discussion

Since ion selective optodes are known to exhibit a pH cross-response, the sample pH is usually fixed or monitored at the same time during the measurement. This has limited to a great extent the application of ion selective optode sensors. To overcome this disadvantage, one can consider measurements in an exhaustive mode using the same type of sensors. Ideally, the sample analyte will be completely consumed by the sensors. The sensor response will only depend on the total amount of the analyte and make the exhaustive sensors potentially calibration free. In classical equilibrium based sensing mode, on the other hand, the sample concentration is usually considered unchanged before and after exposure to the sensor. Of course, the equilibrium sensing mode is preferred in cases where the sample concentrations do not wish to be altered.

While the analyte is consumed during the exhaustive sensing process, the remaining analyte concentration should still be at equilibrium with the sensor. For the exhaustive mode to be valid, the remaining analyte concentration must be negligible compared to the initial concentration. Based on mass balance and partition equilibria of the analyte, a theoretical consideration is proposed here for exhaustive sensors based on absorbance measurement.

According to the law of mass conservation for an analyte ion with a charge of  $z + (M^{z+})$ , the following relationship should generally apply:

$$n_{M^{s,*}}^{tot} = n_{M^{s,*}}^{aq} + n_{M^{s,*}}^{ns} \tag{5.1}$$

where  $n_{M^{z^+}}^{tot}$ ,  $n_{M^{z^+}}^{aq}$ , and  $n_{M^{z^+}}^{ns}$  are the number of moles of  $M^{z^+}$  in the system, remaining in the aqueous phase, and in the nanospheres, respectively. This relationship may be reformulated on the basis of analytical concentrations,  $c_{M}$ , and volumes of the respective phases:

$$c_{M^{z}}^{tot}, V_{tot} = c_{M^{z}}^{aq}, V_{aq} + c_{M^{z}}^{ns}, V_{ns}$$
(5.2)

In the absence of interference, the total concentration of extracted metal ions in the nanospheres is expected to obey established ion-exchange equilibria. Specifically, for a nanosphere containing an electrically neutral hydrogen ion-selective chromoionophore, Ind, a neutral ionophore selective for  $M^{z+}$ , L, forming complexes of the type  $ML_p$  with a complex stoichiometry of p, and a lipophilic ion-exchanger,  $R^z$ , one may formulate the ion-exchange equilibrium constant,  $K_{ex}$ , between hydrogen ions and  $M^{z+}$  as:

$$K_{ex} = \frac{[ML_p^{z_+}]}{a_{M^{z_+}}^{aq}[L]^p} \left( \frac{a_{H^+}^{aq}[Ind]}{[IndH^+]} \right)^z$$
 (5.3)

where concentrations (strictly, activities) in the nanosphere phase are shown in square brackets. Inserting the charge balance condition,  $c_{R^-}^{ns} = p[ML_p^{z+}] + [IndH^+]$ , and the mass balance equations for the ionophore,  $c_L^{ns} = [L] + p[ML_p^{z+}]$ , and chromoionophore,  $c_{R^-}^{ns} = [Ind] + [HInd^+]$ ), one obtains in analogy to earlier work: <sup>6,27-29</sup>

$$a_{M^{z^{+}}}^{aq} = \left(\frac{a_{H^{+}}^{aq}}{[IndH^{+}]}\right)^{z} \frac{(c_{Ind}^{ns} - [IndH^{+}])^{z+1}}{zK_{ex}((p/z)\{c_{R}^{ns} - [IndH^{+}]\} + c_{L}^{ns})^{p}}$$
(5.4)

In the absence of ion complexation in the aqueous phase, the ion activity of  $M^{z+}$  is related to the analytical concentration by the activity coefficient,  $a^{aq}_{M^{z+}} = g^{aq}_{M^{z+}} c^{aq}_{M^{z+}}$ . This relationship is now used to insert Eqn. 5.4 into Eqn. 5.2. Similarly,  $c^{ns}_{M^{z+}} = [ML_p^{z+}]$  if no other analyte species are considered in the nanoparticle phase, and, together with the charge balance condition shown above, inserted into Eqn. 5.2. This provides for an implicit equation (see Eqn. S5.1 in Supporting Information) that relates the initial metal ion concentration with the concentration of unprotonated indicator dye. The latter defines the optical readout of the assay, which in absorbance mode is through Beer's law. In the case of a charged ionophore, such as DNNS for protamine, a slightly different treatment is required (See Eqns S5.2 to S5.5 in Supporting Information).

Figure 5.2 shows the comparison of the optical response curves for classical optode theory in the absence (Eqn. 5.4) and presence (see Eqn. S5.1 in Supporting Information) of analyte loss by extraction into the nanospheres for two different pH values. The pH cross-response always observed with such ion-exchanger optodes disappears when the sensor operates in an exhaustive mode, with an associated steeper slope of the calibration curves, signaling a more sensitive assay.

When a nanosphere suspension operates exhaustively, one is better served to plot the optical response as a function of the linear sample concentration, rather than its logarithmic value. Figure 5.3 demonstrates the influence of pH for exhaustive nanosensor suspensions. As the pH decreases, the linear calibration range is shortened to lower concentrations, transitioning gradually to classical optode response behavior.

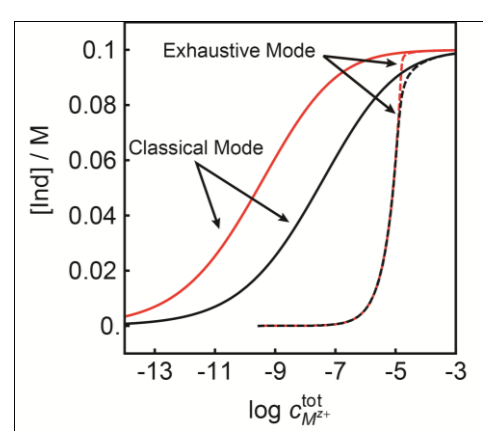


Figure 5.2. Comparison of the theoretical optode responses operating under classical equilibrium mode and exhaustive mode at pH 7 (red trace) and pH 8 (black trace). Parameters:  $K_{ex} = 10^{-4}$ ,  $V_{ns} = 0.001$  mL,  $V_{aq} = 3$  mL, p = 3,  $\gamma_{M^{crt}}^{aq} = 0.8$ ,  $c_R^{ns} = 0.1$  M,  $c_L^{ns} = 0.3$  M,  $c_{Ind}^{ns} = 0.1$  M,  $c_L^{ns} = 0.3$  M,  $c_{Ind}^{ns} = 0.1$  M,  $c_L^{ns} = 0.3$  M,  $c_L^{$ 

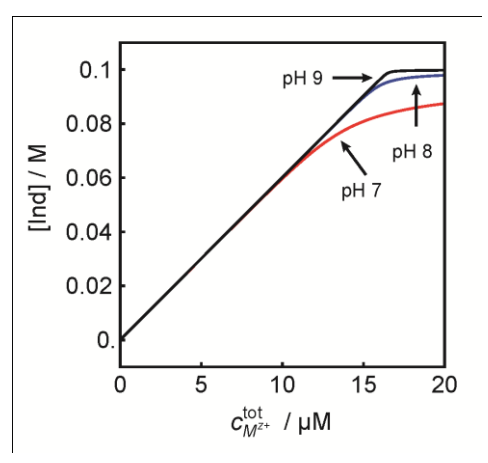


Figure 5.3. Effect of pH (as indicated) for the theoretical optode responses operating under exhaustive mode. Parameters:  $K_{ex} = 10^{-4}$ ,  $V_{ns} = 0.001$  mL,  $V_{aq} = 3$  mL, p = 3,  $\gamma_{M^{2+}}^{(aq)} = 0.8$ ,  $C_R^{ns} = 0.1$  M,  $C_{hnd}^{ns} = 0.3$  M,  $C_{hnd}^{ns} = 0.1$ M, z = 2.

In order to allow for exhaustive sensing, the sensor should have a relative low detection limit to be of practical relevance: the detection limit in equilibrium mode must be lower than the concentration at which one wishes to achieve exhaustive sensing. The low detection of ion selective optodes can be achieved in various ways according to theory. For example, one could utilize ionophores that form highly stable complexes with the analyte, resulting in larger values of  $K_{\rm ex}$  in Eqn. 5.3. A larger complex formation constant will shift the extraction competition in favor of the analyte ion.

Early on, ion selective optodes had been constructed as polymeric films cast onto a solid support. In recent years, however, ion selective bulk optodes have been miniaturized in various ways to form microspheres or nanospheres. The miniaturized sensors allow for ion sensing in untrasmall spaces and have enabled intracellular applications. Moreover, the response time of the micro/nanosensors is found to be much shorter than film based bulk optodes because of the reduced sensor dimensions. On the other hand, however, turbid and highly scattering samples could make the quantification of the analyte in absorbance mode more problematic compared with film based optodes.

The nanosensors used in this work were prepared by a precipitation method (see experimental section for detailed procedure). Nanosensors for oxygen and other metal ions have been reported using similar precipitation procedures.<sup>36</sup> The sensor preparation is simple and convenient and the nanospheres produced exhibited a high thermal stability.

While the first example for an exhaustive nanosensor suspension was demonstrated using calcium selective nanospheres<sup>20</sup>, the sensing principle is here extended to protamine, a polycation. To make the calcium selective exhaustive nanosensors, Calcium ionophore IV was used owing to the high complex formation constant between Calcium ionophore IV and calcium ion.<sup>29,37</sup> This helps to lower the detection limit of the sensors. As shown in Figure 5.4a, calcium selective nanosensors operating under exhaustive mode exhibited a linear range from 0 to 10 µM, covering the intracellular free calcium levels.

Protamine is a difficult but nevertheless important analytical target. <sup>38,39</sup> Similar to the calcium ionophore, DNNS has been reported to form a stable complex with protamine and is a promising candidate for the exhaustive detection of protamine. <sup>31,40</sup> DNNS and a newly introduced near-infrared chromoionophore (ox blue) were embedded in the nanosphere core made of DOS and F127. <sup>26</sup> Here, DNNS acts as both ion exchanger and ionophore for protamine. The detection of protamine is also based on the ion exchange principle. When protamine is extracted by DNNS, ox blue, initially in the protonated state, will deprotonate to release H<sup>+</sup> into the aqueous phase. The acid-base reaction of ox blue is shown in Figure 5.1 (b). Upon protonation, the ring opened form of ox blue exhibited strong absorbance centered around 641

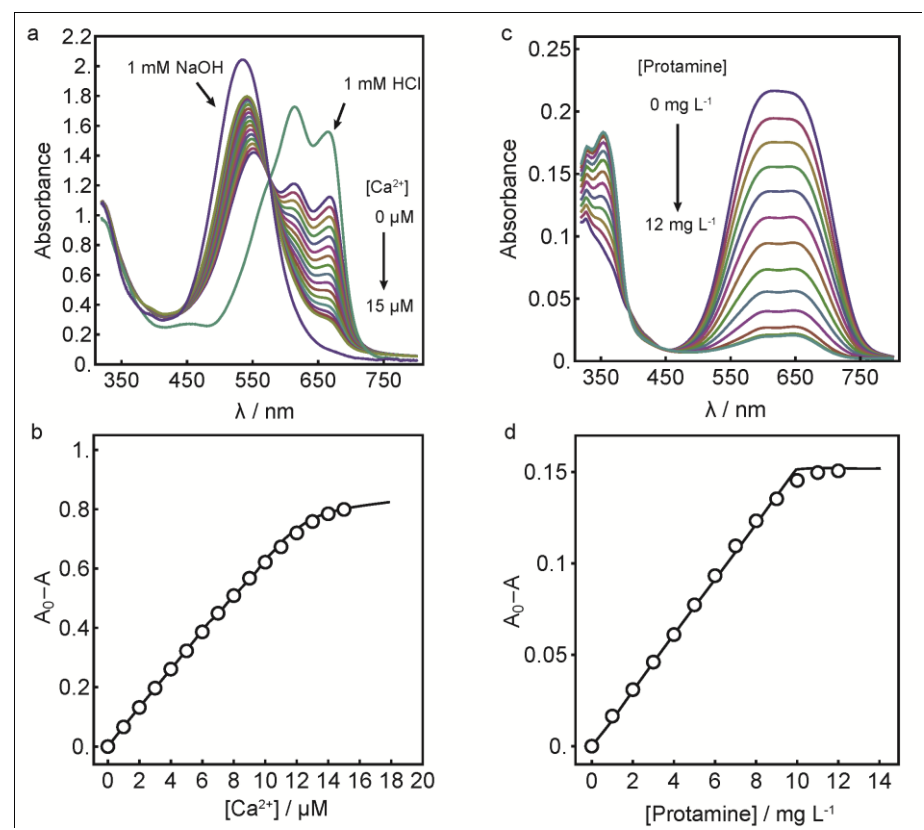


**Figure 5.4.** (a) Absorption spectra of Ca<sup>2+</sup> selective exhaustive nanosensors in response to various Ca<sup>2+</sup> concentrations.

Background: 10 mM tris-HCl buffer, pH 7.4; (b) Calibration curve for the Ca<sup>2+</sup> nanosensors using the absorbance difference at 663 nm fit with theoretical curve; (c) Absorption spectra of protamine exhaustive selective nanosensors in response to various protamine levels. Background: 10 mM tris-HCl buffer and 0.1 M NaCl, 7.4; (d) Calibration curve for the protamine nanosensors using absorbance difference 641 nm, fit with Eqn. S5.5.

nm and resulted in deep blue color. As the protamine concentration in the sample increased, protons were exchanged out from the nanospheres and the ox blue gradually became deprotonated and resulted in the decrease in maximum absorption around 641 nm (See Figure 5.4 (c)).

One of the advantages of exhaustive detection is that the response range can be tuned by adjusting the nanosphere loading (i.e., amount of sensing material).<sup>20</sup> Moreover, the sensitivity is dramatically improved relative to classical optode theory, with the highest improvement expected for higher analyte charge. As shown in Figure 5.4 (c) and 5.4 (d), the protamine nanosensors exhibited very high sensitivity for

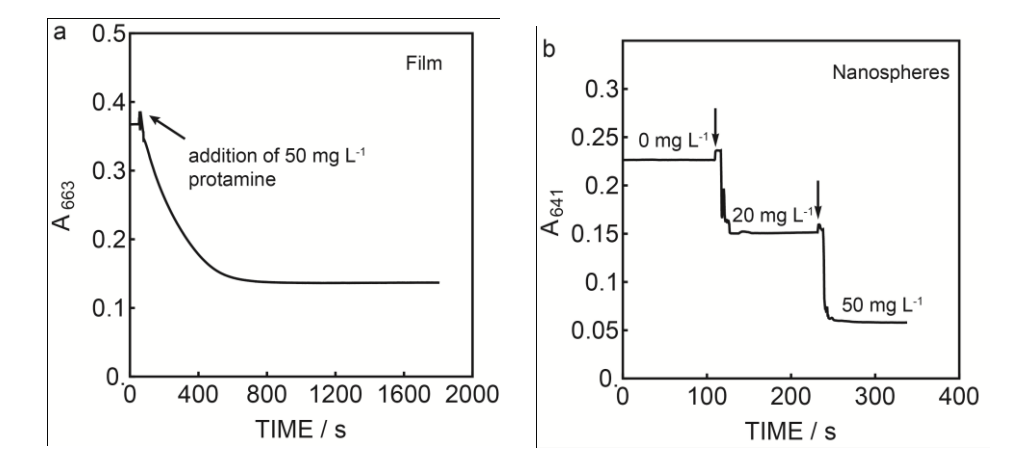


**Figure 5.5.** (a) Protamine response (absorbance at 663 nm) for a PVC-DOS membrane containing Chromoionophore I and DNNS upon addition of 50 mg L-1 of protamine. (b) Protamine selective nanosensors response upon addition of different levels of protamine as indicated. Spikes indicate the addition and mixing of the sample.

protamine even in the presence of 0.1 M NaCl as background electrolyte. A high sensitivity is preferred for protamine-heparin titration. If the loading of the nanosensor was increased, the response range became wider. As shown in Figure S5.1, by adjusting the nanosensor concentration, calibration that covers the physiological range was achieved. One the other hand, at high concentrations, the nanosensors became progressively saturated, resulting in a deviation from linearity (compare to theoretical behavior in Figure 5.3 above). The loading of the nanosensors can be monitored by the absorbance of the nanosphere suspension or by calculating the amount of materials used (ox blue or DNNS).

The response time of film based optodes can be quite long, which is particularly true for polyions such as protamine since the diffusion in the organic sensing phase can be quite slow.<sup>22,23</sup> Previous film-based optical sensors for protamine based on similar principles have been reported, and indeed the response times were too long to obtain an equilibrium signal.<sup>22,23</sup> While for the nanosensors reported here, the response is expected to be much faster due to the small size of the nanospheres. Figure 5.5(a) demonstrates that the response time for a PVC-DOS membrane (of ca. 10 µm thickness) based sensor was indeed very long, whereas the nanosensors responded to protamine almost instantaneously. The exact response time is difficult to infer here since the response time appears to be limited by the speed of mixing the nanoparticle suspension.

As an early application of the exhaustive sensing mode, we explored the calcium selective nanosensors to determine the total calcium concentration in human plasma. Since the selectivity of the calcium selective nanospheres was confirmed to be satisfactory (Figure S5.2), other cations in the plasma sample, such as Na<sup>+</sup>, should not cause significant interference.<sup>20</sup>

Calcium ions exist in blood plasma in two main forms: free calcium ions and bound calcium (such as those bound to proteins (mainly albumin) and phosphate). Therefore, the total calcium level in plasma cannot be accessed without freeing the bound calcium. Traditional total plasma calcium measurement requires pretreatment of the plasma sample under harsh conditions (HNO<sub>3</sub> and H<sub>2</sub>O<sub>2</sub>) followed by neutralization before analysis (for example by EDTA titration). The entire protocol is time consuming. For the calcium selective nanosensors, the total calcium in plasma can be accessed without any pretreatment since the nanospheres have very high affinity for  $Ca^{2+}$ . Given that the binding affinity for common calcium binding proteins (e.g.,  $K\sim10^7$  for calmodulin)<sup>42</sup> is much smaller than that for the ionophore ( $K\sim10^{15}$  to  $10^{25}$ ),<sup>29</sup> the consumption of bound  $Ca^{2+}$  can be regarded as complete. The total calcium concentration in a human

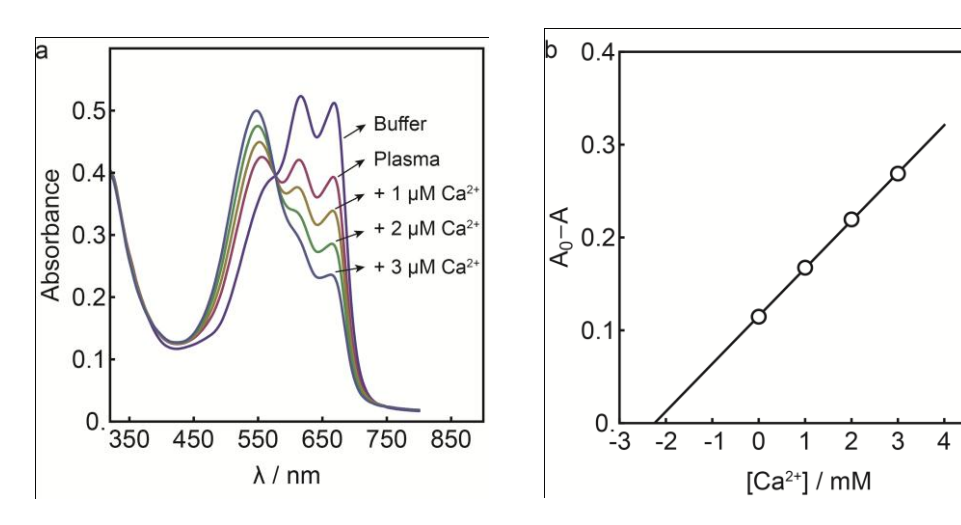


**Figure 5.6.** Determining total calcium level in human blood plasma by the Ca<sup>2+</sup> selective nanosensors in exhaustive mode. (a) Absorption spectra for the nanosensor suspension in 10 mM pH 7.4 Tris-HCl buffer with plasma and known additional CaCl<sub>2</sub>. (b) Calibration line used to determine the Ca<sup>2+</sup> concentration. The total calcium level is found by the intercept on the x-axis.

5

blood plasma sample was determined to be 2.2 mM using standard addition calibration (Figure 5.6) using the exhaustive nanosensors, which is within the normal human total plasma calcium range (2.0-2.6 mM).<sup>41</sup> The total calcium level was found to be 2.1 ±0.1 mM by EDTA titration, which confirmed the viability of the nanosensor based measurement. In addition, the response was observed to be instantaneous, indicating that no kinetic limitation during the release of bound calcium is present during the measurement.

Assessment of protamine in blood or plasma is also of great biological and medical importance since protamine is routinely used to determine heparin levels in blood samples by titration.<sup>21,43</sup> Here, the nanosensors for protamine were also used to measure the protamine levels in human blood plasma. However, we noted that the plasma sample without added protamine caused a spontaneous deprotonation of the chromoionophore as well. In the beginning, this led us to question the stability of the nanospheres in the plasma. However, later the same effect was observed with a PVC-DOS film based sensor for protamine containing Chromoionophore I and DNNS (data not shown), pointing instead to an insufficient selectivity or stability of the sensing components in the plasma. Research to determine and remove this limitation is currently continuing in our group.

### 5.4 Conclusion

In conclusion, ionophore based nanosensors for calcium and protamine operating in an exhaustive sensing mode is presented here. A theory for the exhaustive detection mode was developed. The exhaustive nanosensors showed a rapid response, tunable detection range and high stability. Total calcium in human blood plasma was successfully assessed with the Ca<sup>2+</sup> selective nanosensors in an exhaustive mode.

## 5.5 Supporting Information for Chapter 5

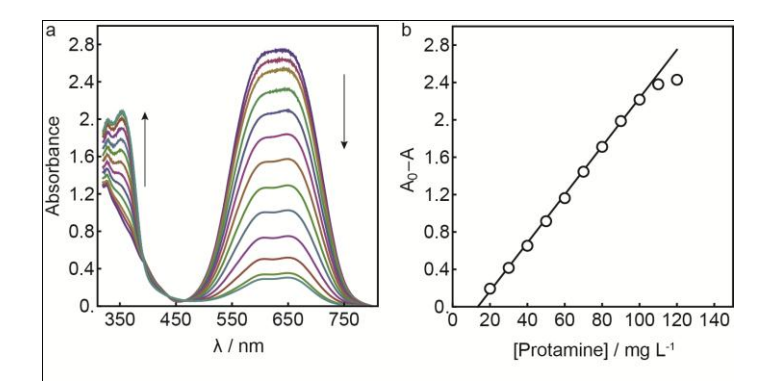


**Figure S5.1.** (a) Absorption spectra of protamine selective exhaustive nanosensors in response to various protamine levels. Background: 10 mM Tris-HCl buffer and 0.1 M NaCl, pH 7.4; (b) Calibration curve for the protamine nanosensors using the absorbance difference at 641 nm.

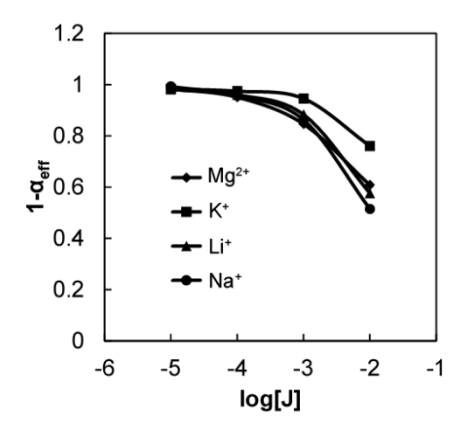


**Figure S5.2.** Selectivity of the  $Ca^{2+}$ -selective nanooptodes in 10 mM pH 7.4 Tris-HCl buffer measured in absorbance mode.  $1-\alpha_{eff}$  is calculated by A/A<sub>0</sub> where A<sub>0</sub> is the absorbance intensity at 663 nm measured in 10 mM pH 7.4 Tris-HCl buffer solution.

Eqn. S5.1 shows the theoretical response function for neutral ionophore based optodes operating in exhaustive mode.

$$c_{M^{z+}}^{tot} = \frac{\gamma_{M^{z+}}^{aq} K_{ex} V_{ns} (\frac{[IndH^{+}]p - c_{R}^{ns} p + z c_{L}^{ns}}{z})^{p}}{\gamma_{M^{z+}}^{aq} K_{ex} z (V_{aq} + V_{ns})}$$

$$- \frac{([IndH^{+}] - c_{R}^{ns}) (\frac{[IndH^{+}]p - c_{R}^{ns} p + z c_{L}^{ns}}{z})^{-p} ((\frac{a_{H^{+}}^{aq} ([c_{Ind}^{ns} - [IndH^{+}])}{[IndH^{+}]})^{z} V_{aq}}{\gamma_{M^{z+}}^{aq} K_{ex} z (V_{aq} + V_{ns})}$$
(Eqn. S5.1)

For electrically charged ionophore such as DNNS, the following equations apply. The exchange equilibrium is expressed with Eqn. S5.2, where  $[IndH^+ \bullet L]$  is the concentration of protonated chromoionophore –DNNS ion pair in the nanosphere phase and  $[prot \bullet L_z]$  is the the concentration of protamine –DNNS complex in the nanosphere phase.

$$K_{ex}a_{prot}^{aq} = \left(\frac{a_{H^{+}}^{aq}[Ind]}{[IndH^{+} \bullet L]}\right)^{z}[prot \bullet L_{z}]$$
 (Eqn. S5.2)

The mass balance equations for DNNS and chromoionophore are expressed in Eqn. S5.3 and Eqn. S5.4.

$$c_L^{ns} = z[prot \bullet L_z] + [IndH^+ \bullet L]$$
 (Eqn. S5.3)

The mass balance chromoionophore and DNNS are listed in Eqn. S5.4 and Eqn S5.5.

$$c_{Ind}^{ns} = [Ind] + [IndH^+ \bullet L]$$
 (Eqn. S5.4)

From Eqn. S5.2, Eqn. S5.3 and Eqn S5.4, one can derive the response function shown in Eqn. S5.5 for the protamine selective exhaustive optodes containing a neutral chromoionophore and an electrically charged ionophore DNNS.

$$c_{prot}^{tot} = \frac{([Ind] - c_{Ind}^{ns} + c_{L}^{ns})((\frac{a_{H^{+}}^{aq}[Ind]}{c_{Ind}^{ns} - [Ind]})^{z} V_{aq} + \gamma K_{ex} V_{ns})}{K_{ex} \gamma (V_{aq} + V_{ns}) z}$$
(Eqn. S5.5)

The following parameters were used to fit the data shown in Figure 5.4 (d):

$$K_{ex} = 10^{-53}$$
,  $V_{ns} = 0.0063$  mL,  $V_{aa} = 3$  mL,  $a_{H^+}^{aq} = 10^{-7.4}$  M,  $c_{Ind}^{ns} = 0.1$  M,  $c_{L}^{ns} = 0.1$  M,  $\gamma = 0.8$ ,  $\gamma = 0$ 

# 5.6 References for Chapter 5

- (1) Burns, A.; Sengupta, P.; Zedayko, T.; Baird, B.; Wiesner, U. Small 2006, 2, 723.
- (2) Jokic, T.; Borisov, S. M.; Saf, R.; Nielsen, D. A.; Kühl, M.; Klimant, I. Anal. Chem. 2012, 84, 6723.
- (3) Telting-Diaz, M.; Bakker, E. Anal. Chem. 2002, 74, 5251.
- (4) Aragay, G.; Pons, J.; Merko q, A. Chem. Rev. 2011, 111, 3433.
- (5) Liebsch, G.; Klimant, I.; Krause, C.; Wolfbeis, O. S. Anal. Chem. 2001, 73, 4354.
- (6) Bakker, E.; Bühlmann, P.; Pretsch, E. Chem. Rev. 1997, 97, 3083.
- (7) Dubach, J. M.; Harjes, D. I.; Clark, H. A. J. Am. Chem. Soc. 2007, 129, 8418.
- (8) Kim, S. B.; Cho, H. C.; Cha, G. S.; Nam, H. Anal. Chem. 1998, 70, 4860.
- (9) Morf, W. E.; Seiler, K.; Rusterholz, B.; Simon, W. Anal. Chem. 1990, 62, 738.
- (10) Komatsu, H.; Miki, T.; Citterio, D.; Kubota, T.; Shindo, Y.; Kitamura, Y.; Oka, K.; Suzuki, K. J. Am. Chem. Soc. 2005, 127, 10798.
- (11) Zeng, L.; Miller, E. W.; Pralle, A.; Isacoff, E. Y.; Chang, C. J. J. Am. Chem. Soc. 2006, 128, 10.
- (12) Xie, X.; Qin, Y. Sens. Actuators, B 2011, 156, 213.
- (13) Kurihara, K.; Ohtsu, M.; Yoshida, T.; Abe, T.; Hisamoto, H.; Suzuki, K. Anal. Chem. 1999, 71, 3558.
- (14) Xie, X.; Mistlberger, G.; Bakker, E. J. Am. Chem. Soc. 2012, 134, 16929.
- (15) Xie, X.; Pawlak, M.; Tercier-Waeber, M.-L.; Bakker, E. Anal. Chem. 2012, 84, 3163.
- (16) Barker, S. L. R.; Shortreed, M. R.; Kopelman, R. Anal. Chem. 1997, 69, 990.
- (17) Badr, I. H. A.; Johnson, R. D.; Diaz, M.; Hawthorne, M. F.; Bachas, L. G. Anal. Chem. 2000, 72, 4249.
- (18) Zhou, X.; Su, F.; Tian, Y.; Youngbull, C.; Johnson, R. H.; Meldrum, D. R. J. Am. Chem. Soc. 2011, 133, 18530.
- (19) Farruggia, G.; Iotti, S.; Prodi, L.; Montalti, M.; Zaccheroni, N.; Savage, P. B.; Trapani, V.; Sale, P.; Wolf, F. I. J. Am. Chem. Soc. 2006, 128, 344.
- (20) Xie, X.; Zhai, J.; Bakker, E. Anal. Chem. 2014, 86, 2853.
- (21) Ramamurthy, N.; Baliga, N.; Wahr, J. A.; Schaller, U.; Yang, V. C.; Meyerhoff, M. E. Clin. Chem. 1998, 44, 606.
- (22) Dai, S.; Ye, Q.; Wang, E.; Meyerhoff, M. E. Anal. Chem. 2000, 72, 3142.

- (23) Kim, S. B.; Kang, T. Y.; Cho, H. C.; Choi, M. H.; Cha, G. S.; Nam, H. Anal. Chim. Acta 2001, 439, 47.
- (24) Xie, X.; Mistlberger, G.; Bakker, E. Anal. Chem. 2013, 85, 9932.
- (25) Borisov, S. M.; Mayr, T.; Mistlberger, G.; Waich, K.; Koren, K.; Chojnacki, P.; Klimant, I. Talanta 2009, 79, 1322.
- (26) Mistlberger, G.; Xie, X.; Pawlak, M.; Crespo, G. A.; Bakker, E. Anal. Chem. 2013, 85, 2983.
- (27) Antico, E.; Lerchi, M.; Rusterholz, B.; Achermann, N.; Badertscher, M.; Valiente, M.; Pretsch, E. *Anal. Chim. Acta* **1999**, *388*, 327.
- (28) Perera, H.; Shvarev, A. Anal. Chem. 2008, 80, 7870.
- (29) Qin, Y.; Mi, Y.; Bakker, E. Anal. Chim. Acta 2000, 421, 207.
- (30) Si, D.; Epstein, T.; Lee, Y.-E. K.; Kopelman, R. Anal. Chem. 2012, 84, 978.
- (31) Bell-Vlasov, A. K.; Zajda, J.; Eldourghamy, A.; Malinowska, E.; Meyerhoff, M. E. Anal. Chem. 2014, 86, 4041.
- (32) Xie, X.; Crespo, G. A.; Zhai, J.; Szil ágyi, I.; Bakker, E. Chem. Commun. 2014, 50, 4592.
- (33) Dubach, J. M.; Das, S.; Rosenzweig, A.; Clark, H. A. PNAS 2009, 106, 16145.
- (34) Brasuel, M.; Kopelman, R.; Miller, T. J.; Tjalkens, R.; Philbert, M. A. Anal. Chem. 2001, 73, 2221.
- (35) Brasuel, M.; Kopelman, R.; Miller, T. J.; Tjalkens, R.; Philbert, M. A. Anal. Chem. 2001, 73, 2221.
- (36) Mistlberger, G.; Koren, K.; Scheucher, E.; Aigner, D.; Borisov, S. M.; Zankel, A.; Pölt, P.; Klimant, I. *Adv. Funct. Mater.* **2010**, 20, 1842.
- (37) Qin, Y.; Peper, S.; Radu, A.; Ceresa, A.; Bakker, E. Anal. Chem. 2003, 75, 3038.
- (38) Reynolds, F.; Weissleder, R.; Josephson, L. Bioconjugate Chem. 2005, 16, 1240.
- (39) Meyerhoff, M. E.; Yang, V. C.; Wahr, J. A.; Lee, L. M.; Yun, J. H.; Fu, B.; Bakker, E. Clin. Chem. 1995, 41, 1355.
- (40) Yuan, Y.; Amemiya, S. Anal. Chem. 2004, 76, 6877.
- (41) Marshall, W. J.; Bangert, S. Clinical Chemistry, 5th Edition; Mosby, 2004.
- (42) Alberts, B.; Johnson, A.; Lewis, J.; Raff, M.; Roberts, K.; Walter, P. In *Molecular Biology of the Cell*; 5 ed.; Garland Science, Taylor&Francis Groups, LLC: 2007.
- (43) Shvarev, A.; Bakker, E. J. Am. Chem. Soc. 2003, 125, 11192.

# Chapter 6. Potentiometric Response from Ion-Selective Nanospheres with Voltage-Sensitive Dyes

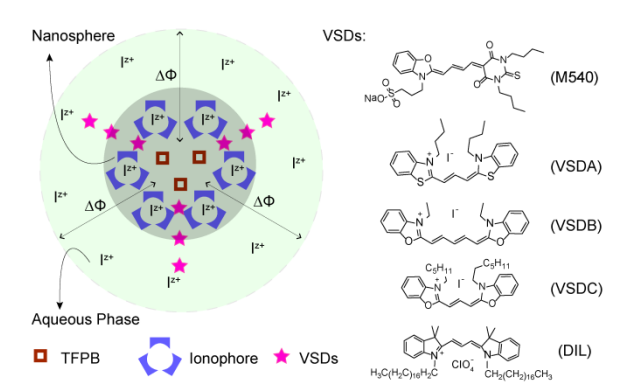
This work has been published in: Xiaojiang Xie, Jingying Zhai, and Eric Bakker\*, J. Am. Chem. Soc., 2014, 136, 16465–16468

Potentiometry is a well-established electrochemical technique that has been extensively studied since the last century. <sup>1,2</sup> Ionophore-based ion-selective electrodes (ISEs) have been widely applied in clinical and environmental monitoring during the past few decades. Ion receptors (ionophores) and ion exchangers are embedded in water immiscible materials, forming a permselective sensing membrane. The phase boundary potential difference ( $\Delta\phi$ ), also referred to as the Nernst potential difference, between the aqueous sample and the sensing membrane is related to the analyte ion activity according to the Nernst equation. For ISEs,  $\Delta\phi$  is measured as an electromotive force with a high input impedance interface at zero current and relative to a reference electrode.

Miniaturization of ISEs holds great promises for a number of cutting-edge applications such as lab-on-a-chip, scanning electrochemical microscopy and in vivo and intracellular monitoring as well as chemical imaging. <sup>3-8</sup> Microfabrication technologies have entered the field of potentiometry to reduce the size of ISEs down to micrometers and even hundreds of nanometers. Microelectrodes have been designed to monitor the ion activity in cells such as for H<sup>+</sup> and Li<sup>+</sup>. <sup>9,10</sup> However, they do not provide information on spatial distribution from a single, unmoving electrode. Although they have been described in scanning probe microscopy<sup>11</sup>, ISEs are not yet able to image the ion distribution at the sub-micrometer scale. The intracellular imaging of ions is instead typically performed with fluorescent (bio)molecular probes and nanomaterials. <sup>12-16</sup>

Today, nanoparticles containing ionophore and ion exchangers can be prepared quite readily, but the direct measurement of  $\Delta\phi$  of individual nanoparticles using electrochemical equipment is not practical. Voltage-sensitive dyes (VSDs) have been previously used to perform membrane potential measurements in organelles and in cells that are too small for microelectrodes. <sup>10,17-20</sup> This work shows that  $\Delta\phi$  can be translated into optical signals by fluorescent VSDs, confirming that  $\Delta\phi$  does not vanish and the chemical principle for ionophore based ISEs is still valid even at the nanoscale, thereby establishing a new sensing platform.

The nanoparticles were composed of copolymer Pluronic F-127 and lipophilic plasticizer bis(2-ethylhexyl) sebacate (DOS). Driven by van der Waals forces, the lipophilic sensing components, ion-exchanger and ionophore, self-assembled into the lipophilic nanoparticle core. <sup>21-23</sup> The nanospheres produced in this way exhibited an average diameter of ca. 40 nm with excellent thermal stability in aqueous suspension (see Supporting Information for detailed preparation).



**Scheme 6.1.** Nernstian potential difference  $(\Delta\phi)$  established between the aqueous phase and the organic phase of ion selective nanosphere. Voltage sensitive dyes (VSDs) are able to indicate variations in  $\Delta\phi$  as the  $I^{z^+}$  activity in the aqueous phase changes. The free  $I^{z^+}$  concentration in the nanosphere remains constant owing to a fixed amount of ion-exchanger (TFPB) and ionophore. For detailed chemical structures see Fig. S6.1.

In analogy to bulk membrane based ISEs, we presume that an electrical potential difference,  $\Delta \phi$ , is established between the nanosphere interior and the surrounding aqueous phase.<sup>24,25</sup> At electrochemical equilibrium, the electrochemical potential for any target ion,  $I^{z+}$ , must be equal for both phases. One may therefore express  $\Delta \phi$  by Eqn. 6.1:

$$\Delta \phi = \Delta \phi_I^{0,aq \to org} + \frac{RT}{z_I F} \ln \frac{a_I(aq)}{a_I(org)}$$
(6.1)

where  $Df_I^{\theta,aq\to org}$  is the standard ion transfer potential of  $I^{z+}$ ,  $a_I(aq)$  and  $a_I(org)$  are the activities of the uncomplexed ion in the two phases, R is the ideal gas constant, T is the absolute temperature, and F is Faraday's constant.

In an ideally behaving ISE membrane,  $a_{\rm I}({\rm org})$  is constant and dictated by the ion-exchange properties and selectivity of the organic phase. In agreement with Eqn. 6.1,  $\Delta \phi$  increases with increasing ion activity  $a_{\rm I}$  in the aqueous solution in a Nernstian fashion.

Due to their amphipathic nature, VSDs will distribute in the aqueous phase, the organic nanospheric core and the interface, with each state contributing to the fluorescence signal (see Scheme 6.1). The fluorescence of the VSDs used here is sensitive to the polarity of the microenvironment while the Stark effect is negligible.<sup>20</sup> For instance, 3,3'-dibutylthiacarbocyanine iodide (VSDA) showed a much higher emission intensity in the organic plasticizer DOS than in water (Fig. S6.2).

As VSDs are ionic species, their distribution between the organic and aqueous phase is dictated by the electrical potential difference,  $\Delta\phi$ , imposed by Eqn. 6.1. When  $\Delta\phi$  changes, the VSDs will re-partition to adapt to the imposed  $\Delta\phi$  and cause a fluorescence signal change. This repartitioning of VSDs must have negligible influence on  $\Delta\phi$  for them to work as indicators. Indeed, the amount of VSD used here was much smaller than the other components to ensure that VSDs did not themselves influence the value of  $\Delta\phi$ .

VSDs have been explored to make macro-scale sensors for K<sup>+</sup>, but the relative signal change, response time and stability were not yet satisfactory.<sup>26,27</sup> Here, K<sup>+</sup> and Ca<sup>2+</sup> were chosen as model ions. Calcium ionophore IV and valinomycin were used as ionophores for Ca<sup>2+</sup> and K<sup>+</sup>, respectively. Several different VSDs were screened for nanoscale potentiometry, among which M540 and VSDA showed the most

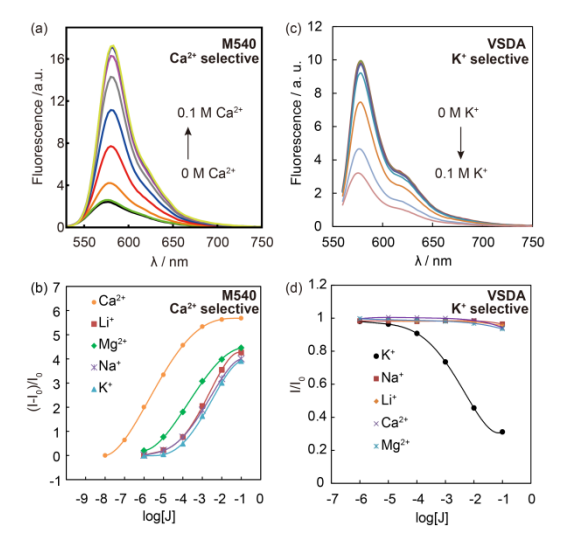


**Figure 6.1.** (a) Fluorescence spectra of the M540 containing Ca<sup>2+</sup> selective nanospheres with increasing CaCl<sub>2</sub> concentration. (b) Selective response of the M540 containing Ca<sup>2+</sup> selective nanospheres. (c) Fluorescence spectra of the VSDA containing K<sup>+</sup> selective nanosphere.

substantial signal change and were used as the dyes of choice for further experiments. Other VSDs exhibited relatively smaller fluorescence sensitivity but remained functional (Fig. S6.3 in Supporting Information). An optimization in the VSD-ionophore combination is necessary to obtain optimum response. Fig. 6.1 shows the fluorescence response of the potentiometric nanospheres to various analyte concentrations. With increasing (K<sup>+</sup> or Ca<sup>2+</sup>) concentration, the fluorescence intensity for M540 containing system increased (Fig. 6.1a, Fig. S6.4) while for the VSDA based system, a decrease in emission intensity was observed (Fig. 6.1c, Fig. S6.5). When used as probes for biological membrane potential, the fluorescence of VSDA is indeed known to decrease upon electric polarization, while for Merocyanine 540 (M540), the emission intensity increases.<sup>20,28</sup> This indicated that electric polarization occurred as the analyte concentration increased.<sup>20,28</sup> Nanospheres that contained no ion-exchanger TFPB, on the other hand, showed no response to analyte concentration changes, presumably owing to the lack of permselectivity as established by Karpfen and Randles and B thlmann et al.<sup>29,30</sup>

The incorporation of ionophores improved the selectivity of the nanospheres and lowered the detection limit. Nanospheres based on VSDA (Fig. 6.1d, Fig. S6.5) exhibited excellent selectivity similar to conventional ISEs and optodes. In the case of M540 (Fig. 6.1b, Fig. S6.4), the selectivity was inferior to that of conventional ISEs, possibly due to its anionic nature. The detection limit reached 10 nM for  $Ca^{2+}$  and 10  $\mu$ M for  $K^+$ . Fluorescence time traces for the  $Ca^{2+}$  selective nanospheres are shown in Fig. 6.2a, confirming that the signal is stable, the response time is reasonably rapid ( $t_{95\%}$  of ca. 3-s) and the nanosensor response is fully reversible. Without the use of ionophore, non-discriminative responses to different ions of the same charge were observed instead and the detection limit was much higher (Fig. S6.6).

VSDs not only distribute between the bulk phases but are known to also orient themselves at the interface, the extent of which depends on the local electric field and the effective Debye length.<sup>20</sup> Here, VSDA containing K<sup>+</sup> selective nanospheres were also evaluated in a constant background of either 10 mM HCl or 10 mM NaOH. As shown in Fig. 6.2b, the fluorescence responses under these different conditions were the same compared to those without added electrolyte. This confirms that the optical response is not due to a simple change in Debye length. We assume therefore that the mole fraction of VSDA at the very interface is much smaller than in the two bulk phases, likely owing to the larger thickness of the nanospheres compared to typical bilayer membranes. Moreover, the data demonstrates convincingly that these types of optodes behave largely independent of pH. Ionophore based optodes have suffered from pH cross response that limited their

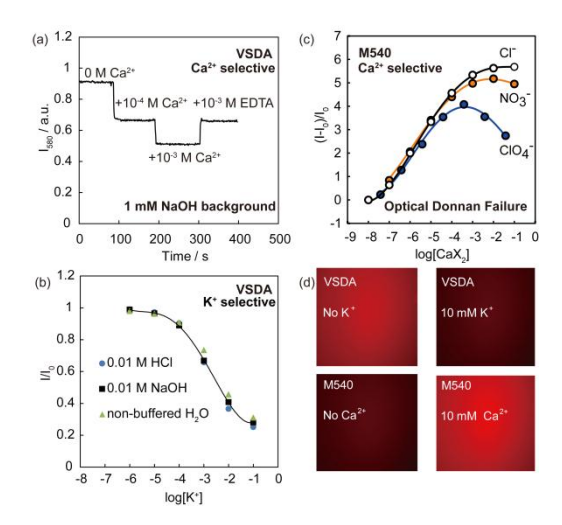


**Figure 6.2.** (a) Time trace of fluorescence signal of the VSDA containing  $Ca^{2+}$  selective nanospheres at 580 nm with gradual addition of  $CaCl_2$  and EDTA as indicated. (b) Response of the VSDA containing  $K^+$  selective nanospheres in 0.01 M HCl, 0.01 M NaOH, and non-buffered water. (c) Relative emission intensity change,  $(I-I_0)/I_0$ , as a function of  $CaX_2$  concentration for the M540 containing  $Ca^{2+}$ -selective nanospheres, with various anions X as indicated. (d) Fluorescence microscopic images of the VSDA containing  $K^+$  selective nanosphere suspension and M540 containing  $Ca^{2+}$  selective nanosphere suspension without and with 10 mM  $K^+/Ca^{2+}$  as background.

widespread application to a great extent.<sup>24,31</sup> This disadvantage appears to be overcome here by the use of fluorescent potentiometric nanospheres.

For cation-selective ISEs, the upper detection limit is a consequence of coextraction of primary cation and interfering anion from the aqueous phase into the organic phase.<sup>32-35</sup> This effect is loosely known as Donnan (exclusion) failure, although Donnan's experiment did not involve ionophores.<sup>36</sup> More lipophilic anions such as perchlorate are expected to cause more interference compared to less lipophilic anions such as chloride. An optical Donnan failure is observable. As shown in Fig. 6.2c, at high anion concentration, the M540-containing Ca<sup>2+</sup> selective nanospheres started to show anionic responses in complete analogy to electrochemical devices.<sup>37</sup> Perchlorate and nitrate caused a deviation at lower concentrations and exhibited a lower upper detection limit than chloride in agreement with the Hofmeister sequence.

VSDs are known to be compatible with fluorescence microscopy. Fig. 6.2d shows the fluorescence images of VSDA containing  $K^+$  selective nanosphere suspensions and M540 containing  $Ca^{2+}$  selective nanosphere suspensions. A clear contrast can be observed between nanospheres with and without addition of  $Ca^{2+}$  or  $K^+$ .

In the steepest region of the calibration curves, the slope for  $K^+$  is double the value for  $Ca^{2+}$ , which is again in agreement with the Nernst equation. The sigmoidal shape of the calibration curve is expected on the basis of the optical potential window, beyond which the VSD is fully contained in either phase. Earlier, some other VSDs have been used in reference ion free optodes for  $K^+$  and  $Cl^{-38,39}$  The sensor response had been simply explained by an extraction equilibrium, but we believe that the physical origin of the distribution process of VSDs is much better described with the interfacial potential difference, especially under experimental conditions where the ion concentrations in the organic phase are effectively not altered by the distribution changes of the VSD.

To summarize, the potentiometric response for neutral ionophore and ion-exchanger containing nanospheres has been investigated using VSDs to translate the Nernst potential difference into fluorescence readout. The results confirmed that even at this small scale, ion-selective electrode theory is still applicable. This work provides a new ion detection platform which is compatible with optical imaging equipment.

## 6.1 Supporting Information for Chapter 6

# 6.1.1 Experimental Section

**6.1.1.1 Reagents.** Pluronic<sup>®</sup> F-127 (F127), bis(2-ethylhexyl) sebacate (DOS), Ca<sup>2+</sup> ionophore IV, tetrahydrofuran (THF), methanol, ethylenediaminetetraacetic acid disodium salt dehydrate (EDTA), potassium tetrakis-[3,5-bis(trifluoromethyl)phenyl]borate (KTFPB), merocyanine 540 (M540), 3,3'-dibutylthiacarbocyanine iodide (VSDA), 3,3'-diethyloxadicarbocyanine iodide (VSDB), 3,3'-dihexyloxacarbocyanine iodide (VSDC) and 1,1'-dioctadecyl-3,3,3',3'-tetramethylindocarbocyanine perchlorate (DIL) were obtained from Sigma-Aldrich. All solutions were prepared by dissolving appropriate salts into deionized water (Mili-Q). All salts used were analytical grade or better.

**6.1.1.2 Nanosphere Preparation.** The Ca<sup>2+</sup>-selective nanospheres were prepared by dissolving 0.3 mg of NaTFPB, 0.008 mg of VSDs, 8 mg of DOS, 4.5 mg of F127, and 1.2 mg of calcium ionophore IV in 3.0 mL of methanol to form a homogeneous solution. 0.2 mL of this solution was pipetted and injected into 4.5 mL of deionized water on a vortex with a spinning speed of 1000 r/min. The resulting clear mixture was blown with compressed air on the surface for 20 min to remove methanol, giving a clear particle suspension. The K<sup>+</sup>-sensitive nanospheres were prepared with the same procedure from a methanol (3 mL) cocktail containing 0.5 mg of KTFPB, 0.01 mg of VSDs, 8.0 mg of DOS, 4.5 mg of F127, and 2 mg of valinomycin.

**6.1.1.3 Instrumentation and Measurement.** The size of the nanospheres was measured with the particle size analyzer Zetasizer Nano ZS (Malvern Inc.). Fluorescence responses of the nanospheres were measured with a fluorescence spectrometer (Fluorolog3, Horiba Jobin Yvon) using disposable poly(methyl methacrylate) cuvettes with path length of 1 cm as sample container. Excitation wavelength was chosen as follows: 510 nm (M540), 550 nm (VSDA), 550 nm (VSDB), 460 nm (VSDC) and 520 nm (DIL). Desired analyte concentration in the nanosphere suspension was achieved by addition of calculated mount of stock solutions or solid. To characterize the response time (Fig. 6.2a), excitation wavelength was fixed at 550 nm while the emission at 580 nm was recorded overtime. The microscopic images (Fig. 6.2d) were obtained on an inverted fluorescence microscope (ECLIPSE Ti-E, Nikon) through a standard Texas Red filter cube (excitation 542 nm – 582 nm, emission: 604 nm – 644 nm).

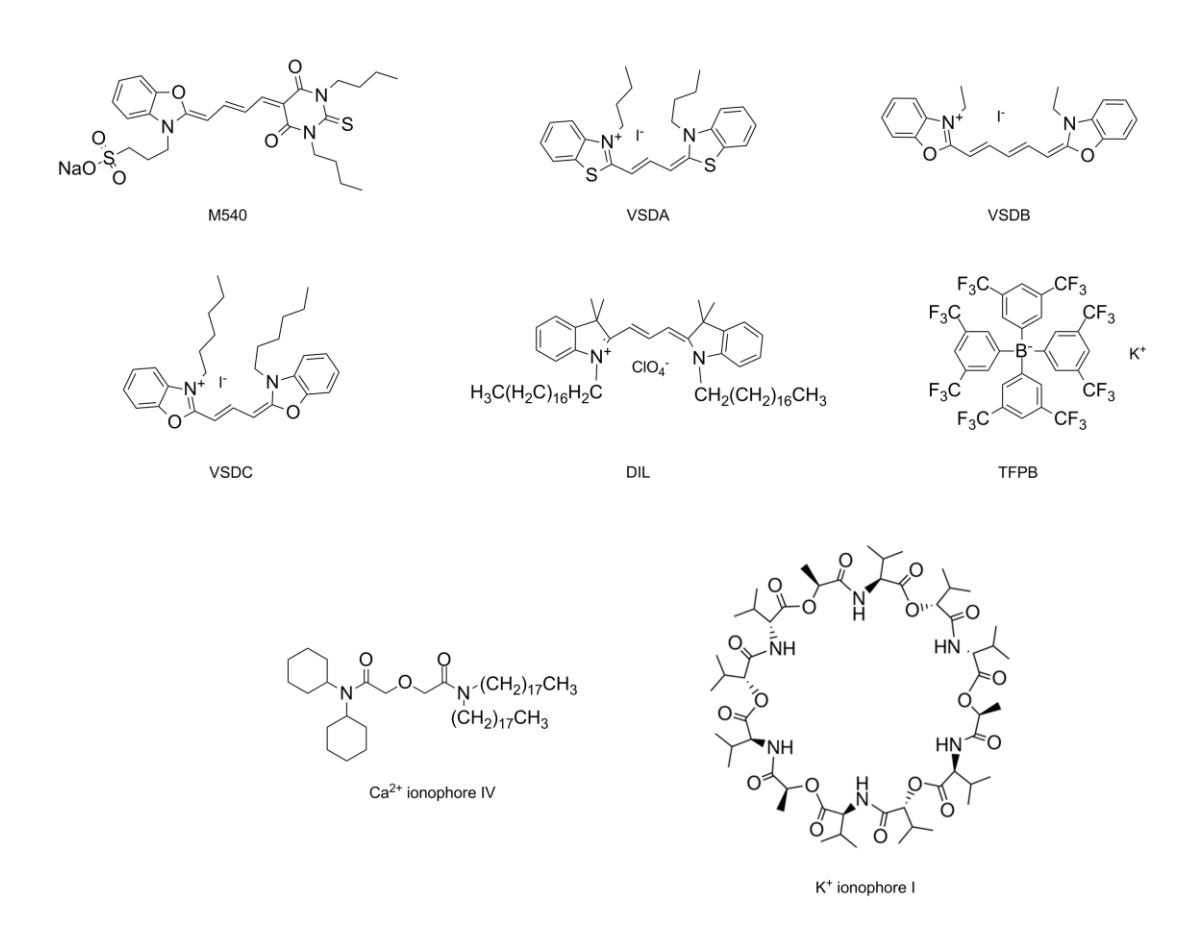
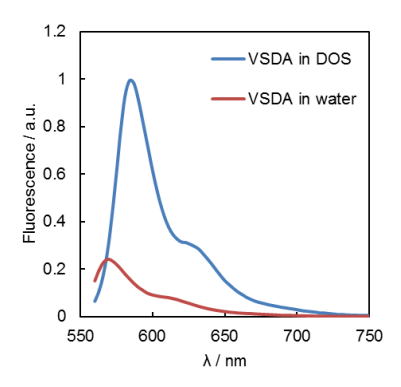


Figure S6.1. Chemical structures and abbreviations of VSDs, ionophores and ion exchanger used in this work.



**Figure S6.2.** Fluorescence spectra of 10 μM of VSDA in H<sub>2</sub>O and in DOS.

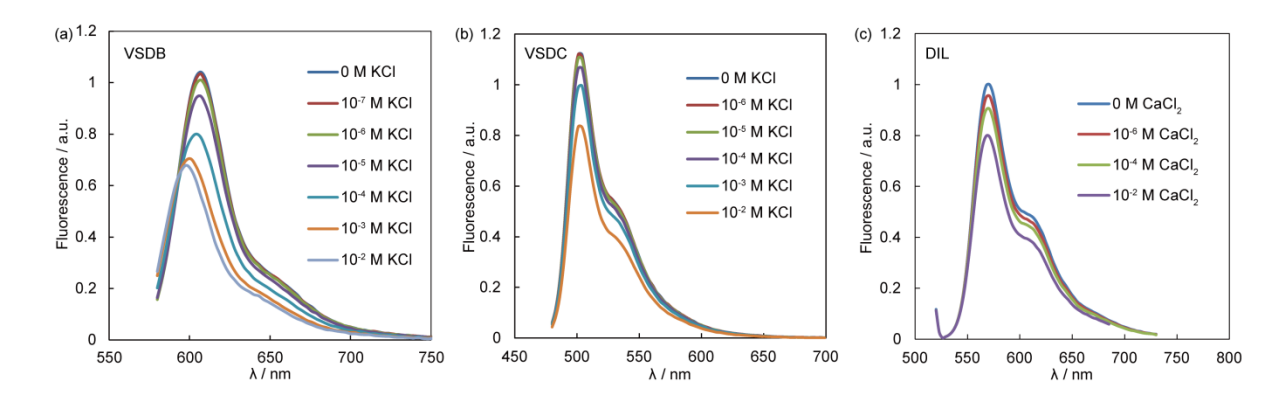
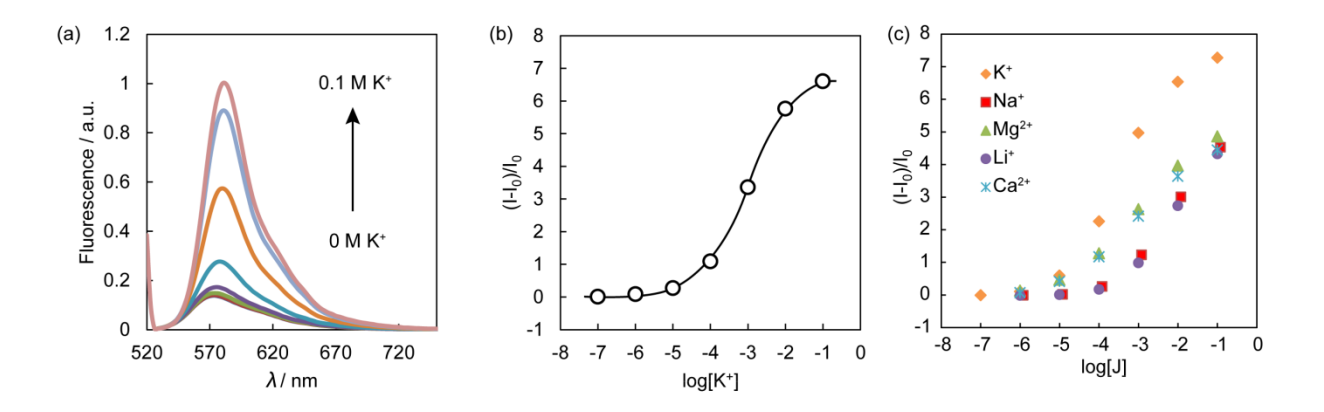
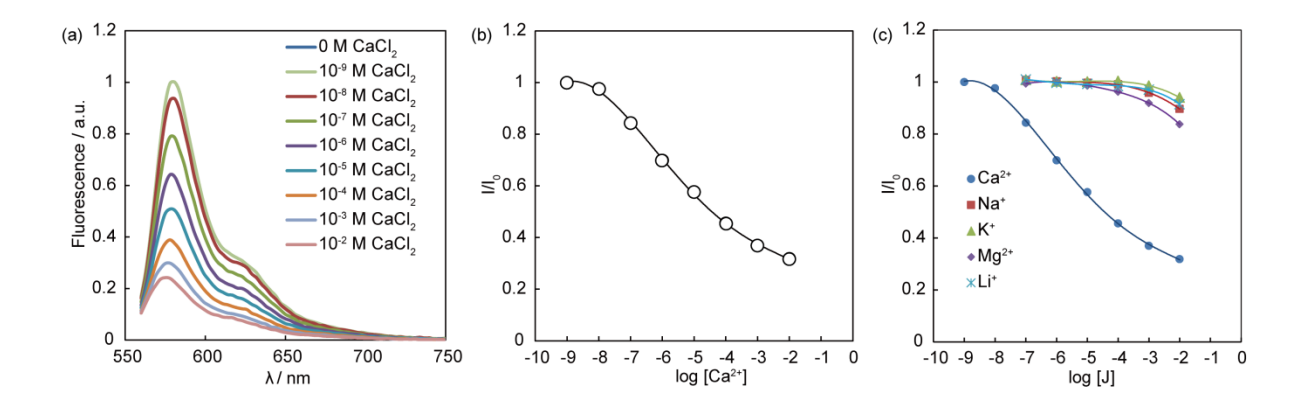


Figure S6.3. Emission spectra for  $K^+$  selective nanospheres containing VSDB (a) and VSDC (b) and  $Ca^{2+}$  selective nanospheres containing DIL (c) to different KCl and CaCl<sub>2</sub> concentrations as indicated.



**Figure S6.4.** (a) Fluorescence spectra of M540 containing K<sup>+</sup>-sensitive nanosphere suspension with increasing KCl concentration as indicated on the x-axis of Figure S6.4 b (white circles); excitation: 510 nm). (b) Corresponding calibration using emission intensity at 582 nm. (I-I<sub>0</sub>)/I<sub>0</sub> represents the relative intensity change where I<sub>0</sub> is the emission intensity without addition of KCl. (c) Selectivity for the M540 containing K<sup>+</sup>-sensitive nanospheres in H<sub>2</sub>O. The counter ion for all salts is Cl<sup>-</sup>.



**Figure S6.5.** (a) Fluorescence spectra of VSDA containing  $Ca^{2+}$ -sensitive nanosphere suspension with increasing  $CaCl_2$  concentration as indicated on the x-axis of Figure S4 b (white circles). (b) Corresponding calibration using emission intensity at 582 nm.  $I/I_0$  represents the relative intensity change, where  $I_0$  is the emission intensity without addition of  $CaCl_2$ . (c) Selectivity for the VSDA containing  $Ca^{2+}$ -sensitive nanospheres in  $H_2O$ . The counter ion for all salts is  $CI^-$ .

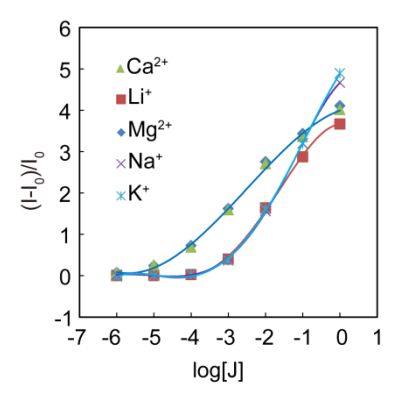


**Figure S6.6.** Ion selectivity of M540 containing Ca<sup>2+</sup>-selective nanospheres without ionophore. Chloride was used as counter ion for all salts.

# 6.2 References for Chapter 6

- (1) Bakker, E.; Pretsch, E. Angew. Chem. Int. Ed. 2007, 46, 5660.
- (2) Shim, J. H.; Kim, J.; Cha, G. S.; Nam, H.; White, R. J.; White, H. S.; Brown, R. B. Anal. Chem. 2007, 79, 3568.
- (3) Denuault, G.; Nagy, G.; Toth, K. In *Scanning Electrochemical Microscopy*; 2 ed.; Bard, A. J., Mirkin, M. V., Eds.; CRC Press: Boca Raton, 2012, p 275.
- (4) Jágerszki, G.; Tak ács, Á.; Bitter, I.; Gyurcs ányi, R. E. Angew. Chem. Int. Ed. 2011, 50, 1656.
- (5) Lee, C.; Miller, C. J.; Bard, A. J. Anal. Chem. 1991, 63, 78.
- (6) Rabinowitz, J. D.; Vacchino, J. F.; Beeson, C.; McConnell, H. M. J. Am. Chem. Soc. 1998, 120, 2464.

- (7) Marzouk, S. A. M.; Buck, R. P.; Dunlap, L. A.; Johnson, T. A.; Cascio, W. E. Anal. Biochem. 2002, 308, 52.
- (8) Numnuam, A.; Chumbimuni-Torres, K. Y.; Yun Xiang, R. B.; Thavarungkul, P.; Kanatharana, P.; Pretsch, E.; Wang, J.; Bakker, E. J. Am. Chem. Soc. 2008, 130, 410.
- (9) Ammann, D.; Lanter, F.; Steiner, R. A.; Schulthess, P.; Shijo, Y.; Simon, W. Anal. Chem. 1981, 53, 2267.
- (10) Thomas, R. C.; Simon, W.; Oehme, M. *Nature* **1975**, 258, 754.
- (11) Kissa, A.; Nagy, G. Electrochim. Acta 2014, 119, 169.
- (12) He, Q.; Miller, E. W.; Wong, A. P.; Chang, C. J. J. Am. Chem. Soc. 2006, 128, 9316.
- (13) Buccella, D.; Horowitz, J. A.; Lippard, S. J. J. Am. Chem. Soc. 2011, 133, 4101.
- (14) Mank, M.; Griesbeck, O. Chem. Rev. 2008, 108, 1550.
- (15) Carter, K. P.; Young, A. M.; Palmer, A. E. Chem. Rev. 2014, 114, 4564.
- (16) Han, J.; Burgess, K. Chem. Rev. 2010, 110, 2709.
- (17) Reeve, J. E.; Corbett, A. D.; Boczarow, I.; Kaluza, W.; Barford, W.; Bayley, H.; Wilson, T.; Anderson, H. L. *Angew. Chem. Int. Ed.* **2013**, *52*, 9044.
- (18) Yan;, P.; Millard, A. C.; Wei, M.; Leslie M. Loew J. Am. Chem. Soc. 2006, 128, 11030.
- (19) Kenet, T.; Bibitchkov, D.; Tsodyks, M.; Grinvald, A.; Arieli, A. Nature 2003, 425, 954.
- (20) Waggoner, A. S. Ann. Rev. Biophys. Bioeng. 1979, 8, 47.
- (21) Xie, X.; Mistlberger, G.; Bakker, E. Anal. Chem. 2013, 85, 9932.
- (22) Xie, X.; Zhai, J.; Bakker, E. Anal. Chem. 2014, 86, 2853.
- (23) Xie, X.; Bakker, E. ACS Appl. Mater. Interfaces 2014, 6, 2666.
- (24) Bakker, E.; Buhlmann, P.; Pretsch, E. Chem. Rev. 1997, 97, 3083.
- (25) Bakker, E.; Buhlmann, P.; Pretsch, E. *Talanta* **2004**, *63*, 3.
- (26) Murkovic, I.; Lobnik, A.; Mohr, G. J.; Wolfbeis, O. S. Anal. Chim. Acta 1996, 334, 125.
- (27) Wolfbeis, O. S. Sens. Actuators, B 1995, 29, 140.
- (28) Dragstent, P. R.; Webb, W. W. Biochemistry 1978, 17, 5228.
- (29) Karpfen, F. M.; Randles, J. E. B. Trans. Faraday Soc. 1953, 49, 823.
- (30) Bühlmann, P.; Yajima, S.; Tohda, K.; Umezawa, Y. Electrochim. Acta 1995, 40, 3021.
- (31) Xie, X.; Zhai, J.; Bakker, E. Anal. Chem. 2014, 86, 8770.
- (32) Boles, J. H.; Buck, R. P. Anal. Chem. 1973, 45, 2057.
- (33) Buck, R. P.; Cosofret, V. V.; Lindner, E. Anal. Chim. Acta 1993, 282, 273.
- (34) Buck, R. P.; Toth, K.; Graf, E.; Horvai, G.; Pungor, E. J. Electroanal. Chem. 1987, 223, 51.
- (35) Yajima, S.; Tohda, K.; Buhlmann, P.; Umezawa, Y. Anal. Chem. 1997, 69, 1919.
- (36) Donnan, F. G. Z. Elktrochem. Angew. P 1911, 17, 572.
- (37) Qin, Y.; Bakker, E. Anal. Chem. 2002, 74, 3134.
- (38) Huber, C.; Werner, T.; Krause, C.; Wolfbeis, O. S. Analyst 1999, 124, 1617.
- (39) Krause, C.; Werner, T.; Huber, C.; Wolfbeis, O. S. Anal. Chem. 1999, 71, 5304.

# Chapter 7. Oxazinoindolines as Fluorescent $H^+$ Turn-On Chromoionophores for Optical and Electrochemical Ion Sensors

This work has been published in: Xiaojiang Xie, Gast on A. Crespo, and Eric Bakker\*, Anal. Chem., 2013, 85, 7434–7440

#### 7.1 Introduction

Chromoionophores are lipophilic pH indicators that are essential components of modern ion-selective optical sensors. <sup>1-4</sup> These sensors often contain additionally a lipophilic receptor for the analyte ion, also called ionophore and an ion-exchanger. The simultaneous existence of chromoionophore and analyte-selective ionophore results in a sensing mechanism that relies on a competition (for cationic analytes) or cooperation (for anions) between the analyte and H<sup>+</sup> in the sample. <sup>5</sup> Here, H<sup>+</sup> functions as a reference ion in the sensing film so that the change in the analyte concentration also alters the concentration of H<sup>+</sup> amount in the membrane, which in turn changes the optical properties of the chromoionophore.

Today, most commercially available chromoionophores are derivatives of Nile blue, such as chromoionophore I (CH 1) and a number of other structurally similar analogs.<sup>6</sup> Despite numerous reports for pH sensitive dyes in aqueous solutions or organic solvents, Nile blue derivatives are still predominantly used in ion-selective optical sensors.<sup>7</sup> CH 1 was first invented by the group of Simon in 1989 for use in a calcium-selective optode.<sup>8</sup> Soon afterwards, pH electrodes and optical sensors selective for ammonium, Pd<sup>2+</sup> and K<sup>+</sup> based on this compound were reported.<sup>9-12</sup> Structure modification provides the opportunity to tune the pKa values of the Nile blue derivatives. Still, the availability basicity range is limited and the synthesis can be challenging.<sup>13</sup> Moreover, the spectra of these compounds are quite similar and lack variation since they belong to the same family. Lipophilic derivatives of fluorescein, such as Chromoionophore VI and XI, are also used for anion-selective sensors.<sup>14,15</sup> Other types of compounds that belong to the azobenzene and stilbene families, such as Chromoionophore IV, X and IX are also used for ion-selective sensors, however, they are not fluorescent and thus their application is limited.<sup>16,17</sup> There is still an urgent need to expand the available palette of chromoionophores for sensing applications.

The spectrum of the chromoionophore normally acts as the signal output and a preferred type of signaling is the fluorescent "turn-on" type. This results in an important contrast with the background, which is important in fluorescence microscopy. <sup>18</sup> There have been many reports on fluorescent turn-on sensors in aqueous or organic phase for various ions such as  $Zn^{2+}$ ,  $Cu^{2+}$ ,  $Hg^{2+}$  and others, <sup>19-22</sup> but membrane based sensors of this type have not been frequently reported. <sup>23-25</sup>

We have observed that oxazinoindolines (Ox), a class of compounds initially reported for photoswitches, <sup>26-29</sup> are very sensitive to pH changes. Here, through rational design, oxazinoindolines with tunable pKa values and variable emission wavelengths that extends to the near infrared region were synthesized. These compounds may exist in a ring-closed (RC) or a ring-opened (RO) form. The ring opened form is strongly colored and more basic while the ring closed form is colorless and much less basic. Therefore, the acid-base reaction is not only dominated by the protonated and deprotonated form, as in classical pH indicators, but also by a third species that arises from thermal isomerization. This gives rise to a substantially different apparent basicity when interrogated by potentiometry or spectroscopy. Ion-selective liquid membranes were prepared from these compounds and were characterized with different techniques including potentiometry, fluorescence spectrometry, and chronopotentiometry. The basicity of these compounds was quantified by comparison with chromoionophore I (CH 1). The results suggest that these oxazinoindoline compounds form promising candidates as a new family of chromoionophores for polymeric ion-selective systems.

## 7.2 Experimental Section

**7.2.1 Reagents.** Poly(vinyl-chloride) (PVC, high molecular weight), bis(2-ethylhexyl) sebacate (DOS), 2-nitrophenyl octyl ether (NPOE), sodium ionophore X, potassium tetrakis[3,5-bis(trifluoromethyl)phenyl]borate (KTFPB), 2-amino-2-hydroxymethyl-propane-1,3-diol (Tris), Chromoionophore I, acetic acid (HA), sodium chloride (NaCl), fluorescein, rhodamine B, cryptocyanine, and tetrahydrofuran (THF) were obtained from Sigma-Aldrich. Oxazinoindolines were synthesized according to synthesis of similar compounds in previous reports. <sup>28</sup> (See supporting information for structural information) All buffer solutions were prepared by dissolving appropriate salts into deionized water (Mili-Q). All solvents and reagents used were analytically pure unless otherwise specified.

**7.2.2 Membranes.** The membranes for potentiometric measurements were prepared by dissolving 150 mg of the mixture composed of 0.002 mmol of Ox or CH 1, 0.55 mmol (0.5 mg) of KTFPB, 50 mg of PVC and 100 mg NPOE or DOS, in 2 ml of THF. The cocktail solution was then poured into a glass ring (22 mm in diameter) placed on a slide glass and dried overnight at room temperature under a dust-free environment. Small disks were punched from the cast films and mounted in Ostec electrode bodies (Ostec, Sargans, Switzerland).

When porous polypropylene (PP) membranes (Celgard, 0.237 cm<sup>2</sup> in surface area, 25 µm in thickness, and kindly provided by Membrana Wuppertal, Germany) were used as supporting material. The same amount of KTFPB, Ox or CH 1 was dissolved in 90 mg of NPOE. For chronopotentiometric measurements, the organic cocktail contains 120 mmol kg<sup>-1</sup> of Ox or CH 1, 60 mmol kg<sup>-1</sup> of KTFPB, 90 mmol kg<sup>-1</sup> of ETH 500 and 190 mg of NPOE. The membranes were soaked in THF for 10 min to remove any possible contaminants. When the membrane was found to be completely dry, 3 µL (large excess) of the cocktail solution was deposited on it. The impregnation of the cocktail was found to be instantaneous; however, the membrane was let in the Petri dish for ca. 10 min to ensure a homogenous and reproducible impregnation of the pores. Afterwards, the membrane was conditioned in the buffer solution for 40 min. Finally, the membrane was mounted in the Ostec electrode body.

For optical sodium selective membrane, 0.002 mmol of Ox or CH 1, 0.002 mmol of KTFPB, 0.005 mmol of sodium ionophore X, 32 mg of PVC and 64 mg of NPOE were dissolved in 1 mL of THF. Likewise, for pH optode, 0.001 mmol of Ox, 0.001 mmol of KTFPB, 32 mg of PVC and 64 mg of NPOE were dissolved in 1 mL of THF. A thin film was formed by drop casting 50  $\mu$ L of the cocktail onto a quartz disk with a diameter of 35 mm and evaporating the solvent for 30 min. The quartz disk was then mounted onto a previously described flow cell<sup>30</sup> for spectroscopic measurements.

**7.2.3 Instrumentation and Measurements.** The glass pH electrode with combined Ag/AgCl reference (Ecotrode Plus) and a double-junction Ag/AgCl/3M KCl/1M LiOAc reference electrode were purchased from Metrohm (Mettler-Toledo AG, Schwerzenbach, Switzerland). The potentiometric sensor responses are measured with an EMF-16 precision electrochemistry EMF interface from Lawson Labs Inc. Chronopotentiometric measurements were performed with an Autolab PGSTAT302N (MULTI 16 module, Metrohm Autolab, Utrecht, The Netherlands) that allows one to read up to 16 working electrodes placed in the same electrochemical cell. A Faraday cage was used to protect the system from undesired noise.

The absorbance was measured with a UV-Vis spectrometer (SPECORD 250 plus, Analytic Jena, AG, Germany) and fluorescence was measured with a fluorescence spectrometer (Fluorolog3, Horiba Jobin Yvon). For fluorescent pH and Na<sup>+</sup> calibration, excitation wavelength of 410 nm, 478 nm, 660 nm and 600 nm was chosen for Ox Y, Ox R, Ox B and CH 1, respectively, while the emission at 520 nm, 605 nm, 720 nm and 700 nm was monitored. The excitation light was guided with a liquid waveguide onto the surface of the quartz disk in the flow cell and the emission light was collected from the same end. The membrane was in contact with aqueous solution in which

the pH or Na<sup>+</sup> concentration was adjusted. The sample solution was circulated through the flow cell with a peristaltic pump (Gilson Miniplus 3). The excitation slit was set at 3 nm for all measurements. The apparent degree of protonation  $(1-\alpha^*)$  was calculated according to Eqn. 7.1 in supporting information.

#### 7.3 Results and Discussion

Three oxazinoindoline derivatives, labeled here as Ox Y, Ox R and Ox B, have been synthesized in two facile steps from commercial starting materials, as shown in Scheme 7.1a. Compared to the established Nile blue family of chromoionophores, the synthesis is much less cumbersome and the yields are attractive. The details of the synthesis and the structural information can be found in the supporting information. The ring opening/closing isomerization reaction (Scheme 7.1 b) is a thermally driven process and can, in some cases, be achieved through UV irradiation, making oxazinoindolines photochromic compounds. The photo-switching behavior depends on the chemical structure and no photochromic effect was observed for the compounds reported here. The ring opened (RO, see scheme 7.1) and the ring closed (RC) form should differ in basicity since the RO form possesses a phenolate group that is absent in the RC form. Therefore, the compounds are pH sensitive and equilibrium state of the reaction can be shifted with hydrogen ions.

a) 
$$O_2N$$
  $O_3N$   $O_4N$   $O_5N$   $O_5N$ 

**Scheme 7.1.** a) Synthetic route for the oxazinoindoline dyes. i: acetonitrile, room temperature, 12 h., ii: ethanol, reflux,  $N_2$ , 12 h. b) Thermal isomerization reaction for oxazinoindoline and the protonation of the ring-opened form.

The RO form is colored owing to the extended conjugation in the merocyanine moiety of the molecule and results in absorbance in the visible range. However, the RC form does not show any absorption region in the visible range with the exception of Ox R. Slight maxima at 424 nm and 552 nm that belong to the 4-nitrobenzophenolate and the merocyanine moieties, respectively, were observed in acetonitrile, indicating that in such environment, the existence of the RO form is not negligible (see Figure S7.1 in supporting information). The absorption and emission spectra are shown in Figure 7.1. The absorption maxima for Ox Y, Ox R and Ox B were found at 409 nm (ε=1.6×10<sup>4</sup> L•mol<sup>-1</sup>•cm<sup>-1</sup>), 558 nm (ε=1.2×10<sup>5</sup> L•mol<sup>-1</sup>•cm<sup>-1</sup>) and 637 nm (ε=6.4×10<sup>4</sup> L•mol<sup>-1</sup>•cm<sup>-1</sup>). Compared with Ox R, the addition of one more double bond (Ox B) red shifted the absorption maximum by 79 nm and the emission maximum by 100 nm in acetonitrile. In contrast, Ox Y showed a blue shift of 149 nm in the absorption maximum and 78 nm in emission maximum. The blue shift was caused by the replacement of the N,N-dimethylamino group on the benzene ring to the isopropyl group. This replacement reduces the electron pushpull effect on the absorbance of the RO form since the isopropyl group is less effective electron donor than N,N-dimethylamino group. It is worth mentioning that the absorption and emission of Ox B has reached the near infrared region, which is advantageous in biological imaging since the excitation and emission at this region will cause much less background interference. The quantum yield of these compounds was determined in ethanol to be 0.12, 0.04 and 0.01 for Ox B, Ox R and Ox Y respectively, using fluorescein, rhodamine B and cryptocyanine as references.

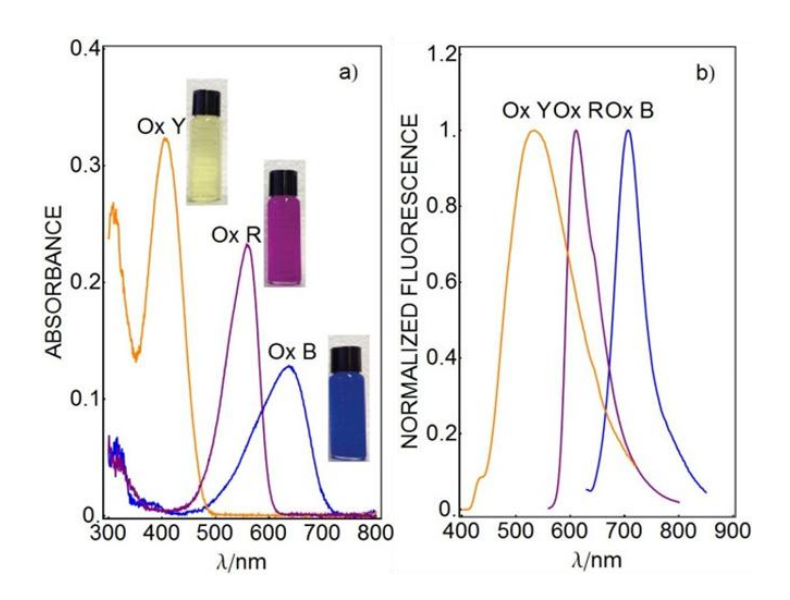
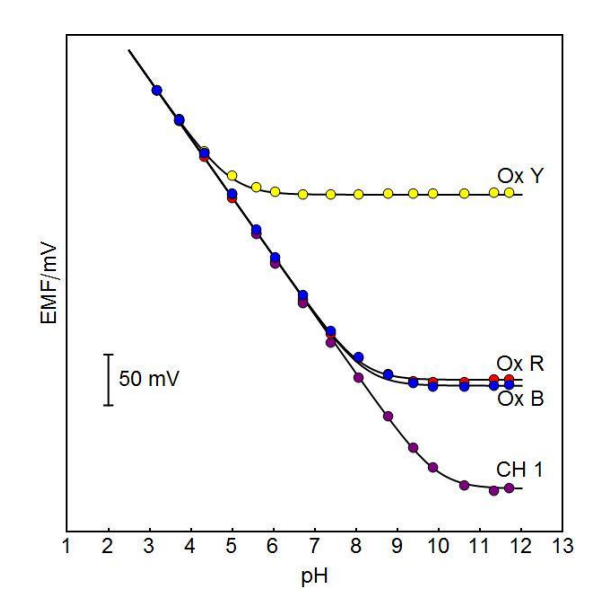


Figure 7.1. a) Absorbance spectra for Ox Y (5  $\times$  10<sup>-5</sup> M), Ox B (5  $\times$  10<sup>-6</sup> M), and Ox R (5  $\times$  10<sup>-6</sup> M) in acetonitrile with 10 equivalents of trifluoroacetic acid. Insets: photographs of the corresponding solutions. b) Normalized fluorescence emission spectra for 5  $\times$  10<sup>-5</sup> M of the three Ox compounds in acetonitrile with 10 equivalents of trifluoroacetic acid.

The oxazinoindoline dyes were incorporated into NPOE plasticized PVC membranes and polypropylene membranes for the fabrication of potentiometric pH selective electrodes. In order to estimate the pKa values, CH 1 was selected as a reference compound. The pKa value of CH 1 was reported to be 14.80±0.03<sup>13</sup> in PVC–NPOE and by comparing the unbiased detection limits at high pH, one can quantify the pKa values. For this purpose, the pH response of the electrodes was measured in a buffer solution containing 0.01 M of tetramethylammonium chloride (TMA<sup>+</sup>) as interfering ion that, owing to its symmetrical structure, is expected not to chemically interact with any of the dyes. The experimentally observed response curves are shown in Figure 7.2 (see Figure S7.2 in supporting information for the pH response of the corresponding supported polypropylene membrane based electrodes).



**Figure 7.2.** Potentiometric pH response for PVC–NPOE based electrodes based on one the three oxazinoindoline derivatives or CH 1 as chromoionophore. The pH of the buffer solution (2.5 mM NaH<sub>2</sub>PO<sub>4</sub>, 2.5 mM boric acid, 2.5 mM citric acid, 0.1 M NaCl and 0.01 M TMA<sup>+</sup>Cl) was adjusted by addition of 1 M NaOH solution. The solid line was calculated from the Nicolsky-Eisenman equation.

The lipophilic TMA<sup>+</sup> cation acted as a strong interference here so that the detection limit at high pH can be observed in all cases. Without such strong interference, even with 0.1 M NaCl as a background, a Nernstian response was obtained over the whole buffer range, making the detection limits too difficult to determine. The p $K_a$  values were extracted from the lower detection limit for  $H^+$  using Eqn. 7.1, where pH(LDL) and pH(LDL,CH1) are the pH values at the lower detection limit for a membrane containing the dye of interest and CH 1, respectively.<sup>5</sup>

$$pK_a - pK_a(CH1) = pH(LDL) - pH(LDL, CH1)$$
(7.1)

This equation should be valid for membranes of otherwise identical composition. Figure 7.2 shows the potentiometric calibration curves from which the pK<sub>a</sub> values were extracted for Ox Y, Ox R and Ox B as  $9.80 \pm 0.03$ ,  $12.85 \pm 0.03$  and  $12.95 \pm 0.03$ , respectively. Note that the basicity of Ox Y is particularly low compared with the others. This difference is a consequence of the replacement of the N,N-dimethylamino group in Ox R and Ox B with the isopropyl group in Ox Y. The presence of the nitrogen atom enables Ox R and Ox B to exist in resonance structures and brings additional stabilization to the RO form, while for Ox Y, resonance structures cannot be formed (see Figure S7.3 in supporting information).

In next step, optically responsive pH sensitive films containing the compounds were prepared (see membrane composition above). The pH response was re-evaluated in the same buffer solution using fluorescence emission as signal output. The emission intensity at the emission maximum was monitored during the experiment. Under this operating mode, the Ox compounds exhibited an advantage since the emission intensity change at the maximum emission wavelength was larger than for CH 1.

One should note that for CH 1 only the protonated form and the deprotonated form are involved in the optode response:

$$H^+ + Ind \rightleftharpoons HInd^+ \tag{7.2}$$

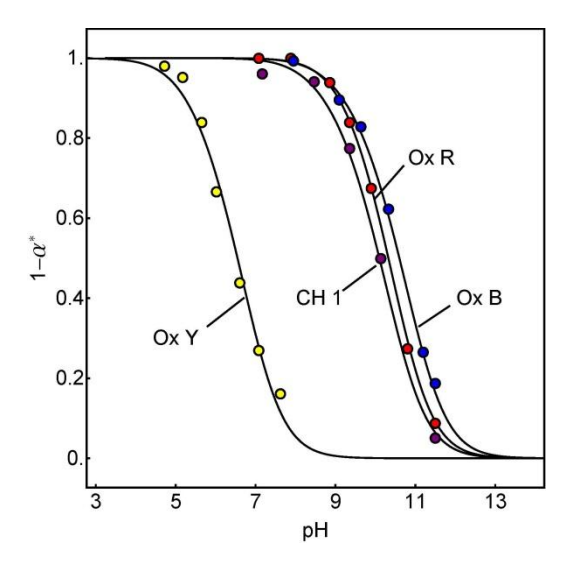


**Figure 7.3.** Optode pH response for films containing Ox dyes or CH 1 as chromoionophore, as indicated, without additional cation-selective ionophore. The same buffer solution as for Figure 7.2 was used.

For oxazinoindoline dyes, on the other hand, three forms, namely, the RC, RO and the protonated ring-opened form ROH $^+$ , are potentially important, with  $K_a$  the acid dissociation constant in the membrane (note that the ring closed form is used here as the conjugate base)

$$ROH^+ \xrightarrow{K_a} RC + H^+$$
 (7.3)

The isomerization equilibrium between non-protonated RO and RC form is given as:

$$RO \stackrel{K_r}{\longleftarrow} RC$$
 (7.4)

Because of the possible presence of the RO species, the fluorescence intensity was taken to calculate a  $1-\alpha^*$  value (see supporting information). Consequently, the  $1-\alpha^*$  value, meaning the mole fraction of the protonated form, depends on both the basicity of RO ( $K_a$ ) and the thermal equilibrium between RC and RO ( $K_r$ ). The response function of a pH sensitive optode containing Ox B and KTFPB in the presence of a monovalent interfering ion can be derived from charge and mass balances, the ion-exchange equilibrium and the chemical equilibria shown in Eqn. 7.3 and 7.4 (see supporting information for details) to give:

$$a_{H^{+}}^{aq} = a_{J^{+}}^{aq} K_{a} K_{ex} \frac{1 + K_{r}}{K_{r}} \frac{1 - \alpha^{*}}{\alpha^{*}} \frac{1}{(1 - \alpha^{*}) Ind_{T} - R_{T}}$$

$$(7.5)$$

where  $a_{H^+}^{aq}$  and  $a_{J^+}^{aq}$  are the activities of H<sup>+</sup> and the interfering ion (TMA<sup>+</sup> or Na<sup>+</sup>) in aqueous solution,  $Ind_T$  and  $R_T$  are the total concentration of Ox B and KTFPB, and  $K_{ex}$  is the exchange constant for the so-called free hydrogen and interfering ions. The observed optical pH response is shown in Figure 7.3 where the solid lines are theoretical fittings according to Eqn. 7.5. From the optode response, one can predict the theoretical potentiometric response. The correlation between the optode response and the potentiometric response (Figure 7.2) can be established by considering the free proton concentration in the membrane ( $a_{H^+}^m$ ), as shown in Eqn. 7.6. The potential

(EMF) in Figure 7.2 measured under the same conditions can then be expressed by Eqn. 7.7, where s is the Nernstian slope and  $E^0$  a constant.

$$a_{H^{+}}^{m} = \frac{K_{a}(K_{r} - (1 + K_{r})\alpha^{*})}{\alpha^{*}K_{r}}$$
(7.6)

$$EMF = E^{0} + s \log \frac{a_{H^{+}}^{aq}}{a_{H^{+}}^{m}} = E^{0} + s \log \frac{(1 - \alpha^{*}) a_{J^{+}}^{aq} K_{ex}(1 + K_{r})}{(\alpha^{*} + (\alpha^{*} - 1)K_{r})((\alpha^{*} - 1) Ind_{T} + R_{T})}$$
(7.7)

The correlation between the optical response and potentiometric response for a PVC-NPOE membrane containing Ox B is presented in Figure 7.4 a. The solid line is the theoretical potentiometric response curve calculated according to Eqn. 7.7 using  $K_a$ ,  $K_r$ , and  $K_{ex}$  values obtained from the corresponding optical calibration curve (Figure 7.3). As shown in Figure 7.4 a, in PVC-NPOE, the measured data differed from the theoretical curve by 2.6 units. The oxazinoindoline compounds exhibit an apparently higher basicity than CH1 in fluorescent mode, which seemingly contradicts the potentiometric data in Figure 7.2, which had suggested a lower basicity for all oxazinoindolines relative to CH1.

This unusual discrepancy is perhaps partly explained by the presence of the RO species in the optode equilibrium. The fluorescence and absorbance spectra of pH sensitive films containing the Ox dyes are measured and shown in Figure S7.4 and Figure S7.5. Comparing the emission intensity at high and low pH conditions where the RO form of Ox dyes should be completely deprotonated and protonated, it is clear that in a polar environment, such as PVC–NPOE, the formation of the zwitterionic species may be preferred relative to the RC form. The concentration of RC is reduced relative to all unprotonated indicators, thereby diminishing the apparent basicity of the dye. This perhaps explains the poorer selectivity of the ion-selective electrode towards the interfering ion. In agreement with theoretical expectations (see Figure S7.6 in supporting information) where the zwitterion is preferred in a polar environment such as PVC–NPOE, the potentiometric low detection limit for H<sup>+</sup> shifted to lower pH. The formation of the zwitterionic RO form in nonpolar PVC–DOS should be suppressed compared with the polar PVC/NPOE since it is less preferred in nonpolar environment. The dependence of such entropy-driven thermal isomerization on microenvironments, such as solvents, for compounds with similar structure has been reported before.<sup>31</sup>

To confirm, the pH response for a PVC–DOS membrane containing Ox B was also measured and the correlation between the optical response (see Figure S7.7 in supporting information) and potentiometric response is presented in Figure 7.4 b. In PVC–DOS, the chromoionophore is expected to more closely function as a typical two component system (in analogy to CH 1) due to the suppression of the thermal ring-opening reaction, and a good correlation was indeed observed.

A Na<sup>+</sup>-selective optode was prepared with Ox B and Ox R as an early example of a fluorescent ion sensor. Ox Y was not tested due to its relatively low pKa. Selectivity for Na<sup>+</sup> was assured by addition of sodium ionophore X to the sensing film. Here, H<sup>+</sup> and Na<sup>+</sup> in the sample will compete with each other for extraction into the optode film and hence, with a constant hydrogen ion background, the concentration of Na<sup>+</sup> alters the fluorescence output. Figure S7.8 shows the calibration curves for the sensors in 0.01 M Tris-HCl buffer at pH 7.2. The results were compared with a conventional CH 1 based Na<sup>+</sup>-selective optode and the calibration curves are consistent with the basicity tendency displayed in Figure 7.3. Again, the signal to noise ratio was better for the Ox dyes than CH 1 since the Ox dyes exhibit a larger emission intensity variation at their emission maxima (see Figure S7.9 in supporting information).

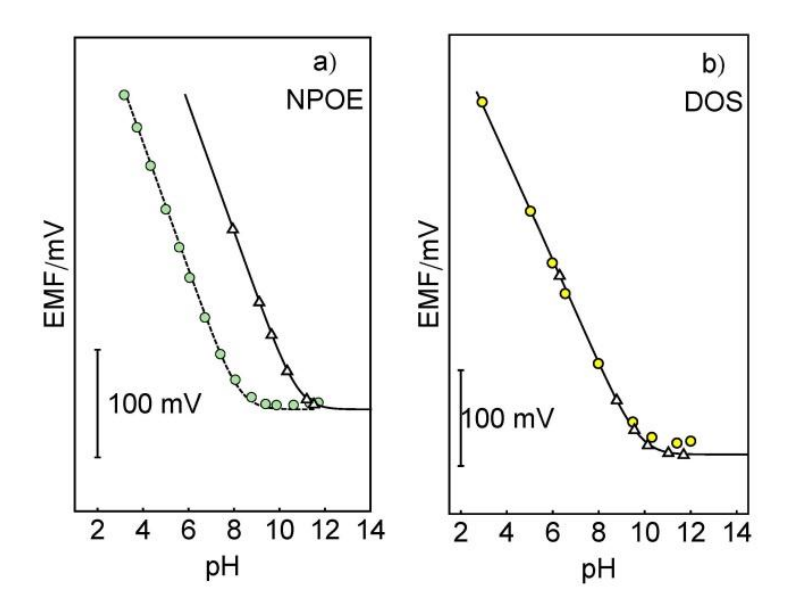


**Figure** 7.4. Correlation between the potentiometric pH response and optode pH response for membrane using Ox B as chromoionophore, a) in PVC–NPOE and b) in PVC–DOS. The solid lines and triangles are calculated according to Eqn. 7.7 with constants obtained from Figure 7.3 and Figure S7.7. The dashed line is a shift of the solid line in a) to the left by 2.6 units to fit the potentiometric data. The circles are experimentally measured potentiometric responses.

CH 1 has been recently incorporated in chronopotentiometric sensors to determine total alkalinity and total acidity *in-situ* in artificial samples.<sup>32</sup> Here, Ox B and Ox R were also evaluated as potential proton ionophore candidates under electrodynamic conditions. A sequence of galvanostatic and potentiostatic pulses allows one to achieve dynamic electrochemistry perturbations between the membrane and sample interface.<sup>33</sup> For instance, if an anodic pulse is applied, protons are released from the membrane to the sample. When a base is present, it will become protonated near the electrode surface. While the proton flux is constant, the flux of this base from the solution bulk to the electrode membrane can only be maintained up to a transition time ( $\tau$ ), after which time the proton flux can no longer be maintained and the resulting phase boundary pH change gives rise to a observed potential change. The transition time is visualized as the maximum of the time derivative of the potential as shown in Figure 7.5 (see Figure S7.10 in the supporting information for raw data of E vs. time). By increasing the concentration of Tris at a constant applied current, the transition times move to larger values, in quantitative agreement with the Sand equation. The diffusion coefficient of Tris in aqueous phase is obtained from the linear plot of  $\tau^{0.5}$  vs [Tris] for each individual dye. The estimated diffusion coefficients for Tris are  $(6.59\pm0.05)$   $10^{-6}$  cm<sup>2</sup> s<sup>-1</sup> when Ox R is used,  $(5.89\pm0.05)$   $10^{-6}$  cm<sup>2</sup> s<sup>-1</sup> for Ox B and  $(5.89\pm0.05)$   $10^{-6}$  cm<sup>2</sup> s<sup>-1</sup> for CH 1. There is some difference between Ox R and Ox B in terms of diffusion coefficient estimation that may be attributed to experimental variations in the effective membrane area, since only geometric areas were estimated here.

# 7.4 Conclusion

The H<sup>+</sup>-chromoionophore family for ion-selective sensors has been stagnant and lacked excitement for many years. The variety of available chromoionophores have unfortunately been quite limited for practical applications. A family of fluorescent turn-on oxazinoindoline dyes have been introduced here that exhibit a tunable absorbance, fluorescence and pKa values and that will expand the palette of available chromoionophores. Their pH response was characterized by potentiometry and fluorescence spectrometry and their basicity values compared with CH 1. When used in optical mode, most dyes showed higher basicity than CH 1 while in ISEs, the pKa values were smaller. This surprising observation was qualitatively explained by an additional thermal isomerization reaction of the Ox dyes. As a more practical

example, a Na<sup>+</sup>-selective optode was successfully prepared and characterized. Compared with the established Nile blue derivatives, the Ox dyes showed a better signal to noise ratio when the emission maxima were used as signal output, since they are H<sup>+</sup> turn-on chromoionophores. The compounds were also tested in chronopotentiometry and shown to function without obvious limitation in dynamic electrochemical detection protocols as well.

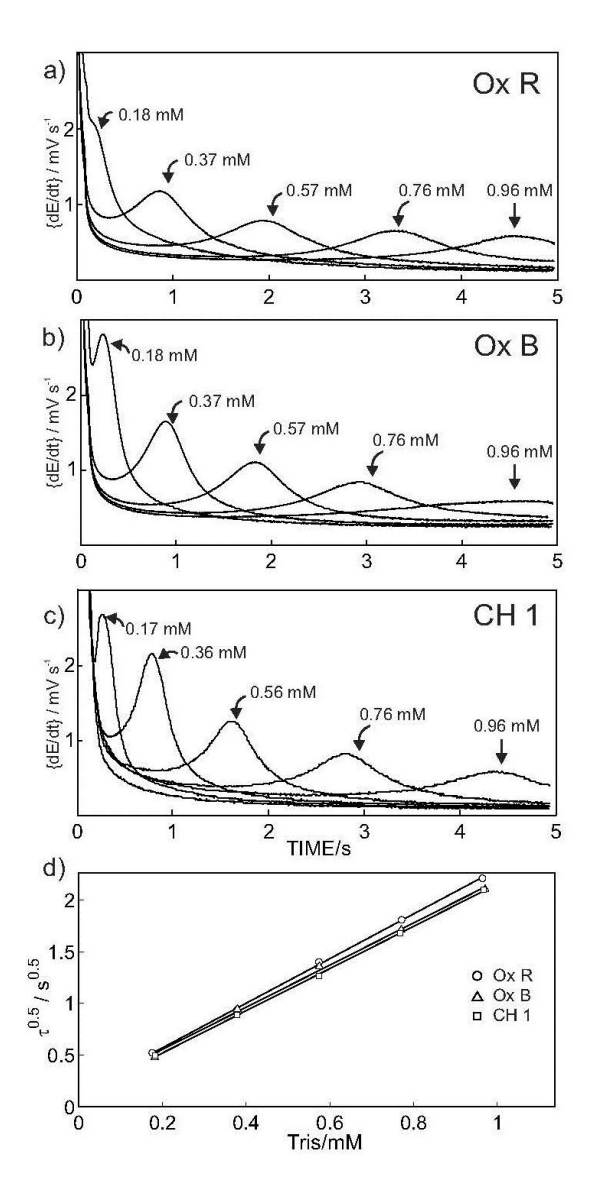


Figure 7.5. Time derivative of the chronopotentiometric response in contact with a sample containing 0.1 to 1.0 mM of Tris base for a) Ox R, b) Ox B and c) CH 1. The transition time increases with increasing Tris concentration, as expected from the Sand equation. d) Square root of the transition time ( $\tau^{1/2}$ ) as a function of Tris concentration for all dyes follows a linear relationship.

# 7.5 Supporting Information for Chapter 7

The precursor A:

was synthesized according to the literature. 26 For the synthesis of Ox Y, Ox R and Ox

B, a general procedure as follows was used:

155 mg of A (0.5 mmol) and 0.5 mmol of the corresponding aldehyde were dissolved in 10 mL anhydrous ethanol. To the solution was added 0.3 mL of trifluoroacetic acid. The solution was then refluxed under  $N_2$  for 12 h. After cooling down to ambient temperature, the solvent was distilled off under reduced pressure and the residue was dissolved in  $CH_2Cl_2$  (2 mL). The addition of  $Et_2O$  (30 mL) caused the precipitation of a solid, which was filtered off, dissolved in  $CH_2Cl_2$  (20 mL) and washed with  $H_2O$  (50 mL). The organic phase was dried over  $Na_2SO_4$  and the solvent was distilled off under reduced pressure to give the corresponding oxazinoindolines.

# Ox R:

<sup>1</sup>H NMR (CDCl<sub>3</sub>):  $\delta$  =8.02-7.97 (2H, m), 7.34-7.32 (2H, d), 7.17-7.11 (2H, m), 6.91-6.86 (2H, m), 6.77-6.64 (4H, m), 6.18-6.14 (1H, d), 4.61 (2H, s), 2.99 (6H, s), 1.4 (6H, s) ESI-MS: m/z=442.1 [M+H]<sup>+</sup>

Estimated Log P: 6.7

## Ox Y:

<sup>1</sup>H NMR (CDCl<sub>3</sub>):  $\delta$  =8.17-8.13 (1H, d), 8.02-7.95 (2H, m), 7.8-7.58 (6H, m), 7.45-7.39 (2H, t), 6.34 (2H, bs), 5.80 (2H, s), 3.00-2.93 (1H, m), 1.84 (6H, s), 1.27-1.25 (6H, d) ESI-MS: m/z=441.3 [M+H]<sup>+</sup>

Estimated Log P: 8.0

### Ox B:

<sup>1</sup>H NMR (CDCl<sub>3</sub>):  $\delta$  =8.07-7.93 (2H, m), 7.31-7.29 (2H, d), 7.15-7.06 (2H, m), 6.88 (2H, bs), 6.70-6.56 (6H, m), 5.87 (1H, bs), 4.61 (2H, bs), 2.98 (6H, s), 1.38 (6H, bs) ESI-MS: m/z=468.4 [M+H]<sup>+</sup>

Estimated Log P: 7.3

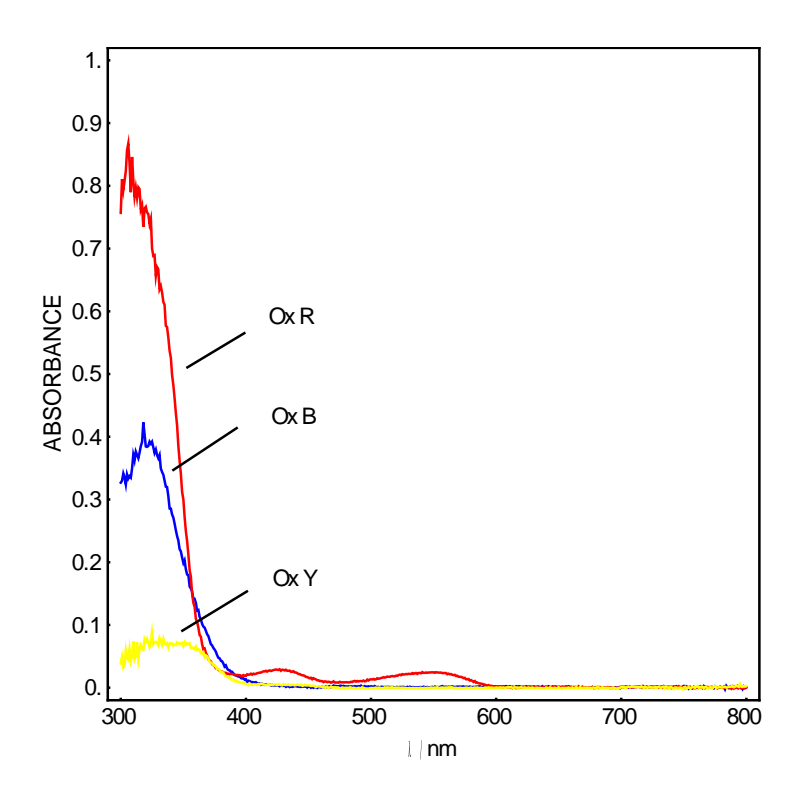


**Figure S7.1.** Absorption spectra of  $5 \times 10^{-5}$  M Ox in MeCN without addition of trifluoroacetic acid.

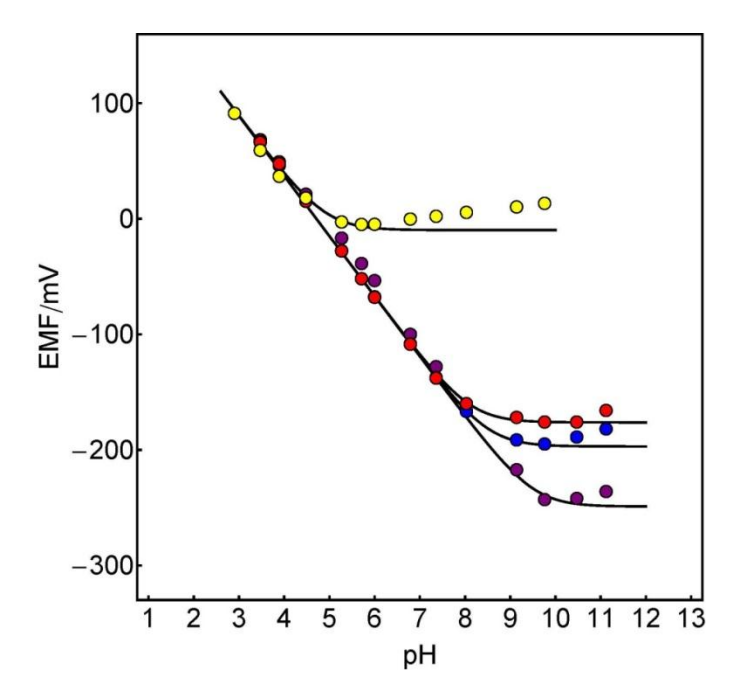


**Figure S7.2.** Potentiometric pH response for polypropylene (Celgard 2400) based electrode using Ox Y (yellow), Ox R (red), Ox B (blue) and CH 1 (purple) as chromoionophore. The pH of the buffer solution (2.5 mM NaH<sub>2</sub>PO<sub>4</sub>, 2.5 mM boric acid, 2.5 mM citric acid, 0.1 M NaCl and 0.01 M TMACl) was adjusted with addition of 1 M NaOH solution. The solid line was calculated from the Nicolsky-Eisenman equation.

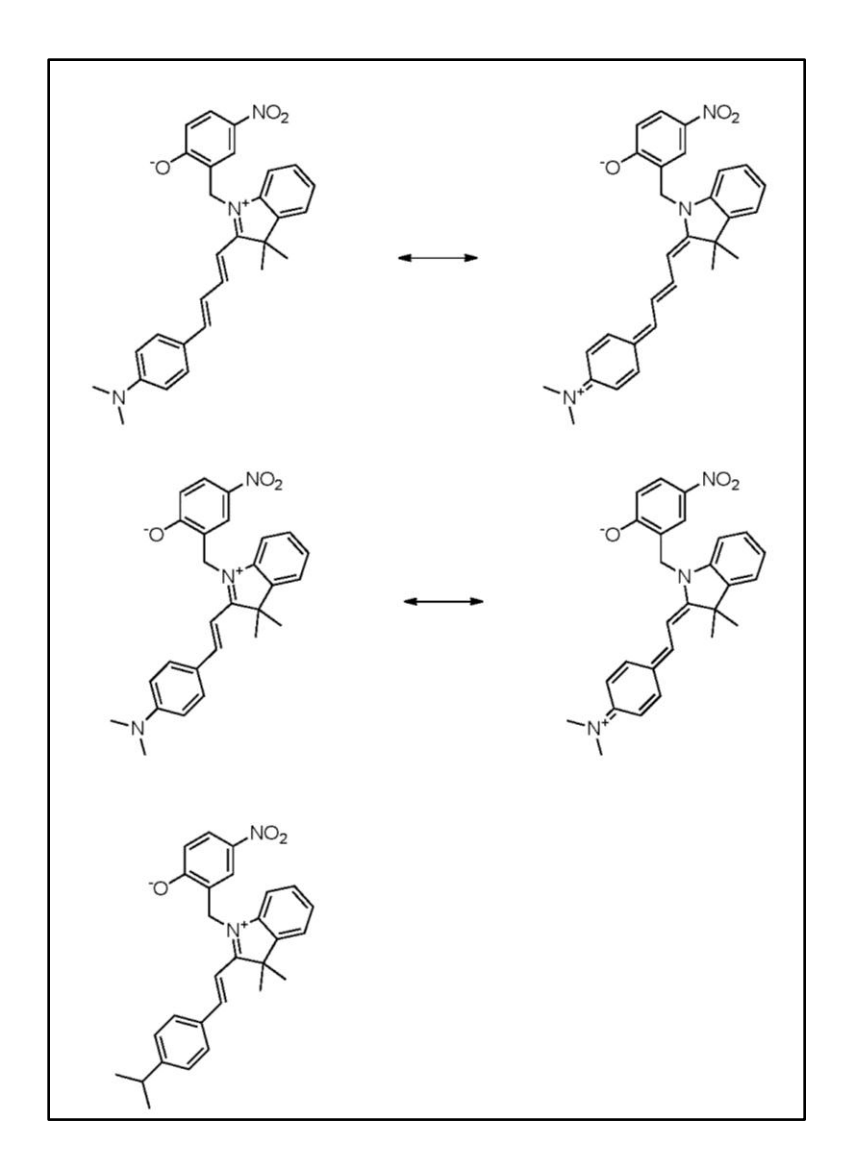


Figure S7.3. Resonance structure of Ox R and Ox B, Ox Y cannot form resonance structure.

Derivation of Eqn. 7.5 and 7.6:

$$R_T = ROH^+ + a_{J^+}^m + a_{H^+}^m$$
 (a)

$$a_{H^{+}}^{m} a_{J^{+}}^{aq} K_{ex} = a_{J^{+}}^{m} a_{H^{+}}^{aq}$$
 (b)

$$RC = K_r RO$$
 (c)

$$ROH^{+}/(RO+RC) = (1-\alpha)/\alpha$$
 (d)

$$K_a ROH^+ = RC a_{H^+}^m$$
 (e)

$$Ind_{T} = RO + RC + ROH^{+}$$
 (f)

(a): charge balance; (b): phase equilibrium; (c): isomerization equilibrium of Ox; (d): definition of  $\alpha$ ; (e): acid-base reaction equilibrium; (f): mass conservation for Ox. Elimination undesired variables gives Eqn. 7.5 and 7.6.

The potentiometric response for a pH selective electrode based on Ox is shown in Figure 7.4 (left). At lower detection limit (LDL), the interference concentration in the membrane equals the ion exchanger concentration. The proton activity in the aqueous solution is then calculated as a function of  $K_r$ , the lower detection limit of the pH electrode containing Ox as chromoionophore is expressed in the Eqn. g. The influence of  $K_r$  to the lower detection limited is shown in Figure S7.4. As the  $K_r$  decreases, i.e., the RO form gets more and more preferred, LDL moves towards the lower pH direction. However, quantitatively understanding the deviation may require further insight of the system and more complicated model.

$$(aH^{+})_{LDL} = \frac{a_{J^{+}}^{aq}(1 + K_{r})K_{a}K_{ex}}{K_{r}(Ind_{T} - R_{T})}$$
 (g)

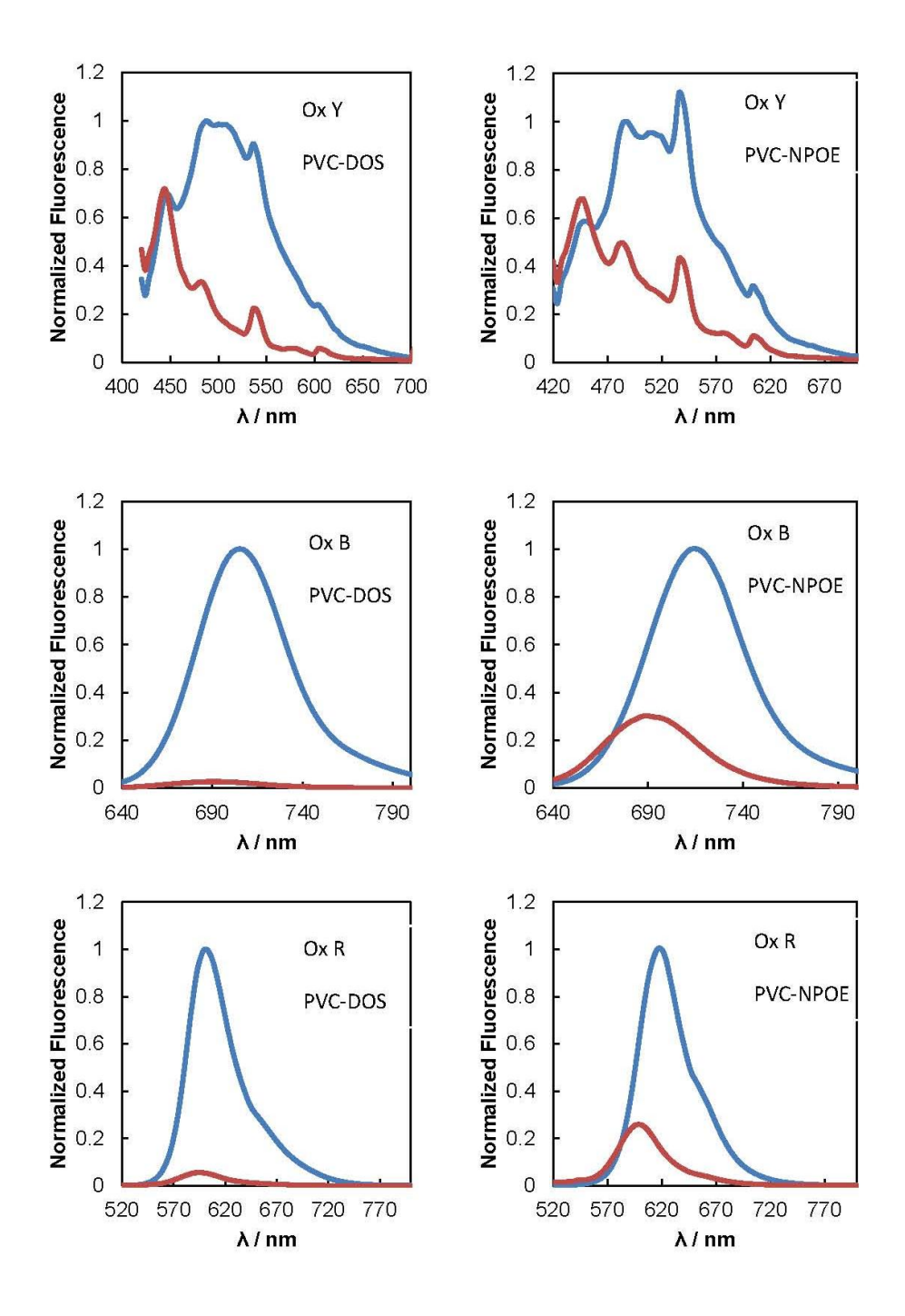


**Figure S7.4.** Fluorescence Spectra of Optode pH response for DOS and NPOE plasticized films containing Ox dyes. Blue line: measured in pH 3 buffer solution containing 10 mM TMA<sup>+</sup>Cl<sup>-</sup>, Red line: measured in 0.1 M NaOH solution containing 50 mM TMA<sup>+</sup>Cl<sup>-</sup>. The observed fine structure for Ox Y based membranes is not visible in solution phase and therefore likely caused by a measurement artifact.

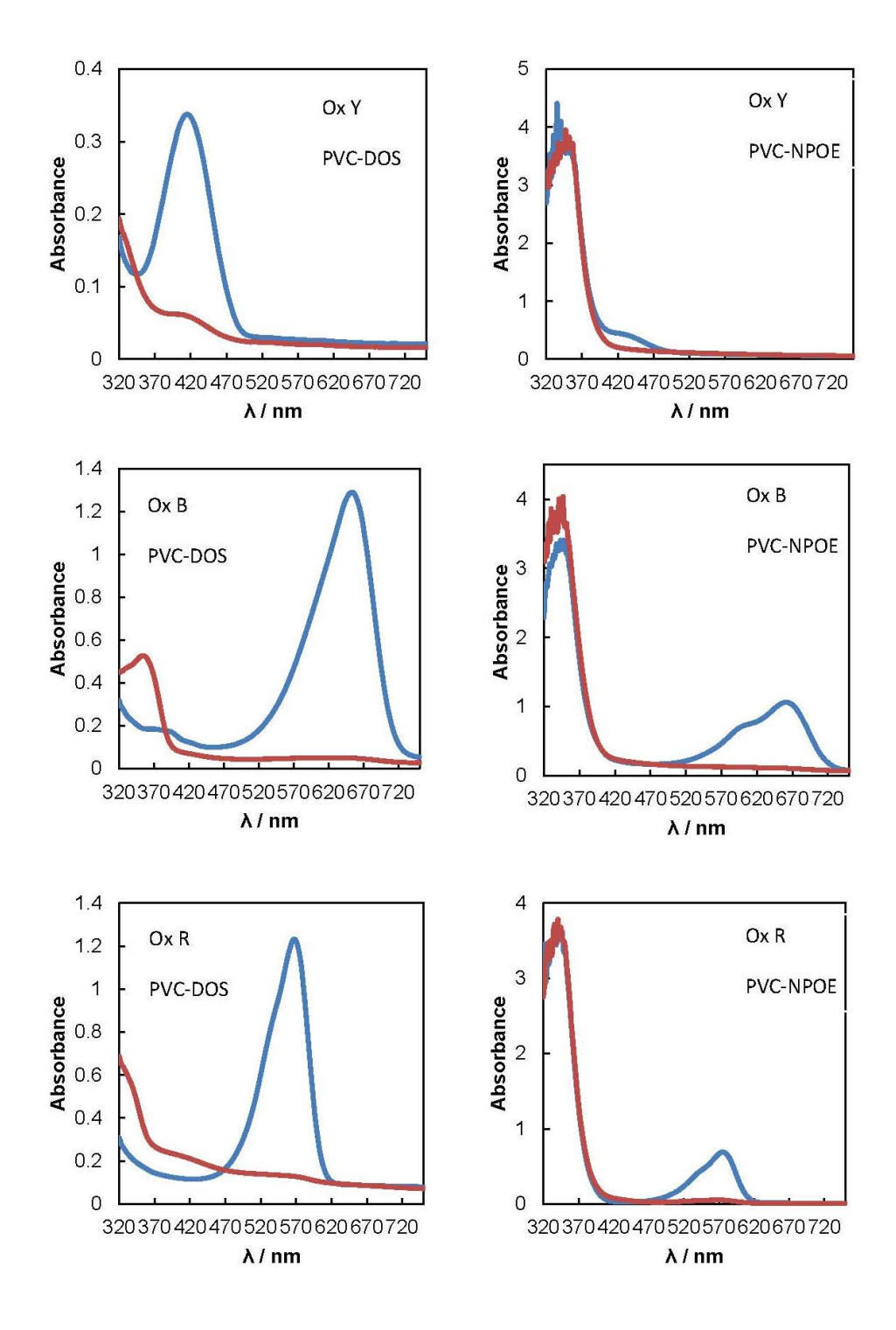


**Figure S7.5.** Absorbance Spectra of Optode pH response for DOS and NPOE plasticized films containing Ox dyes. Blue line: measured in pH 3 buffer solution containing 10 mM TMA<sup>+</sup>Cl<sup>-</sup>, Red line: measured in 0.1 M NaOH solution containing 50 mM TMA<sup>+</sup>Cl<sup>-</sup>.

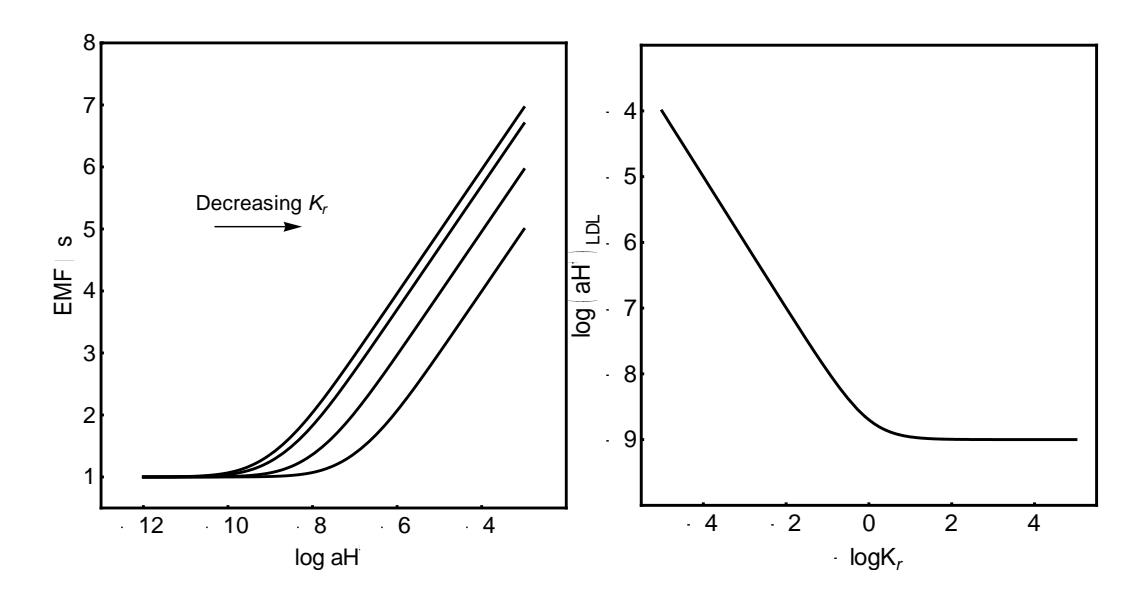


**Figure S7.6.** Theoretically predicted effect of isomerization equilibrium constant  $K_r$  on the potentiometric response curve (left) and the lower detection limit (right) for pH electrodes based on the Ox dyes.

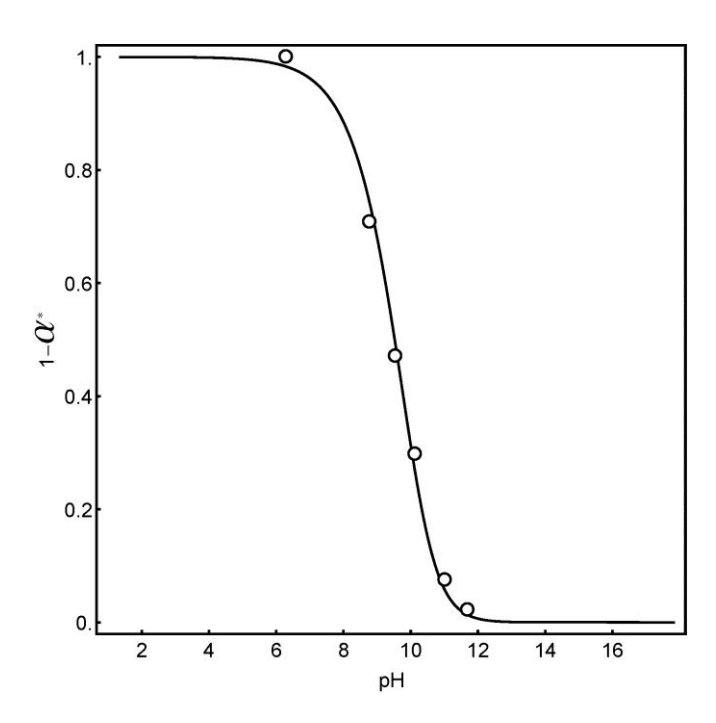


**Figure S7.7.** Optical pH response of a pH sensitive membrane containing 10 mmol/kg Ox B and 10 mmol/kg KTFPB in PVC/DOS. The pH of the buffer solution (2.5 mM NaH<sub>2</sub>PO<sub>4</sub>, 2.5 mM boric acid, 2.5 mM citric acid and 0.1 M NaCl) was adjusted with addition of 1 M NaOH solution.

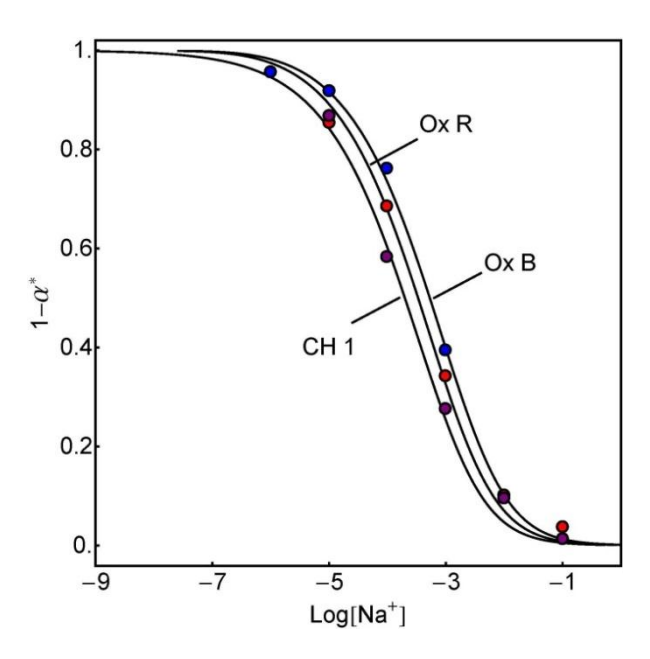


**Figure S7.8.** Calibration curves measured in 0.01 M pH 7.2 Tris-HCl buffer for Na<sup>+</sup>-selective fluorescent optode membranes containing Ox R, Ox B and CH 1 as chromoionophore.

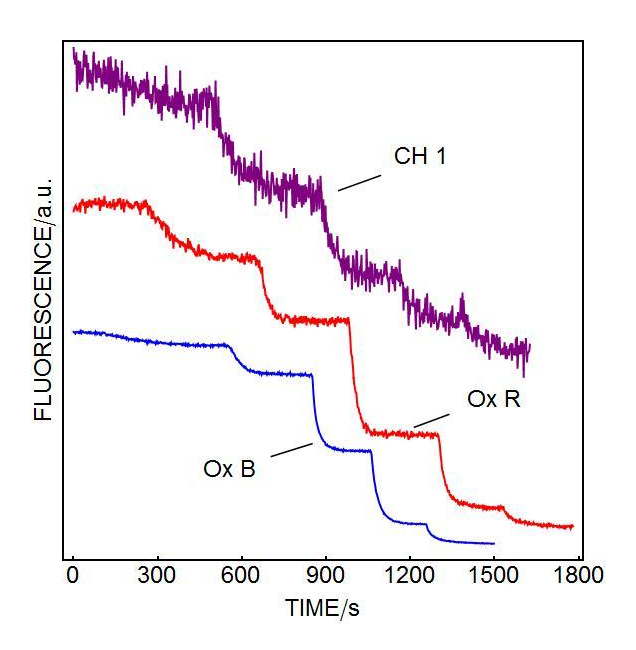


**Figure S7.9.** Raw data for Na<sup>+</sup> concentration measurement experiment using a Na<sup>+</sup>-selective membrane. Different volume of 1 M NaCl solution or NaCl solid was added into a pH 7.2 Tris-HCl buffer solution to reach different Na<sup>+</sup> concentrations (as indicated by the flat shoulders in the figure).

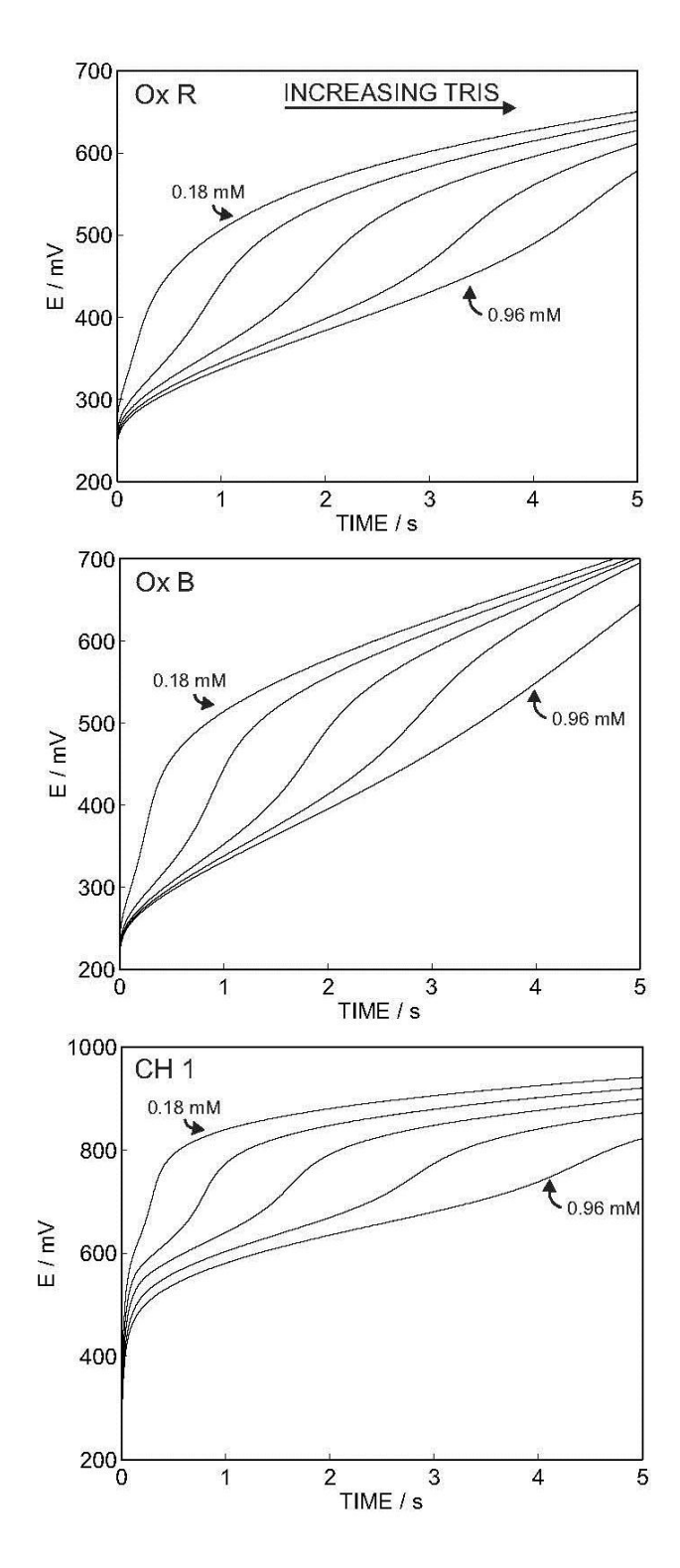


**Figure S7.10.** Raw data for alkalinity determination of Tris. Tris solution is successively added to the cell to a final concentration of 0.1 to 1.0 mM. By increasing the concentration of Tris, the observed transition time shift to higher values, as expected. Ox R, Ox B and CH 1 were respectively tested.

The  $\alpha$  value in this work was determined using the following equation:

$$\alpha^* = \frac{A}{A_0}$$

where  $A_0$ , for pH selective systems, is the emission value measured in 0.1 M HCl, represents the fully protonated state, and A is the measured emission value. For sodium selective membrane,  $A_0$  is the emission value measured in the buffer solution without any  $Na^+$  in presence.

# 7.6 References for Chapter 7

- (1) Dubach, J. M.; Harjes, D. I.; Clark, H. A. J. Am. Chem. Soc. 2007, 129, 8418.
- (2) Xu, C.; Wygladacz, K.; Retter, R.; Bell, M.; Bakker, E. Anal. Chem. 2007, 79, 9505.
- (3) Dür üst, N.; Meyerhoff, M. E.; Ünal, N.; Na ç, S. Anal. Chim. Acta 2011, 699, 107.
- (4) Xie, L.; Qin, Y.; Chen, H.-Y. Anal. Chem. 2012, 84, 1969.
- (5) Bakker, E.; Bühlmann, P.; Pretsch, E. Chem. Rev. 1997, 97, 3083.
- (6) Bakker, E.; Lerchi, M.; Rosatzin, T.; Rusterholz, B.; Simon, W. Anal. Chim. Acta 1993, 278, 211.
- (7) Bühlmann, P.; Pretsch, E.; Bakker, E. *Chem. Rev.* **1998**, 98, 1593.
- (8) Morf, W. E.; Seiler, K.; Rusterholz, B.; Simon, W. Anal. Chem. 1990, 62, 738.
- (9) Cosofret, V. V.; Nahir, T. M.; Lindner, E.; Buck, R. P. J. Electroanal. Chem. 1992, 327, 137.
- (10) Wang, K.; Seiler, K.; Morf, W. E.; Spichiger, U. E.; Simon, W.; Lindner, E.; Pungor, E. Anal. Sci. 1990, 6, 715.
- (11) Lerchi, M.; Bakker, E.; Rusterholz, B.; Simon, W. Anal. Chem. 1992, 64, 1534.
- (12) Seiler, K.; Morf, W. E.; Rusterholz, B.; Simon, W. Anal. Sci. 1989, 5, 557.
- (13) Qin, Y.; Bakker, E. Talanta 2002, 58, 909.
- (14) Ortuño, J. A.; Albero, M. I.; García, M. S.; García, M. I.; Expósito, R.; Sánchez-Pedre ño, C. Talanta 2003, 60, 563.
- (15) Badr, I. H.; Meyerhoff, M. E. J. Am. Chem. Soc. 2005, 127, 5318.
- (16) Mohr, G. J.; Klimant, I.; Spichiger-Keller, U. E.; Wolfbeis, O. S. Anal. Chem. 2001, 73, 1053.
- (17) Xie, X.; Pawlak, M.; Tercier-Waeber, M.-L.; Bakker, E. Anal. Chem. 2012, 84, 3163.
- (18) Yu, Z.; Ho, L. Y.; Lin, Q. J. Am. Chem. Soc. 2011, 133, 11912.
- (19) Huang, D.; Niu, C.; Wang, X.; Lv, X.; Zeng, G. Anal. Chem. 2013, 85, 1164.
- (20) Wang, J.; Ha, C.-S. Tetrahedron 2009, 65, 6959.
- (21) Ojida, A.; Takashima, I.; Kohira, T.; Nonaka, H.; Hamachi, I. J. Am. Chem. Soc. 2008, 130, 12095.
- (22) Li, M.; Lu, H.-Y.; Liu, R.-L.; Chen, J.-D.; Chen, C.-F. J. Org. Chem. 2012, 77, 3670.
- (23) Ma, X.; Song, F.; Wang, L.; Cheng, Y.; Zhu, C. J. Polym. Sci., Part A: Polym. Chem. 2011, 50, 517.
- (24) Ma, B.; Wu, S.; Zeng, F. Sens. Actuators, B 2010, 145, 451.
- (25) Fries, K. H.; Driskell, J. D.; Samanta, S.; Locklin, J. Anal. Chem. 2010, 82, 3306.
- (26) Tomasulo, M.; Sortino, S.; White, A. J. P.; Raymo, F. M. J. Org. Chem. 2005, 70, 8180.
- (27) Petersen, M. Å.; Deniz, E.; Nielsen, M. B.; Sortino, S.; Raymo, F. M. Eur. J. Org. Chem. 2009, 4333.
- (28) Deniz, E.; Tomasulo, M.; Cusido, J.; Yildiz, I.; Petriella, M.; Bossi, M. L.; Sortino, S.; Raymo, F. i. M. *J. Phys. Chem. C* **2012**, *116*, 6058.

- (29) Tomasulo, M.; Sortino, S.; Raymo, F. i. M. J. Photochem. Photobiol., A 2008, 200, 44.
- (30) Xie, X.; Pawlak, M.; Tercier-Waeber, M.-L.; Bakker, E. Anal. Chem. 2012, 84, 3163.
- (31) Shiraishi, Y.; Inoue, T.; Sumiya, S.; Hirai, T. J. Phys. Chem. A 2011, 115, 9083.
- (32) Crespo, G. A.; Afshar, M. G.; Bakker, E. Anal. Chem. 2012, 84, 10165.
- (33) Shvarev, A.; Bakker, E. Anal. Chem. 2003, 75, 4541.

# Chapter 8. Direct Optical Carbon Dioxide Sensing Based on a Polymeric Film Doped with a Selective Molecular Tweezer Type Ionophore

This work has been published in: Xiaojiang Xie, Marcin Pawlak, Mary-Lou Tercier-Waeber, and Eric Bakker\*, *Anal. Chem.*, 2012, 84, 3163–3169

# 8.1 Introduction

As one of the culprits responsible for the greenhouse effect, carbon dioxide is receiving significant attention from the scientific community and political leadership. Monitoring CO<sub>2</sub> levels in the atmosphere and aquatic environments is therefore an urgent and important task. CO<sub>2</sub> sensors are important tools with increasing relevance to measure the gas concentration in air, in bioprocesses and as dissolved CO<sub>2</sub> in real process liquids. Generally, however, CO<sub>2</sub> is a poorly reactive molecule, and the direct molecular recognition of CO<sub>2</sub> is difficult to accomplish. Membrane-covered electrochemical CO<sub>2</sub> sensors based on the Severinghaus principle and solid electrolyte sensors operating at high temperatures have been widely applied for a long time.<sup>1</sup> Other measuring methods base on infrared and nondispersive infrared spectroscopy, photoacoustic effect and thermal conductivity are increasingly being used.<sup>2-5</sup> While Severinghaus based electrochemical sensors are inexpensive and relatively simple, the CO<sub>2</sub> partial pressure is still determined by monitoring indirectly the pH values of a hydrogen carbonate solution and other similarly behaving dissolved gases may potentially interfere with this measurement principle. Unfortunately, there seems to be a lack of reports on CO<sub>2</sub> sensors based on direct molecular recognition.

Since Severinghaus-type potentiometric probes require a low sample pH (<5.5) for optimal operation, their sensitivity deteriorates at the higher pH value of typical aquatic systems.<sup>6 7</sup> Under such circumstances, the abundance of carbonate becomes higher and one may consider the analysis of carbonate instead of carbon dioxide gas itself. For this purpose, a highly selective receptor for carbonate is required to reduce interference from other species in natural water samples. Indeed, carbonate selective receptors have been developed that bind with carbonate through hydrogen bonding or reversible covalent bonding.<sup>8-10</sup> A few years ago, a new ionophore with a very high selectivity for carbonate was developed by the group of Nam and was successfully applied in ion-selective electrodes to determine oceanic carbon dioxide.<sup>11</sup> The compound contains two trifluoroacetophenone moieties that interact selectively with CO<sub>3</sub><sup>2-</sup> to form a 1:1 complex. By utilizing this ionophore, we report here on a CO<sub>2</sub> selective optical sensor that works on the basis of a selective molecular recognition. To our knowledge, this is the first report of such an optical CO<sub>2</sub> sensor system.<sup>12,13</sup>

A traditional PVC-Plasticizer bulk optode usually consists of a pH indicator, also referred to as chromoionophore, an ion-exchanger, and an ionophore specific for the analyte. <sup>14,15</sup> As optical counterparts of ion-selective electrodes, optodes may be developed for the analysis of ionic species. The response mechanism depends on a mass transfer between the sensing film (or particle) and the sample. There are two key modes of mass transfer for ion-selective optodes, one being ion-exchange between sample analyte and protons or another reference ion from the sensing phase; the other the coextraction of analyte together with a counter ion from the sample into the sensing phase. Either way, the degree of protonation of an indicator dye (also called chromoionophore) changes as a function of analyte concentration. These response principles may be optimized by adjusting the sensing phase composition, including the use of ion-exchangers. <sup>14</sup> A wide range of chromoionophores is commercially available and the associated pKa values can be determined by the so called sandwich membrane method. <sup>16</sup>

This paper introduces a carbon dioxide sensing principle based conceptually on the concurrent extraction of CO<sub>2</sub> and H<sub>2</sub>O into the sensing phase, yielding carbonate and protons as part of the established dissociation process that are each selectively recognized by an ionophore.

## 8.2 Theory

Carbon dioxide is known to undergo pH controlled dissociation reactions. The value of  $K_{a1}$  relates to the sum of hydrated carbon dioxide and carbonic acid, while the carbonic acid amounts to just 0.2% of this sum, so the relevant equilibria can be expressed as:

$$H_2CO_3 \stackrel{K_{a1}}{\iff} H^+ + HCO_3^- \stackrel{K_{a2}}{\iff} 2H^+ + CO_3^{2-}$$
 (8.1)

Consequently, the carbon dioxide activity in water is related to the carbonate ion activity as a function of the solution pH and the two stepwise acid dissociation constants as follows:

$$a_{CO_2} = \frac{a_{CO_3^{2-}}(a_{H^+})^2}{K_{a1}K_{a2}}$$
(8.2)

Ionophore-based optical sensors often make use of a H<sup>+</sup>-selective chromoionophore (a lipophilic pH indicator, Ind<sup>-</sup>) to visualize the ion extraction process. Anionic analytes A<sup>z-</sup> may be measured according to the following electrolyte coextraction equilibrium, in which the aqueous anion is extracted together with protons into a solvent polymeric phase that contains an anion ionophore, L, that complexes and stabilizes the analyte with a complex stoichiometry 1: n, and the indicator that binds the proton:

$$A^{z-}(aq) + nL(org) + zH^{+}(aq) + zInd^{-}(org) \stackrel{K_{coex}}{\Longleftrightarrow} AL_{n}^{z-}(org) + zIndH(org)$$
(8.3)

The protonation of the indicator is followed spectroscopically and indicates the level of extraction. If ion pairing in the sensing phase is inconsequential, the corresponding coextraction constant may be formulated:

$$K_{coex} = \frac{1}{a_{A^{z-}}(a_{H^{+}})^{z}} \frac{[AL_{n}^{z-}][IndH]^{z}}{[L]^{n}[Ind^{-}]^{z}}$$
(8.4)

where species in square brackets denote concentrations in the sensing phase, while aqueous species are indicated with activity symbols. The mass balance condition for the ionophore is written as:

$$L_T = [L] + n[AL_n^{z-}] (8.5)$$

where  $L_T$  is the total ionophore concentration in the membrane. Similarly, the charge balance equation is given as:

$$R_T = [Ind^-] + z[AL_n^{z-}] \tag{8.6}$$

where  $R_T$  is the anion-exchanger concentration. Eqn. 8.4 to 8.6, together with the relevant mole fractions of indicator ([IndH] =  $(1-\alpha)$  Ind $_T$ ; [Ind $^-$ ] =  $\alpha$  Ind $_T$ ) gives the response function of the optical sensor as a function of the mole fraction of unprotonated indicator dye,  $\alpha$ :

$$a_{A^{z-}}(a_{H^{+}})^{z} = \left(\frac{1-\alpha}{\alpha}\right)^{z} \frac{R_{T} - \alpha \operatorname{Ind}_{T}}{zK_{\operatorname{coex}}\left(L_{T} - \frac{n}{z}(R_{T} - \alpha \operatorname{Ind}_{T})\right)^{n}}$$
(8.7)

If the analyte is the carbonate anion, eq 7 may equally be expressed as a function of carbon dioxide concentration by incorporating eq 2 to give an optode response function that is now independent of solution pH:

$$a_{CO_2} = \left(\frac{1-\alpha}{\alpha}\right)^2 \frac{R_T - \alpha Ind_T}{2K_{a1}K_{a2}K_{coex}^I \left(L_T - \frac{1}{2}(R_T - \alpha Ind_T)\right)^2}$$
(8.8)

Of course, the ratio of carbon dioxide activity and carbonate ion activity that give the same optode response are directly related in eq 2 and depends on the solution pH:

$$\frac{a_{CO_2}}{a_{CO_3^{2^-}}} = \frac{\left(a_{H^+}\right)^2}{K_{a1}K_{a2}} \tag{8.9}$$

Quite generally, the selectivity of an ion optode can be conveniently expressed as the ratio of the two anion activities (analyte ion activity divided by the interfering ion activity) that, separately measured, give the value of  $\alpha$  (which is used as a normalized sensor response). The carbon dioxide response was obtained by considering eq 7 for carbonate and by inserting eq 2, while the interfering ion response was described, simplistically, by assuming that the interfering anion forming 1:1 complexes with the ionophore. This latter assumption is arbitrary and was not tested experimentally, but note that the stoichiometry changes will not significantly change the observed sensor selectivity for a given sensing phase composition. The selectivity of the sensor for carbon dioxide over another potentially interfering anion is subsequently predicted as follows: <sup>18</sup>

$$k_{CO_{2},J}^{OSel} = \frac{a_{CO_{2}}}{a_{J^{n-}}} = \left(\frac{1-\alpha}{\alpha}\right)^{2-z} \left(a_{H^{+}}\right)^{z} \frac{zK_{coex}^{J} \left(L_{T} - \frac{1}{z}(R_{T} - \alpha Ind_{T})\right)^{z}}{2K_{a1}K_{a2}K_{coex}^{I} \left(L_{T} - \frac{1}{2}(R_{T} - \alpha Ind_{T})\right)^{2}}$$
(8.10)

where  $k^{Osel}$  is the selectivity coefficient and the overall extraction constant for carbon dioxide is denoted with a superscript I, while the one for the interfering ion is labeled with J. For divalent interfering anions, eq 10 simplifies to the following relationship:

$$k_{CO_2,J}^{OSel} = \frac{a_{CO_2}}{a_{J^{n-}}} = \frac{K_{coex}^J \left(a_{H^+}\right)^2}{K_{a1} K_{a2} K_{coex}^I}$$
(8.11)

While monovalent interfering ions give the following expression for the selectivity coefficient:

$$k_{CO_{2},J}^{OSel} = \frac{a_{CO_{2}}}{a_{J^{-}}} = \frac{a_{H^{+}}}{K_{a1}K_{a2}} \frac{1 - \alpha}{\alpha} \frac{K_{coex}^{J} \left( L_{T} - (R_{T} - \alpha Ind_{T}) \right)}{2K_{coex}^{I} \left( L_{T} - \frac{1}{2} (R_{T} - \alpha Ind_{T}) \right)^{2}}$$
(8.12)

which can be approximated as follows for sensing phases where the ionophore is in significant excess to the ion-exchanger and indicator:

$$k_{CO_2,J}^{OSel} \approx \frac{a_{H^+}}{K_{al}K_{a2}} \frac{1 - \alpha}{\alpha} \frac{K_{coex}^J}{2K_{coex}^I L_T}$$
 (8.13)

Note that the value of the selectivity coefficient for carbon dioxide over all other ions is always dependent on the solution pH. The selectivity increases with increasing pH and deteriorates under acidic conditions. Interference by other competing anions under acidic conditions could be largely eliminated by coupling the above mentioned sensor equilibrium to a gas permeation step, for example by the use of a gas and humidity permeable membrane placed on the sensing phase or by an intermediate gaseous phase between the aqueous sample and polymeric sensing phase.

Alternatively, the sensor approach is expected to work equally well for gas phase carbon dioxide sensing, in which case the sensor response is expected to be co-dependent on the humidity of the gas phase. For this case, the overall equilibrium (adapted from eq 3) can be rewritten as:

$$CO_2(g) + H_2O(g) + nL(org) + zInd^-(org) \Leftrightarrow CO_3L_n^{z-}(org) + 2IndH(org)$$
(8.14)

The partition coefficient of carbon dioxide gas between the gas and sensing phase,

$$K_{CO_2} = \frac{a_{CO_2}(org)}{PCO_2} \tag{8.15}$$

is combined with a similar relationship for the partitioning of humidity,

$$K_{H_2O} = \frac{a_{H_2O}(org)}{PH_2O} \tag{8.16}$$

to give the sensor response to  $PCO_2$  in the gas phase:

$$PCO_{2} = \left(\frac{1-\alpha}{\alpha}\right)^{2} \frac{R_{T} - \alpha Ind_{T}}{2K_{overall}\left(L_{T} - \frac{1}{2}(R_{T} - \alpha Ind_{T})\right)^{2}}$$
(8.17)

where *K*<sub>overall</sub> is a constant incorporating the partition coefficients for H<sub>2</sub>O and CO<sub>2</sub> as well as the acidity constant of the indicator and stability constant of the carbonate ionophore. One may write down a thermodynamic cycle to show that a three phase system consisting of an aqueous electrolyte in contact with a gas phase and the sensing phase. If all phases are at equilibrium, one should obtain the same optical sensing response, independent of whether this response is related to the carbon dioxide partial pressure in the gas phase or aqueous phase. A reduction of humidity in the gas phase is expected to attenuate the sensor response.

### 8.3 Experimental Section

**8.3.1 Reagents.** Aqueous solutions were prepared by dissolving the appropriate salts in Milli-Q purified water. All solvents and reagents used were analytically pure unless otherwise specified. Poly(vinyl-chloride) (PVC, high molecular weight), o-nitrophenyl-octyl-ether (o-NPOE), bis(2-ethylhexyl) adipate (DOA), chromoionophore IV (ETH 2412), tridodecylmethylammonium chloride (TDDMACl), 2-Amino-2-hydroxymethyl-propane-1,3-diol (Tris) and tetrahydrofuran (THF) were obtained from Sigma-Aldrich. Carbon dioxide (5.0 vol-% in

nitrogen) and nitrogen gas (99.9 vol-%) were purchased from PenGas in Switzerland. Carbonate selective ionophore VII was purchased from Fluka.

**8.3.2 Apparatus.** pH values were determined using a Metrohm 826 pH meter. Spectrophotometric studies on optode membranes were performed with a conventional double-beam spectrophotometer (Perkin-Elmer Lambda 2 UV/Vis spectrophotometer). The membrane was spin-coated on a glass plate that was mounted into the measuring cell and placed into the spectrophotometer. The flow cell has been previously described<sup>14</sup>, see scheme S8.1 in the supporting information, but the second glass plate was here left uncoated. CO<sub>2</sub> and N<sub>2</sub> gas were mixed in a gas mixing chamber with a magnetic stirring bar and the gas mixture was subsequently bubbled into a sample compartment in contact with the sample that was passed into the measuring cell fluidically. The measuring compartment was filled with the same gas mixture and the tubing that connected the sample compartment and measuring compartment was covered with the same gas mixture to ensure no CO<sub>2</sub> diffusion during the transportation and measurement. The flow rate was controlled by a four-channel IPC Microprocessor controlled dispensing pump from ISMATEC. All experiments were done at 25±1 °C unless otherwise stated.

8.3.3 Membranes and Measurements. For optode membrane preparation, a total amount of 140 mg high molecular weight PVC and o-NPOE (1:2 by weight), 15 mmol/kg (total mass of sensing film) ETH 2412 (Hind), 15 mmol/kg TDDMACl and 15 mmol/kg carbonate selective ionophore were dissolved in 1 ml of THF. A minor mismatch between ion-exchanger and indicator has only a minor influence on optical sensor response, unlike the behavior of their potentiometric counterparts where complete ionophore-mediated selectivity breakdown may occur. <sup>14</sup> The cocktail was then spin-coated on a specially designed glass plate to allow evaporation of THF. The membrane was washed with 0.05 M NaOH solution before any measurement. The carbonate-selective membranes were prepared by dissolving the mixture composed of 8.3 mg of carbonate ionophore VII, 60 mg of PVC, 2 mg of TDDMACl and 100 μL DOA in 2 ml of THF. The cocktail solution was then poured into a glass ring (22 mm in diameter) placed on a slide glass and dried overnight at room temperature under a dust-free environment. Small disks were punched from the cast films and mounted in Ostec electrode bodies (Ostec, Sarganz, Switzerland).

All solutions or gases were pumped through the cell at 3 ml/min flow rate. To ensure the carbon dioxide equilibrium between solution and the air above, pH value of the hydrogen carbonate solution  $(10^{-3} \text{ M})$  was monitored along the measurement. Different level of  $CO_2$  and  $N_2$  were first mixed in the gas mixing compartment and then bubbled through the hydrogen carbonate solution  $(10^{-3} \text{ M})$  where the pH and carbonate response were measured with a pH probe and carbonate selective electrodes. After the both the pH and carbonate response from the ion-selective electrodes became stable, the solution was pumped into the cell through the plastic tubing placed inside another in which gas with the same  $PCO_2$  value was flowing as protecting layer. The absorbance of the membrane at 550 nm was measured. For the measurement in gaseous phase, instead of using solution, the air above the solution was pumped into the cell. For selectivity evaluation,  $H_3BO_3$ -Na $H_2PO_4$  buffer solutions  $(10^{-3} \text{ M})$  with fixed anion concentration (0.01M) were prepared and pumped through the cell for the measurement under the protection of  $N_2$  with pH values increasing by addition of NaOH (1 M). To show that the sensor response to  $CO_2$  was pH dependent, a 0.01M NaHCO $_3$  solution was saturated with  $CO_2$  (PCO $_2$ =0.05) to reach a stable pH value. Afterwards, the solution was diluted with water and reverted to original PCO $_2$  value to reach a different pH point. At each point the absorbance at 550 nm was recorded and converted to 1- $\alpha$  value. To characterize the response time and reproducibility of the sensor, the absorbance of the membrane at 550 nm was recorded while the partial pressure of  $CO_2$  was switched between 0.004 and 0.05 atm.

To evaluate the influence of different humidity to the sensor response, dry  $CO_2$  gas  $(PCO_2 = 0.05 \text{ atm})$  and  $CO_2$  gas with 100% relative humidity at 25  $^{\circ}$ C were guided into the gas mixing chamber and the relative humidity was controlled by changing the flow rate of the above mentioned two incoming  $CO_2$  and measuring the relative humidity with a commercial hygrometer. After mixing of the gas, it was guided

into the measuring cell and the sensor response was recorded. The aqueous sample in Scheme S8.1 was not needed here, instead, a hygrometer was placed inside the sample container to determine the relative humidity of the gas mixture.

$$CO_{2}(g) \xrightarrow{H_{2}O} CO_{2}(aq) \xrightarrow{H_{2}O} 2 \overset{H^{+}(aq)}{CO_{3}^{2-}(aq)}$$

$$CO_{2}(g) \xrightarrow{H_{2}O} CO_{2}(aq) \xrightarrow{H_{2}O} 2 \overset{H^{+}(aq)}{CO_{3}^{2-}(aq)}$$

$$CO_{2}(aq) \xrightarrow{Q} CO_{2}(aq) \xrightarrow{Q} CO_{2}(aq) \xrightarrow{Q} CO_{3}^{2-}(aq)$$

$$CO_{3}(aq) \xrightarrow{Q} CO_{2}(aq) \xrightarrow{Q} CO_{3}(aq) \xrightarrow{Q} CO_{3}(aq)$$

**Figure. 8.1** Illustration of sensor mechanism in aqueous and gaseous phase and interaction between the carbonate selective ionophore and CO<sub>3</sub><sup>2-</sup>. Before exposure to carbon dioxide, the deprotonated, negatively charged indicator Ind<sup>-</sup> form the counterion of the anion-exchanger R<sup>+</sup> in the sensing film, while the carbonate ionophore L remains uncomplexed and therefore electrically neutral. Upon carbon dioxide extraction, this counterion is replaced by the doubly negatively charged carbonate–ionophore complex, while the indicator becomes the neutral, protonated Hind species.

The influence of temperature to the optode response was determined by pumping the solution saturated with  $CO_2$  ( $PCO_2 = 0.05$  atm) at different temperatures (37-19°C) into the measuring cell where the absorption intensity of the membrane at 550 nm was recorded. The temperature of the solution inside the measuring cell was controlled by a water bath and determined in situ with a thermocouple probe (type J).

### 8.4 Results and Discussion

The speciation of carbon dioxide in aqueous solution depends on its partial pressure, temperature and acid base reactions within the solution. At varying ionic strength and pH, carbon dioxide co-exists with different concentrations of  $HCO_3^{-1}$  and  $CO_3^{-2}$ . In turn, the solution pH and the activity of  $CO_3^{-2}$  dictate the partial pressure of  $CO_2$ . A direct, selective detection of carbon dioxide is possible by extracting the carbonate species together with protons into a sensing film that contains selective receptors for both. Figure 8.1 illustrates the sensing mechanism for the solution and gas phase. A carbonate-selective ionophore containing two trifluoroacetyl groups anchored onto a steroid backbone to form a molecular tweezer geometry was previously introduced by Nam and coworkers for use in ion-selective electrodes. Indeed, the selectivity of membranes containing this receptor was demonstrated to be very attractive, with carbonate measurements

demonstrated in undiluted sea water samples.<sup>11</sup> This tweezer type ionophore has now become commercially available and explored in an optical carbonate sensor.

As explained in the theoretical section above, a classical bulk optode operating on the basis of the coextraction of an anion with protons should give rise to an optical sensor for the direct detection of  $PCO_2$ , independent of solution pH. This sensing principle is attractive because optical detection can be achieved via concentration changes of the lipophilic pH indicator. Protonation of the indicator is ideally only possible by concurrent extraction of carbonate anions and protons.

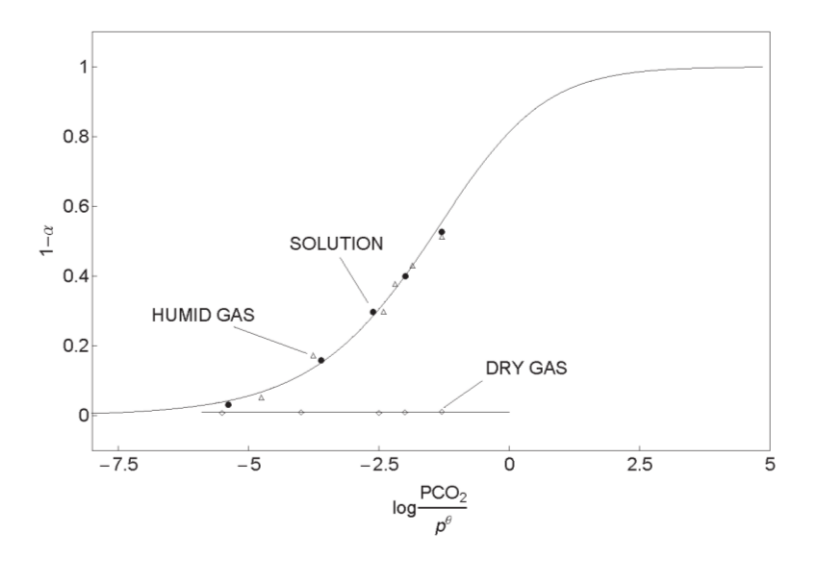


**Figure. 8.2** Calibration curves of the sensor response to  $CO_2$  in a  $10^{-3}$  M hydrogen carbonate solution, the gas phase above  $10^{-3}$  M hydrogen carbonate solution, and dry  $CO_2 + N_2$  gas mixture with different levels of  $PCO_2$ . The absorbance of the sensing film at 550 nm was converted into the mole fraction of protonated indicator,  $1-\alpha$ , and shown as symbols with theoretical expectations according to eq 5 (lines). The term  $p^{\Theta}$  on the x-axis is the partial pressure under standard conditions (1 atm).

Initial experiments explored the combination of the carbonate ionophore with the established lipophilic nile blue derivative, ETH 5294, which exhibits a pKa value of about 14.8 in a PVC–oNPOE sensing phase. However, extraction of carbon dioxide did only visibly occur above a concentration of 0.07 atm, which is not sufficiently sensitive for practical use. Consequently, a lipophilic pH indicator of a much higher basicity was required to shift the measuring range to environmentally relevant concentrations. An electrically charged base (referring to the non-protonated form) is expected to increase its pKa quite dramatically in a non-polar organic solvent compared to water, since the dissociation equilibrium results in a separation of charge. Indeed, such electrically charged H<sup>+</sup>-chromoionophores are commercially available, and their pK<sub>a</sub> values were quantified in the polymeric sensing phase with the so-called sandwich membrane technique. The chromoionophore ETH 2412, which exhibits a pKa of 17.0 in PVC–DOS and 20.5 in PVC–NPOE, <sup>16</sup> was chosen for further studies. The use of an electrically charged chromoionophore, along with a neutral carbonate ionophore, necessitates the addition of a lipophilic anion-exchanger into the sensing film to provide for the cationic counterions of the unprotonated dye. As carbon dioxide is extracted along with protons, the anion-exchanger forms the counterions of the anionic ionophore–carbonate complex, instead that of

chromoionophore which now becomes neutral. The higher pKa in PVC-NPOE appeared to be more attractive in view of attaining an adequate operational measuring range and was selected over PVC-DOS.

After the sensing film was solvent cast on a glass plate and fitted into flow cell system, it was washed with dilute NaOH solution to assure a complete deprotonation of the chromoionophore in the film. This was especially important for the gas phase measurements, where contact with aqueous electrolyte was no longer possible during measurement. To perform carbon dioxide measurements appropriately, the initial 5 vol% CO<sub>2</sub> gas was diluted with nitrogen and equilibrated with the aqueous solution in a closed cell, which was subsequently

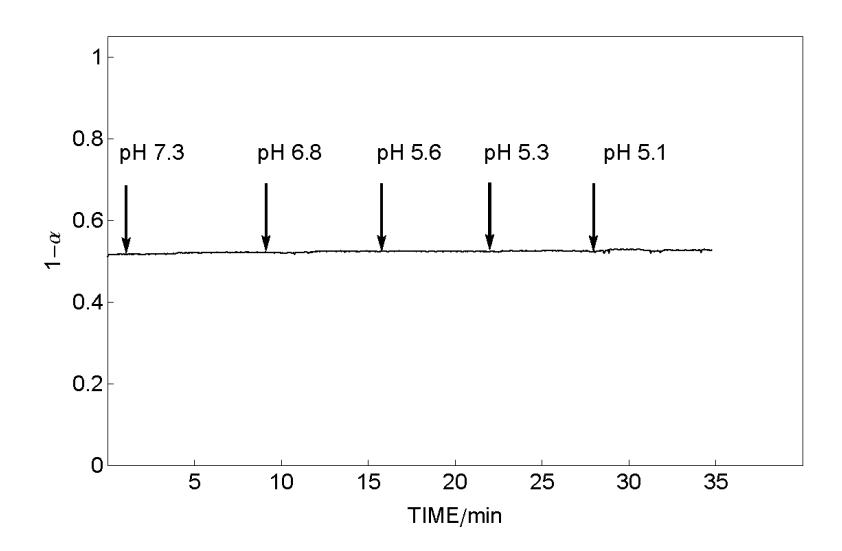
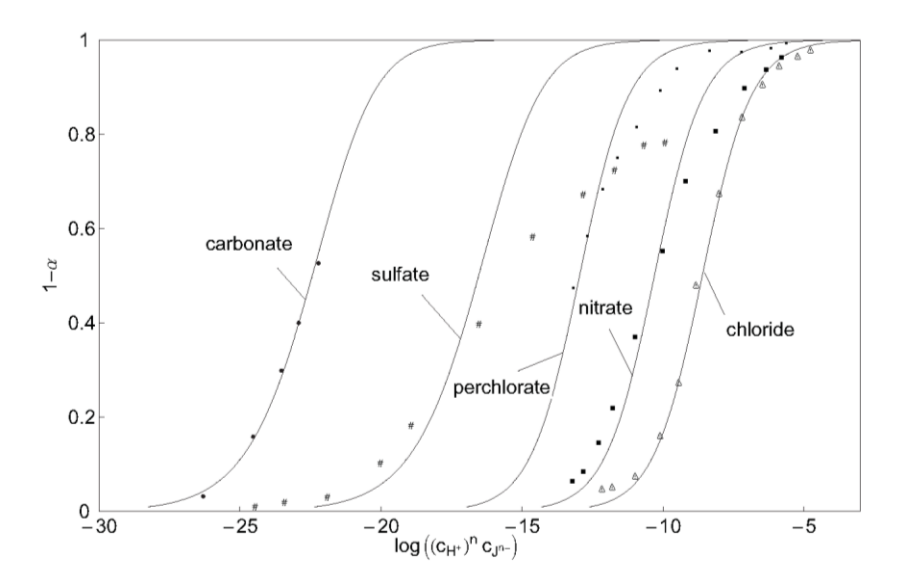


Figure. 8.3 Evidence showing the pH independence of the carbon dioxide sensor in accordance to eq 6.  $PCO_2$  was fixed at 0.05 atm above the hydrogen carbonate solution ( $10^{-3}$  M). The solution was diluted by addition of water to reach different pH values while maintaining an equilibration with the contacting gas phase.

guided to the measurement cell. The corresponding optode response curves to aqueous carbon dioxide were obtained by determining the  $\alpha$  value from the absorbance changes of the film and are shown in Figure 8.2. The use of the more basic chromoionophore indeed shifts the measuring range to lower  $PCO_2$  values. Atmospheric  $PCO_2$  is currently at about 380 ppm or 0.04% by volume. The lowest concentration measured and presented in Figure 8.2 is  $3 \times 10^{-4}$  % by volume, while the detection limit (3 x SD of the background) is estimated as 200 ppm. This appears to be adequate for routine environmental monitoring, although a further optimization of the measuring range would certainly be possible if needed by adjustment of the sensing film composition.

Eqn. 8.8 postulates that if the optical sensor responds to the product of the carbonate ion concentration and the square of the hydrogen ion activity, this should be independent of pH, i.e., the  $\alpha$  value (mole fraction of unprotonated indicator, calculation shown in the supporting information) should be the same at different pH value as long as  $PCO_2$  stays constant. To confirm this assumption experimentally, the absorbance of the sensing film at 550 nm was recorded at the same partial pressure of carbon dioxide (0.05 atm) while the sodium hydrogen carbonate solution was diluted with water to reach lower pH values. At each dilution step, the solution was equilibrated with carbon dioxide from the gas phase before measurement. If the sensor response would be pH dependent, one would expect



**Figure. 8.4** Response of the optode membrane to pH (symbols) in 10<sup>-3</sup> M H<sub>3</sub>BO<sub>3</sub>-NaH<sub>2</sub>PO<sub>4</sub> buffer solutions containing the indicated anions fixed at 0.01 M. The pH of the solution was increased by adding 1 M NaOH.

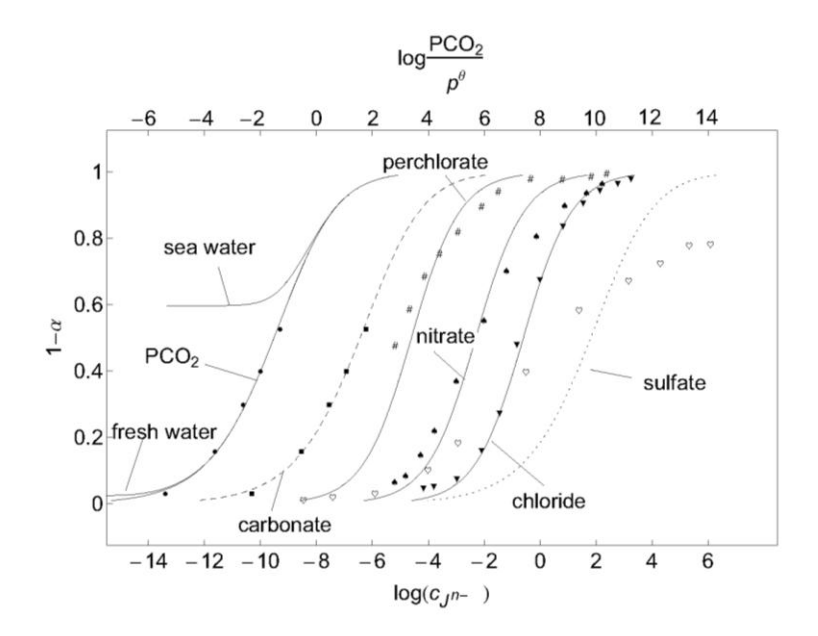


**Figure. 8.5** Presentation of sensor selectivity for carbon dioxide at pH 8 using the theoretical curves from Fig. 8.4. The *P*CO<sub>2</sub> responses for seawater and freshwater solutions relate to the upper x-axis while the anion concentrations are described by the values on the lower x-axis. The carbonate ion is added to compare the selectivity between this anion and other potentially interfering anion species. It should not be used to infer a sensor selectivity of carbon dioxide over carbonate, since this shift is only due to the relevant protonation equilibria (see text).

a dramatic decrease of  $\alpha$  value. However, as shown in Figure 8.3, the  $\alpha$  value was indeed found to be independent of pH, supporting the optode response mechanism proposed here.

The tweezer type ionophore was demonstrated to exhibit excellent selectivity when used in ion-selective electrode membranes, but the ionophore had, so far, never been explored in an optical sensor or for the direct detection of carbon dioxide. The selectivity was characterized by evaluating the response to solutions of separate electrolytes. Specifically, and in agreement with earlier procedures, the measurements were performed in contact with buffer solutions at varying pH but at a fixed 0.01 M anion concentration. Figure 8.4 shows the data together with the theoretical curves according to eq 7 to obtain the coextraction constants for each anion–proton pair. The curves correlate well with experimental data except for sulfate, which may be due to partial protonation of this anion in the sensing phase, which the theory is not considering.

For a better representation of selectivity a plot of the sensor response against the logarithm of analyte activity at pH 8 is shown in Figure 8.5. As pointed out in Eqn. 8.10, even though the  $CO_2$  response is pH independent, the selectivity depends on the sample pH. At pH 8 the selectivity coefficient for carbonate over chloride is around 6 orders of magnitude, which agrees with the previous report for this tweezer type ionophore in ion-selective membranes. Since Eqn. 8.10 is used to express carbon dioxide, the selectivity for carbonate and  $CO_2$  will run in the opposite direction. For increasing pH the selectivity for  $CO_2$  improves while for carbonate it deteriorates, and vice versa for lower pH values (see supporting information). The chloride concentration in surface fresh water is typically in a range of 0.1 to 0.6 mmol/L,  $^{21,22}$  and Figure 8.5 shows that these conditions give minimal interference ( $1-\alpha \approx 0.02$  to 0.05). This means that chloride interference in fresh water will be sufficiently suppressed for direct  $CO_2$  measurement at the typical environmental pH of 8. However, seawater contains much more chloride than fresh water (average: 545 mmol/L)<sup>21</sup> and will cause severe interference at the same pH. At higher pH, the selectivity improves (see supporting information). This may necessitate the placement of a gas permeable membrane on the sensing film, essentially blocking the extraction of ionic species into the sensing film. While this is a common strategy for many potentiometric carbon dioxide sensors, the selectivity of the system described here is expected to be more attractive based on a direct molecular recognition of the analyte species.<sup>23</sup>

As shown in Figure 8.2, the sensor responds to humid carbon dioxide gas in a similar manner as to dissolved carbon dioxide. The observed difference points to a diminished water activity in the gas phase. Indeed, removing the humidity completely by using dry gas completely suppresses the dissociation equilibria that are required to form the carbonate and proton species that are required for the sensor response. This is conceptual evidence that a gas permeable membrane placed between the sample and the sensing phase will allow one to reliable measure carbon dioxide even in the high chloride concentration of seawater.

The response time of the membrane is affected by diffusion process and also the thickness of the membrane. Response time is expected to decrease with a kinetically rapid coextraction (and hence molecular binding/dissociation process) and a decreasing thickness of the sensing film. Even though the sensing films studied here did not exhibit optimal thickness (3.0 µm via absorbance measurements and applying

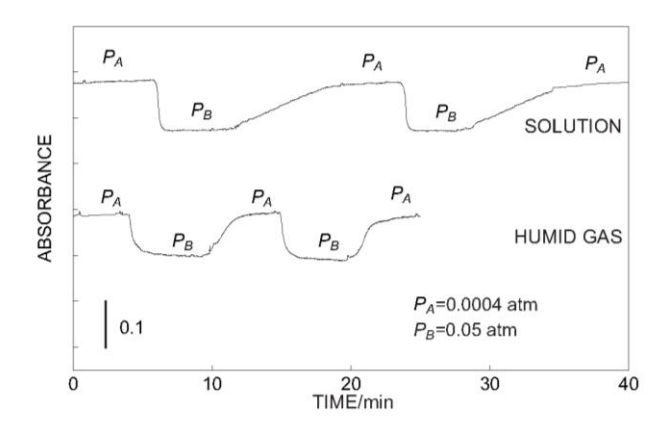


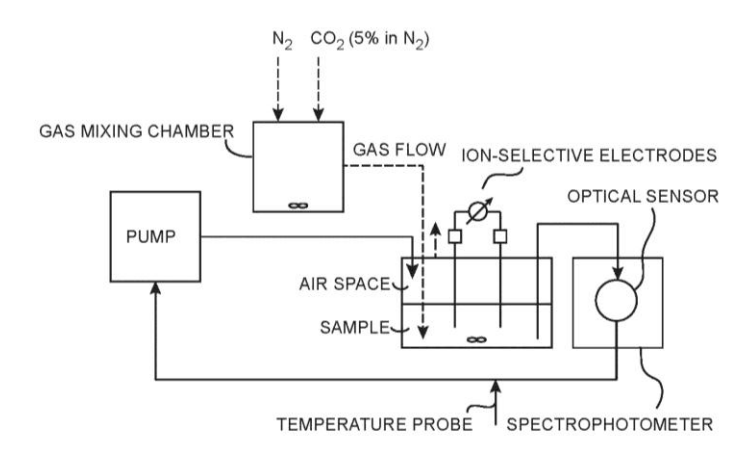
**Figure. 8.6** Top: response time of the sensor in contact with an aqueous  $10^{-3}$  M hydrogen carbonate solution equilibrated with  $PCO_2$  of 0.004 atm and 0.05 atm. Bottom: corresponding experiment in direct contact with a humid gas phase containing the same levels of  $PCO_2$ .

Beer's law), a reasonable response time was observed, see Figure 8.6, that suggests mass transport is limited by diffusion in the sensing phase. For this experiment, the carbon dioxide partial pressure was alternated between 0.004 and 0.05 atm and the aqueous phase was allowed to equilibrate with the aqueous sample before it was fluidically guided into the flow cell to record the sensor response. Note that the measurement in gaseous phase shows a shorter response time than that in solution, suggesting that the optical sensor response is largely diffusion limited.

### 8.5 Conclusion

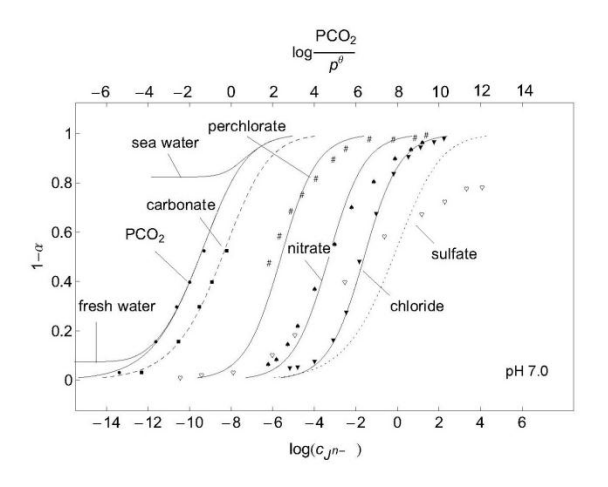
A novel direct carbon dioxide sensing method has been presented. Unlike conventional methods based on Severinghaus's principle, molecular recognition between carbonate and a tweezer type ionophore is used in plasticized PVC films. The optode membrane shows a detection limit of 200 ppm which should be adequate for routine environmental monitoring. A selectivity analysis shows a satisfactory result for practical CO<sub>2</sub> monitoring in fresh water. Oceanic water usually contains several hundred mmol/L of chloride ions, thus the chloride interference is detrimental. However, this may be overcome by a direct sensing of a gaseous phase in equilibrium with the sample solution. Indeed, it is conceptually demonstrated that the optode sensing film not only responded to aqueous CO<sub>2</sub> but also to humid CO<sub>2</sub> gas.

### **8.6 Supporting Information for Chapter 8**



**Scheme S8.1.** Representation of the experimental apparatus. The sample compartment is placed in a thermostated water bath (not shown). A photograph of the setup is shown below.





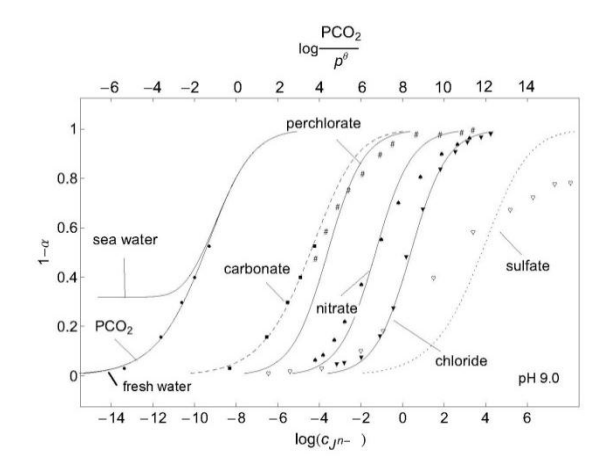


**Figure S8.1.** Presentation of sensor selectivity for carbon dioxide at pH 7.0 (left) and pH 9.0 (right) using the theoretical curves from Fig. 8.5. The *P*CO<sub>2</sub> response in seawater and freshwater response relates to the upper x-axis and the ion concentrations are denoted on the lower x-axis.

According to theory the selectivity of the sensor is pH dependent. It was shown in Figure 8.5 that at pH 8 the chloride from fresh water has little interference for carbon dioxide monitoring while the chloride interference from sea water could be detrimental. Such interference can be suppressed when we measure at a higher sample pH, e.g. pH 9.0, and in turn, lower pH, e.g. pH 7.0, will cause more interference from other species as shown in Figure S8.1.

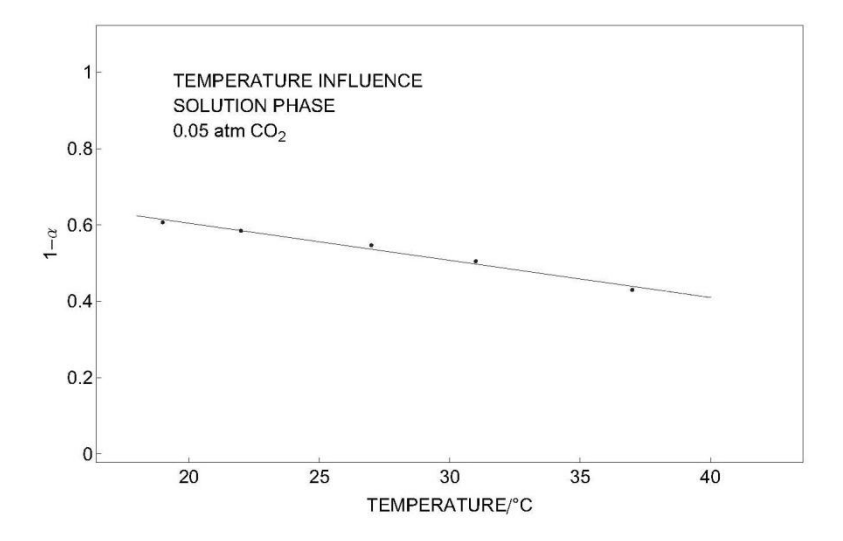


Figure S8.2. Influence of temperature on the optode response in solution.  $CO_2$  ( $PCO_2 = 0.05$  atm) at different temperatures (37-19 °C) was pumped into the measuring cell where the absorption intensity of the membrane at 550 nm was recorded and converted into 1- $\alpha$  value. The temperature of the solution inside the measuring cell was controlled by a water bath and determined in situ with a thermocouple probe (type J).

Since the carbon dioxide equilibrium in aqueous solution is affected by temperature, the sensor response should also vary with it. Indeed as shown in Fig. S8.2, the response of the optical sensor decreases linearly as the temperature is increased.

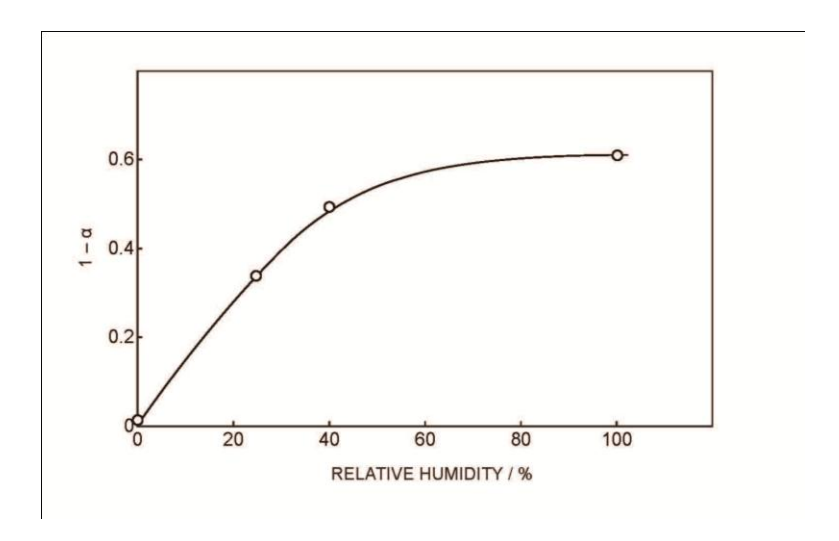


Figure S8.3. Dependence of the  $CO_2$  sensor response to the humidity of the air when working in the gaseous phase.  $CO_2$  gas ( $PCO_2 = 0.05$  atm) with different relative humidity at 25 °C was guided into the optical sensor and the absorbance at 550 nm was recorded.

In order to work in the gaseous phase, water is indispensable because the sensing principle is based on the coextraction of proton and carbonate ions after CO<sub>2</sub> is dissolved in water, either in solution or in gas phase. From Fig. S8.3 we can see that the sensor is more sensitive to humidity at lower humidity levels (<50%), and as water gets more saturated, the response increases more slowly to approach the response value in solution.

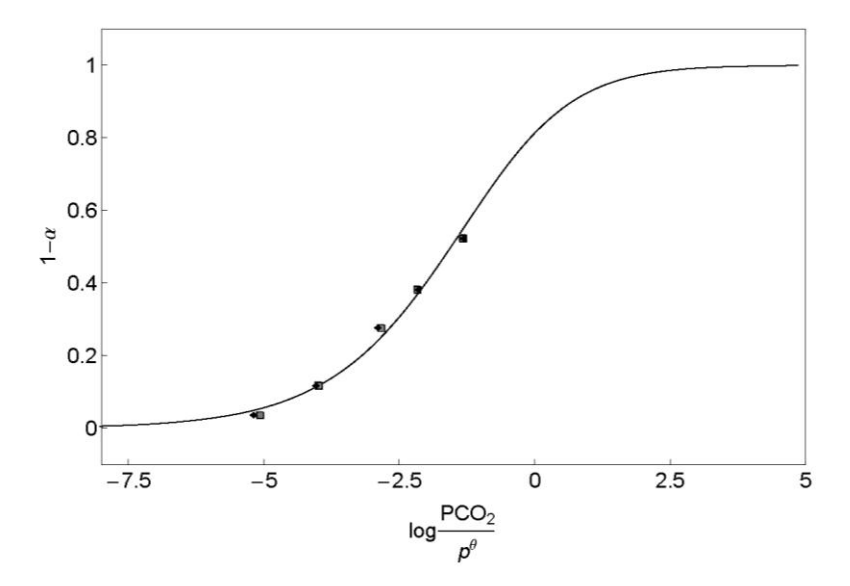


Figure S8.4. Comparison of the accuracy between the optical  $CO_2$  sensor and ion selective electrodes. The squared dots represent the optical  $CO_2$  sensor response related to  $CO_2$  partial pressure calculated from the pH value while the diamond dots were related to the potentiometrically determined  $CO_2$  partial pressure.

To show the accuracy of the sensor described in this work, a comparison with other methods is necessary. Potentiometric method is chosen and the CO<sub>2</sub> partial pressure was measured using a carbonate selective electrode and a pH electrode independently. The potential of these two electrodes were measured against the same reference electrode in the same solution, therefore the difference between the two electrodes potential should reflect the change in carbonic acid activity in the solution which could be thermodynamically related to CO<sub>2</sub> partial pressure. Fig. S8.5 shows the optical CO<sub>2</sub> sensor response related to potentiometrically determined CO<sub>2</sub> partial pressure and calculated value from pH of the solution. Obviously the accuracy of the optical CO<sub>2</sub> sensor is very good.

The  $\alpha$  value in this work was determined using the following equation:

$$\alpha = \frac{A_D - A}{A_D - A_P}$$

where  $A_D$  is the absorbance value of the sensing film where the chromoionophore exists in its fully deprotonated form at 550 nm,  $A_P$  is the absorbance value of the sensing film where the chromoionophore exists in its fully protonated form at 550 nm, and A is the absorbance value of the sensing film at 550 nm.

To determine the thickness of the optical sensing film, a solution of the chromoionophore ETH 2412 was prepared in THF  $(7.5 \times 10^{-5} \text{M})$  containing one drop of 1M NaOH and its absorbance value at 550 nm was measured to get the corresponding extinction coefficient, which was applied to Beer's law together with  $A_D$  to calculate the thickness.

### 8.7 References for Chapter 8

- (1) Severinghaus, J. W. J. Appl. Physiol. 2004, 97, 1599.
- (2) Herman, P.; Murtaza, Z.; Lakowicz, J. Anal. Biochem. 1999, 272, 87.
- (3) Burke, C. S.; Markey, A.; Nooney, R. I.; Byrne, P.; McDonagh, C. Sensors and Actuators B: Chemical 2006, 119, 288.
- (4) Abderrahim, H.; Berrebia, M.; Hamou, A.; Kherief, H.; Zanoun, Y.; Zenata, K. J. Mater. Environ. Sci. 2011, 2, 94.
- (5) Plata, M.; Hernando, J.; Zougagh, M.; Contento, A.; Villasenor, M.; Sanchezrojas, J.; Rios, A. Sensors and Actuators B: Chemical 2008, 134, 245.
- (6) Severinghaus, J. W.; Bradley, A. F. J. Appl. Physiol. 1958, 13, 515.
- (7) Suzuki, H.; Arakawa, H. Anal. Chem. 1999, 71, 1737.
- (8) Mar ń-Garc á, L.; Frontana-Uribe, B. A.; Reyes-Grajeda, J. P.; Stojanoff, V.; Serrano-Posada, H. J.; Moreno, A. Crystal Growth & Design 2008, 8, 1340.
- (9) Makarychev-Mikhailov, S.; Goryacheva, O.; Mortensen, J.; Legin, A.; Levitchev, S.; Vlasov, Y. Electroanalysis 2003, 15, 1291.
- (10) Guo, Y.; Shao, S.-J.; Xu, J.; Shi, Y.-P.; Jiang, S.-X. Inorganic Chemistry Communications 2004, 7, 333.
- (11) Choi, Y. S.; Lvova, L.; Shin, J. H.; Oh, S. H.; Lee, C. S.; Kim, B. H.; Cha, G. S.; Nam, H. Anal. Chem. 2002, 74, 2435.
- (12) Fabbrizzi, L.; Leone, A.; Taglietti, A. Angew. Chem. Int. Ed. 2001, 40, 3066.
- (13) Baldini, L.; Melegari, M.; Bagnacani, V.; Casnati, A.; Dalcanale, E.; Sansone, F.; Ungaro, R. J. Org. Chem. 2011, 76, 3720.
- (14) Bakker, E.; Bühlmann, P.; Pretsch, E. Chem. Rev. 1997, 97, 3083.
- (15) Hauser, P. C.; Perisset, P. M. J.; Tan, S. S. S.; Simon, W. Anal. Chem. 1990, 62, 1919.
- (16) Qin, Y.; Bakker, E. Talanta 2002, 58, 909.
- (17) Butler, J. N. Carbon Dioxide Equilibria and Their Applications.; Addison-Wesley: USA., 1982.
- (18) Bakker, E.; Simon, W. Anal. Chem. 1992, 64, 1805.

- (19) Jin Lee, H.; Yoon, I. J.; Yoo, C. L.; Pyun, H.-J.; Cha, G. S.; Nam, H. Anal. Chem. 2000, 72, 4694.
- (20) Barker, S. L. R.; Shortreed, M. R.; Kopelman, R. Anal. Chem. 1997, 69, 990.
- (21) Chester, R. Marine Geochemisty; 2 ed.; Blackwell Publishers: London, U.K., 2000.
- Unsworth, E. R.; Warnken, K. W.; Zhang, H.; Davison, W.; Black, F.; Buffle, J.; Cao, J.; Cleven, R.; Galceran, J.; Gunkel, P.; Kalis, E.; Kistler, D.; Leeuwen, H. P. v.; Martin, M.; Noel, S.; Nur, Y.; Odzak, N.; Puy, J.; Riemsdijk, v. W.; Sigg, L.; Temminghoff, E.; Tercier-Waeber, M.-L.; Toepperwien, S.; Town, R. M.; Weng, L.; Xue, H. *Env. Sci. Tech.* **2006**, *40*, 1942.
- (23) Kobos, R. K.; Parks, S. J.; Meyerhoff, M. E. Anal. Chem. 1982, 54, 1976.

## Chapter 9. A Non-Severinghaus Potentiometric Dissolved CO<sub>2</sub> Sensor with Improved Characteristics

This work has been published in: Xiaojiang Xie and Eric Bakker\*, Anal. Chem., 2013, 85, 1332–1336

### 9.1 Introduction

The importance of dissolved carbon dioxide sensing cannot be overemphasized because of the key roles it plays in the clinical, biological, environmental, and eco-biological sciences. Carbon dioxide is a poorly reactive molecule and for this reason, receptors based on the direct molecular recognition for carbon dioxide are rarely reported. Recently, measuring methods based on infrared and non-dispersive infrared spectroscopy, photoacoustic effect, surface plasmon resonance and thermal conductivity have been increasingly being explored. <sup>1-5</sup> Carbonate selective membrane electrodes have been used in commercial clinical analyzers to measure the total CO<sub>2</sub> levels of blood via adjustment of the samples to high pH (8.5 to 9.5). <sup>6</sup> At the same time, the conventional and widely used carbon dioxide sensors in blood gas analyzers and in environmental monitoring are still based on the Severinghaus principle. <sup>7-9</sup>

The Severinghaus CO<sub>2</sub> probe was first conceived by Richard Stow in 1954 and further improved by Dr. John W. Severinghaus.<sup>7</sup> In 1958, it was applied to the first blood gas analysis system for the measurement of carbon dioxide partial pressure in blood.<sup>10</sup> Today, the Severinghaus CO<sub>2</sub> probe is relatively inexpensive and easy to handle. Specifically, it utilizes a pH electrode in contact with a thin layer of bicarbonate solution that is separated from the sample by a gas permeable membrane such as rubber or Teflon. CO<sub>2</sub> dissolved in the sample is able to diffuse through the membrane into the inner NaHCO<sub>3</sub> solution where it is allowed to change the pH until CO<sub>2</sub> partition equilibrium is established. The resulting pH value of the bicarbonate solution is then recorded and related to dissolved CO<sub>2</sub> levels in the sample. Oceanographic CO<sub>2</sub> measurements are typically done in the same manner, but sometimes make use of a stream of dissolved pH indicator dye to report on the internal pH change in a highly reproducible fashion.<sup>11</sup>

Despite its wide use, some key drawbacks of the Severinghaus CO<sub>2</sub> probe are still very difficult to overcome. In general, the use of the Severinghaus CO<sub>2</sub> probe has been confined to the studies of media with high carbon dioxide concentration. Because it works on the basis of spontaneous diffusion and the establishment of bulk phase equilibrium between the internal compartment and the sample, the response time of the Severinghaus CO<sub>2</sub> probe is typically 1 min or longer. This response time increases with higher inner NaHCO<sub>3</sub> levels. <sup>10,12</sup> This slow response of the Severinghaus CO<sub>2</sub> probe has been characterized by numerical simulations and is therefore well understood. <sup>13,14</sup> It is not really an adequate tool when rapid real time variations of CO<sub>2</sub> need to be monitored, as in the depth profiling of aquatic systems or the rapid analysis of clinical blood samples.

The sensitivity of the Severinghaus  $CO_2$  probe also decreases as the carbon dioxide partial pressure drops, requiring a careful calibration in order to work at low  $CO_2$  levels.<sup>10</sup> Moreover, while it prevents interference from ionic solutes, the gas permeable membrane allows the penetration of other volatile acids such as  $H_2S$ , and HCl in their neutral form that can potentially cause interference.<sup>12,15-17</sup> The analysis of total carbon balance near the sediment-water interface may be affected by the presence of  $H_2S$ , resulting in an experimental bias. <sup>18,19</sup>

Carrier based ion-selective electrodes (ISEs) have evolved in the past years to become a well-established routine analysis technique in clinical laboratories, process control and environmental analysis.<sup>20,21</sup> Note that many interference problems mentioned above can be avoided by using a carbonate-selective electrode at the backside of a Severinghaus type CO<sub>2</sub> probe, rather than a pH electrode, as established by Meyerhoff.<sup>22</sup>

We postulate here based on thermodynamic considerations<sup>23</sup> that a pH electrode measured directly against a carbonate electrode without the use of a traditional reference electrode gives a direct measurement of free dissolved CO<sub>2</sub> levels. This strategy has recently been applied in some analogy for the optical detection of CO<sub>2</sub> (Chapter 8) and has earlier been applied for the potentiometric detection of dissolved H<sub>2</sub>S.<sup>24,25</sup> Any earlier attempts to develop a CO<sub>2</sub> probe based on this attractive principle would have required a highly selective carbonate responsive membrane electrode, which was not available at the time. More recently, a new class of carbonate selective ionophore based on a molecular tweezer architecture was reported by the groups of Nam and Cha for the realization of highly selective carbonate selective ISEs.<sup>26,27</sup> The optical carbon dioxide sensor mentioned above made use of this very ionophore (see Chpater 8).<sup>24</sup> We report here on an attractive potentiometric carbon dioxide sensing probe that does not require a gas permeable membrane and offers improved sensing characteristics for a wide range of potential applications.

### 9.2 Experimental Section

**9.2.1 Reagents.** Poly(vinyl-chloride) (PVC, high molecular weight), bis(2-ethylhexyl) adipate (DOA), *N,N*-Dioctyl-3α,12α-bis(4-trifluoroacetylbenzoyloxy)-5β-cholan-24-amide (carbonate ionophore VII), tridodecylmethylammonium chloride (TDMACl), 2-amino-2-hydroxymethyl-propane-1,3-diol (Tris) and tetrahydrofuran (THF) were obtained from Sigma-Aldrich. Carbon dioxide (5.0 vol-% in nitrogen) and nitrogen gas (99.9 vol-%) were purchased from PenGas in Switzerland. Aqueous solutions were prepared by dissolving the appropriate salts in Milli-Q purified water. All solvents and reagents used were analytically pure unless otherwise specified.

**9.2.2 Apparatus.** The glass pH electrode with combined Ag/AgCl reference (Ecotrode Plus) and the double junction Ag/AgCl reference electrode were purchased from Metrohm AG in Switzerland. CO<sub>2</sub> and N<sub>2</sub> gas were mixed in a gas mixing chamber with a magnetic stirring bar and the gas mixture was subsequently bubbled into the sample compartment with a specially designed sealed cap. The commercial Severinghaus CO<sub>2</sub> probe was purchased from Lazar Research Laboratories, Inc., US. Potential responses of the electrodes were measured with an EMF-16 precision electrochemistry EMF interface from Lawson Labs Inc. The aquarium was prepared by planting 3 specimen of E. densa in 10 L of fresh water.

**9.2.3 Membrane and Measurements.** The carbonate-selective membranes were prepared by dissolving the mixture composed of 8.3mg of carbonate ionophore VII, 60 mg of PVC, 2 mg of TDMACl and 100 µL DOA in 2 ml of THF. The cocktail solution was then poured into a glass ring (22 mm in diameter) placed on a slide glass and dried overnight at room temperature under a dust-free environment. Small disks were punched from the cast films and mounted in Ostec electrode bodies (Ostec, Sargans, Switzerland).

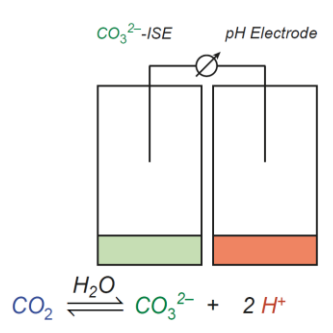
The calibration was done in  $10^{-4}$  M NaHCO<sub>3</sub> solution equilibrated with different partial pressures of CO<sub>2</sub>. The selectivity and response time of the sensor were characterized in 0.1 M pH 8.0 Tris-H<sub>2</sub>SO<sub>4</sub> buffer solutions. For the experiments shown in Fig. 8.3, PCO<sub>2</sub> was kept at 5 % while different amount of NaHCO<sub>3</sub> was added to the solution and the potential response was monitored.

To evaluate the influence of sample pH to the sensor response (Figure 8.3), the ion-selective electrodes were placed into  $0.01 \text{ M NaHCO}_3$  solution equilibrated with  $0.05 \text{ atm CO}_2$  partial pressure. Aliquots of HCl were added to reduce the sample pH. After each addition step, the sample was allowed to re-equilibrate to the same CO<sub>2</sub> partial pressure (PCO<sub>2</sub> = 0.05 atm) and the sensor response was recorded.

For the CO<sub>2</sub> measurement in the aquarium, the water solution containing 3 E. densa specimen was prepared and maintained in the same condition for the plants to stabilize before the electrodes were deployed. A 10 W incandescent light bulb was placed 10 cm above the water surface. The light was alternatively kept on for 16 h and off for 8 h while the electrodes were immersed in the aquarium and the sensor response was recorded.

#### 9.3 Results and Discussion

The sensor principle is presented in Scheme 9.1. The pH of the sample solution is monitored against a carbonate selective electrode. No potentially cumbersome liquid junction based reference element is required. The difference of potentials between the pH electrode and the carbonate-selective ISE is directly related to the dissolved  $CO_2$  and the partial pressure of  $CO_2$  in the atmosphere, which is at equilibrium with the sample solution.



Scheme 9.1. Representation of the ion-selective CO<sub>2</sub> sensor and its working principle.

According to established dissociation equilibria, dissolved CO<sub>2</sub> activity is coupled to carbonate and hydrogen ion activity through the acid dissociation equilibria as follows:

$$a_{CO_2} = \frac{a_{CO_3^{2-}}(a_{H^+})^2}{K_{a1}K_{a2}}$$
(9.1)

where and  $K_{a1}$  and  $K_{a2}$  are the two acid dissociation constants for dissolved  $CO_2$ . Note that dissolved  $CO_2$  is understood as the sum of carbonic acid and free carbon dioxide, the concentration ratio of which is constant at equilibrium. As ion-selective electrodes are established to respond to single ion activities, an electrochemical cell comprising a pH glass electrode and a carbonate-selective electrode responds to dissolved carbon dioxide quite naturally, without extra-thermodynamic assumptions:

$$E_{comb} = K' + \frac{s}{2} \log \left( a_{CO_3^{2-}} (a_{H^+})^2 \right) = K + \frac{s}{2} \log a_{CO_2}$$
(9.2)

where K and K' are constants that vary with the inner solution composition of the electrodes. The constants are related through Eqn. 9.1

The  $CO_2$  response of the new gas sensing probe is shown in Figure 9.1. According to Eqn. 9.2, a Nernstian slope for a divalent ion is expected for carbon dioxide, and which was indeed observed. The calibration was performed with three different electrodes and the mean values are plotted in Figure 9.1. As can be seen, the sensor is able to measure  $PCO_2$  at levels as low as 30 ppm ( $3 \times 10^{-5}$  atm), which is sufficient for routine environmental  $CO_2$  measurements (180-300 ppm)<sup>28,29</sup>. The sensor response to even lower  $PCO_2$  could not be evaluated due to the difficulty in sample preparation at very low  $PCO_2$ . For the Severinghaus  $CO_2$  probe, since it measures pH indirectly, a Nernstian slope is observed above 0.001 atm. Note that, at low  $PCO_2$  levels, the sensitivity becomes lower and a deviation from the ideal Nernstian response is observed. This sensitivity loss at low  $PCO_2$  region is due to deteriorating buffer capacity of the  $HCO_3$ -/ $CO_2$  couple as already reported by Severinghaus.  $PCO_2$  couple as already reported by Severinghaus.

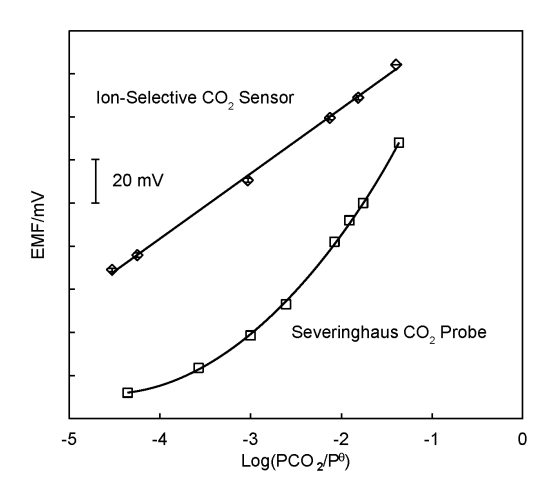


**Figure 9.1.** Calibration curves of the sensor responses to  $CO_2$  in a  $10^{-4}$  M hydrogen carbonate solution, the gas phase above  $10^{-4}$  M hydrogen carbonate solution, and dry  $CO_2 + N_2$  gas mixture with different levels of  $PCO_2$ . The term  $P^{\theta}$  on the x-axis is the partial pressure under standard conditions (1 atm).

As shown in Figure 9.2, even at quite high  $PCO_2$  levels, it takes at least 5 min for the signal of the Severinghaus  $CO_2$  probe to stabilize. The lower the  $PCO_2$  value, the slower it gets. Previous numerical simulations have fully characterized this diffusion controlled process. <sup>13,14</sup> The lagging behind in the response is not desired when real time monitoring of  $PCO_2$  is needed. Signal drifting will accumulate during the long equilibrating process and contribute also in part to the deviation from the ideal behavior of the Severinghaus  $CO_2$  probe shown in Figure 9.1.

The normal mean PCO<sub>2</sub> in arterial blood is in the range of 35-45 mmHg (0.046-0.059 atm), and a slow response time is currently tolerated for lack of a more performing sensor principle.<sup>30</sup> However, at lower PCO<sub>2</sub>, the diffusion of CO<sub>2</sub> from the sample through the gas permeable membrane of the Severinghaus probe into the inner HCO<sub>3</sub> containing solution becomes even slower and may become untolerable for practical use. Direct detection by potentiometry without the overlay of a diffusion membrane is orders of magnitude faster and may reach the tens of millisecond time scale with optimized fluidic control.<sup>31</sup> In batch mode, a time scale on the order of seconds is typical, which is attributed to the equilibration of the Nernst layer with the bulk solution. As shown in Figure 9.2 for the proposed ion-

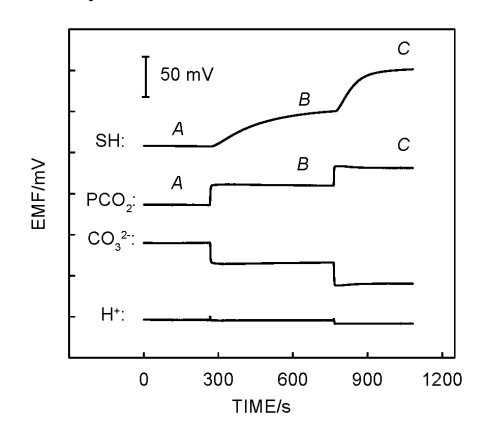


**Figure 9.2.** Comparison of response time between the Severinghaus CO<sub>2</sub> probe (SH) and the ion-selective CO<sub>2</sub> sensor (PCO<sub>2</sub>) in 0.1 M pH 8.0 Tris-H<sub>2</sub>SO<sub>4</sub> buffer solution equilibrated with different CO<sub>2</sub> partial pressures: A, 0.0004 atm; B, 0.0066 atm; C, 0.0655 atm.

selective  $CO_2$  sensor, the potential indeed stabilizes typically within 5 s ( $t_{95\%}$ ) upon change of different  $PCO_2$  values. The response time for the experiment of stepping from high  $PCO_2$  to low  $PCO_2$  conditions is shown in Figure S9.1 (see supporting information). The response in this direction is also fast, with  $t_{95\%} < 10$  s.

At high PCO<sub>2</sub> values, the diffusion of CO<sub>2</sub> from the sample into the inner solution might cause signal drift if the inner solution is not well buffered in carbonate, but this was not observed here. Carbon dioxide partitioning from the membrane into the sample may also result in potential drifts at very low values of PCO<sub>2</sub>. While these effects may be mainly relevant under rather specialized measurement conditions, they could be minimized by moving to an all solid state electrode design.<sup>32</sup>

The combination of a pH electrode, a carbonate-selective electrode and a reference electrode allows one to monitor pH, PCO<sub>2</sub> and carbonate concentration at the same time. Note that the measurements of pH and carbonate activity are, despite their acceptance in practice, thermodynamically less defined than the direct monitoring of PCO<sub>2</sub> with the proposed methodology.

As shown in Figure S9.2, when the sample solution was equilibrated after each NaHCO<sub>3</sub> addition step with 5 % CO<sub>2</sub> (vol-% in N<sub>2</sub>), the amount of dissolved CO<sub>2</sub> is controlled by Henry's law and thus does not change. This means that the PCO<sub>2</sub> response from the sensor should remain the same. However, the level of dissociation of CO<sub>2</sub> to the carbonate species depends on the alkalinity of the solution. Therefore, when the NaHCO<sub>3</sub> concentration is increased gradually, an increase in pH is expected along with the increase of carbonate activity. All this information may now be obtained from a single experiment as shown in Figure S9.2. Each addition of NaHCO<sub>3</sub> is followed by the decrease in potential of the pH and carbonate-selective electrode, indicating the increase of pH and carbonate concentration. However, the observed PCO<sub>2</sub> value, which is obtained from the difference of the two mentioned potentials, is confirmed to remain the same after the solution is brought to equilibrium with the atmosphere. Note that there is a spike of PCO<sub>2</sub> immediately after each addition of NaHCO<sub>3</sub>. After equilibrating with the atmosphere (the equilibration time varies with the volume and effectiveness of stirring the solution), the signals come back to the same level. The ion-selective CO<sub>2</sub> sensor is able to monitor these real time changes of the PCO<sub>2</sub> re-equilibration process. In contrast, since the response time of the Severinghaus CO<sub>2</sub> probe is on the order of many minutes and therefore longer than the equilibration time of the solution, it cannot access this kinetic information.

The selectivity of the ion-selective CO<sub>2</sub> sensor is mainly limited by the selectivity of the carbonate-selective electrode, since the pH electrode is highly selective to hydrogen ions. The carbonate-selective electrode has been carefully characterized earlier by other groups. <sup>26,27</sup> Here, the selectivity was revaluated under the same experimental conditions used in the previous reports (see supporting information). <sup>26</sup> As shown in Figure S9.3, and in agreement with previous work, interference from Cl<sup>-</sup> remains highly suppressed, suggesting that the sensor may potentially work in unmodified sea water samples as well as blood samples where Cl<sup>-</sup> is abundant. In addition, the interference of HS<sup>-</sup> has been studied here for the first time. Hydrogen sulfide is a common component of the coastal environment generated by bacterial metabolism. <sup>33,34</sup> Sulfide is found under anaerobic conditions such as the sediment covered with or inundated by sea water. When CO<sub>2</sub> levels in these environments need to be determined, H<sub>2</sub>S will cause interference to the traditional Severinghaus CO<sub>2</sub> probe because it is able to diffuse through the gas permeable membrane as a neutral species as well and change the pH of the inner NaHCO<sub>3</sub> in analogy to CO<sub>2</sub>. At neutral pH, sulfides exist mainly in the form of HS<sup>-</sup> and H<sub>2</sub>S. From Figure S9.3, it is clear that HS<sup>-</sup> is suppressed by 3.5 orders of magnitude. The hydrogen sulfide levels are reported to be at a maximum of 100 µmol per liter. <sup>35,36</sup> On the basis of these results, one may reason that HS<sup>-</sup> will not cause interference to the ion-selective CO<sub>2</sub> sensor in such environments.

The carbonate-selective electrode is intrinsically responsive to carbonate activity in the sample. As the solution pH is lowered to below the  $pK_{a1}$  of CO<sub>2</sub>, free carbonate will become an ever smaller fraction of total carbonate in the sample and one expects a critical pH at which other ions such as chloride will start to effectively interfere. In Figure 9.3 the sample solution was equilibrated at every point with 0.05 atm

CO<sub>2</sub> while the pH of the sample was continuously lowered with HCl. The ideal PCO<sub>2</sub> sensor response should be the same at all points as indicated by the broken line. The PCO<sub>2</sub> detection limit is reached at pH values of around 4.8, below which value this probe is no longer recommended for determination of PCO<sub>2</sub>.

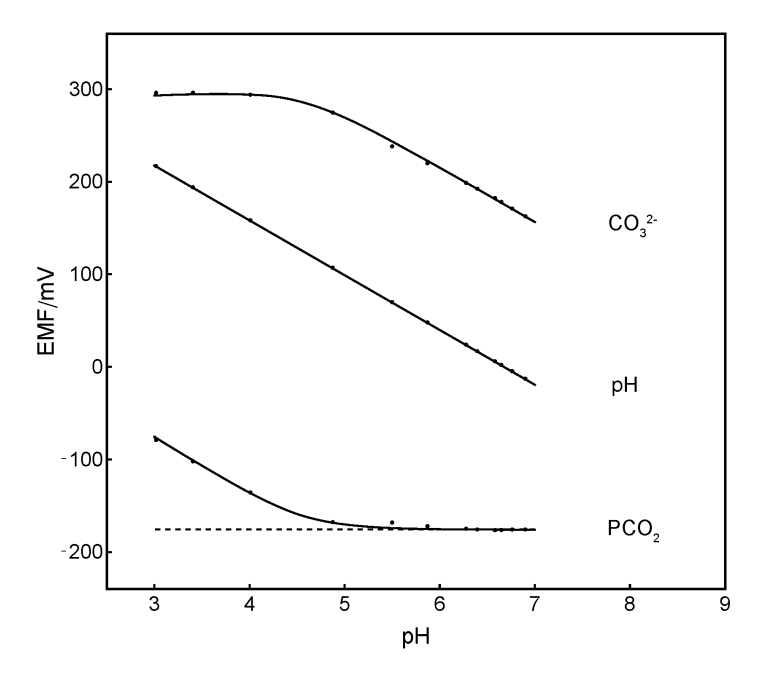


**Figure 9.3.** Response of the ion-selective  $CO_2$  sensor as a function of pH at a constant  $PCO_2$  of 0.05 atm. Solid lines for  $CO_3^{2-}$  and  $PCO_2$  are fitted with the modified Nicolsky-Eisenman equation<sup>20</sup> with a logarithmic selectivity coefficient for  $CO_3^{2-}$  over  $CI^-$  of -6.2. The broken line indicates the ideal behavior of the sensor.

As an early example, we demonstrated that the ion-selective  $CO_2$  sensor could be used to monitor the metabolic cycles of aquatic plants. The aquarium contained specimens of E. densa planted in sand. Light was alternatively switched on for 16 h and off for 8 h. As shown in Figure S9.4, when the light was on, the photosynthesis process of the plants consumed carbon dioxide and thus decreased the  $CO_2$  concentration in the aquarium. When light was switched off, the plants started to produce  $CO_2$  because of cellular respiration and resulted in an increase in  $CO_2$  concentration. The ups and downs in  $CO_2$  response were observed both for the Severinghaus  $CO_2$  probe and the ion-selective  $CO_2$  sensor. The ion-selective  $CO_2$  sensor showed a dissolved  $CO_2$  concentration of  $85.3\pm0.8$  mmol/L towards the end of the night and  $58.2\pm0.7$  mmol/L towards the end of the day. In contrast, the Severinghaus  $CO_2$  probe gave the dissolved  $CO_2$  concentration as  $87.1\pm17.1$ mmol/L towards the end of the night and  $60.8\pm2.0$  mmol/L towards the end of the day. While the dissolved  $CO_2$  concentration is difficult to quantify independently owing to the dynamic and spatially distributed nature of the experiment, the ion-selective  $CO_2$  sensor gave more stable and reproducible results since a stronger drift of the signals was observed for the Severinghaus  $CO_2$  probe. Nevertheless, the  $CO_2$  concentrations from the two sensors were close to each other and confirmed the ability of the sensor for such an application.

### 9.4 Conclusion

In conclusion, a potentiometric method of using pH and carbonate selective electrodes to measure carbon dioxide in solution and in its equilibrated atmosphere was introduced. The sensor showed the expected Nernstian response for a divalent ion with a detection limit sufficiently low for most environmental and clinical applications of interest. The response was orders of magnitude faster than for the

conventional Severinghaus  $CO_2$  probe and allowed us to trace  $CO_2$  changes in real time. Further, the combined electrodes could also provide information about pH and carbonate while  $CO_2$  was measured, in which case the use of a reference electrode becomes necessary. As an example, the sensor was applied in an aquarium to monitor the  $CO_2$  level as a result of the aquatic plant's metabolism.

### 9.5 Supporting Information for Chapter 9

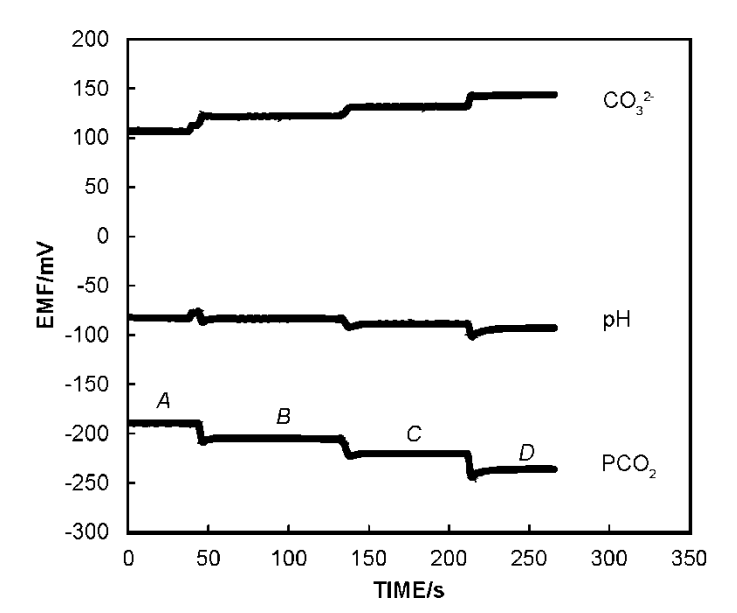


**Figure S9.1.** Response time of the ion-selective  $CO_2$  sensor to different  $PCO_2$ . A: 0.000320 atm, B: 0.000106 atm, C: 0.000035 atm, D: 0.000012 atm. The  $PCO_2$  values were reduced by a quick dilution of a NaHCO<sub>3</sub> solution (3 times more diluted after each step).

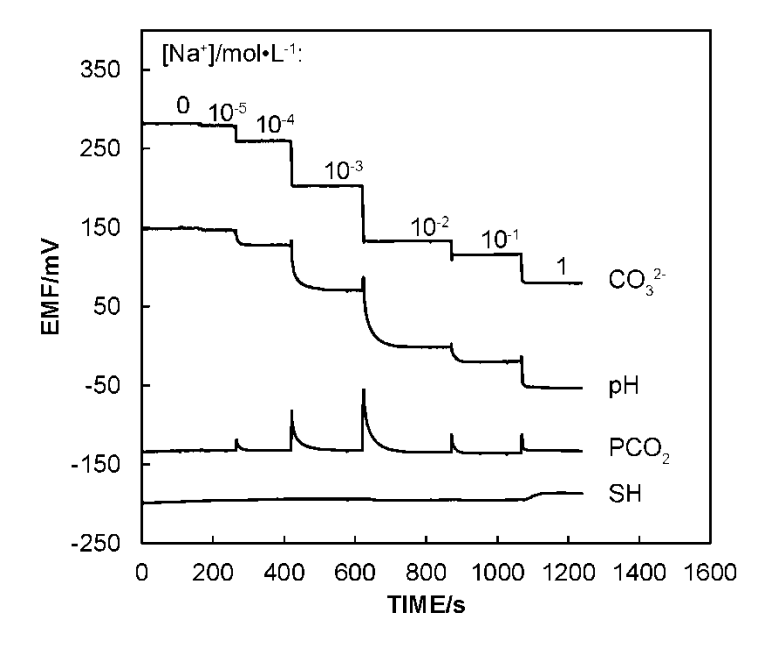


**Figure S9.2.** Simultaneous monitoring of pH,  $PCO_2$  and  $CO_3^{2-}$  concentration in solution equilibrated with 0.05 atm  $PCO_2$  using the Severinghaus  $CO_2$  probe (SH) and the ion-selective  $CO_2$  sensor ( $PCO_2$ ). Freshly prepared  $NaHCO_3$  solutions were gradually added to reach the designated  $Na^+$  concentration while the solution was re-equilibrated with a constant  $PCO_2$  value (0.05 atm).

The selectivity of the carbonate electrode was re-evaluated here in  $0.1 \text{ M pH } 8.0 \text{ TRIS-H}_2\text{SO}_4$  buffered solutions with the separate solutions method.

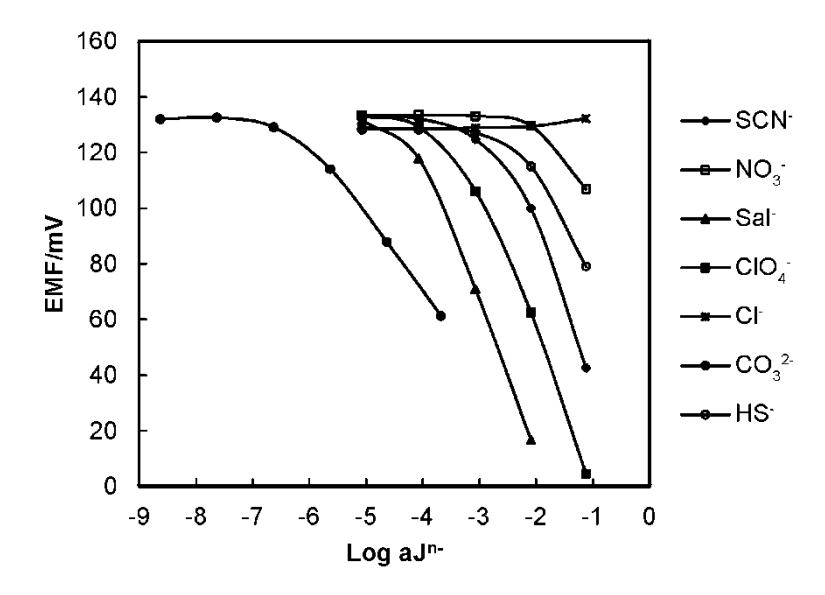


**Figure S9.3.** Calibration plots (activity scale) for the ion-selective CO<sub>2</sub> sensor to various anions. Background electrolyte: 0.1 M Tris-H<sub>2</sub>SO<sub>4</sub> buffer, pH 8.0.

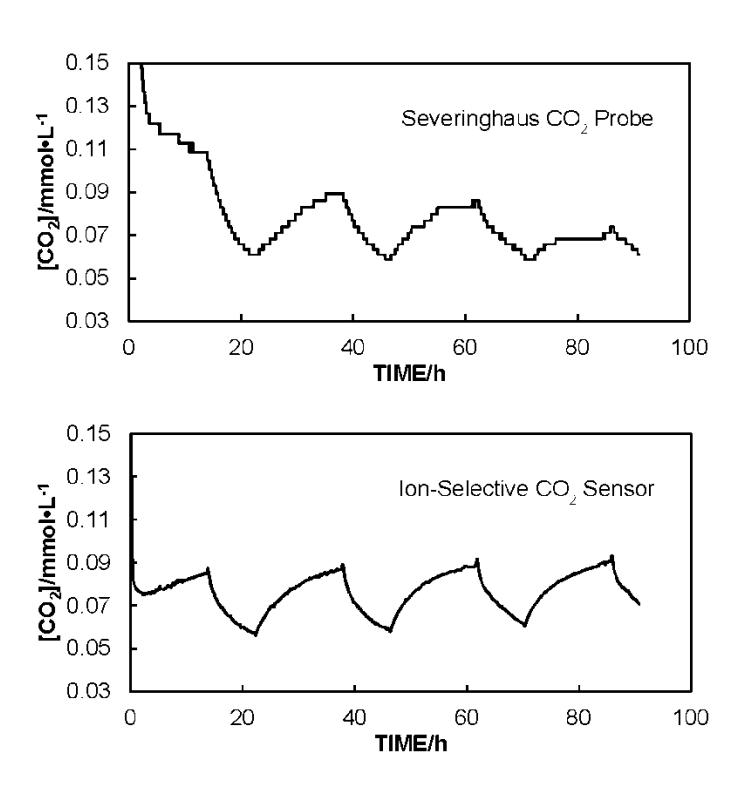


Figure S9.4. Monitoring the  $CO_2$  level change in a freshwater aquarium using the ion-selective  $CO_2$  sensor and the Severinghaus  $CO_2$  probe.

### 9.6 References for Chapter 9

- (1) Herman, P.; Murtaza, Z.; Lakowicz, J. Anal. Biochem. 1999, 272, 87.
- (2) Burke, C. S.; Markey, A.; Nooney, R. I.; Byrne, P.; McDonagh, C. Sens. Actuators B 2006, 119, 288.
- (3) Plata, M.; Hernando, J.; Zougagh, M.; Contento, A.; Villasenor, M.; Sanchezrojas, J.; Rios, A. Sens. Actuators B 2008, 134, 245.
- (4) Abderrahim, H.; Berrebia, M.; Hamou, A.; Kherief, H.; Zanoun, Y.; Zenata, K. J. Mater. Environ. Sci. 2011, 2, 94.
- (5) Lang, T.; Hirsch, T.; Fenzl, C.; Brandl, F.; Wolfbeis, O. S. Anal. Chem. 2012, 84, 9085.
- (6) Shin, J. H.; Sakong, D. S.; Nam, H.; Cha, G. S. Anal. Chem. 1996, 68, 221.
- (7) Severinghaus, J. W. J. Appl. Physiol. **2004**, 97, 1599.
- (8) Gambino, S. R. Clin. Chem. 1960, 7, 236.
- (9) Burnett, R. W.; Noonan, D. C. Clin. Chem. 1974, 20, 1499.
- (10) Severinghaus, J. W.; Bradley, A. F. J. Appl. Physiol. 1958, 13, 515.
- (11) Wang, Z. A.; Liu, X.; Byrne, R. H.; Wanninkhof, R.; Bernstein, R. E.; Kaltenbacher, E. A.; Patten, J. Anal. Chim. Acta 2007, 596, 23.
- (12) Suzuki, H.; Arakawa, H.; Sasaki, S.; Karube, I. Anal. Chem. 1999, 71, 1737.
- (13) Schoot, B. V. d.; Bergveld, P. Anal. Chim. Acta 1985, 166, 93.
- (14) Samukawa, T.; Ohta, K.; Onitsuka, M.; Ito, Y.; Motohashi, R. Anal. Chim. Acta 1995, 316, 83.
- (15) Guilbault, G. G.; Shu, F. R. Anal. Chem. 1972, 44, 2161.
- (16) Morf, W. E.; Mostert, I. A.; Simon, W. Anal. Chem. 1985, 57, 1122.

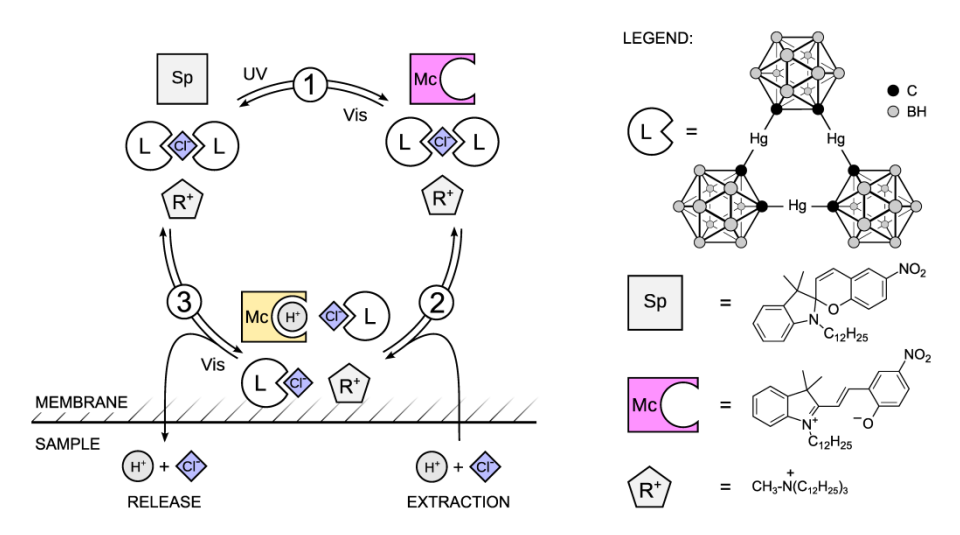
- (17) Lopez, M. E. Anal. Chem. 1984, 56, 2360.
- (18) DeVries, C. R.; Wang, F. Environ. Sci. Technol. 2003, 37, 792.
- (19) Clement, R. E.; Yang, P. W. Anal. Chem. 2001, 73, 2761.
- (20) Bakker, E.; Bühlmann, P.; Pretsch, E. Chem. Rev. 1997, 97, 3083.
- (21) Bakker, E.; Pretsch, E. Angew. Chem. Int. Ed 2009, 46, 5660.
- (22) Hyoung, S. Y.; Geun, S. C.; Meyerhoff, M. E. Anal. Chim. Acta 1990, 273, 115.
- (23) Butler, J. N. Carbon Dioxide Equilibria and Their Applications.; Addison-Wesley: USA., 1982.
- (24) Xie, X.; Pawlak, M.; Tercier-Waeber, M.-L.; Bakker, E. Anal. Chem. 2012, 84, 3163.
- Gulens, J.; Herrington, H. D.; Thorpe, J. W.; Mainprize, G.; Cooke, M. G.; Bello, P. D.; Macdougall, S. *Anal. Chim. Acta* **1982**, 138, 55.
- (26) Choi, Y. S.; Lvova, L.; Shin, J. H.; Oh, S. H.; Lee, C. S.; Kim, B. H.; Cha, G. S.; Nam, H. Anal. Chem. 2002, 74, 2435.
- (27) Jin Lee, H.; Yoon, I. J.; Yoo, C. L.; Pyun, H.-J.; Cha, G. S.; Nam, H. Anal. Chem. 2000, 72, 4694.
- (28) Cawley, G. C. Energy Fuels 2011, 25, 5503.
- (29) Zeebe, R. E. Annu. Rev. Earth Planet. Sci. 2012, 40, 141.
- (30) Weil, M. H.; Rackow, E. C.; Trevino, R.; Grundler, W.; Falk, J. L.; Griffel, M. I. N. Engl. J. Med. 1986, 315, 153.
- (31) Huser, M.; Gehrig, P. M.; Morf, W. E.; Simon, W. Anal. Chem. 1991, 63, 1380.
- (32) Song, F.; Ha, J.; Park, B.; Kwak, T. H.; Kim, I. T.; Nam, H.; Cha, G. S. *Talanta* **2002**, *57*, 263.
- (33) Christensen, J. K.; Hoyer, B.; Kryger, L.; Pind, N.; Kong, L. S. J. Chem. Educ. 1998, 75, 1605.
- (34) Brouwer, H. J. Chem. Educ. 1995, 72, 182.
- (35) Phillips, B. M.; Anderson, B. S.; Hunt, J. W. Mar. Environ. Res. 1997, 44, 117.
- (36) Black, K. D.; Kiemer, M. C. B.; Ezzi, I. A. J. Appl. Ichthyol 1996, 12, 15.

# Chapter 10. Reversible Photodynamic Chloride-Selective Sensor Based on Photochromic Spiropyran

This work has been published in: Xiaojiang Xie, Günter Mistlberger, and Eric Bakker\*, J. Am. Chem. Soc., 2012, 134, 16929–16932

Modern optical ion sensors that benefit from commercially available ionophores within a polymeric system such as plasticized poly(vinyl chloride) (PVC) have been introduced and applied for over two decades.<sup>1-4</sup> Such sensors often use a lipophilic pH indicator (also called chromoionophore) to monitor the level of hydrogen ion which functions as a reference ion. Most of these sensors work on the basis of a competitive ion-exchange or an electrolyte co-extraction equilibrium between the hydrophobic sensing phase and the contacting aqueous phase. Consequently they work only in a passive measurement mode.

Recent progress to make these sensors able to work in an active way includes the use of a photoacid generator that releases acid upon UV light illumination.<sup>5</sup> However, the photolysis of the photoacid generator is an irreversible process, and thus can only be used once. Our group recently proposed a photodynamic sensing concept based on a light induced pKa change of the chromoionophore.<sup>6</sup> We report here for the first time on a reversible photodynamic sensor that utilizes the pKa change of a spiropyran derivative (Sp) upon UV and visible light irradiation. Spiropyran has been extensively studied because of its pronounced photo-switching capability. Chelators for metal ions and amino acids based on modification on the structure of spiropyran or copolymerization methods have been reported.<sup>7-9</sup> Poly(terthiophene) membranes bearing spiropyran functionalities can be switched both photo- and electrochemically.<sup>10</sup> However, robust photo-switchable ion sensors based on bulk optode principles have, to the best of our knowledge, not been reported. Chloride is the major extracellular anion and is principally responsible for maintaining proper hydration, osmotic pressure, and a normal cation-anion balance in the vascular and intestinal fluid compartments. Chloride imbalance causes either hypochloremia or hyperchloremia. It is chosen here as a model ion for this "proof of concept" study.



Scheme 10.1. Photodynamic sensing mechanism and chemical structures for the compounds used in this work.

A plasticized PVC film contains a lipophilic spiropyran derivative, a chloride selective ionophore (L) and anionic exchanger ( $R^+Cl^-$ ), see scheme 10.1. Under visible light, spiropyran exists in a stable ring-closed form (Sp) with very low basicity (pKa=2.3±0.1)<sup>11</sup>. When illuminated by UV light, it transforms into a strongly colored ring-opened merocyanine (Mc) form.

The exposed phenolic group in this form tremendously increases the basicity of the molecule compared to the Sp form. This transformation is designed here to encourage the co-extraction of H<sup>+</sup> and Cl<sup>-</sup> from the contacting aqueous solution into the sensing film where Cl<sup>-</sup> is stabilized by the ionophore and H<sup>+</sup> will protonate Mc to form McH<sup>+</sup>. The spectral difference between Mc and McH<sup>+</sup> helps visualize the co-extraction process using optical techniques. Visible light will reverse the process by promoting the ring closing reaction. H<sup>+</sup> and Cl<sup>-</sup>, being highly hydrophilic species, will leave the sensing film to the contacting aqueous phase. In addition to the switching capability of optical sensors, the light induced ion flux may also be used for local ion perturbation in biological systems such as cells.

As shown in Fig. 10.1, under visible light (>400 nm), the colorless Sp form exhibits no absorbance above 400 nm. Increasing the chloride concentration up to 0.1 M in the buffered (pH 7.4) sample is still incapable of initiating the co-extraction process and thus, the absorbance remains close to zero above 400 nm. Upon UV irradiation (350 nm - 370 nm) in the absence of Cl<sup>-</sup>, the mole fraction of the Mc form increases. This change is visible by a color change from colorless to purple which is also manifested in a strong absorption band at 570 nm. The increase of dye basicity triggers HCl uptake and the formation of McH<sup>+</sup> in the sensing film with increasing concentration in the sample. This process results in a color change from purple (Mc) to yellow (McH<sup>+</sup>), which can be quantified by the measuring the absorbance at 450 and 570 nm, respectively.

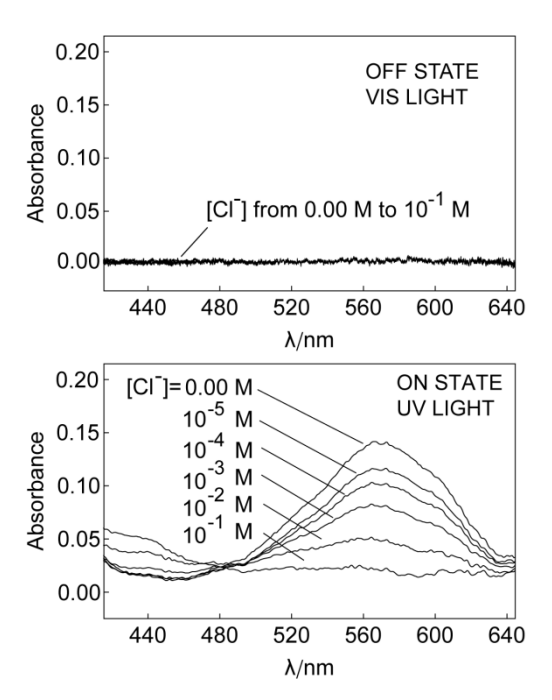


**Figure 10.1.** Absorption spectrums of the sensing membrane under illumination of visible (upper) and UV light (lower) in pH 7.4 MOPS buffer solution with different concentrations of Cl<sup>-</sup>.

Previous work on this chloride ionophore established that it is able to form both 1:1 and 2:1 complexes with Cl<sup>-</sup>. <sup>12,13</sup> In the initial state, i.e., without co-extraction, the ionophore forms a 2:1 complex with Cl<sup>-</sup> since the molar ratio of R<sup>+</sup>Cl<sup>-</sup> to L is 2:1. Co-extraction of Cl<sup>-</sup> and H<sup>+</sup> forces to form a 1:1 complex. The process under UV light illumination can be expressed with the following equation:

$$Cl^{-}(aq) + L_{2}Cl^{-}(m) + H^{+}(aq) + MC + R^{+} \rightleftharpoons MCH^{+}(m) + 2LCl^{-}(m) + R^{+}$$
 (10.1)

The response function can be expressed with the following equation according to the optode theory<sup>14</sup>:

$$a_{Cl}^{-a}_{H^{+}} = K_{coex}^{-1} \left(\frac{1-\alpha}{\alpha}\right) \left(\frac{\left\{2R^{+}_{T} + 2(1-\alpha)Ind_{T} - L_{T}\right\}^{2}}{L_{T} - R^{+}_{T} - \left(1-\alpha\right)Ind_{T}}\right)$$
(10.2)

where  $a_{Cl}^-$  and  $a_{H}^+$  are the sample activities of Cl'and H<sup>+</sup>, respectively,  $K_{coex}$  is the coextraction constant for Eqn. 10.1,  $\alpha$  is the mole fraction of unprotonated Mc, which can be calculated from the absorption spectrum<sup>1</sup>, and  $R^+_T$ ,  $Ind_T$  and  $L_T$  are the total concentrations of R<sup>+</sup>, Sp and L, respectively. The theoretical response curve (Fig. 10.2) shows satisfactory correlation with the experimental calibration data.

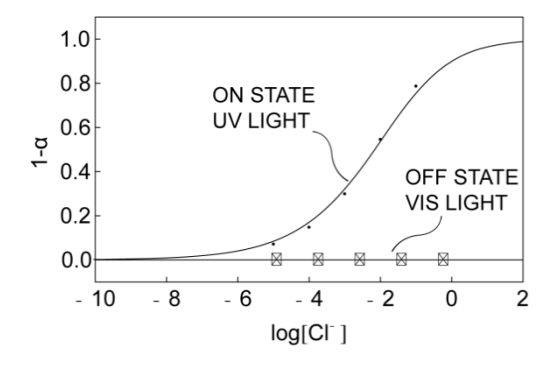


Figure 10.2. Calibration curves for the response of the membrane to Cl<sup>-</sup> with UV and Visible light illumination.

The presence of a lipophilic anion-exchanger  $R^+$  in the membrane may seem redundant because it is not required to assure HCl uptake. Indeed, the membrane without additional anion exchanger, shown in Figure 10.3, gives a similar response to chloride from  $10^{-7}$  M to  $10^{-2}$  M at pH 7.4. However, the addition of  $R^+$  shifts the response window to higher concentration of  $Cl^-$  which is more physiologically relevant. The shift is attributed to the different stability constants of the 1:1 and 2:1 complex. Since the 1:1 complex is less stable, it results in a response at higher concentrations of  $Cl^-$ .<sup>13</sup>

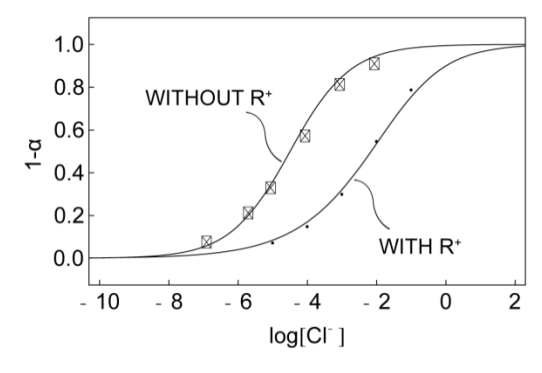


Figure 10.3. Cl response for membranes with and without ion-exchanger in pH 7.4 MOPS buffer solution under UV light.

The introduction of anion-exchanger R<sup>+</sup> allows one to evaluate the system electrochemically using potentiometric methods. Membranes with the same constitution as for the optical measurement are prepared by solvent casting and mounted onto commercial Ostec electrode bodies. The potential of the electrode is measured in the same buffer solution with different Cl<sup>-</sup> level against a double junction Ag/AgCl reference electrode. Without cationic sites R<sup>+</sup>, the potential of the electrode is not well defined because of the lack of permselective properties. A membrane with additional R<sup>+</sup> behaves as chloride selective membrane under visible light illumination, because the pKa of Sp is too low to cause any interference at pH 7.4. Under these conditions, one should observe a Nernstian response slope for chloride. UV illumination, co-extraction is triggered and a sub-Nernstian response curve is expected. Figure 10.4 demonstrates a slope of -57.9 mV per 10-fold concentration change of Cl<sup>-</sup> for the electrode measured under visible light. Exposing the electrode membrane to UV light causes the slope of the response curve to decrease to -37.2 mV. The leveling off at high concentration (> 0.1 M) is explained with the co-extraction of NaCl. <sup>16</sup>

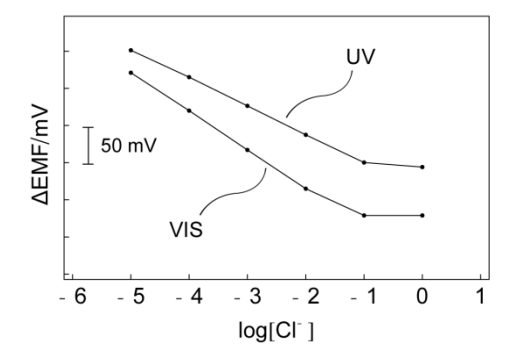
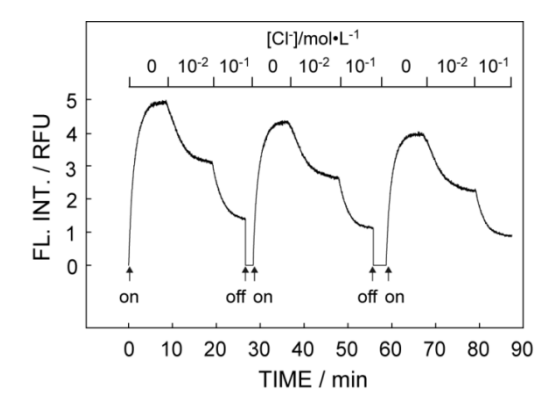


Figure 10.4. Potentiometric response for membrane containing R<sup>+</sup> under UV and visible light illumination.

The selectivity of the photoswitchable membrane was evaluated and the selectivity coefficients for chloride against common anions are presented in Table 10.1. In agreement with previous reports, anions such as perchlorate, sulfate, nitrate and salicylate are highly suppressed while SCN shows significant interference. <sup>13</sup> This also indicates that the Mc form has no profound interaction with the incoming anions.

<b>Table 10.1.</b> Selectivity coefficients Log K <sub>Cl,J</sub> <sup>Opt</sup> at pH 7.4 for Chloride	
Ion J	${ m K_{Cl,J}}^{ m Opt}$
ClO <sub>4</sub>	-3.6
NO <sub>3</sub> -	-3.8
Sal	-2.9
SCN <sup>-</sup>	+0.6
$\mathrm{SO_4}^{2 ext{-}}$	-9.3

The dynamic photoactivated sensor response behavior is illustrated in Figure 10.5. The fluorescence intensity at 650 nm was used as signal output. When illuminated with UV, the emission intensity started to respond to different Cl<sup>-</sup> concentrations. Afterwards, visible light was introduced to deactivate the sensor and release Cl<sup>-</sup>, preparing it for the next photoactivated sensing step. After each on-off step, an emission intensity drop was observed that is ascribed to the photofatigue of spiropyran. A covalent attachment of modified spiropyran into polymeric film or a replacement of spiropyran with spirooxazine, a compound proposed to have better photo stability, could potentially solve this problem. <sup>20,21</sup>



**Figure 10.5.** Reversible photochromism and switching with alternative UV and Vis light in pH 7.4 MOPS buffer with different Cl<sup>-</sup> concentrations.

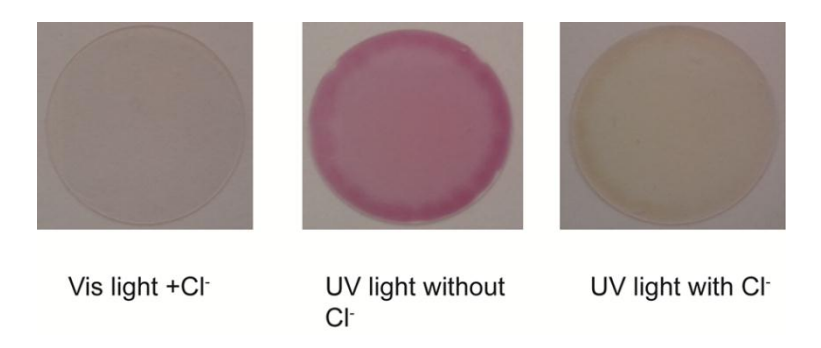
To conclude, an active Cl<sup>-</sup>-selective optical sensor with tunable measuring range based on a photochromic spiropyran derivative was presented. Spectroscopic and electrochemical measurements confirmed the anticipated mechanism for the system. This work forms a new platform for the realization of a toolbox of dynamic optical ion sensors and selective systems for triggered, localized ion perturbation.

### 10.1 Supporting Information for Chapter 10

Reagents. Poly(vinyl-chloride) (PVC, high molecular weight), bis(2-ethylhexyl) sebacate (DOS), tridodecylmethylammonium chloride (TDMAC), were obtained from Sigma-Aldrich. Spiropyran and the chloride ionophore were synthesized in our lab according to literature. (*Anal. Chem.* 1999, 71, 1371 and *Tetrahedron Letters* 2007, 48, 657) All solvents and reagents used were analytically pure unless otherwise specified. Aqueous solutions were prepared by dissolving the appropriate salts in Milli-Q purified water. The membrane cocktail was prepared by dissolving 0.96 mg (20 mmol/kg) spiropyran,4.2 mg (40 mmol/kg) chloride ionophore, 1.15 mg TDMAC (if needed), 31.2 mg PVC, and 62.4 mg DOS in 1 mL of THF.

Instrumentation and Setup: Absorption spectrums were measured using a CCS 200 spectrometer from THORLABS. Fluorescence was determined with Fluorolog-3 spectrometer (Horiba Jobin Yvon). The membrane (ca. 3 µm thick) was spin-coated onto a round quartz slide (DA. 35 mm) which was mounted into a flow cell with inner volume of around 1 mL. 1 mM MOPS buffer solutions at pH 7.4 with different Cl<sup>-</sup> concentrations were pumped through the flow cell for absorbance and fluorescence measurements.

Pictures for color changes of the membrane in different conditions:



The  $\alpha$  value in this work was determined using the following equation:

$$\alpha = \frac{A_D - A}{A_D - A_P}$$

where  $A_D$  is the absorbance value of the sensing film at 570 nm when Mc is fully deprotonated,  $A_P$  is the absorbance value of the sensing film where Mc exists in its fully protonated form at 570 nm, and A is the absorbance value of the sensing film at 570 nm. For calculation under emission mode, the emission intensity at 650 nm was used instead.

Simulations for potentiometric response with and without co-extraction of H<sup>+</sup> and Cl<sup>-</sup>:

### 1. With co-extraction

The 1:1 and 2:1 binding complexes are expressed as follows:

$$K_{b1} = \frac{[LCl^{-}]}{[L] \times [Cl^{-}]}$$

$$K_{b2} = \frac{[L_2Cl^-]}{[L]^2 \times [Cl^-]}$$

where, L, LCl $^-$ , L $_2$ Cl $^-$ , and Cl $^-$  represent the free ionophore, 1:1 complex, 2:1 complex and free chloride ions in the membrane;  $K_{b1}$  and  $K_{b2}$  are the binding constants for 1:1 and 2:1 complexes, respectively.

The dissociation of the protonated Mc form is expressed by  $K_a = \frac{[H^+] \times [Ind]}{[HInd^+]}$ , where  $K_a$ ,  $H^+$ , Ind and HInd<sup>+</sup> represent the dissociation

constant, and free concentrations of protons, Mc and McH<sup>+</sup> in the membrane, respectively.

The mass balances for spiropyran and chloride ionophore are expressed with the following two equations:

$$Ind_T = [HInd^+] + [Ind]$$

$$L_T = [LCl^-] + 2[L_2Cl^-]$$

The charge balance within the membrane is expressed with

$$[HInd^{+}] + [H^{+}] + R_{T}^{+} = [LCl^{-}] + [L_{2}Cl^{-}] + [Cl^{-}]$$

The coextraction of H<sup>+</sup> and Cl<sup>-</sup> is represented by  $a_{H^+}a_{Cl^-} = K_{coex}[H^+][Cl^-]$ , with  $a_{H^+}$  and  $a_{Cl^-}$  meaning the activities of proton and Cl<sup>-</sup> in the aqueous solution.

Solving the equations above and plotting in Mathematica with the following parameters results in the potentiometric response with UV light illumination, as shown in Fig. S10.1 (blue curve).

Parameters:

$$K_{b1=10^{9.9}}$$
,  $K_{b2=10^{13.4}}$ ,  $K_{coex=10^{-5}}$ ,  $K_{a=10^{8.6}}$ ,  $Ind_{T=20}$ ,  $a_{H^{+}=10^{-7.4}}$ ,  $L_{T=40}$ ,  $R_{T=20}^{+}$ 

2. Without co-extraction, a Nernstian response is expected, therefore, Nernst equation is used for visible light illumination:

$$E = C + 59.2 \log a_{Cl}$$

with C as a constant and E representing the potential.

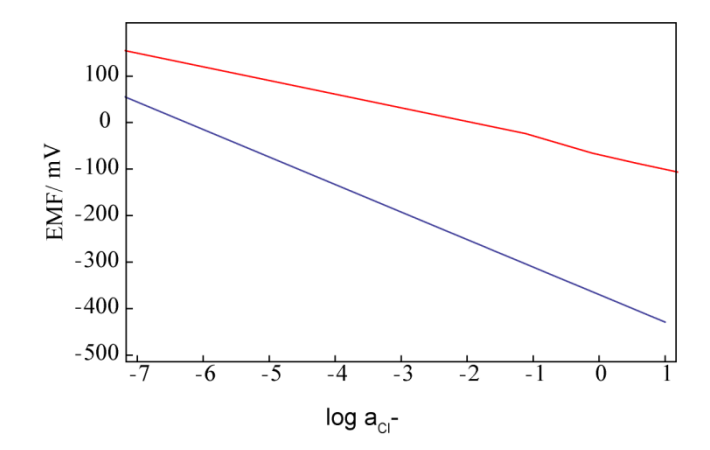


**Figure S10.1.** Simulation for potentiometric response of the electrodes towards Cl<sup>-</sup> under UV (red curve) and VIS light illumination (blue curve).

### 10.2 References for Chapter 10

- (1) Bakker, E.; Buhlmann, P.; Pretsch, E. Chem. Rev. 1997, 97, 3083.
- (2) Buhlmann, P.; Pretsch, E.; Bakker, E. *Chem. Rev.* **1998**, 98.
- (3) Morf, W. E.; Seiler, K.; Rusterholz, B.; Simon, W. Anal. Chem. 1990, 62, 738.
- (4) Wygladacz, K.; Radu, A.; Xu, C.; Qin, Y.; Bakker, E. Anal. Chem. 2005, 77, 4706.
- (5) Shvarev, A. J. Am. Chem. Soc. 2006, 128, 7138.
- (6) Bakker, E.; Crespo, G.; Grygolowicz-Pawlak, E.; Mistlberger, G.; Pawlak, M.; Xie, X. Chimia 2011, 65, 141.
- (7) Byrne, R.; Ventura, C.; Lopez, F. B.; Walther, A.; Heise, A.; Diamond, D. Biosensors and Bioelectronics 2010, 26, 1392.
- (8) Fries, K. H.; Driskell, J. D.; Samanta, S.; Locklin, J. Anal. Chem. 2010, 82, 3306.
- (9) Liu, Y.; Fan, M.; Zhang, S.; Sheng, X.; Yao, J. New J. Chem. **2007**, 31, 1878.
- (10) Wagner, K.; Byrne, R.; Zanoni, M.; Gambhir, S.; Dennany, L.; Breukers, R.; Higgins, M.; Wagner, P.; Diamond, D.; Wallace, G.G.; Officer, D. L. J. Am. Chem. Soc. 2011, 133, 5453.
- (11) Mistlberger, G.; Crespo, G. A.; Xie, X.; Bakker, E. Chem. Commun. 2012, 48, 5662.
- (12) Badr, I. H. A.; Diaz, M.; Hawthorne, M. F.; Bachas, L. G. Anal. Chem. 1999, 71, 1371.
- (13) Ceresa, A.; Qin, Y.; Peper, S.; Bakker, E. Anal. Chem. 2003, 75, 133.
- (14) Barker, S. L. R.; Shortreed, M. R.; Kopelman, R. Anal. Chem. 1997, 69, 990.
- (15) Bakker, E.; Pretsch, E. Angew. Chem., Int. Ed. 2007, 46, 5660.
- (16) Qin, Y.; Bakker, E. Anal. Chem. 2002, 74, 3134.
- (17) Tong, R.; Hemmati, H. D.; Langer, R.; Kohane, D. S. J. Am. Chem. Soc. 2012, 134, 8848.
- (18) Wen, G.; Yan, J.; Zhou, Y.; Zhang, D.; Mao, L.; Zhu, D. Chem. Commun. 2006, 3016.
- (19) Minkin, V. I. Chem. Rev. 2004, 104, 2751.
- (20) Deniz, E.; Tomasulo, M.; Cusido, J.; Sortino, S.; Raymo, F. M. Langmuir 2011, 27, 11773.
- (21) Radu, A.; Byrne, R.; Alhashimy, N.; Fusaro, M.; Scarmagnani, S.; Diamond, D. J. Photochem. Photobiol., A 2009, 206, 109.

### Chapter 11. Light Controlled Reversible Release and Uptake of Potassium Ions from Ion-Exchanging Nanospheres

This work has been published in: Xiaojiang Xie\* and Eric Bakker\*, ACS Appl. Mater. Interfaces, 2014, 6, 2666–2670

### 11.1 Introduction

It has been recognized that metal ions such as Ca<sup>2+</sup>, K<sup>+</sup>, Zn<sup>2+</sup> and Mg<sup>2+</sup> are involved in many vital biological processes. In Artificial control of parameters such as the concentration of certain ions or molecules can help understand the function and mechanism of diverse *in vivo* biochemical processes. It is challenging, however, to bring about ionic perturbation in a confined area without perturbation to other "innocent" areas. Such localized perturbation may allow one not only to passively observe cellular processes, but also to stimulate cellular chemistry.

Photo-triggered ionic perturbation is an attractive direction given by the relative ease of combining spatial and temporal control of the trigger by using readily available imaging equipment such as microscopes or spectrometers. Local increase of free Ca<sup>2+</sup> concentration using "caged calcium" such as NP-EGTA shown in Figure 11.1 (a) has been successful.<sup>7,10-13</sup> The photolysis, albeit irreversible, is able to raise the free Ca<sup>2+</sup> level in a short time. Caged compounds for other chemical messengers such as ATP and glutamate have been also reported.<sup>8,14</sup> Photoacid generators (PAG) have been used to induce a pH imbalance in cancer cells.<sup>15</sup> Despite the continuing emergence of caging compounds for various targets in recent years, the number of ions that can be released is still rather limited.

The transformation of spiropyrans into protonated merocyanines in the presence of acid and the visible light induced release of protons from the latter species have been well established. <sup>16-19</sup> UV light can also induce the spiropyran ring-opening reaction and since the thermal back reaction is much slower than the ring-opening reaction, <sup>20</sup> the photo-stationary state is dominated by the merocyanines. Our group recently reported on the photoinduced basicity change of a derivative of the photochromic dye spiropyran in plasticized PVC membranes. <sup>21</sup> Protons can be taken up or released by the membrane due to a basicity change of Sp (Chapter 13). <sup>22</sup> Based on light-induced ion-exchange or co-extraction processes, active sensors for Cl<sup>-</sup> (Chapter 10), Na<sup>+</sup>, and Ca<sup>2+</sup> have been subsequently demonstrated. <sup>23,24</sup> We hypothesize that such light-induced ion-exchange and co-extraction processes can be used to trigger local ion concentration perturbations as well. With readily available and highly selective ionophores for various ions, this may potentially form a new platform for light-induced ion perturbation.

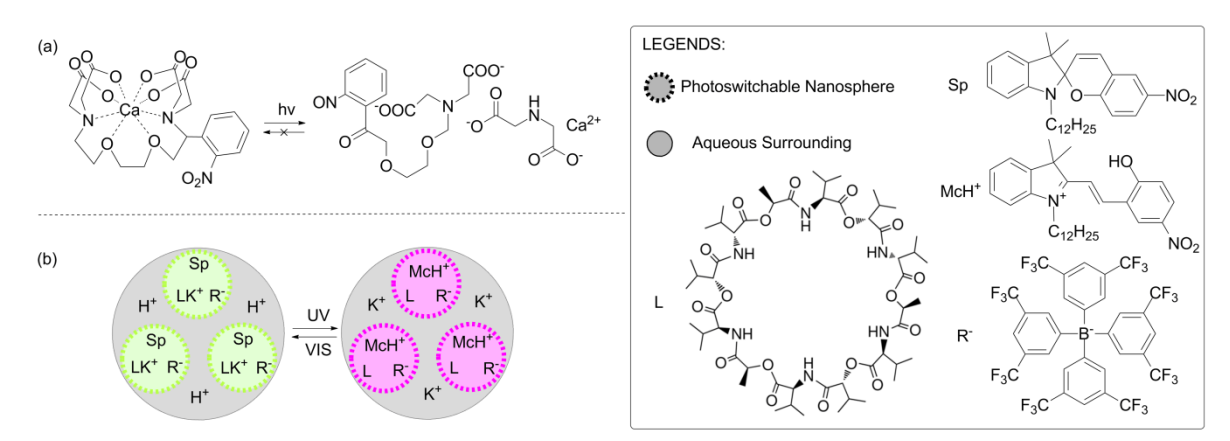


**Figure 11.1.** (a) Photolysis of caged calcium NP-EGTA. (b) Representation of light controlled  $K^+$  release and uptake with the photoswitchable nanospheres containing spiropyran.

In this work, we present a general approach to the realization of nanospheres that can alter the surrounding ion concentration upon light irradiation.  $K^+$  is used as a model ion to demonstrate the chemical principle. The nanospheres are very small, stable and biocompatible and can release  $K^+$  upon UV illumination. The release of  $K^+$  from the nanospheres is reversible. Upon visible (VIS) light irradiation, the nanospheres can take up  $K^+$  and thus decrease the surrounding  $K^+$  concentration. Direct monitoring of the ion concentration changes in solution phase is demonstrated with a  $K^+$ -selective probe.

### 11.2 Experimental Section

**11.2.1 Reagents.** Pluronic® F-127 (F127), bis(2-ethylhexyl) sebacate (DOS), valinomycin (L), acetic acid, tetrahydrofuran (THF), potassium or sodium tetrakis-[3,5-bis(trifluoromethyl)phenyl]borate (K<sup>+</sup>R<sup>-</sup>) and poly(vinyl chloride) (PVC) were obtained from Sigma-Aldrich. Sp was synthesized according to the literature.<sup>23,25</sup> All solvents and reagents used were analytically pure unless otherwise specified. Aqueous solutions were prepared by dissolving the appropriate salts in Milli-Q purified water.

**11.2.2 Nanosphere Preparation.** For spectroscopic experiments, 2.74 mg of NaTFPB, 1 mg of Sp, 8 mg of DOS, 25 mg of Pluronic<sup>®</sup> F-127, and 4.1 mg of potassium ionophore valinomycin were dissolved in 3 mL of THF to form a homogeneous solution. 0.5 mL of the solution was pipetted and injected into 4.5 mL of deionized water on a vortex with a spinning speed of 1000 r/min. Compressed air was blown on the surface of the clear particle suspension for 20 min to remove THF. For Figure 11.3, a THF cocktail containing 2.66 mg of NaTFPB, 4.1 mg of valinomycin and 3 mg of Sp were used for nanosphere preparation.

**11.2.3** K\*-Selective Electrode. The membrane cocktail was prepared by dissolving 0.3 mg of KTFPB, 1.18 mg of valinomycin, 40 mg of PVC, and 80 mg of DOS in 1.5 mL of THF. The cocktail solution was then poured into a glass ring (22 mm in diameter) placed on a glass slide and dried overnight at room temperature under a dust-free environment. Small disks were punched from the cast films and mounted in Ostec electrode bodies (Ostec, Sargans, Switzerland).

**11.2.4 Instrumentation and Measurement.** The size of the nanospheres was measured with a particle size analyzer Zetasizer Nano ZS (Malvern Inc.). For transmission electron microscopy (TEM) imaging of the nanospheres, the nanosphere suspension was dispersed on to a Formvar/Carbon film coated TEM grid, counter-stained with uranyl acetate, dried in the air and visualized using a FEI Tecnai<sup>™</sup> G2 Sphera transmission electron microscope.

The absorbance was measured with a UV-Vis spectrometer (SPECORD 250 plus, Analytic Jena, AG, Germany). The fluorescence was measured with a fluorescence spectrometer (Fluorolog3, Horiba Jobin Yvon), with excitation at 365 nm (1 nm slit) or 409 nm (1 nm slit). Emission intensity at 650 nm (10 nm slit) was recorded for samples containing various K<sup>+</sup> concentration in 10 mM acetic acid background. The percentage of Mc, [Mc]/[Sp<sub>tot</sub>] was calculated using the following equation:

$$[Mc]/[Sp_{tot}] = \frac{I}{I_{max} - I_{min}}$$

where,  $I_{min}$  is the minimum emission intensity measured in blank and  $I_{max}$  is the maximum emission intensity measured in 1 mM KOH.

For direct monitoring of K<sup>+</sup> concentration as shown in Figure 11.3, the above mentioned K<sup>+</sup> electrode was inserted into a glass cylinder together with a Ag/AgCl wire as reference element (Figure S11.2). A Lambda DG-4 Plus Xenon Source (Sutter Instruments) was as light source for illumination with UV light (ZET365/20x filter, Chroma Inc.) and visible light (FF02-409/LP BrightLine long-pass filter, Semrock Inc.) On the bottom of the cylinder was placed a thin layer of nanosphere suspension (1 mM HCl and 10<sup>-5</sup> M KCl). The EMF response from the K<sup>+</sup>-selective electrode was recorded with an EMF-16 precision electrochemistry EMF interface from Lawson Labs Inc.

### 11.3 Results and Discussion

Recently, we found that ultra-small nanospheres (<100 nm in dia.) can be easily prepared by precipitation of bis(2-ethylhexyl) sebacate (DOS) and an amphoteric copolymer (Pluronic® F-127) in water (see Chapter 2).<sup>26</sup> Lipophilic compounds could be incorporated in the nanosparticle core. Pluronic® F-127 has been shown to exhibit attractive biocompatibility.<sup>27</sup> Including PVC in the nanosphere was found to result in a larger, less desired particle size. The nanospheres are very stable in solution and can be stocked over months without sedimentation. To develop nanospheres for localized ion perturbation, a photoswitchable compound, spiropyran (Sp), an ion-exchanger (R<sup>-</sup>), and a K<sup>+</sup> ionophore valinomycin (L) were incorporated into the nanosphere core. Sp undergoes a UV light induced photoreaction to form a ring-opened merocyanine form (Mc) with a quantum yield of ca. 0.1.<sup>28</sup> The Mc form carries a phenolate group and exhibits much higher basicity than Sp.<sup>23,24</sup> As shown in Figure 11.1 (b), in the presence of H<sup>+</sup>, the Mc form will be protonated to become positively charged McH<sup>+</sup>. However, in order to protonate Mc, K<sup>+</sup>, which was bound to L, must be ejected to keep the nanosphere core neutral (even in such small dimensions).<sup>29</sup> When illuminated with visible light (>409 nm), the McH<sup>+</sup> will transform back to Sp and release H<sup>+</sup>, which will exchange with K<sup>+</sup> for charge balance reasons, thereby reducing the surrounding K<sup>+</sup> concentration. This reverse process is difficult for caged compounds since photolysis reactions are normally irreversible. To our knowledge, a nanoscale tool that is able to both increase and reduce local ion concentration by light has never been reported before.

The size of the nanospheres was determined by dynamic light scattering (DLS) as well as transmission electron microscopy (TEM) (see Figure S11.1 in Supporting Information). An average diameter of 71 nm was obtained from DLS with a polydispersity index of 0.23, indicating a relatively narrow size distribution. The size obtained from light scattering measurements is slightly larger than that observed in TEM. While the former technique is dependent on hydrodynamic size, <sup>26</sup> shrinkage and aggregation of the nanospheres were observed in TEM, and outgassing of the plasticizer more likely explains the size difference.

Since the release and uptake of K<sup>+</sup> is accompanied with protonation of Mc and deprotonation of McH<sup>+</sup>, the processes can be observed spectroscopically as both Mc and McH<sup>+</sup> are fluorescent. However, the emission intensity at 650 nm for Mc is much higher than for McH<sup>+</sup>. As shown in Figure 11.2 (a), upon UV (365 nm) illumination, the fluorescence intensity grows due to the ring-opening photoreaction of Sp. In the absence of K<sup>+</sup>, the photoproduct is protonated to form McH<sup>+</sup>, for which the emission intensity is relatively low. As the K<sup>+</sup> concentration increases, more Mc is formed while the percentage of McH<sup>+</sup> is reduced due to the exchange between K<sup>+</sup> and H<sup>+</sup>. Therefore, the steady state emission intensity increases with increasing K<sup>+</sup> concentration, confirming the exchange between H<sup>+</sup> and K<sup>+</sup>. Moreover, fitting the calibration with equilibrium response theory gives satisfactory results (Figure 11.2 (b)), indicating that electroneutrality indeed

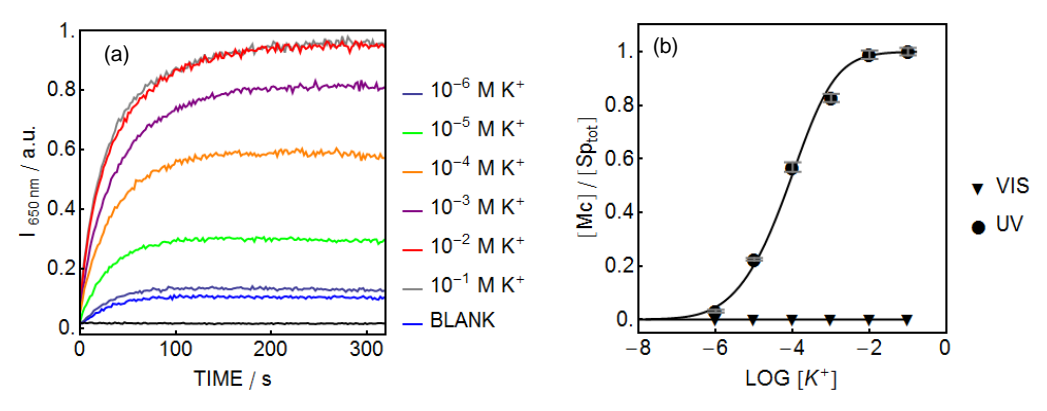


**Figure 11.2.** (a) Fluorescence emission intensity (650 nm) of the nanospheres with various KCl concentration as indicated and 10 mM acetic acid as buffer. The black line was recorded with VIS light (409 nm) as excitation while the rest was excited with 365 nm UV light. (b) Percentage of Mc ( $[Mc]/[Sp_{tot}]$ ) under UV and VIS irradiation from Figure 11.2(a). Error bars are standard deviations.

holds for the nanosphere bulk. When irradiated with visible light (409 nm), the ring-opened forms are suppressed, which renders  $K^+$  more competitive than  $H^+$  since the basicity of Sp is very low.

While spectroscopic characterization shows very encouraging results, it is only indirect evidence since the release and uptake of  $K^+$  are inferred from the behavior protonation of the incorporated dye. To obtain direct evidence that  $K^+$  in the aqueous surroundings is being perturbed by the nanospheres, a  $K^+$ -selective electrode was used to monitor the  $K^+$  concentration in the aqueous solution containing the photoswitchable nanospheres. The setup is shown in Figure S11.2; a confined layer (ca. 1 mm) of suspension containing the nanospheres was pipetted into a transparent glass cylinder. A  $K^+$ -selective electrode (see Supporting Information for the preparation procedure) was placed in direct contact with the suspension while light illumination was brought about from the bottom of the cylinder. The  $K^+$  concentration was obtained by comparing the electromotive force (EMF) readout with an external calibration curve (see Figure S11.3 in Supporting Information).

As shown in Figure 11.3, when UV light (ca. 2.9 mW•cm²) was switched on, a substantial potential jump of ca. 78 mV that corresponds to a ca. 25-fold K<sup>+</sup> concentration increase was achieved after 30-s of illumination. Upon illumination with visible light, the K<sup>+</sup> concentration dropped by a factor of 17, indicating K<sup>+</sup> uptake into the nanospheres. Compared to caged compound with milliseconds response time, the current system is appreciably slower. The kinetics is limited by the photoreaction rate of Sp, which in this case is rather sluggish due to the relatively weak light intensity. The conversion from excited state Sp to Mc form has been shown to take place in less than 10 ps³0,31, and the overall conversion from Sp to Mc is proportional to light intensity. With typical laser intensities (ca. 100 mW/cm²) from a conventional confocal fluorescence microscope, the response time should approach tens of microseconds.

The light triggered  $K^+$  perturbation was observed under acidic conditions due to the relatively low basicity of the ring opened Mc in the nanospheres. The pKa of the Mc form was determined to be ca. 4.6 in the nanospheres by comparison of similar particles with chromoionophore I, which has a pKa of ca. 11.4 in PVC-DOS membrane<sup>32</sup> and ca. 7.4 in the nanospheres. For applications at physiological pH, the basicity needs be increased, which could potentially be achieved through structural modification of the spiropyran or improving on the nanosphere core materials.

Some deterioration in the repeatability was noted with time. This is probably due to photofatigue of Sp<sup>23,30,33,34</sup> as stronger light resulted in even larger attenuation of the signal (See Figure S11.4 in Supporting Information). A similar effect was also observed in spectroscopic

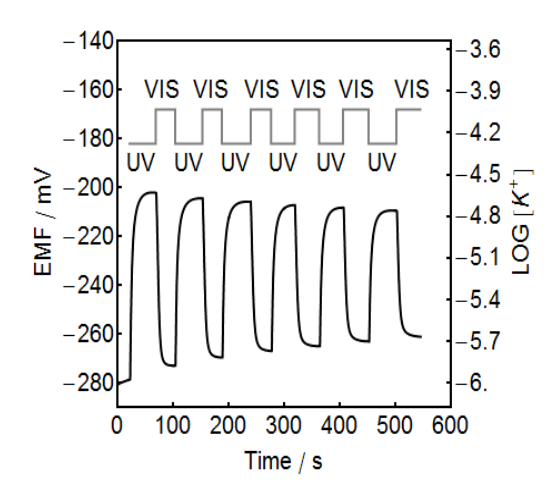


**Figure 11.3.** Direct monitoring of  $K^+$  concentration oscillation (lower trace) induced by the photoswitchable nanospheres in 1 mM HCl under alternating UV and VIS illumination, using a  $K^+$ -selective probe. The applied light sequence is indicated by the gray square wave on the top part.

characterization (See Figure S11.5 in Supporting Information). The choice of light intensity should be a balance between the required speed and photostability.

Although the photolysis of conventional caged ions (Figure 11.1 (a)) is irreversible, the ion concentration after light activation is normally thermally independent. The back reaction of spiropyran from the ring-opened form to the ring-closed form can be accelerated by light, but is also thermally driven.<sup>30</sup> Therefore, it is necessary to confirm that the UV induced  $K^+$  concentration increase remains indifferent when illumination is stopped. If the thermal back reaction were too rapid, the UV induced elevated  $K^+$  concentration should start to decrease. However, after UV light illumination, the EMF response from the  $K^+$  selective electrode was found to remain stable in the dark (See Figure S11.6 in Supporting Information), which confirms that the thermal back reaction for McH $^+$  is in fact sufficiently slow.

Spiropyran has recently been reported to decompose under acidic aqueous conditions, <sup>16</sup> prompting us to study its thermal stability. As shown in Figure S11.7, when the nanospheres were stored in 1 mM HCl, Sp gradually protonated to form MCH<sup>+</sup>, resulting in an increase in the absorbance around 420 nm. On the other hand, this was not the case in the presence of K<sup>+</sup> in the nanosphere suspension. As shown in Figure S11.8, the absorption spectra remained the same even after 20 h in the dark without the appearance of the absorption maxima from Mc or McH<sup>+</sup>, unless UV light was used to activate the nanospheres. No dramatic change in the absorption spectra after UV light illumination was observed, indicating that the nanospheres are thermally quite stable.

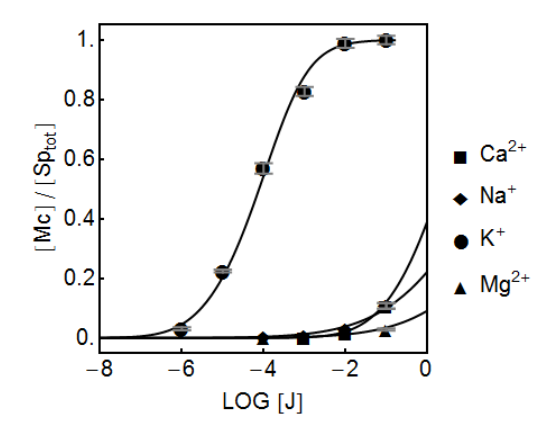


Figure 11.4. Selectivity of the photoswithable nanospheres for K<sup>+</sup> determined in 10 mM acetic acid in fluorescence mode.

Selectivity is also an important aspect one should consider in designing any molecular probe or caging reagent. Ensuring selectivity is usually challenging in developing caged reagents. However, for the system we present here, the selectivity may be superior due to the availability of very selective ionophores.<sup>35</sup> For this model system, valinomycin, for which the selectivity to K<sup>+</sup> is known to be excellent, was chosen as the K<sup>+</sup> receptor.<sup>36,37</sup> The selectivity was confirmed with fluorescence spectroscopy. As shown in Figure 11.4, other metal ions such as Na<sup>+</sup>, Mg<sup>2+</sup> and Ca<sup>2+</sup> did not cause appreciable interference.

### 11.4 Conclusion

In conclusion, a general approach to develop nanospheres that can bring about localized ion concentration perturbation by light has been presented with  $K^+$  as a model ion. The nanospheres can be conveniently produced by precipitation in large quantities. The photoswitchable compound Sp was incorporated into the nanospheres. Upon UV irradiation, the nanospheres increased the surrounding  $K^+$  concentration by releasing  $K^+$ . Unlike most caged reagents, the process could be reversed by illumination with visible light, thereby resulting in a subsequent decrease in the surrounding  $K^+$  concentration. The nanospheres exhibited excellent selectivity for  $K^+$  and may form the chemical basis for a new generation of cage-like nanomaterials.

### 11.5 Supporting Information for Chapter 11

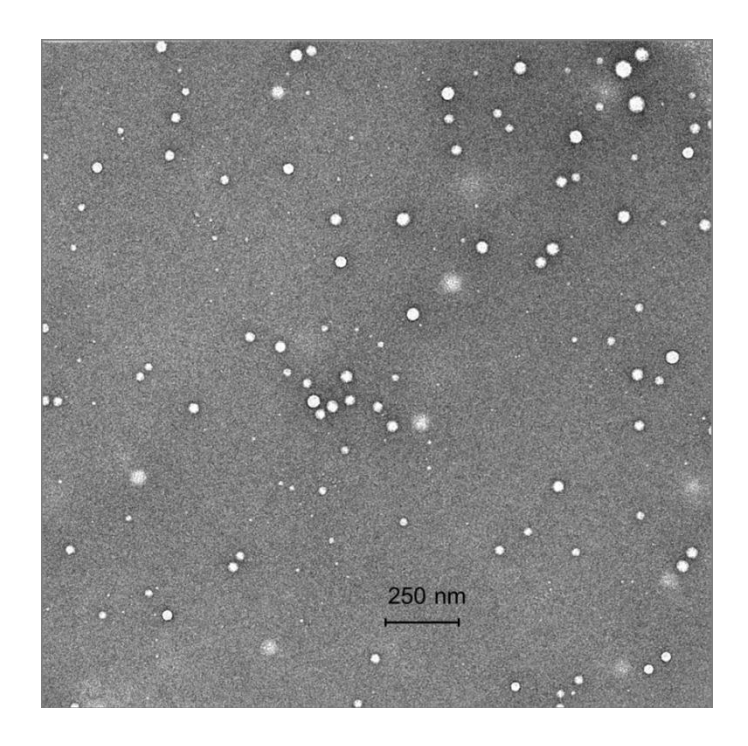


Figure S11.1. Transmission electron microscopic image of the photoswitchable nanospheres.

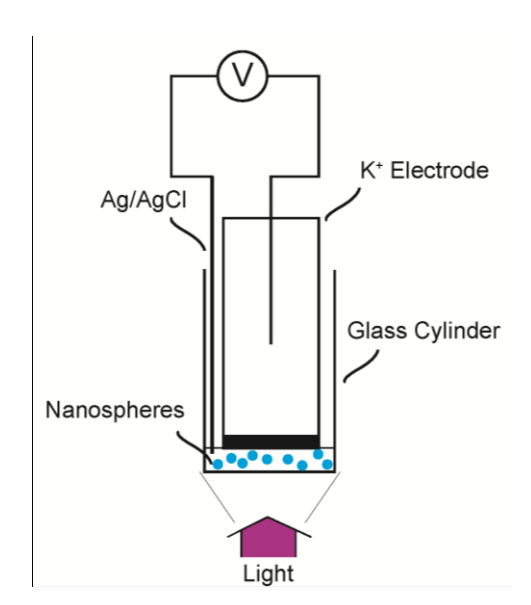


Figure S11.2. Schematic representation for the setup used to direct monitoring light triggered  $K^+$  level oscillation in a suspension of photoswitchable nanospheres.

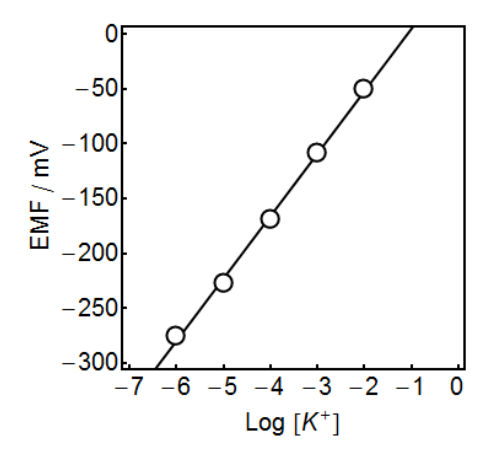


Figure S11.3. External calibration in 1 mM HCl for the K<sup>+</sup>-selective potentiometric probe, used as shown in Figure S11.2.

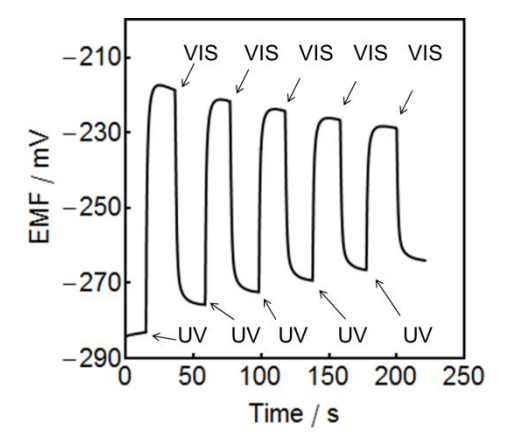
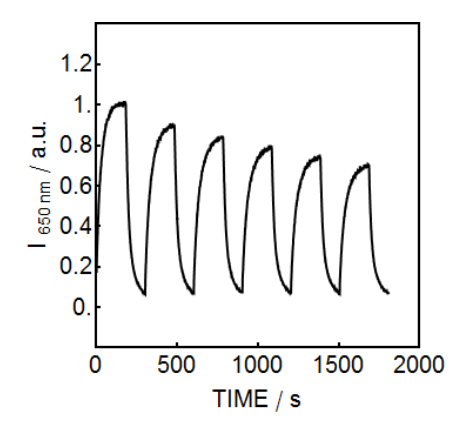
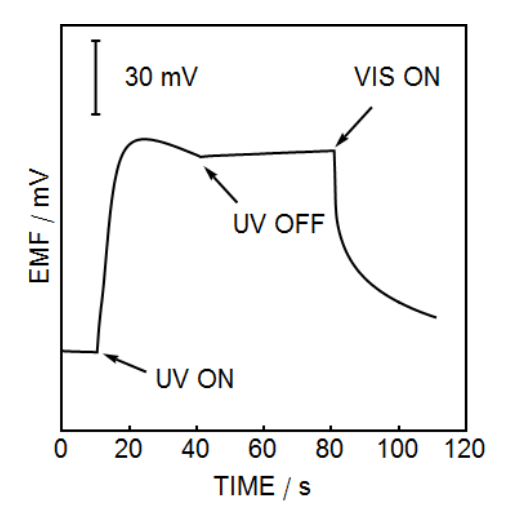


Figure S11.4.  $K^+$  concentration oscillation induced by the photoswitchable nanospheres in 1 mM HCl under UV and VIS illumination. Light intensity: 6 mW cm<sup>-2</sup>



**Figure S11.5.** Photofatigue effect from the nanospheres under spectroscopic interrogation. Light sequence: UV ( 365 nm slit 1.5) 0-300 s, 420-720 s, 840-1140 s,1260-1560 s. VIS (409 nm slit 5) 300-420 s, 720-840 s, 1140-1260 s, 1560-1680 s.



**Figure S11.6.** EMF response from the  $K^+$  selective probe recorded when the nanospheres were first illuminated by UV and kept in the dark for 20 s before VIS light was switched on.

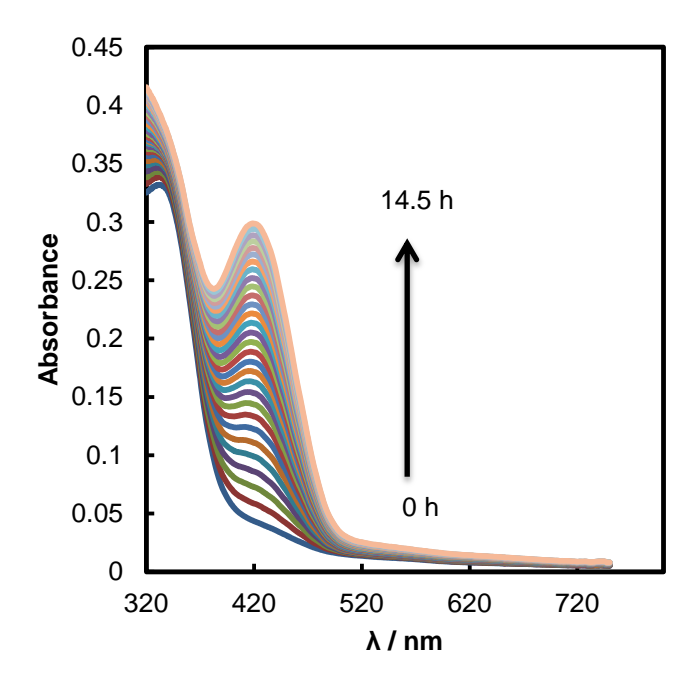
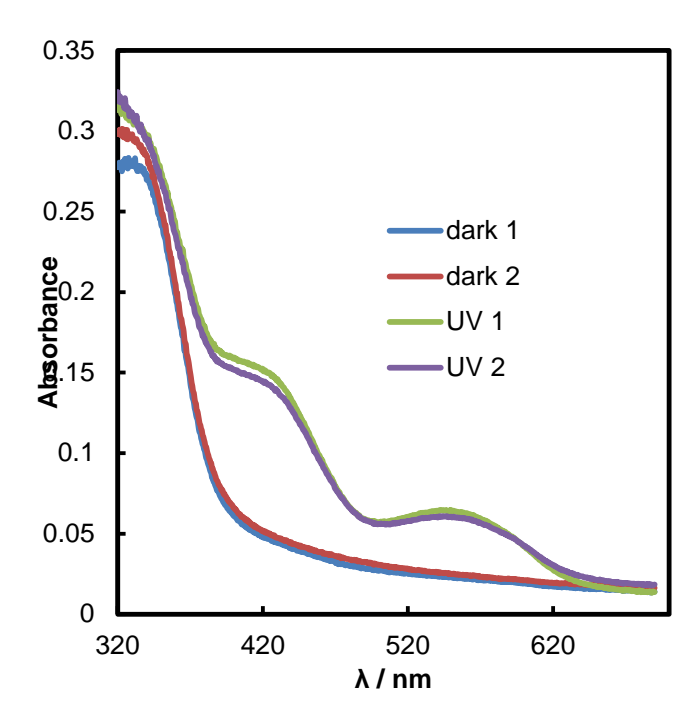


Figure S11.7. Absorption spectra obtained every 0.5 h for photoswitchable nanospheres in 1 mM HCl in the dark.



**Figure S11.8.** Absorption spectra of photoswitchable nanospheres in 10 mM acetic acid containing 1 mM of KCl. dark 1: Spectrum in the dark; UV 1: after UV light illumination for 40 s with a 40 mW cm<sup>-2</sup> UV LED; dark 2: after 20 h in the dark; UV 2: after 20 h in the dark followed by UV illumination for 40 s.

# 11.5 References for Chapter 11

- (1) Wang, K.; Terrenoire, C.; Sampson, K. J.; Iyer, V.; Osteen, J. D.; Lu, J.; Keller, G.; Kotton, D. N.; Kass, R. S. *J. Physiol.* **2011**, 589, 6093.
- (2) Minami, A.; Sakurada, N.; Fuke, S.; Kikuchi, K.; Nagano, T.; Oku, N.; Takeda, A. J. Neurosci. Res. 2006, 83, 167.
- (3) Dudek, F. E. Epilepsy Curr. 2001, 1, 66.
- (4) Lipscomb, W. N.; Sträter, N. Chem. Rev. 1996, 96, 2375.
- (5) Kass, R. S.; Freeman, L. C. *Trends Cardiovas. Med.* **1993**, *3*, 149.
- (6) Michel, H.; Oesterhelt, D. *Biochemistry* **1980**, *19*, 4607.
- (7) Ellis-Davies, G. C. R. Chem. Rev. 2008, 108, 1603.
- (8) Yu, H.; Li, J.; Wu, D.; Qiu, Z.; Zhang, Y. Chem. Soc. Rev. 2010, 39, 464.
- (9) Figueroa, L.; Shkryl, V. M.; Zhou, J.; Manno, C.; Momotake, A.; Brum, G.; Blatter, L. A.; Ellis-Davies, G. C. R.; R ós, E. J. Physiol. 2012, 590, 1389.
- (10) Adam, S. R.; Kao, J. P. Y.; Grynkiewicz, G.; Minta, A.; Tsien, R. Y. J. Am. Chem. Soc. 1988, 110, 3212.
- (11) Ellis-Davies, G. C. R.; Kaplan, J. H. J. Org. Chem. 1988, 53, 1966.
- (12) Adams, S. R.; Kao, J. P. Y.; Tsien, R. Y. J. Am. Chem. Soc. 1989, 111, 7957.
- (13) Ellis-Davies, G. C. R.; Kaplan, J. H. Proc. Natl. Acad. Sci. 1994, 91, 187.

- (14) Olson, J. P.; Kwon, H.-B.; Takasaki, K. T.; Chiu, C. Q.; Higley, M. J.; Sabatini, B. L.; Ellis-Davies, G. C. R. *J. Am. Chem. Soc.* **2013**, *135*, 5954.
- (15) Yue, X.; Yanez, C. O.; Yao, S.; Belfield, K. D. J. Am. Chem. Soc. 2013, 135, 2112.
- (16) Hammarson, M.; Nilsson, J. R.; Li, S.; Beke-Somfai, T.; Andr éasson, J. J. Phys. Chem. B 2013, 117, 13561.
- (17) Kong, L.; Wong, H.-L.; Tam, A. Y.-Y.; Lam, W. H.; Wu, L.; Yam, V. W.-W. ACS Appl. Mater. Interfaces 2014, in press.
- (18) Ziółkowski, B.; Florea, L.; Theobald, J.; Benito-Lopez, F.; Diamond, D. Soft Matter 2013, 9, 8754.
- (19) Giordani, S.; Cejas, M. A.; Raymo, F. M. Tetrahedron 2004, 60, 10973.
- (20) Levitus, M.; Talhavini, M.; Negri, R. M.; Atvars, T. D. Z.; Aramend á, P. F. J. Phys. Chem. B 1997, 101, 7680.
- (21) Mistlberger, G.; Crespo, G. A.; Xie, X.; Bakker, E. Chem. Commun. 2012, 48, 5662.
- (22) Xie, X.; Crespo, G. A.; Mistlberger, G.; Bakker, E. Nat. Chem. 2014, 6, 202.
- (23) Xie, X.; Mistlberger, G.; Bakker, E. J. Am. Chem. Soc. 2012, 134, 16929.
- (24) Mistlberger, G.; Xie, X.; Pawlak, M.; Crespo, G. A.; Bakker, E. Anal. Chem. 2013, 85, 2983.
- (25) Renkecz, T.; Mistlberger, G.; Pawlak, M.; Horv áth, V.; Bakker, E. ACS Appl. Mater. Interfaces 2013, 5, 8537.
- (26) Xie, X.; Mistlberger, G.; Bakker, E. Anal. Chem. 2013, 85, 9932.
- (27) Wang, X.-d.; Stolwijk, J. A.; Lang, T.; Sperber, M.; Meier, R. J.; Wegener, J.; Wolfbeis, O. S. *J. Am. Chem. Soc.* **2012**, *134*, 17011.
- (28) Görner, H. Phys. Chem. Chem. Phys. 2001, 3, 416.
- (29) Bakker, E.; Bühlmann, P.; Pretsch, E. Chem. Rev. 1997, 97, 3083.
- (30) Minkin, V. I. Chem. Rev. 2004, 104, 2751.
- (31) Krysanov, S. A.; Alfimov, M. V. Chem. Phys. Lett. 1982, 91, 77.
- (32) Qin, Y.; Bakker, E. *Talanta* **2002**, *58*, 909.
- (33) Wen, G.; Yan, J.; Zhou, Y.; Zhang, D.; Mao, L.; Zhu, D. Chem. Commun. 2006, 3016.
- (34) Tong, R.; Hemmati, H. D.; Langer, R.; Kohane, D. S. J. Am. Chem. Soc. 2012, 134, 8848.
- (35) Bühlmann, P.; Pretsch, E.; Bakker, E. Chem. Rev. 1998, 98, 1593.
- (36) Anker, P.; Jenny, H. B.; Wuthier, U.; Asper, R.; Ammann, D.; Simon, W. Clin. Chem. 1983, 29, 1447.
- (37) Pietrzak, M.; Meyerhoff, M. E. Anal. Chem. 2009, 81, 5961.

# Chapter 12. Visible Light Induced Photoacid Generation within Plasticized PVC Membranes for Copper (II) Ion Extraction

This work has been published in: Xiaojiang Xie, Günter Mistlberger, and Eric Bakker\*, Sensors and Actuators B 2014, 204, 807–810

# 12.1 Introduction

Inorganic ions play key roles in a number of important biological processes. For example, the proper cellular distributions of K<sup>+</sup> and Na<sup>+</sup> maintain the electrochemical gradients across the cell membrane.<sup>1</sup> Ca<sup>2+</sup> controls the contraction of mammalian muscle cells and is involved in neuron signal transductions.<sup>1</sup> Cu<sup>2+</sup> deficiency is closely associated with Menkes syndrome<sup>2</sup> while Cu<sup>2+</sup> accumulation in liver and brain is characteristic for Wilson's disease.<sup>3</sup> Cell compartments are small and also vulnerable to mechanical intrusion by conventional tools. This makes imposing local ion perturbations within cells quite challenging, while it is an attractive approach to study ion equilibration and transport processes.

In recent years, the concept of light controlled ion perturbation has received attention. Light is relatively noninvasive and could be easily coupled with state of art imaging equipment such as fluorescence microscopes. Several techniques already exist for light controlled ion concentration perturbation. Among these, caged molecules such as those for calcium and glutamate have been most welcome due to their fast response to light. <sup>4-6</sup> Photoacid generators (PAG) that decompose after light illumination have also been reported to induce intracellular pH imbalance. <sup>7</sup> However, to ensure good selectivity and light sensitivity, the design of these molecules is quite challenging and usually requires sophisticated synthesis.

It has been recently introduced that photoswitchable nanospheres containing neutral ionophores can change the local potassium ion concentration (Chapte 11).<sup>8</sup> These nanospheres behave on the basis of photodynamic optode theory, <sup>9-11</sup> and one imposes a light triggered

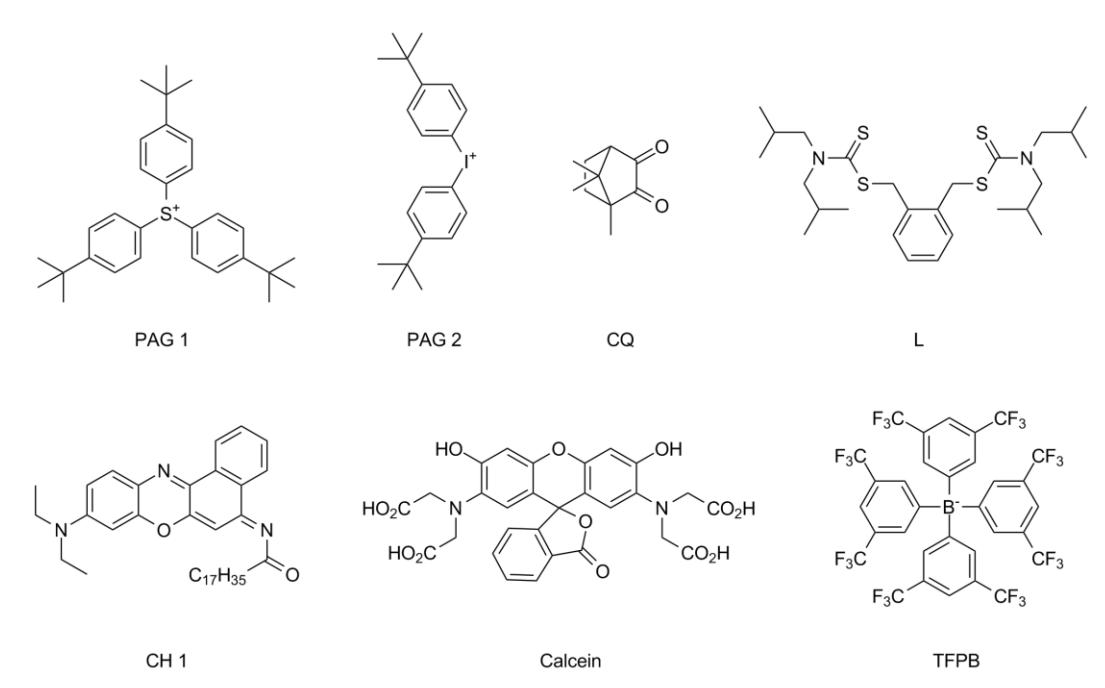


Figure 12.1. Chemical structures and abbreviations of the key compounds used in this work.

pKa change of the chromoionophore. 12

Nanoparticles could penetrate cell membrane and be delivered into cells, making them promising candidates to bring about local ion concentration perturbation when properly functionalized. Furthermore, a combination of these local perturbation tools and other sensing methods can be used to obtain more chemical information. For instance, particles that change the local pH can be used along with conventional pH sensors to study intracellular buffer capacity. Microelectrodes can be inserted in cells to evaluate the concentration of chemicals such as K<sup>+</sup> and glucose. <sup>13,14</sup>

In addition to the strategies mentioned above, one may also consider light triggered formation of ionic sites for ion-exchange and triggered structural changes in ionophore to change the affinity for the target ion. As a case in point, some crown-ether derivatives bearing photoswitchable azobenzene moieties have been devised to show different ionic preferences.<sup>15-19</sup>

On the other hand, the light triggered formation of ionic sites within a polymeric membrane has not been attempted before. Chumbimuni-Torres and coworkers recently reported the activation of ion sensing using spiropyran modified polymer for calcium detection.<sup>20</sup> Here we introduce a strategy to generate ionic sites inside plasticized poly (vinyl chloride) (PVC) membrane upon visible light illumination. After exposure to light, the membrane could extract Cu<sup>2+</sup> ions from the aqueous phase. The polymeric system contained a Cu<sup>2+</sup>-selective ionophore,<sup>21</sup> the photosensitizer camphoroquinone (CQ), and photoacid generator. (see Figure 12.1 for structures) Upon visible light illumination, the photoacid generator decomposed to produce protons that endowed the membrane with ion-exchange properties. In the presence of ionophore, this process triggered the selective uptake of ions from the contacting aqueous environment. Cu<sup>2+</sup> was chosen as a model ion. To visualize and understand this process, fluorescence microscopy imaging was performed with calcein acting as a fluorescent indicator for Cu<sup>2+</sup>.

### 12.2 Material and Methods

**12.2.1 Reagents:** Poly(vinyl-chloride) (PVC, high molecular weight), tetrahydrofuran (THF), chromoionophore I (CH 1), calcein, nitrophenyloctyl ether (NPOE), Cu<sup>2+</sup> ionophore I (L), 2-amino-2-(hydroxymethyl)-1,3-propanediol (Tris), CuCl<sub>2</sub>, sodium tetrakis[3,5-bis(trifluoromethyl)phenyl]borate (NaTFPB), camphorquinone (CQ), tris(4-tert-butylphenyl)- sulfonium triflate (PAG 1) and bis(4-tert-butylphenyl)iodoniumtriflate (PAG 2) were obtained from Sigma-Aldrich and used without purification. In order to replace the hydrophilic trifluoromethanesulfonate counter-anion with a lipophilic counter anion, PAG 1 and PAG 2 and NaTFPB with 1.1 to 1 ratio were dissolved in dichloromethane and extracted with 0.01 M sodium hydroxide aqueous solution. The organic phase was evaporated under reduced pressure to give the desired salt (PAG TFPB).

**12.2.2 Membrane Preparation and Measurements:** To assess the efficiency of photoacid generation, thin films were drop cast on microscopy glass slides from THF cocktails containing 0.3 mg (5 mmol/kg) CH 1, 0.28 mg (5 mmol/kg) of PAG 2, 30 mg of PVC and 60 mg of NPOE and different amount of CQ (0 mg, 0.82 mg, 8.2 mg). The emissions at 640 nm from the films were recorded on a fluorescence spectrometer (Fluorolog3, Horiba Jobin Yvon) with excitation at 470 nm (slit: excitation 14.4, emission 14.4).

Fluorescence response of calcein to  $Cu^{2+}$  was measured in 0.1 M pH 7.4 Tris-HCl buffer solution containing 1  $\mu$ M of calcein.  $CuCl_2$  was added gradually into the solution and emission spectra were recorded.

Figure 12.2. Proton generation from PAG 2 under deep UV irradiation and visible light illumination (sensitized by CQ).

For fluorescence microscopy imaging as shown in Figure 12.5, a THF cocktail containing 1.5 mg (30 mmol/kg) of  $Cu^{2+}$  ionophore I, 5.0 mg (40 mmol/kg) of PAG TFPB, 3.3 mg (200 mmol/kg) of CQ, 30 mg of PVC and 60 mg of NPOE was poured into a 22 mm glass ring in a dustless environment to allow THF evaporation overnight. To image the  $Cu^{2+}$  uptake process, small pieces of membrane was cut with sharp edges and placed in contact with a  $10^{-4}$  M  $CuCl_2$  solution containing  $10^{-4}$  M calcein in a 0.1 M Tris-HCl buffer at pH 7.4. A blue light beam (482±35 nm, ca. 5 mW) was used to initiate the photodynamic process and the fluorescence images across the boundary were recorded through the FITC filter (530 ±43 nm) on an inverted fluorescence microscope (ECLIPSE Ti-E, Nikon) every 10 s.

#### 12.3 Results and Discussion

Ion-exchangers are normally required to endow polymeric membrane with permselective properties. Without cation exchanger, such as TFPB, it is very difficult for hydrophilic cations, such as Cu<sup>2+</sup>, to be exchanged into a PVC-NPOE film. Coextraction of Cu<sup>2+</sup> together with lipophilic anions is possible but only happens when the product of the two ion concentrations is sufficiently high. The presence of ion-exchanger in the polymeric phase is crucial to how the membrane responds to ionic species. It should be noted, however, that even in the presence of TFPB, the counter cation has to be sufficiently hydrophilic to allow for cation exchange with the target ion. As shown in Figure 12.1, when bulk cations such as PAG 1 and PAG 2 act as the counter ion of TFPB, Cu<sup>2+</sup> cannot be exchanged into the membrane.

PAG 1 and PAG 2 are known as photoacid generators that decompose to produce H<sup>+</sup> under deep UV irradiation. They have been widely used in UV coating and lithography as photo initiators for cationic polymerization.<sup>22,23</sup> However, deep UV light is much too destructive

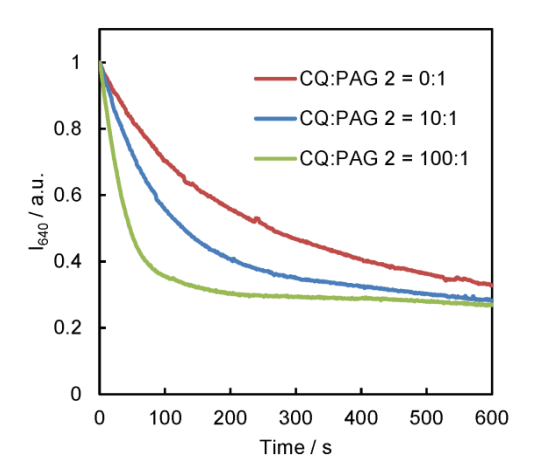


**Figure 12.3.** Scavenging the H<sup>+</sup> generated in situ by CH 1 inside PVC-NPOE film containing different molar ratios of CQ to PAG 2, as indicated.

especially for biological samples. UV light is absorbed by and can degrade a number of biological molecules such as proteins, peptides and nucleic acids. Visible light and near infrared light are much less destructive in this regard. It has been reported that cationic polymerizations using PAG 2 as initiator can be sensitized by organic dyes that absorb in the near UV and even in the visible range. As shown in Figure 12.2, in addition to the direct decomposition under 254 nm deep UV light, PAG 2 could also decompose when it is sensitized by CQ, upon visible light (447-517 nm) irradiation. PAG 1 does not show this effect.

The photoacid generation process has been previously studied.<sup>22</sup> Briefly, CQ absorbs light energy and reaches an excited state, which reacts with the photoacid generator cation via both radical and ionic pathways to yield H<sup>+</sup> and neutral residues. Since only PAG 2 can be sensitized by CQ,<sup>22</sup> only this compound has been employed for further studies.

The proposed NPOE plasticized PVC system contained a Cu<sup>2+</sup> ionophore I (L), a photosensitizer CQ and a cationic photoacid generator, with TFPB<sup>-</sup> as counter anion (PAG TFPB). As mentioned above, Cu<sup>2+</sup> in the contacting aqueous sample could not be extracted into the polymeric phase because the polymeric phase lacked ion exchanging properties. Once the PAG cation was photolysed to give H<sup>+</sup>, a hydrophilic species, the polymeric phase acquired ion exchanging properties and could extract Cu<sup>2+</sup> from the contacting aqueous phase. The driving force for the extraction of Cu<sup>2+</sup> ions is provided by the complexation reaction between L and Cu<sup>2+</sup> in the membrane phase.<sup>21</sup>

The efficiency of the photoacid generation was evaluated by incorporating a pH indicator dye CH 1 into the PVC-NPOE membrane during the acid generation process. The fluorescence emission maximum for deprotonated CH 1 at 640 nm was monitored over time while the membrane was illuminated with 478 nm light. If CH 1 became protonated, the emission intensity at this wavelength should decrease. As shown in Figure 12.3, for membranes containing increasing levels of CQ as photosensitizer, the emission intensity at 640 nm decreased much faster. When a large excess of CQ (CQ:PAG 2=100:1) was used, acid production inside the membrane occurred within 100s.

Followed by the light triggered acid generation, free  $Cu^{2+}$ , if presented in the contacting aqueous sample, would be extracted into the polymeric phase. The extraction of  $Cu^{2+}$  was promoted by the copper ionophore L within the polymeric membrane, which can stabilize  $Cu^{2+}$  forming 1:1 ratio complexes. This extraction of  $Cu^{2+}$  was visualized by fluorescence microscopy using calcein as indicator for  $Cu^{2+}$ .  $Cu^{2+}$  is able to quench the fluorescence of calcein (Figure 12.4). When the concentration of  $Cu^{2+}$  was reduced, the fluorescence intensity of calcein increased.

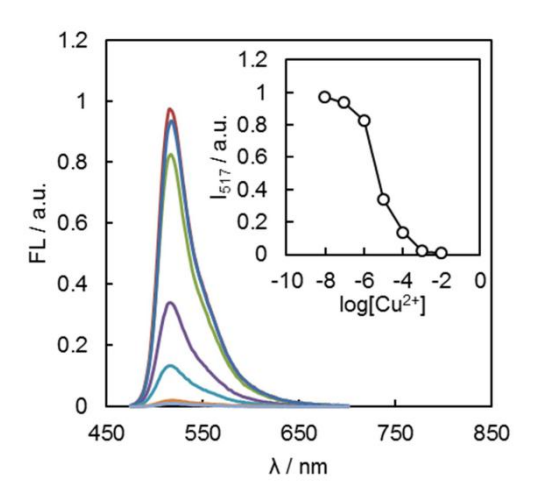
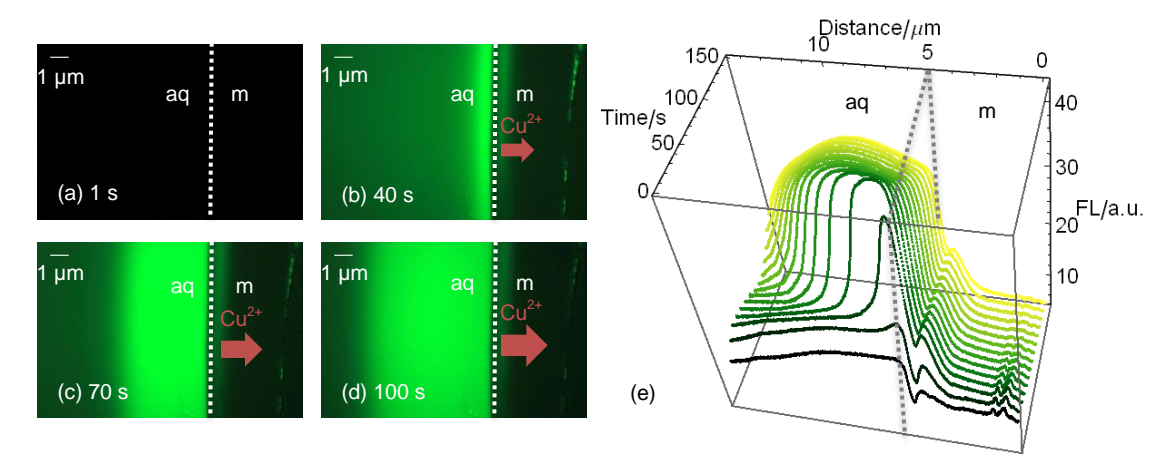


Figure 12.4.  $Cu^{2+}$  induced fluorescence quenching of 1  $\mu$ M of Calcein in 0.1 M of pH 7.4 Tris-HCl buffer. Excitation: 470 nm. Inset: Calibration from emission intensity at 517 nm.



**Figure 12.5.** Fluorescence microscopy images for the visible light induced  $Cu^{2+}$  uptake by the CQ sensitized photoresponsive membrane after blue light exposure of 1 s (a), 40 s (b), 70 s (c), 100 s (d) . (e) Temporal evolution of the fluorescence emission of Calcein across the aqueous-polymeric phase boundary. The red arrows indicate the extraction of  $Cu^{2+}$  ions into the membrane phase while aq and m indicate the membrane and aqueous phases separated by dotted lines. The fluorescence increases as the  $Cu^{2+}$  concentration goes down.

For fluorescence microscopy imaging, a membrane containing 30 mmol/kg of L, 40 mmol/kg of PAG TFPB, 200 mmol/kg of CQ was cut with sharp edges and placed in contact with an aqueous solution containing  $10^{-4}$  M CuCl<sub>2</sub> and  $10^{-4}$  M calcein at pH 7.4 (0.1 M Tris-HCl). The pH of the aqueous phase was buffered in order to avoid the acidification by the H<sup>+</sup> produced within the membrane. The fluorescence profile across the membrane-solution boundary was found stable prior to light exposure, indicating that no spontaneous Cu<sup>2+</sup> extraction occurred in the dark. A blue light beam (482±35 nm) was used to initiate the photodynamic process and the fluorescence images across the boundary was captured by fluorescence microscope every 10 s. As shown in Figure 12.5, the fluorescence intensity in the aqueous solution close to the film increased as the illumination was carried out, indicating the uptake of Cu<sup>2+</sup> by the membrane. The fluorescence profile across the boundary as a function of time was plotted in 3D as shown in Figure 12.5 (e).

# 12.4 Conclusion

In conclusion, photoresponsive PVC-NPOE films have been used here to bring about localized Cu<sup>2+</sup> ion perturbations. Combining photoacid generator and photosensitizer within the membrane makes the membrane responsive to visible light, which is more preferred that deep UV light. The membrane stage experiments successfully support the proposed concept. Further research to miniaturize the system into particle form is continuing in our laboratory.

# 12.5 References for Chapter 12

- (1) Alberts, B.; Johnson, A.; Lewis, J.; Raff, M.; Roberts, K.; Walter, P. In *Molecular Biology of the Cell(fifth edition)*; Garland Science, Taylor & Francis Group: 2008.
- (2) Robinson, N. J. Nature 2011, 475, 41.
- (3) Neumann, P. Z.; Silverberg, M. Nature 1967, 213, 775.
- (4) Ellis-Davies, G. C. R. Chem. Rev. 2008, 108, 1603.
- (5) Figueroa, L.; Shkryl, V. M.; Zhou, J.; Manno, C.; Momotake, A.; Brum, G.; Blatter, L. A.; Ellis-Davies, G. C. R.; R ós, E. *J. Physiol.* **2012**, *590*, 1389.
- (6) Olson, J. P.; Kwon, H.-B.; Takasaki, K. T.; Chiu, C. Q.; Higley, M. J.; Sabatini, B. L.; Ellis-Davies, G. C. R. *J. Am. Chem. Soc.* **2013**, *135*, 5954.

- (7) Yue, X.; Yanez, C. O.; Yao, S.; Belfield, K. D. J. Am. Chem. Soc. 2013, 135, 2112.
- (8) Xie, X.; Bakker, E. ACS Appl. Mater. Interfaces 2014, 6, 2666.
- (9) Xie, X.; Mistlberger, G.; Bakker, E. Anal. Chem. 2013, 85, 9932.
- (10) Xie, X.; Zhai, J.; Bakker, E. Anal. Chem. **2014**, 86, 2853.
- (11) Mistlberger, G.; Xie, X.; Pawlak, M.; Crespo, G. A.; Bakker, E. Anal. Chem. 2013, 85, 2983.
- (12) Xie, X.; Mistlberger, G.; Bakker, E. J. Am. Chem. Soc. 2012, 134, 16929.
- (13) Asifa, M. H.; Alia, S. M. U.; Nura, O.; Willandera, M.; Brännmarkb, C.; Strålforsb, P.; Englundb, U. H.; Elinderb, F.; anielssonc, B. *Biosens. Bioelectron.* **2010**, *25*, 2205.
- Danielsson, C.; Brask, J.; Sköld, A.-C.; Genead, R.; Andersson, A.; Andersson, U.; Stockling, K.; Pehrson, R.; Grinnemo, K.-H.; Salari, S.; Hellmold, H.; Danielsson, B.; Sylvén, C.; Elinder, F. *Cardiovasc. Res.* **2013**, *97*, 23.
- (15) Shinkai, S.; Nakaji, T.; Nishida, Y.; Ogawa, T.; Manabe, O. J. Am. Chem. Soc. 1980, 102, 5860.
- (16) Shinkai, S.; Nakaji, T.; Ogawa, T.; Shigematsu, K.; Manabe, O. J. Am. Chem. Soc. 1981, 103, 111.
- (17) Shinkai, S.; Ogawa, T.; Kusano, Y.; Manabe, O.; Kikukawa, K.; Goto, T.; Matsuda, T. J. Am. Chem. Soc. 1982, 104, 1960.
- (18) Shinkai, S.; Minami, T.; Kusano, Y.; Manabe, O. J. Am. Chem. Soc. 1982, 104, 1967.
- (19) Shinkai, S.; Minami, T.; Kusano, Y.; Manabe, O. J. Am. Chem. Soc. 1983, 105, 1851.
- (20) Johns, V. K.; Patel, P. K.; Hassett, S.; Calvo-Marzal, P.; Qin, Y.; Chumbimuni-Torres, K. Y. Anal. Chem. 2014, 86, 6184.
- (21) Kamata, S.; Murata, H.; Kubo, Y.; Bhale, A. Analyst 1989, 114, 1029.
- (22) Cook, W. D.; Chen, F. J. Polym. Sci. Al 2011, 49, 5030.
- (23) Crivello, J. V. J. Polym. Sci. A1 2008, 46, 3820.
- (24) Chen, S.; Cook, W. D.; Chen, F. *Macromolecules* **2009**, 42, 5965.
- (25) Crivello, J. V. Annu. Rev. Mater. Sci. 1983, 13, 173.
- (26) Crivello, J. V.; Kong, S. *Macromolecules* **2000**, *33*, 833.

# Chapter 13. Photocurrent Generation Based on a Light-Driven Proton Pump in an Artificial Liquid Membrane

This work has been published in: Xiaojiang Xie, Gaston A. Crespo, Günter Mistlberger and Eric Bakker\*, Nat. Chem. 2014, 6, 202-207

## 13.1 Introduction

Light is harvested in many ways in biological systems including photo-synthesis and the regulation of ion transport through lipid bilayers. <sup>1</sup> Energy from sunlight can create an electrochemical gradient across plasma membranes by ion pumps confined to the membrane. Creating artificial light harvesting systems that are inspired by nature has been an interdisciplinary research hotspot. <sup>2-5</sup> Considering the enormous importance of solving the energy problem and addressing global warming, fundamental research on light harvesting can lay the foundation of utilizing solar energy and has the potential to revolutionize the field of solar cell development.

Important research work in recent years includes the use of artificial photosynthetic centres to generate a chemical potential that later can be used either to generate electrical power or carry out some active transport of ions, such as Ca<sup>2+,6,7</sup> Others involve the use of chlorophyll-containing photoproteins to generate photocurrent and oxidizing or reducing potentials. <sup>8,9</sup> Although the current density is small, it has been shown that alternating current is formed by discontinuous illumination of light. <sup>10</sup> These systems mimic the natural photosynthetic process. Upon light, a charge separation (i.e., a positively charged and a negatively charged end) is formed and allows further redox reaction to make use of the established electrochemical potential. However, the lifetime of the charge separated species is generally very short (hundreds of ns to several µs)<sup>11</sup> and can limit the efficiency. An energy state upon light irradiation with longer life time should help surpass the undesired charge recombination process.

Spiropyrans are established photochromic compounds. Irradiated with UV light, the excited state ring closed form (Sp) undergoes a ring opening photoreaction and forms the ring opened merocyanine (Mc) structure. The photoproduct Mc has a higher energy state than the

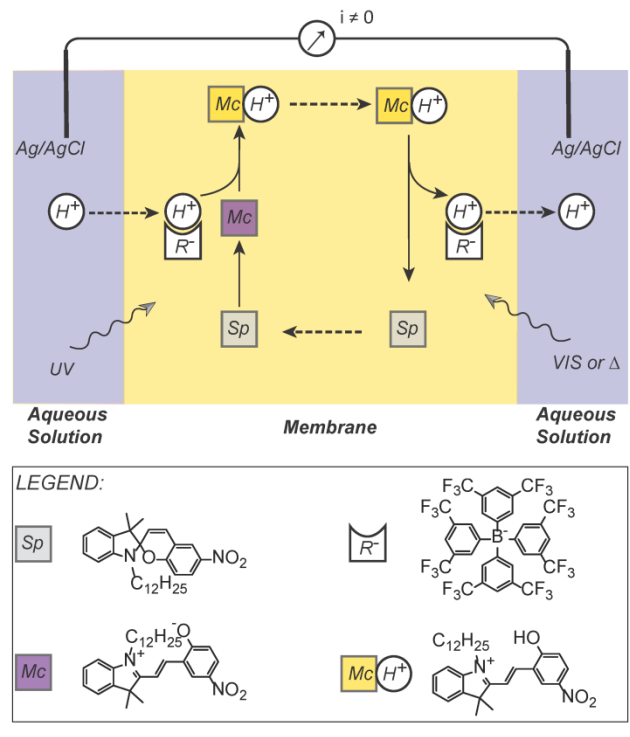


**Figure 13.1.** Scheme showing the photocurrent generation principle. The left side of the membrane is illuminated with UV light while the right side is irradiated with visible light or kept in the dark. The membrane contains 5 mg Sp, 6.5 mg ETH 500 and 3 mg K<sup>+</sup>R<sup>-</sup> in 50 mg nitrophenyloctylether as solvent. The aqueous solutions both contain 0.1M HCl. For simplicity, ETH 500 and Cl<sup>-</sup> are not shown. The Dashed arrows represent mass transport of the species.

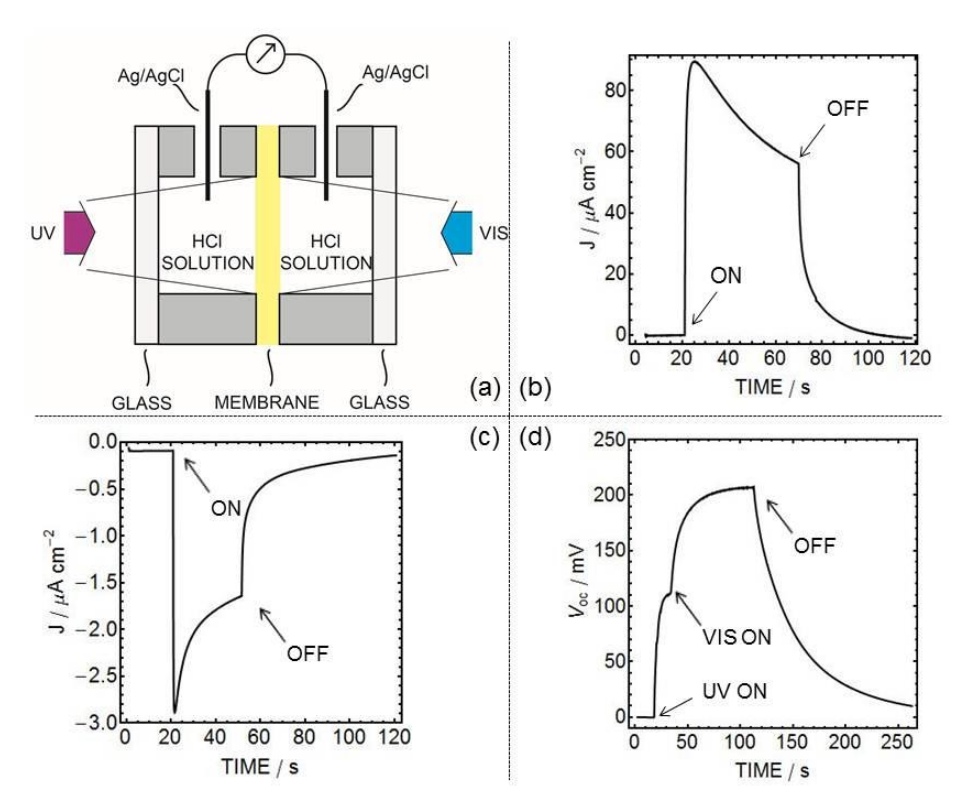


**Figure 13.2.** (a) Representation of the flow cell used to measure the photocurrent generated by the light harvesting membrane. (b) Photocurrents generated when the membrane was placed in 0.1 M HCl and illuminated with UV light on one side. (c) Photocurrent generated with the illumination of VIS (482±35 nm) on one side of the membrane. (d) Observed open-circuit voltage when the membrane is illuminated with UV on one side and subsequently with VIS on the other.

ground state Sp form and a life time of several seconds or minutes, depending on the matrix. <sup>12,13</sup> Compared with previously mentioned lifetimes of the excited state in manmade photosynthetic reaction centres and natural photoproteins, this time scale greatly enhances the chance to make use of the chemical potential before Mc reverts to Sp. The reverse ring-closing reaction is thermally driven and can be accelerated by illumination with visible light. <sup>13</sup>

Recently we found that, in addition to the higher energy state, the Mc form of spiropyran exhibits a much larger pKa value in the liquid organic phase (8.6±0.1) than that of the ring-closed Sp form (2.3±0.1). Using the pKa-change as a driving force, we successfully developed light triggered ion exchange materials selective for Cl<sup>-</sup> (Chapter 10), Ca<sup>2+</sup> and Na<sup>+</sup>. Owing to the basicity difference between Sp and Mc, in principle, proton gradients across a membrane can also be realized. The proton gradient in biological systems serves as a versatile energy source that drives energy-requiring reactions such as ATP synthesis. In Light-driven proton pumps such as bacteriorhodopsin contain retinal compounds that change their conformation upon photon absorption. The resulting conformational change of the protein gives rise to an altered affinity to H<sup>+</sup> and thereby promotes the uptake or release of protons across the plasma membrane. In this sense, the conformational change in spiropyran, followed by an increase in pKa, shows some analogies to light driven proton pumps.

On the basis of the unique properties of photoswitchable spiropyran, we report here on a polymeric membrane based artificial light-harvesting system. A proton gradient is generated across a polymer membrane upon light illumination. Both UV and visible light can be used to induce proton fluxes in the membrane and electrochemical potential. As a proof of concept, we demonstrate that such a principle can be used for photoelectric conversion. Such principle is not found in currently existing solar cells, which are mostly based on photovoltaic effects.<sup>24-26</sup> Compared with rigid conductive glass, the liquid membrane is flexible and foldable, which is attractive for the

design of a more compact cell. Because UV and visible light cause different directions of the proton flux, alternating current is formed when UV and visible light are applied alternatively.

#### 13.3 Results and Discussion

The artificial light harvesting membrane is composed of spiropyran, a cation exchanger (potassium tetrakis[3,5-bis-(trifluoromethyl)phenyl]borate, K<sup>+</sup>R<sup>-</sup>), and a lipophilic salt, tetradodecylammonium tetrakis(4-chlorophenyl)borate (ETH 500) to reduce the resistance of the membrane, dissolved in a supported liquid membrane (nitrophenyloctylether in a Celgard porous polypropylene membrane). The membrane is mounted into a flow cell (Figure 13.2 (a)) where both sides of the membrane are in contact with aqueous solutions of identical composition. The circuit is then completed with Ag/AgCl wires, which allow to define a stable potential and to pass a relatively high current density. As shown in Figure 13.1, when the membrane is illuminated with UV light from the front side and with visible light from the back, the affinity for H<sup>+</sup> becomes significantly higher for the UV illuminated side owing to the formation of the more basic Mc. The concentration gradient of protonated Mc across the membrane results in a net proton flux in the opposite direction, i.e., towards the VIS illuminated side of the membrane.

At the backside, protonated Mc is converted into Sp form by visible illumination, thereby releasing the transported proton into the contacting aqueous phase. The quantitative conversion of Mc into Sp creates a concentration gradient and net flux of the latter in direction of the UV illuminated side of the membrane where the cycle starts anew.

A membrane with the above mentioned composition was symmetrically placed in contact with 0.1 M HCl and initially illuminated from

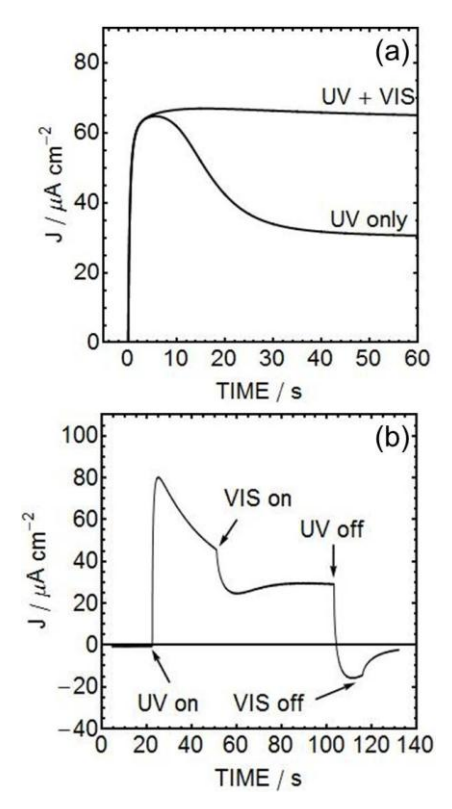


**Figure 13.3.** (a) Photocurrent evolution from numerical simulation showing the difference between UV irradiation at one side only  $(k_1=10^{-1.1} \text{ s}^{-1}, k_2=1 \text{ s}^{-1})$  and asymmetric illumination with UV and VIS  $(k_1=10^{-1.1} \text{ s}^{-1}, k_2=10^{-6} \text{ s}^{-1})$ . (b) Experimental photocurrent generated when the membrane is illuminated with the light sequence indicated in the figure.

only one side which resulted in the photocurrents shown in Figure 13.2. A control experiment with a membrane containing ion exchanger and the optically silent H<sup>+</sup>-carrier tridodecylamine gave no current response, suggesting that the photochromic spiropyran is responsible for photocurrent generation. Illumination with UV light at one side generated a cathodic current (Figure 13.2 (b)), while visible light irradiated from the same side gave an anodic current (Figure 13.2 (c)). The activation of Sp is a much faster process than the ring-closing back reaction and since a large excess of Sp is used with respect to R<sup>-</sup>, the current density caused by UV light is higher than that by visible light.

UV illumination results in spiropyran conversion to protonated McH<sup>+</sup> which is transported from the UV illuminated side along a concentration gradient to the inner membrane side, where visible light will convert this species back to Sp. The net transport of McH<sup>+</sup> results in continuous uptake and transport of hydrogen ions across the membrane, see Figure 13.1.

The ion-exchanger defines the possible concentration of the diffusing McH<sup>+</sup> counterion in the membrane bulk. Its presence enhances the current by maximizing the possible concentration gradient. Indeed, the photocurrent density generated with a membrane without R<sup>-</sup> was much smaller (see Figure S13.1 in Supporting Information).

Previous work on artificial photosynthetic centre embedded membranes shows that a large open-circuit voltage ( $V_{oc}$ ) of ~140 mV can evolve after more than ten hours of light illumination. With the current polymeric light harvesting system, as shown in Figure 13.2 (d), a  $V_{oc}$  of ~210 mV is established after merely a few minutes. Since the solutions contacting the two sides of the membrane have the same pH value, the established  $V_{oc}$  corresponds to a  $\Delta$ pH (pH difference across the interior of the membrane) of 3.6 units. Under such zero current conditions, the pH values in the two aqueous phases do not change. Indeed, only slight deviations in  $V_{oc}$  are observed as one dilutes the HCl solutions to  $10^{-5}$  M (see Figure S13.2 in Supporting Information). Comparing with the  $\Delta$ pH of 6.3 in our previous study in polymeric ion-selective electrodes, this value is significantly smaller. This is explained by the reduced thickness of the membrane, which allows the arrival of some of the light at the opposite side of the membrane. Once the cell is short-circuited, a proton flux will be generated across the membrane, causing the pH in the aqueous phases to change. However, since rather concentrated HCl is used, the pH change in the bulk of the solution is not observable. Instead, the proton transport was visualized by diluting the HCl solution to  $10^{-4}$  M and directly measuring the pH close to the membrane (< 0.5 mm) with a miniature pH probe (1.3 mm tip dia.), see Figure S13.3 for setup. While the current density was lower because of the diminished HCl concentration, a substantial pH decrease of 2.8 units was observed, confirming net proton transport.

The observed current density for the membrane irradiated with UV light started to decrease after reaching a maximum. To understand the magnitude and time evolution of the photocurrent, a numerical simulation was performed. The membrane was divided into 11 equally spaced distance elements. The UV activation and the back reaction were assumed to take place only in the first and the last elements that are in contact with aqueous solutions. The reactions between the ring-open and ring-closed spiropyran were treated as unimolecular reactions, as expressed with Eqn. 13.1, with  $k_1$  and  $k_2$  the rate constants for the forward and backward reactions:

$$Sp \xrightarrow{k_1} Mc \xrightarrow{K_a, H^+} McH^+$$
 (13.1)

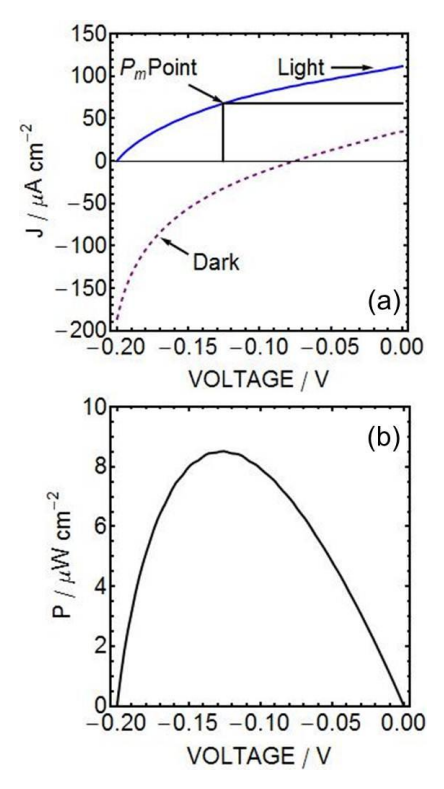


**Figure 13.4** (a) Current density characteristics for the light harvesting cell under light illumination (10 mW cm<sup>-2</sup>) and in the dark. (b) Corresponding power density-voltage relationship under light irradiation.

The shape of the current time transient agrees with the experimental data. According to results from the simulation, as shown in Figure 13.3 (a), when only UV is irradiating one side of the membrane, the current density reaches a maximum and subsequently starts to decrease. The drop in current density is ascribed to the accumulation of the McH $^+$  on the opposite dark side of the membrane. Previous studies reported that the thermal reaction from McH $^+$  to Sp is quite slow but can be accelerated by visible light. The activation of Sp to McH $^+$  and the transport of McH $^+$  across the membrane, however, is a much faster process. The time for such organic compounds to diffuse through the NPOE doped Celgard membrane with a thickness of 30  $\mu$ m is estimated to be around 50 s (estimated from diffusion processes), while the lifetime of the ring-opened spiropyran may reach hours. However, when the membrane is irradiated with asymmetric light, i.e., one side UV and the other VIS, the predicted steady-state current density is more stable, since the back reaction is accelerated by visible light (See Supporting Information for details of the simulation). To confirm this, the membrane was illuminated with UV and visible light from both sides. As shown in Figure 13.3 (b), the current density becomes indeed more stable when visible light is applied to accelerate the back reaction and help to maintain a significant concentration gradient of McH $^+$  across the membrane. Assuming a complete conversion from the open form to Sp at the visible side (i.e.  $k_2$  in Eqn. 13.1 is large), the limiting steady state current density J can be expressed by Eqn. 13.2:

$$J = FD_{McH} \frac{[McH^{+}]_{UV}}{d} = k_{1} F[Sp]_{T}$$
(13.2)

where  $D_{McH}$  is the diffusion coefficient of McH<sup>+</sup> and membrane, d the thickness of the membrane,  $k_I$  the rate constant shown in Eqn. 13.1,  $[McH^+]_{UV}$  the concentration of McH<sup>+</sup> at the UV illuminated side, F the Faraday constant, and  $[Sp]_T$  the total concentration of Sp. A instantaneous decrease of current density is seen immediately after VIS is switched on, indicating that residual visible light may reach the

UV side of the membrane to drive the reaction partly backwards. At steady state, the current density is observed to be around 30  $\mu$ A cm<sup>-2</sup>, which is notably higher than previous reported systems based on photoproteins.<sup>8,10</sup>

A linear potential sweep on the cell from  $V_{oc}$  to 0 under light illumination (10 mW cm<sup>-2</sup>) and in the dark gives the J-V curve shown in Figure 13.4. The maximum power ( $P_m$ ) point is found at -0.13 V which gives a fill factor of 0.6. Therefore, the overall efficiency for the current generation is estimated to be ~0.0012. The quantum efficiency for the activation of Sp is reported to be only 0.1, thus, a compound with better quantum yield will potentially improve the overall efficiency, although further reducing the overall resistance is possible (using an appropriate ionic liquid as pore filling solvent for the membrane support, for instance).

According to Eqn. 13.2, the current density is influenced by a number of factors including membrane composition, the thickness of the membrane, the nature of the polymer matrix, reaction kinetics, and the composition of the contacting aqueous solution. The proton flux induced by light is inversely proportional to the membrane thickness. If photochemical reaction rates are not rate limiting, much larger proton flux and associated current density may be achieved with lipid bilayers that exhibit thicknesses on the order of 5 nm<sup>1</sup>. With the membranes used here, the influence of the light induced proton flux on a thin layer sample can also be easily visualized with fluorescence microscopy (Figure S13.5). When fluorescein was used to image the pH of a sample solution containing 0.1 M NaCl, the spiropyran in the membrane remained deprotonated and no significant change in fluorescence was observed when the membrane–sample interface was illuminated with visible light (482±35 nm). In contrast, when illuminated with UV light, protons in the sample started to be pumped to the other side and an increase in the fluorescence was observed.

Since illumination by light of different wavelength results in a reversal of the direction of the current, the concept is potentially useful for the generation of alternating current. In the light harvesting system described here, the direction of the current can be controlled by light with different wavelength. Indeed, when different light sequences were applied, different photocurrent patterns were observed. As shown in Figure 13.5, the positive current that arises from UV light illumination can be forced to change its direction when UV is switched to visible light. An alternative application of UV and visible light at variable frequency gives a current with corresponding frequency (Seeing Figure S6 and Figure S13.7 in Supporting Information). The current density is much higher compared with recently reported alternating photocurrent. The frequency in this system is limited by the photoreaction kinetics and can be adjusted by varying the light intensity and illumination time. In this particular system, the ring-closing reaction is the slowest step and thereby limits the applicable frequency.

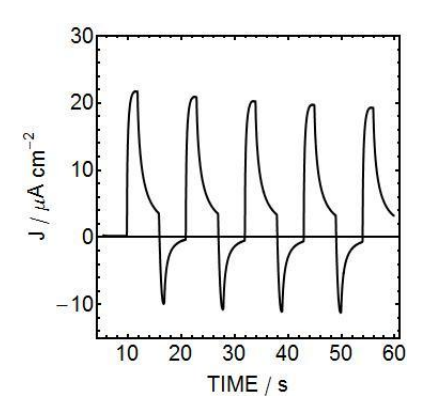


**Figure 13.5.** Alternating photocurrent generation by the membrane in 0.1 M HCl with alternating UV and visible light (UV for 2 s + off 4 s + VIS 1 s + off 4 s) illuminating on one side of the membrane.

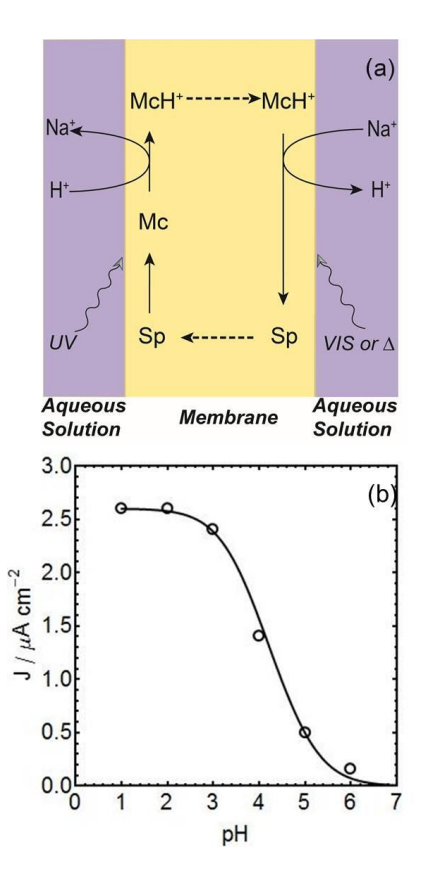


Figure 13.6. (a) Scheme demonstrating light induced counter-diffusion flux of sodium ions in the opposite direction, which competes with the proton pumping and thereby reducing the current; (b) observed photocurrent density from membrane under  $\sim$ 0.2 mW cm<sup>-2</sup> illumination as a function of pH in the two buffer solutions (2.5 mM boric acid + 2.5 mM citric acid + 2.5 mM NaH<sub>2</sub>PO<sub>4</sub>), while the Na<sup>+</sup> background was fixed at 2 M. The counter-diffusion process becomes more important at high pH and results in a decreased current density.

When ions other than H<sup>+</sup> (for example Na<sup>+</sup>) are present in the aqueous phase, the transport of H<sup>+</sup> may be accompanied with counter-transport of that second ion (Figure 13.6 (a)), thereby diminishing the observed current density. While the H<sup>+</sup> transport shown in Figure 13.1 still occurs, the Na<sup>+</sup> counter flux will diminish the observable photocurrent density. This is confirmed when the photocurrent is monitored while the Na<sup>+</sup> concentration of the buffer solution in both chambers in the setup shown in Figure 13.2 (a) is fixed at 2 M and the proton concentration is changed by adjusting the solution pH. As shown in Figure 13.6 (b), as pH increases, Na<sup>+</sup> causes a decrease in current density. For maximum photocurrent, the membrane should be in contact with acidic solutions without competing cations.

## 13.4 Conclusion

In summary, a polymeric membrane light harvesting system that utilizes the photoswitching of spiropyran with UV and visible light is presented. Currents of different signs are observed when the membrane is illuminated with UV or visible light, and alternating current can be produced by applying alternating UV and visible light. A theoretical simulation was performed to understand the current evolution. An energy conversion system based on such a principle has, to our knowledge, not been reported before. The working principles for the system and the current characteristics have been studied by electrochemical and fluorescence methods and lay the foundation for further progress

in this area. The system is potentially useful in photoelectric conversion and the same principle can be applied to other compounds that are able to change their affinity towards charged species upon light irradiation.

## 13.5 Supporting Information for Chapter 13

# 13.5.1 Experimental Section

o-nitrophenyl octyl ether (o-NPOE), tridodecylamine, potassium tetrakis[3,5-bis-(trifluoromethyl)phenyl]borate (K+R), and tetradodecylammonium tetrakis(4-chlorophenyl)borate (ETH 500) were Selectophore grade and purchased from Sigma-Aldrich. Polypropylene microporous membrane (Celgard 2400) was gratefully obtained from Celgard, LLS. Spiropyran was synthesized according to the literature. For the membrane preparation, 3 mg of K+R, 5 mg of spiropyran, and 6.5 mg ETH 500 was dissolved in 50 mg of o-NPOE. The Celgard membrane was then rinsed with the organic solution. A Lambda DG-4 Plus Xenon Source (Sutter Instruments) was used as the illumination system so that rapid switching between UV light (ZET365/20x filter, Chroma Inc.) and visible light (FF01-482/35 BrightLine single-band bandpass filter, Semrock Inc.) can be achieved. The pH electrode (Figure S13.3) was prepared based on plastic pipette tip. The pH sensitive membrane was make through dipping the pipette tip into a THF cocktail and left it in the air for the THF to evaporate. The THF cocktail contained 2 mg of a pH sensitive dye called Ox in previous report<sup>30</sup>, 0.7 mg of K+R-, 50 mg of PVC and 100 mg of bis(2-ethylhexyl) sebacate. After drying, the pipette tip was filled with 10 mM pH 7 Tris-HCl buffer containing 10 mM NaCl as inner solution. A Ag/AgCl wire was inserted into the solution without contacting the membrane. Solutions were prepared by dissolving appropriate salts in deionized water.

An Autolab (Mettler-Toledo AG, Schwerzenbach, Switzerland) was used to measure the photocurrent. In order to measure the short circuit current, the working electrode and the ground electrode from the Autolab were connected to the two Ag/AgCl wires in the cell shown in Figure 13.2 (a). Light from the Lambda DG-4 was guided through liquid waveguides onto the surface of the membrane, and the current was recorded. For the generation of alternating currents, the incident light was switched from UV to visible repeatedly with fixed time intervals. Energy of light is measured with a power meter (FieldMaster, Coherent®, USA). To measure the open-circuit voltage, chronopotentiometry was used with the current set at 0 A (<10 nA variation). The J-V curve is measured in linear potential sweep mode with applied voltage changing from the  $V_{\rm oc}$  to 0.

For experiments in Figure S13.2, a small volume of saturated fluorescein solution (10 µL) was dropped onto a microscope glass slide, on top of which was placed a membrane with the above mentioned composition. The other side of the membrane was in contact with 1 M NaCl. Fluorescein was chose to avoid spectrum overlap. The glass slide was then mounted onto an inverted fluorescence microscope where UV or visible light can illuminate from the fluorescein solution side, acting both as excitation light for fluorescein and activation light for spiropyran.

# 13.5.2 Supplementary Figures

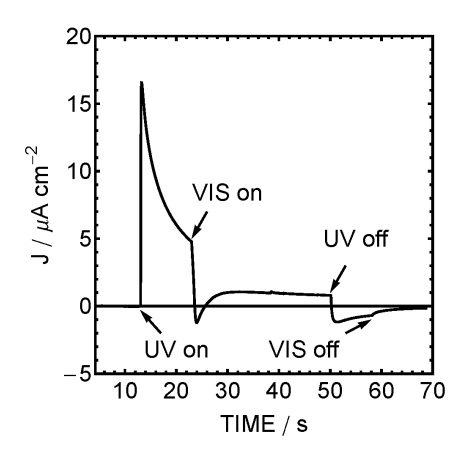


**Figure S13.1.** Photocurrent generated from a membrane without addition of K<sup>+</sup>R<sup>-</sup>, the membrane was in contact with 0.1 M HCl solution.

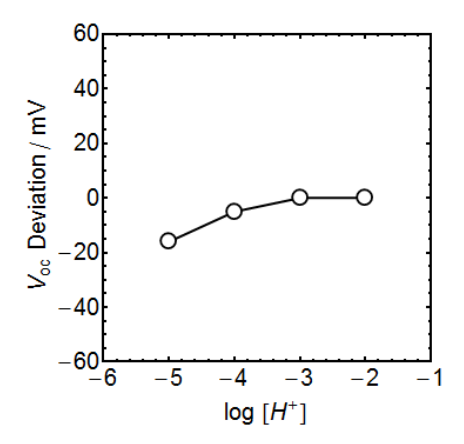
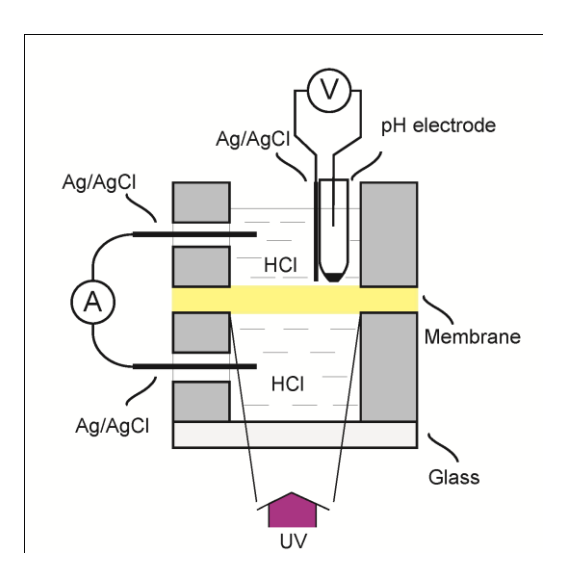
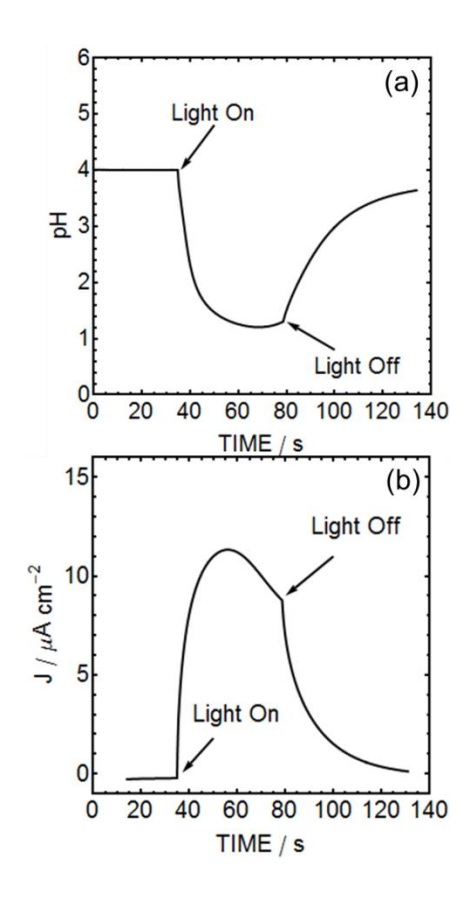


Figure S13.2. Deviation of open circuit voltage ( $V_{oc}$ ) measured as the HCl concentrations were diluted from  $10^{-2}$  M to  $10^{-5}$  M.



**Figure S13.3.** Representation of the setup used to directly measure pH variation shown in Figure S13.4. The HCl concentration is  $10^{-4}$  M in both chambers. The distance between the tip of the pH electrode is less than 0.5 mm.



**Figure S13.4.** (a) Light triggered pH variation measured with setup shown in Figure S13.3. (b) Short Circuit photocurrent density acquired in the same experiment.

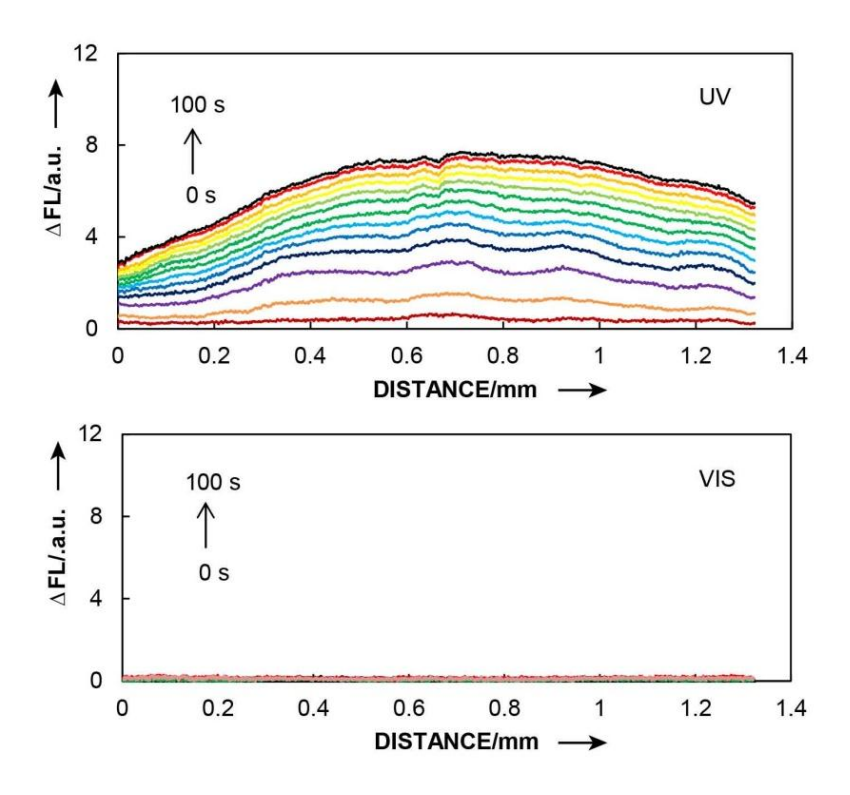


**Figure S13.5.** Fluorescence change of small volume of fluorescein solution caused by the light induced proton transport of the contacting membrane, note that the time intervals between adjacent lines are not equal.

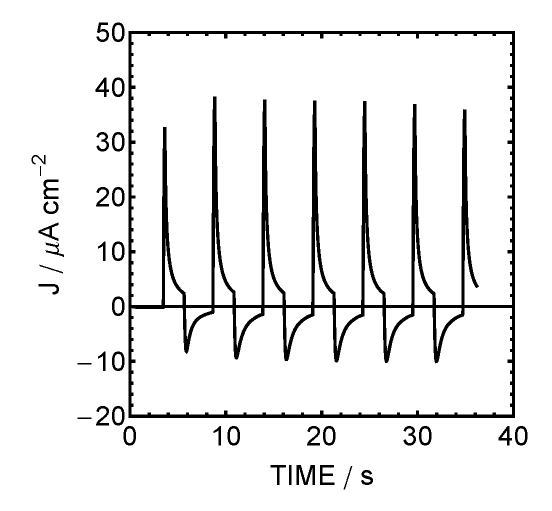


Figure S13.6. Alternating photocurrent generation by the membrane in 0.1 M HCl with alternating UV and visible light illuminating (UV for 0.2 s + off 2 s + VIS 2 s + off 1 s) on one side of the membrane.

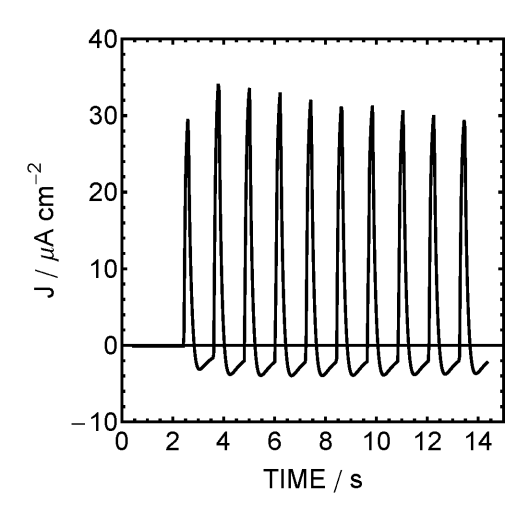


Figure S13.7. Alternating photocurrent generation by the membrane in 0.1 M HCl with alternating UV and visible light illuminating (UV for 0.2 s + VIS 1 s) on one side of the membrane.

# 13.5.3 Derivation of Eqn. 13.2

At steady state, the McH<sup>+</sup> concentration gradient within the membrane is expected to be linear. According to Fick's first Law, the flux for McH<sup>+</sup> can then be written as:

$$J = -D_{McH} \frac{[McH^+]_{UV} - [McH^+]_{vis}}{d}$$

where, J is the flux of McH<sup>+</sup>;  $D_{\text{McH}}$  is the diffusion coefficient of McH<sup>+</sup> in the membrane; d is the membrane thickness;  $[\text{McH}^+]_{\text{UV}}$  and  $[\text{McH}^+]_{\text{vis}}$  are the McH<sup>+</sup> concentration at the UV and visible side, respectively.

Assuming complete conversion from McH<sup>+</sup> to Sp at the visible side, [McH<sup>+</sup>]<sub>vis</sub> is 0 and the flux can be simplified to:

$$J = -D_{McH} \frac{[McH^+]_{UV}}{d}$$

The change of McH<sup>+</sup> concentration at the UV side with time is given as:

$$\frac{d[McH^+]_{UV}}{dt} = k[Sp]_T - J$$

with [Sp]<sub>T</sub> being the spiropyran concentration and k the heterogeneous reaction rate shown in Eqn. 13.1.

At steady state, the concentration change is 0 and we obtain the current density j:

$$j = JF = -FD_{McH} \frac{[McH^+]_{UV}}{d} = Fk_1 [Sp]_T$$

## 13.5.4 Numerical Simulation for the Photocurrent Evolution:

## Symbols:

deltam: membrane thickness

dstep: thickness of each element

dt : duration of each time step

Dmh: diffusion coefficient of proton

Dmmc: diffusion coefficient of Mc

Dmmch: diffusion coefficient of McH+

Dmr: diffusion coefficient of anionic site R

Dmsp: diffusion coefficient of Sp

k1: rate constant for the reaction from Sp to Mc

k2 : rate constant for the reaction from Mc/McH<sup>+</sup> to Sp

rm: initial concentration of R

spm: initial concentration of Sp

ka: dissociation constant of McH+

xmax: number of the last element

tmax: number of the last time step

Rst: resistance of the membrane

F: Faraday's constant

A: area of illumination

mc [t, x]: concentration of Mc at position x for time step t

mch [t, x]: concentration of McH<sup>+</sup> at position x for time step t

sp [t, x]: concentration of Sp at position x for time step t

h [t, x]: concentration of H<sup>+</sup> at position x for time step t

r [t, x]: concentration of R at position x for time step t

i[t]: current at time step t

 $dtaumsp = Dmsp dt / dstep^2$ 

 $dtaummc = Dmmc dt / dstep^2$ 

 $dtaummch = Dmmch dt / dstep^2$ 

 $dtaumh = Dmh dt / dstep^2$ 

 $dtaumr = Dmr dt / dstep^2$ 

Decimeters are used for all units of length. The values of the constants are listed as follows:

 $deltam = 3 \times 10^{-4} dm$ 

 $dstep = 3 \times 10^{-5} dm$ 

dt = 0.01s

 $Rst = 3 \times 10^3 \,\Omega$ 

 $Dmh = 2 \times 10^{-8} dm^2 \cdot s^{-1}$ 

Dmmc =  $1 \times 10^{-9} \text{ dm}^2 \cdot \text{s}^{-1}$ 

Dmmch =  $1 \times 10^{-9} \text{ dm}^2 \cdot \text{s}^{-1}$ 

 $Dmr = 1 \times 10^{-9} dm^2 \cdot s^{-1}$ 

Dmsp =  $1 \times 10^{-9} \text{ dm}^2 \cdot \text{s}^{-1}$ 

 $k1 = 10^{-1.1}$ 

 $k2 = 1 \text{ s}^{-1}$  (visible light) and  $10^{-6} \text{ s}^{-1}$  (dark)

 $rm = 0.01 \\ mol/kg$ 

spm = 0.07 mol/kg

 $ka = 10^{-11}$ 

$$A = 10^{-2} dm^2$$

$$F = 96485 \text{ C} \cdot \text{mol}^{-1}$$

## Initial conditions:

$$sp[0, x] = spm$$

$$mc [0, x] = 10^{-8} mol/kg$$

mch [0, x] = 
$$\frac{mc[0, x] rm}{ka + mc[0, x]}$$

$$r[0, x] = rm$$

$$i[0] = 0 A$$

## **Boundaries and Evolution:**

$$sp[t, 0] = sp[t-1, 0]e^{-k1 dt} + 2 dtaumsp(sp[t-1, 1] - sp[t-1, 0])$$

$$sp[t, x] = sp[t-1, x] + dtaumsp(sp[t-1, x-1] - 2 sp[t-1, x] + sp[t-1, x+1]), for x from 1 to xmax-1$$

$$h[t, 0] = h[t-1, xmax] 10^{-i[t] Rst/0.0592}$$

$$mch\ [t,0] = h\ [t,0]\ sp\ [t-1,0]\ (1-e^{-k1\ dt})\ /\ (h\ [t,0]+ka) + mch\ [t-1,0] + 2\ dtaummch\ (mch[t-1,1]-mch[t-1,0])$$

$$mc[t, 0] = ka sp[t-1, 0] (1-e^{-k1dt}) / (h[t, 0] + ka) + mc[t-1, 0] + 2 dtaummc (mc[t-1, 1] - mc[t-1, 0])$$

$$mc[t, x] = mc[t-1, x] + dtaummc (mc[t-1, x-1] - 2 mc[t-1, x] + mc[t-1, x+1]), for x from 1 to xmax-1$$

$$mch[t, x] = mch[t-1, x] + dtaummch(mch[t-1, x-1] - 2 mch[t-1, x] + mch[t-1, x+1]), for x from 1 to xmax-1$$

h[t, x] = ka mch[t, x] / mc[t, x], for x from 1 to xmax-1

$$mc[t, xmax] = mc[t-1, xmax] e^{-k2 dt} + 2 dtaummc (mc[t-1, xmax-1] - mc[t-1, xmax])$$

$$mch \ [t,xmax] = mch \ [t-1,xmax] \ e^{-k2 \ dt} + 2 \ dtaummch \ (mch \ [t-1,xmax-1] - mch \ [t-1,xmax])$$

$$r[t, 0] = mch[t, 0] + h[t, 0]$$

$$r[t, x] = r[t-1, x] + dtaumr(r[t-1, x-1] - 2r[t-1, x] + r[t-1, x+1]), for x from 1 to xmax-1$$

$$r[t, xmax] = (xmax + 1) rm - \sum_{x=0}^{xmax-1} r[t, x]$$

$$h\left[t, xmax\right] = h\left[t\text{-}1, xmax\right] + 2 \; dtaumh \; (h\left[t\text{-}1, xmax - 1\right] - h\left[t\text{-}1, xmax\right]) + mch\left[t\text{-}1, xmax\right] \; (1-e^{-k2 \; dt})$$

$$sp[t,xmax] = sp[t-1,xmax] + 2 dtaumsp(sp[t-1,xmax-1] - sp[t-1,xmax]) + (mc[t-1,xmax] + mch[t-1,xmax](1-e^{-k2 dt})$$

## 13.6 References for Chapter 13

- (1) Alberts, B.; Johnson, A.; Lewis, J.; Raff, M.; Roberts, K.; Walter, P. In *Molecular Biology of the Cell*; 5 ed.; Garland Science, Taylor&Francis Groups, LLC: 2007.
- (2) Garg, V.; Kodis, G.; Chachisvilis, M.; Hambourger, M.; Moore, A. L.; Moore, T. A.; Gust, D. J. Am. Chem. Soc. 2011, 133, 2944.
- (3) Moore, G. F.; Hambourger, M.; Gervaldo, M.; Poluektov, O. G.; Rajh, T.; Gust, D.; Moore, T. A.; Moore, A. L. *J. Am. Chem. Soc.* **2008**, *130*, 10466.
- (4) Rutherford, A. W.; Moore, T. A. *Nature* **2008**, *453*, 449.
- (5) Moore, G. F.; Brudvig, G. W. Annu. Rev. Condens. Matter Phys 2011, 2, 303.
- (6) Steinberg-Yfrach, G.; Liddell, P. A.; Hung, S.-C.; Moore, A. L.; Gust, D.; Moore, T. A. Nature 1997, 385, 239.
- (7) Bennett, I. M.; Farfano, H. M. V.; Bogani, F.; Primak, A.; Liddell, P. A.; Otero, L.; Sereno, L.; Silber, J. J.; Moore, A. L.; Moore, T. A.; Gust, D. *Nature* 2002, 420, 398.
- (8) Tan, S. C.; Crouch, L. I.; Mahajan, S.; Jones, M. R.; Welland, M. E. ACS Nano 2012, 6, 9103.
- (9) LeBlanc, G.; Chen, G.; Gizzie, E. A.; Jennings, G. K.; Cliffel, D. E. Adv. Mater. 2012, 24, 5959.
- (10) Tan, S. C.; Crouch, L. I.; Jones, M. R.; Wellland, M. Angew. Chem. Int. Ed. 2012, 51, 6667.
- (11) Valentin, M. D.; Bisol, A.; Agostini, G.; Liddell, P. A.; Kodis, G.; Moore, A. L.; Moore, T. A.; Gust, D.; Carbonera, D. *J. Phys. Chem. B* **2005**, *109*, 14401.
- (12) Berkovic, G.; Krongauz, V.; Weiss, V. Chem. Rev. 2000, 100, 1741.
- (13) Kalisky, Y.; Orlowski, T. E.; Williams, D. J. J. Phys. Chem. 1983, 87, 5333.
- (14) Mistlberger, G.; Crespo, G. A.; Xie, X.; Bakker, E. Chem. Commun. 2012, 48, 5662.
- (15) Xie, X.; Mistlberger, G.; Bakker, E. J. Am. Chem. Soc. 2012, 134, 16929.
- (16) Xie, X.; Mistlberger, G.; Bakker, E. Anal. Chem. 2013, 85, 9932.
- (17) Toei, M.; Saum, R.; Forgac, M. Biochemistry 2010, 49, 4715.
- (18) Turina, P.; Samoray, D.; Graber, P. *EMBO* **2003**, 22, 418.
- Weinberg, D. R.; Gagliardi, C. J.; Hull, J. F.; Murphy, C. F.; Kent, C. A.; Westlake, B. C.; Paul, A.; Ess, D. H.; McCafferty, D. G.; Meyer, T. J. Chem. Rev. 2012, 112, 4016.
- (20) Morgan, J. E.; Vakkasoglu, A. S.; Lugtenburg, J.; Gennis, R. B.; Maeda, A. Biochemistry 2008, 47, 11598.
- (21) Dencher, N. A. Photochemistry and Photobiology 1983, 38, 753.
- (22) Oesterhelt, D. Angew. Chem. 1976, 88, 16.
- (23) Trisll, H.-W.; Montal, M. Nature 1977, 266, 655.
- (24) Gregg, B. A.; Hanna, M. C. J. Appl. Phys. 2003, 93, 3605.
- (25) He, F.; Yu, L. J. Phys. Chem. Lett. 2011, 2, 3102.
- (26) Nazeeruddin, M. K.; Baranoff, E.; Grätzel, M. Solar Energy 2011, 85, 1172.
- (27) Levitus, M.; Talhavini, M.; Negri, R. M.; Atvars, T. D. Z.; Aramendia, P. F. J. Phys. Chem. B 1997, 101, 7680.
- (28) Giordani, S.; Cejas, M. A.; Raymo, F. M. Tetrahedron 2004, 60, 10973.
- (29) McCoy, C. P.; Donnelly, L.; Jones, D. S.; Gorman, S. P. *Tetrahedron Lett.* **2007**, *48*, 657.
- (30) Xie, X.; Mistlberger, G.; Bakker, E. Anal. Chem. 2013, 85, 9932.

# Chapter 14. Photoelectric Conversion based on Proton-Coupled Electron Transfer Reactions

This work has been published in: Xiaojiang Xie\* and Eric Bakker\*, J. Am. Chem. Soc. 2014, 136, 7857-7860

Proton-coupled electron transfer (PCET) reactions are ubiquitous in chemistry and play important roles in many enzymatic pathways that control life.<sup>1-3</sup> Light-driven reduction of CO<sub>2</sub> by water in photosynthesis and oxidation of glucose by oxygen in respiration are quintessential examples of PCET reactions in nature. Because of the enormous potential it holds for catalysis and energy conversion, there has been extensive fundamental researches and growing understanding of the importance of various PCET reactions.<sup>4-6</sup>

A PCET reaction involves both electron transfer and proton transfer from or to a substrate, such as the redox reaction of the quinone/hydroquinone pair ( $Q/H_2Q$  in Eqn. 14.1).

$$H_2Q = \frac{-2e^-}{+2e^-} 2H^+ + Q \tag{14.1}$$

The reduction of plastoquinone occurs in the electron transport chain in light dependent reactions in photosynthesis. Other examples that involve metal complexes acting as catalyst have been established. 8-11

PCET reactions have been widely studied for applications in chemical science. They become essential in artificial photosynthesis to produce solar fuels, thereby converting light energy to chemical energy.<sup>12,13</sup> They have also been recently used to achieve long range charge separation in artificial light-harvesting systems.<sup>14</sup> However, photoelectric conversion on the basis of PCET reactions has not been reported before. Considering the enormous importance of solving the energy problem, the development of efficient solar cells is clearly one of the biggest scientific opportunities of our time. In this work, we show for the first time that PCET can be used to directly convert light energy to electrical energy.

Specifically, a Q/ $H_2Q$  pair was placed in contact with an indium tin oxide (ITO) electrode. The redox potential of Q/ $H_2Q$  at the ITO surface is defined by the Nernst equation as shown in Eqn. 14.2, where [Q] and [ $H_2Q$ ] are the concentrations of Q and  $H_2Q$ , respectively

$$E = E^{0} + \frac{RT}{2F} \ln \frac{[Q][H^{+}]^{2}}{[H_{2}Q]}$$
(14.2)

To produce the photovoltage, a photochromic spiropyran (Sp) was added to bring about a Q/H<sub>2</sub>Q redox potential change at the electrode. Under UV light irradiation, Sp will undergo a ring opening reaction to form the ring-opened merocyanine (Mc) form, <sup>15,16</sup> which is much more basic than the Sp form. <sup>17</sup> Based on this light induced basicity increase, photoswitchable ion sensors and potassium nano-cages have recently been reported (see Chapter 10 and 11). <sup>18-20</sup> We subsequently introduced an artificial light controlled proton pump in a polymeric membrane to convert light energy to electricity (see Chapter 13). <sup>21</sup> Despite the conceptual elegance of this approach, the design required two aqueous solutions bracketing the membrane and acting as source and sink for proton transport, and additional Ag/AgCl elements as ion to electron transducers. These elements are not optically transparent and will place a limit on the efficiency of the photoconversion system. The direct photoelectric conversion of a proton gradient to electrical current proposed here requires just a single solution phase that is sandwiched between two transparent electrodes.

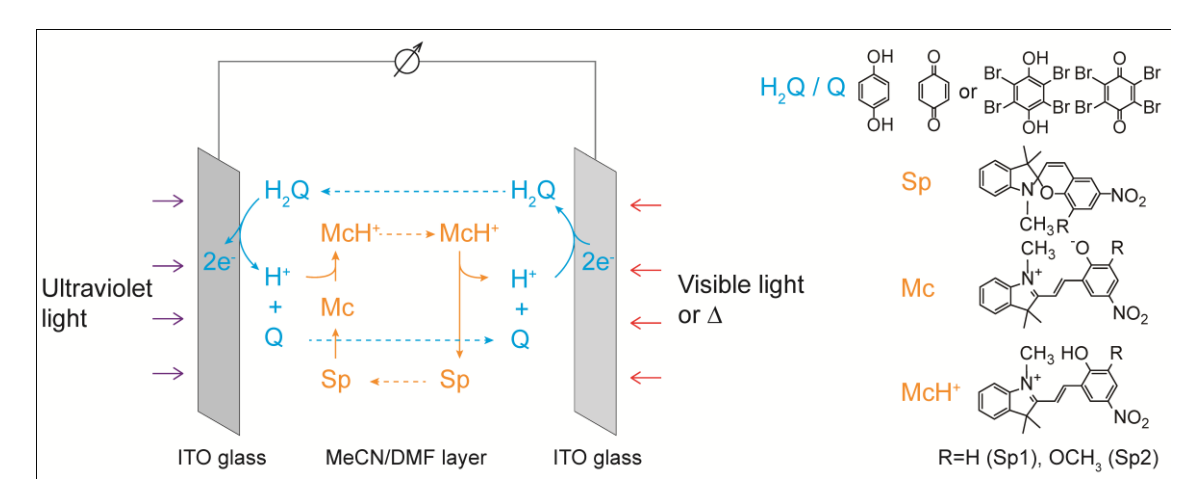


**Figure 14.1.** Schematic illustration of PCET based solar cell. Ultraviolet light (UV) is introduced from one side where Sp is transformed to Mc. The opposite side where the ring-opened form is transformed back to Sp is illuminated by visible light or left in dark ( $\Delta$ ). A photovoltage is formed with the electrode potential at the UV side lower than the other. Tetrabutylammonium hexafluorophosphate is used as supporting electrolyte.

As shown in Figure 14.1, the photoelectric cell is composed of two ITO glass electrodes separated by a thin layer (2 mm thick) of organic liquid (acetonitrile (MeCN) or N,N-dimethylformaldehyde (DMF)) containing spiropyran, the Q/H<sub>2</sub>Q redox pair and supporting electrolyte tetrabutylammonium hexafluorophosphate (Bu<sub>4</sub>N<sup>+</sup>PF<sub>6</sub>). One of the electrode sides is illuminated with UV light (365 nm  $\pm$  10 nm) and the other with visible light (>409 nm) or left in darkness. On the UV side, Sp will transform into the Mc form and reduce the local H<sup>+</sup> concentration because Mc is more basic than Sp. Therefore, the electrode potential at the UV side will decrease. The ring-opened form then diffuses to the opposite side where it will be converted back to the Sp form, resulting in an effective recycling process. At steady state, gradients will be established with an excess of Q and McH<sup>+</sup> on the UV side while H<sub>2</sub>Q and Sp prevail on the opposite side. The concentration asymmetry produces a photovoltage according to Eqn. 14.2.

The light induced open-circuit voltage using Sp1 and unsubstituted  $Q/H_2Q$  in MeCN is shown in Figure 14.2a. Upon UV irradiation, a  $V_{oc}$  of ca. 140 mV was immediately observed, while the  $V_{oc}$  dropped back to zero after UV was switched off. When the light input intensity was increased, a higher  $V_{oc}$  was observed (Supplementary Figure S14.1). No visible light was required on the other side of the ITO surface in this case. Spiropyrans are known to undergo light and thermally driven ring opening reactions. As shown in Figure 14.2b (see Figure S14.2 for spectra after light illumination), no intense absorbance around 550 nm was observed for Sp1 both in MeCN and DMF, indicating that the spontaneous ring closing reaction is sufficiently fast. Instead, visible light may partially leak into the UV illuminated side and suppress the activation of Sp. On the other hand, for the methoxyl substituted Sp2 (see Figure 14.1 for structure), intense absorption peaks that originated from the Mc form were observed in both MeCN and DMF (Figure 14.2b). In this case, visible light illumination on the opposite side was able to further increase the open-circuit voltage, as shown in Figure 14.2c. Since the ring closing reaction is in fact much slower than the ring opening reaction  $^{16}$ , the  $V_{oc}$  increase after applying visible light was slower compared with the increase upon UV irradiation. In DMF, a similar voltage increase was observed (see Supplementary Figure S14.3), but the  $V_{oc}$  value was smaller compared with the one in MeCN. In the absence of the PCET redox pairs, no photovoltage was observed. Moreover, decreasing the cell thickness to 0.5 mm caused cross-irradiation of both UV and VIS on the ITO glass and diminished the photovoltage, while increasing the thickness did not enhance the photovoltage.

A rapid PCET redox reaction rate at the ITO surface is very important in view of achieving a high short-circuit current density ( $J_{sc}$ ) and improved efficiency. The  $J_{sc}$  for the unmodified Q/H<sub>2</sub>Q pair was low (ca. 0.6  $\mu$ A cm<sup>-2</sup>), indicating a rather high PCET activation barrier. However, a structural modification of the PCET redox pair could potentially lower the reaction barrier and increase the current density. For

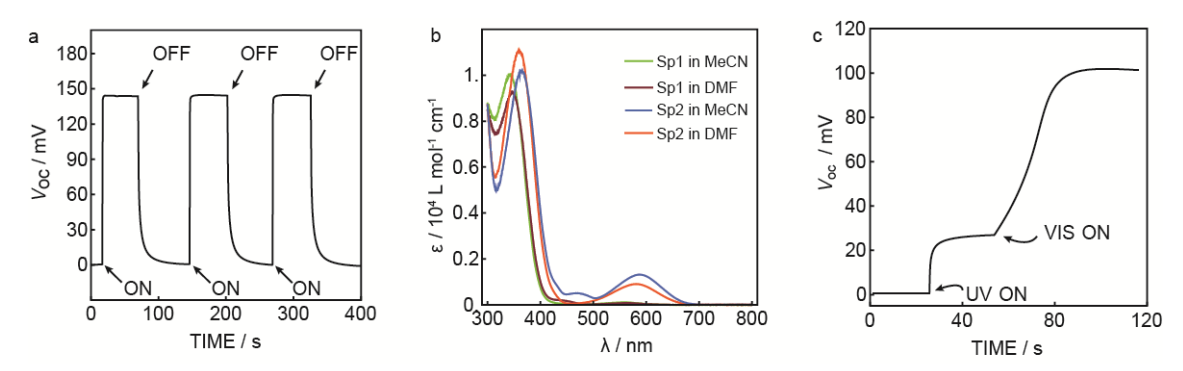


**Figure 14.2.** (a) Open-circuit voltage ( $V_{oc}$ ) evolution for a composition containing Sp1 (0.04 M), Q (0.01M), H<sub>2</sub>Q (0.01 M) and Bu<sub>4</sub>N<sup>+</sup>PF<sub>6</sub><sup>-</sup> (0.1 M) in MeCN with ultraviolet light (UV, 365 nm±10 nm, 5 mW cm<sup>-2</sup>). (b) Absorption spectra of Sp1 and Sp2 in MeCN and DMF. (c) Open-circuit voltage evolution for a composition containing Sp2 (0.03 M), BrQ (0.01), BrH<sub>2</sub>Q (0.01) and Bu<sub>4</sub>N<sup>+</sup>PF<sub>6</sub><sup>-</sup> (0.1M) in MeCN with UV (365 nm±10 nm, 5 mW cm<sup>-2</sup>) at one side and visible light (VIS, >409 nm, 10 mW cm<sup>-2</sup>) at the other.

instance, the bromide substituted quinone/hydroquinone pair (BrQ/BrH<sub>2</sub>Q, see Figure 14.1 for structure) was found to exhibit a much higher redox rate than the unsubstituted Q/H<sub>2</sub>Q. In a linear voltammetric scan (Figure 14.3 a), BrH<sub>2</sub>Q/BrQ showed higher cathodic and anodic current densities than H<sub>2</sub>Q/Q in the overpotential range of 0 to 0.15 V. The short-circuit photocurrent with BrH<sub>2</sub>Q/BrQ and Sp2 in MeCN is shown in Figure 14.3b. The current increased immediately upon UV illumination. Subsequently, likely because of the accumulation of Mc and McH $^+$  on the non-illuminated side of the cell, the current density started to drop after reaching a maximum. Indeed, illumination by visible light on the other side was able to accelerate the conversion from the ring opened forms to Sp, and thus again increase the current density. A current density of ca. 9  $\mu$ A cm $^{-2}$  was obtained when the system reached steady state.

The current photoelectric conversion cell exhibited a linear J-V curve and thus the fill factor<sup>23</sup> is ca. 50 %. Therefore, the efficiency<sup>23</sup> of the current system (0.02 %) is not yet comparable with existing solar cells. Compared with the previously reported proton pump based system, the lower efficiency is mainly due to larger electrode reaction barrier compared with Ag/AgCl.<sup>21</sup> Nevertheless, there are ways that can potentially increase efficiency, such as surface modification on the electrode material to reduce the PCET reaction barrier, structural modification on the redox pair and the light sensitive dye to enhance the quantum yield and increase the light triggered basicity change. While the photostability of spiropyran is known to be limited, the the photoelectric cell was surprisingly robust. No drastic deterioration was observed even after light exposure for several hours. Of course, spiropyrans are not the only compounds that exhibit a light induced basicity change. Other compounds such as azobenzenes<sup>24</sup> have also been reported to possess similar properties and thus, in principle, are

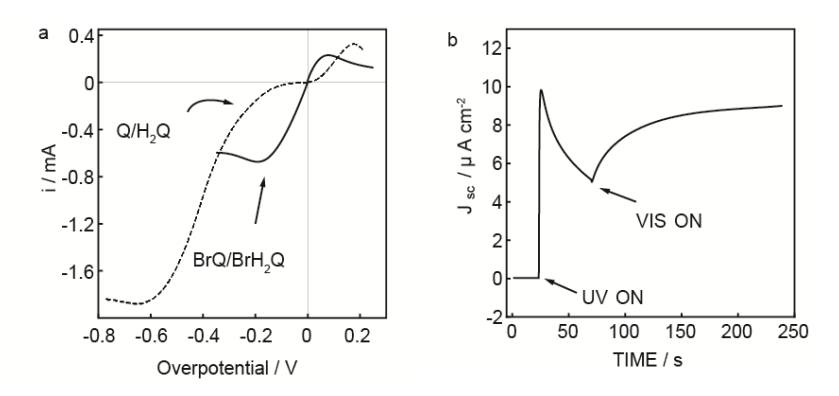


**Figure 14.3.** (a) Linear scan voltammetry of Q/H<sub>2</sub>Q (0.01 M) and BrQ/BrH<sub>2</sub>Q (0.01 M) in MeCN containing 0.02 M tridodecylmethyl ammonium chloride, reference electrode: Ag/AgCl. (b) Short circuit current density ( $J_{sc}$ ) for PCET based solar cell containing 0.01 M BrQ/BrH<sub>2</sub>Q, 0.03 M Sp2 and 0.1 M Bu<sub>4</sub>N<sup>+</sup>PF<sub>6</sub><sup>-</sup> in MeCN. Energy input: UV 5 mW cm<sup>-2</sup>, VIS 10 mW cm<sup>-2</sup>.

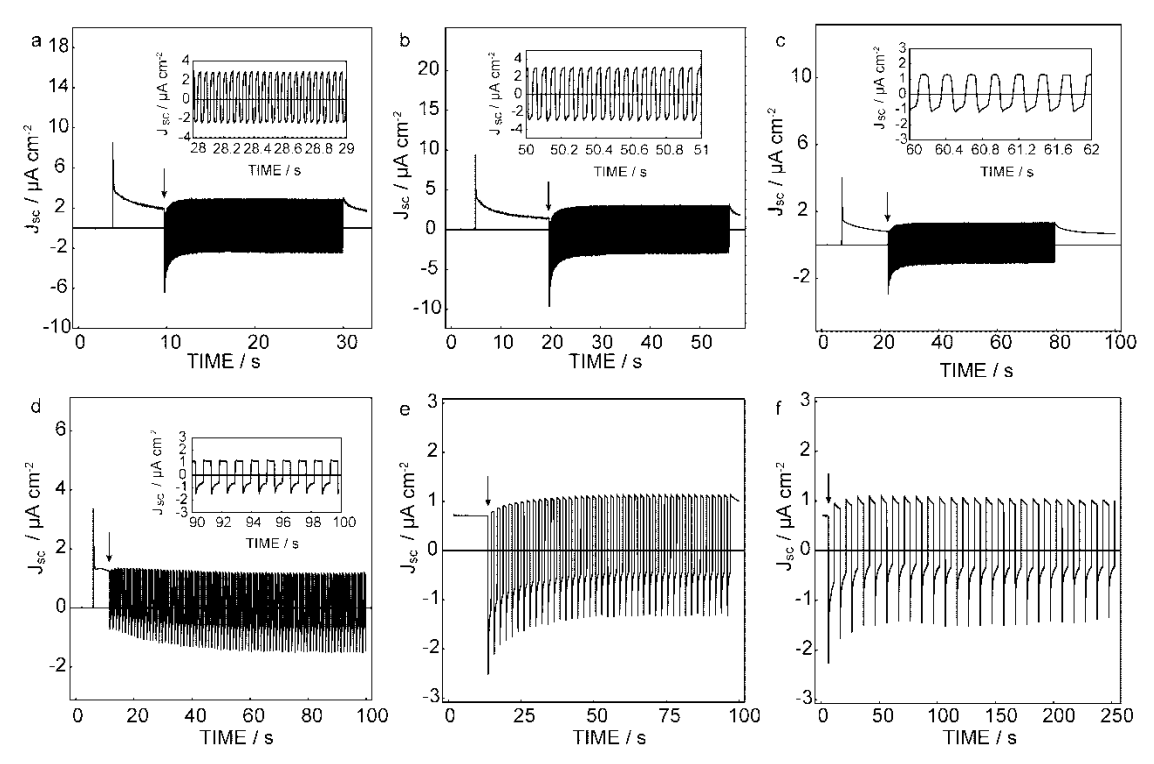


**Figure 14.4.** Alternating current generation from PCET based solar cell containing 0.01 M Q/H<sub>2</sub>Q, 0.04 M Sp1 and 0.1 M Bu<sub>4</sub>N<sup>+</sup>PF<sub>6</sub><sup>-</sup> in MeCN with different frequencies: (a) 24 Hz, (b) 20 Hz, (c) 5 Hz, (d) 1 Hz, (e) 0.5 Hz, (f) 0.1 Hz. One of the two ITO electrodes was illuminated with discontinuous UV light from DG-4 while the other constantly with UVlight.

also suitable for this type of application.

In addition to direct current, we demonstrate here that alternating current (AC) can be obtained through the control of light. Although alternating current can be obtained in other ways with excellent efficiencies, a chemically innovative approach using light can result in new unanticipated directions. Light induced alternating current has been reported by discontinuous illumination or by switching the wavelength of the input light. The frequencies achieved so far are still quite low (0.1 to 0.2 Hz). For the PCET based system, alternating current was achieved by illuminating the ITO on both sides with discontinuous UV light (Figure 14.4). AC was also produced through alternatingly illuminating one ITO surface with UV and visible light (see Supplementary Figure S14.4). Compared to previous systems, a much wider range of alternating frequency from 0.1 Hz up to 200 Hz was achieved with the PCET based solar cell. (See Supplementary Figure S14.5 for 200 Hz AC acquired in fast chronoamperommetry mode).

In conclusion, photoelectric conversion using proton-coupled electron transfer reactions was introduced here for the first time. In order to utilize the PCET reactions, spiropyrans that showed a basicity increase upon UV illumination were utilized to alter the local proton concentration in organic solutions containing the PCET redox couple. Since the redox potentials are dependent on the proton concentration for PCET, a photovoltage was produced between the two transparent electrodes. In addition to direct current, alternating current with frequencies from 0.1 to 200 Hz was achieved with the photoelectric conversion cell. Besides spiropyran, the principle should work with other materials that exhibit light induced basicity changes as well. A catalyst deposited on the ITO should potentially be able to lower the PCET redox barrier, increasing the attainable photocurrent. Further efforts (chemical modification on the PCET redox pair, light sensitive compounds, electrode materials and reaction media) are envisioned to help improve the characteristics of photoelectric conversion systems based on this principle. We estimate that this work opens up new possibilities for photoelectric conversion that could take advantages of PCET reactions.

## 14.1 Supporting Information for Chapter 14

### 14.1.1 Experimental Section

**14.1.1.1 Reagents.** Indium tin oxide coated glasses (surface resistivity 8-12  $\Omega$ /sq), 1',3'-Dihydro-1',3',3'-trimethyl-6-nitrospiro[2H-1-benzopyran-2,2'-(2H)-indole] (Sp1), 1',3'-Dihydro-8-methoxy-1',3',3'-trimethyl-6-nitrospiro[2H-1-benzopyran-2,2'-(2H)-indole] (Sp2), hydroquinone (H<sub>2</sub>Q), p-benzoquinone (Q), 2,3,5,6-tetrabromo-(1,4)benzoquinone (BrQ), tetrabromohydroquinone (BrH<sub>2</sub>Q), tetrachlorohydroquinone (ClH<sub>2</sub>Q), tetrachloro-1,4-benzoquinone (ClQ), tetrabutylammonium hexafluorophosphate (Bu<sub>4</sub>N<sup>+</sup>PF<sub>6</sub><sup>-</sup>), N,N-dimethylformamide (DMF) and acetonitrile (MeCN) were purchased from Sigma-aldrich. Solutions were prepared by dissolving appropriate salts in deionized water.

**14.1.1.2 Instrumentations and Measurements.** UV light was obtained from a UV led (365 nm  $\pm$  10 nm) or from Lambda DG-4 Plus Xenon Source (Sutter Instruments) with a ZET365/20x filter from Chroma Inc.. Visible light was obtained from Lambda DG-4 Plus Xenon Source equipped with a FF02-409 blocking edge BrightLine<sup>®</sup> long-pass filter (Semrock Inc.). Rapid switching between UV light and visible light was achieved with Lambda DG-4. The absorbance was measured with a UV-Vis spectrometer (SPECORD 250 plus, Analytic Jena, AG, Germany).

The photoelectric conversion cell was homemade with two pieces of ITO glass separated by a silicon rubber joint (2 mm in thickness). A total surface area of 2 cm<sup>2</sup> was used for light illumination. The surface of the ITO coated glass was connected with copper wire through conductive epoxy glue.

An Autolab (Mettler-Toledo AG, Schwerzenbach, Switzerland) was used to measure the photocurrent. To evaluate the short circuit current, the working electrode and the ground electrode from the Autolab were connected to the two ITO electrodes. Open-circuit voltage was measured with an EMF-16 precision electrochemistry EMF interface from Lawson Labs Inc. To generate alternating currents, the incident light was switched from UV to visible repeatedly with fixed time intervals on one ITO electrode surface or with one ITO electrode illuminated with the UV led and the other with UV from DG-4 switching between on and off with fixed time intervals. Energy of light is measured with a power meter (FieldMaster, Coherent®, USA).

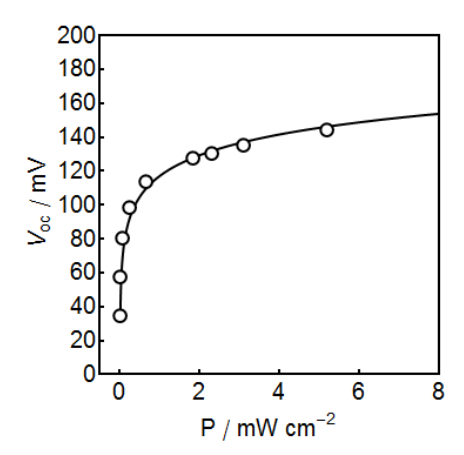


Figure S14.1. Open-circuit voltage dependence on UV light input power for a PCET based solar cell containing Sp1 (0.04 M), Q (0.01M),  $H_2Q$  (0.01 M) and  $Bu_4N^+PF_6^-$  (0.1 M) in MeCN.

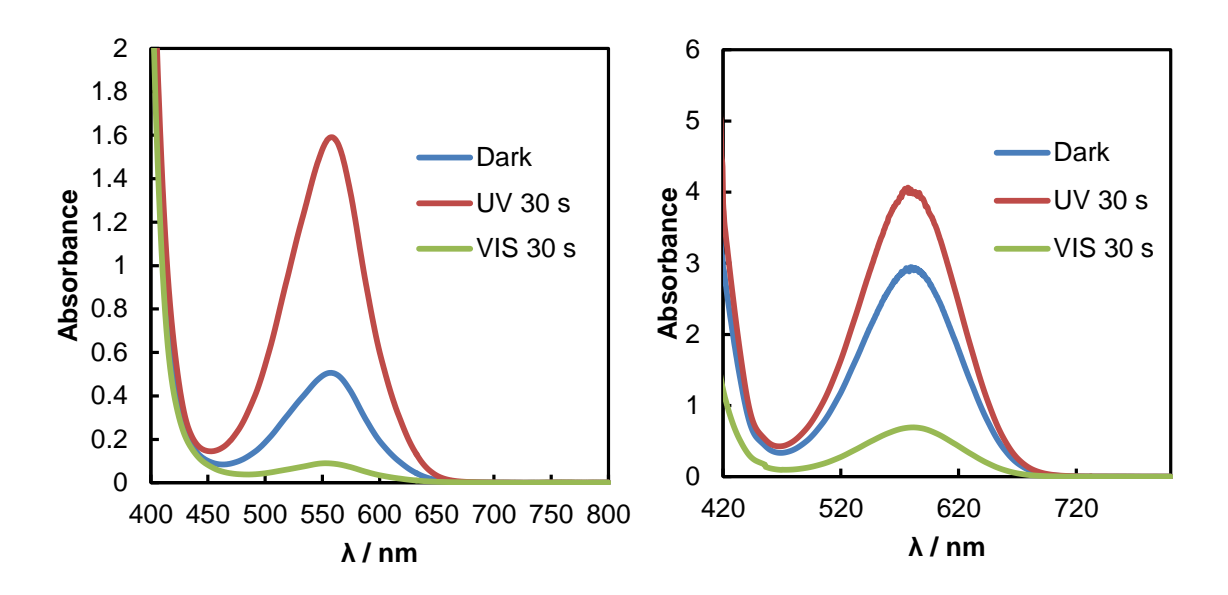


Figure S14.2. Absorption spectra in open circuit condition for cell composition in the dark, after 30 s UV illumination and after 30 s VIS illumination. (left): Sp1 0.04 M, Q 0.01 M,  $H_2Q$  0.01 M and  $Bu_4NPF_6$  0.1 M. (right): Sp2 0.03 M, BrQ 0.01 M,  $BrH_2Q$  0.01 M. Solvent: MeCN.

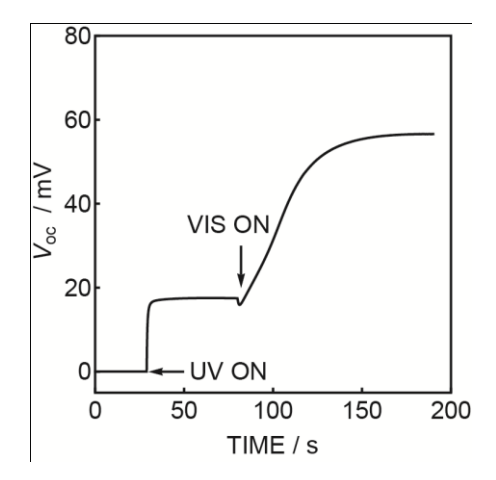
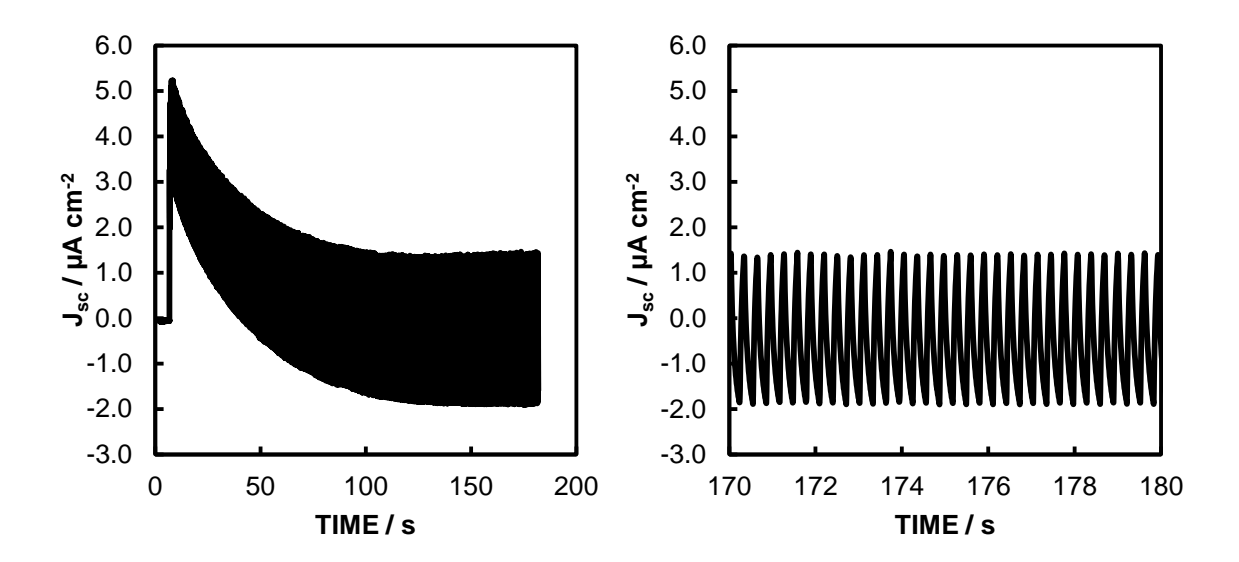
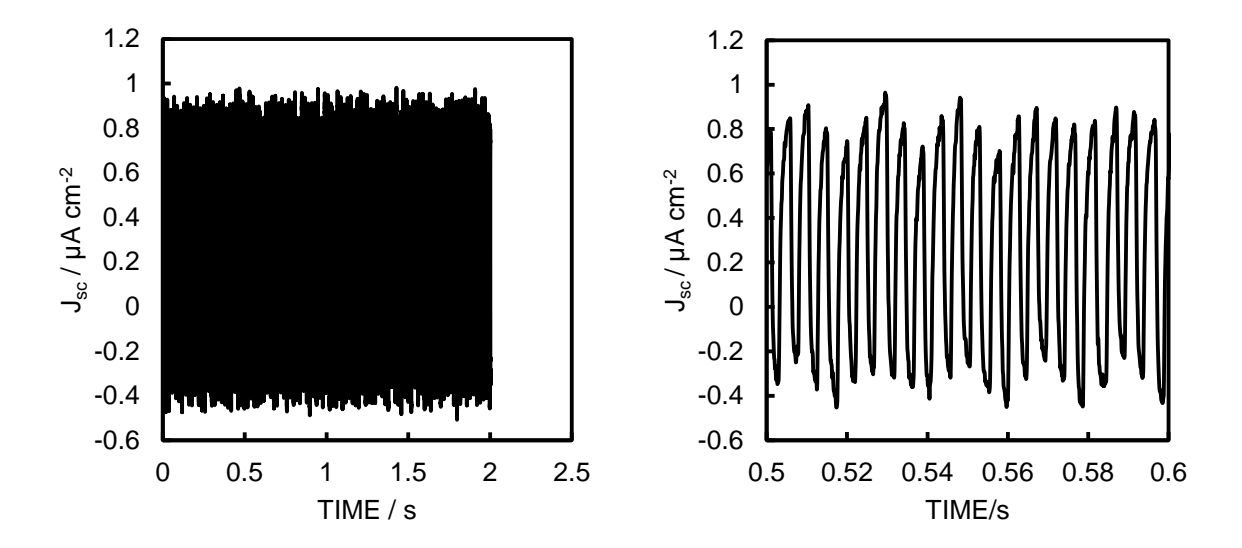


Figure S14.3. Open-circuit voltage evolution for a composition containing Sp2 (0.03 M), BrQ (0.01), BrH<sub>2</sub>Q (0.01) and Bu<sub>4</sub>N<sup>+</sup>PF<sub>6</sub><sup>-</sup> (0.1M) in DMF with UV (365 nm  $\pm 10$  nm, 5 mW cm<sup>-2</sup>) at one side and visible light (VIS, >409 nm, 10 mW cm<sup>-2</sup>) at the other.



**Figure S14.4.** (left) Alternating current generation from PCET based solar cell containing 0.02 M BrQ/BrH<sub>2</sub>Q, 0.08 M Sp2 and 0.1 M Bu<sub>4</sub>N<sup>+</sup>PF<sub>6</sub><sup>-</sup> in DMF. UV (5 mW cm<sup>-2</sup>, 0.5 s) and VIS (10 mW cm<sup>-2</sup>, 1 s) was alternatingly illuminating on one side of the ITO electrode. (right) Zooming from 170 s to 180 s from Fig. S14.3(left).



**Figure S14.5.** (left) Alternating current generation from PCET based solar cell containing 0.01 M Q/H<sub>2</sub>Q, 0.04 M Sp1 and 0.1 M  $Bu_4N^+PF_6^-$  in MeCN. One of the two ITO electrodes was illuminated with discontinuous UV light (5 mW cm<sup>-2</sup>, 0.5 s) from DG-4 while the other constantly with UV. (right) Zooming from 0.5 s to 0.6 s from Fig. S14.4(left).

## 14.2 References for Chapter 14

- Weinberg, D. R.; Gagliardi, C. J.; Hull, J. F.; Murphy, C. F.; Kent, C. A.; Westlake, B. C.; Paul, A.; Ess, D. H.; McCafferty, D. G.; Meyer, T. J. Chem. Rev. 2012, 112, 4016.
- (2) Hammes-Schiffer, S. Chem. Rev. 2010, 110, 6937.
- (3) Belevich, I.; Verkhovsky, M. I.; Wikström, M. Nature 2006, 440, 829.
- (4) Siegbahn, P. E. M.; Blomberg, M. R. A. Chem. Rev. 2010, 110, 7040.
- (5) Wongnate, T.; Surawatanawong, P.; Visitsatthawong, S.; Sucharitakul, J.; Scrutton, N. S.; Chaiyen, P. J. Am. Chem. Soc. 2014, 136, 241.
- (6) Ishida, M.; Kim, S.-J.; Preihs, C.; Ohkubo, K.; Lim, J. M.; Lee, B. S.; Park, J. S.; Lynch, V. M.; Roznyatovskiy, V. V.; Sarma, T.; Panda, P. K.; Lee, C.-H.; Fukuzumi, S.; Kim, D.; Sessler, J. L. *Nat. Chem.* **2013**, *5*, 15.
- (7) Lightbody, J. J.; Krogmann, D. W. Biochim. Biophys. Acta 1966, 120, 57.
- (8) Concepcion, J. J.; Jurss, J. W.; Brennaman, M. K.; Hoertz, P. G.; Patrocinio, A. O. T.; Iha, N. Y. M.; Templeton, J. L.; Meyer, T. J. Acc. Chem. Res. 2009, 42, 1954.
- (9) Concepcion, J. J.; Brennaman, M. K.; Deyton, J. R.; Lebedeva, N. V.; Forbes, M. D. E.; Papanikolas, J. M.; Meyer, T. J. J. Am. Chem. Soc. 2007, 129, 6968.
- (10) Wenger, O. S. Acc. Chem. Res. 2013, 46, 1517.
- (11) Kuss-Petermann, M.; Wolf, H.; Stalke, D.; Wenger, O. S. J. Am. Chem. Soc. 2012, 134, 12844.
- (12) Zhang, M.; Respinis, M. d.; Frei, H. Nat. Chem. 2014, 6, 362.
- (13) Duan, L.; Bozoglian, F.; Mandal, S.; Stewart, B.; Privalov, T.; Llobet, A.; Sun, L. Nat. Chem. 2012, 4, 418.
- Jr, J. D. M.; Méndez-Hern ández, D. D.; Tejeda-Ferrari, M. E.; Teillout, A.-L.; Llansola-Portol &, M. J.; Kodis, G.; Poluektov, O. G.; Rajh, T.; Mujica, V.; Groy, T. L.; Gust, D.; Moore, T. A.; Moore, A. L. Nat. Chem. 2014, 6, 423.
- (15) Berkovic, G.; Krongauz, V.; Weiss, V. Chem. Rev. 2000, 100, 1741.
- (16) Kalisky, Y.; Orlowski, T. E.; Williams, D. J. J. Phys. Chem. 1983, 87, 5333.
- (17) Mistlberger, G.; Crespo, G. A.; Xie, X.; Bakker, E. Chem. Commun. 2012, 48, 5662.
- (18) Xie, X.; Mistlberger, G.; Bakker, E. J. Am. Chem. Soc. 2012, 134, 16929.
- (19) Xie, X.; Mistlberger, G.; Bakker, E. Anal. Chem. 2013, 85, 9932.
- (20) Xie, X.; Bakker, E. ACS Appl. Mater. Interfaces 2014, 6, 2666.
- (21) Xie, X.; Crespo, G. A.; Mistlberger, G.; Bakker, E. Nat. Chem. 2014, 6, 202.
- (22) Minkin, V. I. Chem. Rev. 2004, 104, 2751.
- (23) Gratzel, M. Acc. Chem. Res. 2009, 42, 1788.
- (24) Emond, M.; Saux, T. L.; Allemand, J.-F.; Pelupessy, P.; Plasson, R.; Jullien, L. Chem. Eur. J. 2012, 18, 14375.
- (25) Tan, S. C.; Crouch, L. I.; Jones, M. R.; Wellland, M. Angew. Chem. Int. Ed. 2012, 51, 6667.
- (26) Wen, L.; Hou, X.; Tian, Y.; Zhai, J.; Jiang, L. Adv. Funct. Mater. 2010, 20, 2636.
- (27) Wen, L.; Tian, Y.; Guo, Y.; Ma, J.; Liu, W.; Jiang, L. Adv. Funct. Mater. 2013, 23, 2887.

# Acknowledgements

The thesis work was carried out at the University of Geneva in Switzerland. This wouldn't have happened if not for the sake of the following people, to whom I wish to express my sincere gratitude.

First of all, I thank my advisor Prof. Eric Bakker. He is the one who brought me to his research group and this field of chemistry. I joint the group as a Master student in 2010, but I was treated and paid as a Ph.D student. During the past five years, he has given me numerous instructions, help, supports and the freedom to follow the research directions I like. Working with him has been a real delight and I will surely miss this feeling in the years to come. His enthusiasm and prudence in science will guide my own research paths.

I thank my collegues for the memorable good times inside and outside the labs. These people include Magali Cissokho, Ewa Grygolowicz-Pawlak, Marcin Pawlak, Marylou Tercier, Günter Mistlberger, Gaston Crespo, Thomas Cherubini, Zdenka Jarolimova, Romain Touilloux, Majid Ghahraman Afshar, Bastien Néel, Nadja Pankratova, Jingying Zhai, Miquel Coll Crespi, Sandrine Mongin, Mar á Cuartero, Agust í Guti érez, Dennis Dorokhin, Istvan Szil ágyi, Christoph Bauer, Dawid Kedracki. I thank Prof. Thierry Soldati and Prof. Corrine Nardin for their collaboration. I thank Prof. J érôme Lacour, Prof. Thomas B ürgi and their group members for the research rotations in their labs. If I carelessly missed the name of anyone, please excuse me.

I also thank Prof. Yu Qin for her recommendation to my current advisor and the training I received during my stay in her group at Nanjing University.

And last but not least, I thank my parents for supporting their only child's life far away from home.